Kent Academic Repository

Paupiah, Tobias Andre Tyler (2023) *Structure-property correlations in novel multiferroic materials.* **Master of Research (MRes) thesis, University of Kent,.**

Structure-property correlations in novel multiferroic materials

Chemistry MRes
Tobias Paupiah

A thesis submitted in accordance of the requirements for the degree of masters of research at the university of Kent

Supervisor: Donna C. Arnold
Second supervisor: Paul J. Saines

School of Physical Sciences
University of Kent

Abstract

Ferroic materials have been the subject of decades of intense research into their elastic, magnetic and electronic properties. Primary ferroics are mandated by the presence of one of the aforementioned properties through a single order parameter, usually below a threshold temperature, T_N or T_C.

Further discoveries led to the conception of multiferroic materials that allow for two or more of these properties to be present simultaneously in a single phase. This is important as it allows one to use a single material for multiple functions in a device. Thus saving energy, resources, and space. One such material is $BiFeO_3$ which is multiferroic at room temperature demonstrating magnetic character and electrical behaviour simultaneously. Comprehensive structural analysis of 5% Dy^{3+} doped $BiFeO_3$ along with structural, electronic and magnetic characterisations are reported. The material is shown to crystallise in the $R3c$ symmetry between 5 – 773 K. A broad phase change to $Pbnm$ was observer above this temperature range. The magnetic spin cycloid is preserved with a longer periodicity than is seen for the pure counterpart. Observed magnetic hysteresis is likely due to uncompensated spins as a result of small domain sizes. Doping at this level demonstrates a potential decrease in ferroelectric character, but further measurements are needed to state this definitively. The T_N is increased showing that doping has an effect on the transition temperature. This is potentially due to the dysprosium ion becoming correlated by the iron oxide sublattice's magnetic moment.

We report magnetic properties of Rare Earth orthoferrites $ReFeO_3$ (Re= Dy, Sm) in a solid solution of 25:75, 50:50, and 75:25 % compositions of Dysprosium:Samarium. It was found that mixing these materials with a simple "*shake and bake*" method did not produce solid solutions and instead produced impure phases. As a result, the characterisation of these materials gave complex data further discussed in the complementary section.

An emerging area of multiferroics is where a fourth ferroic order termed ferrotoroidicity can possess an electric and magnetic response simultaneously through a single order parameter instead of two. This new ferroic property could potentially be used in energy and data storage, limiting energy consumption. One material being investigated with this property is $LiCoPO_4$ due to its large magnetoelectric coefficient. Structural and magnetic characterisation are reported for the parent material, as well as Sodium doped $LiCoPO_4$ for compositions containing up to 40% Na. A 10% Na incorporation limit is reported, with compositions above this percentage showing impure phases and polymorphic nature attributed to the Na contribution. The 10% composition shows similar properties to the parent materials with little to no variation in T_N.

Acknowledgments

I would like to thank my parents, wholeheartedly, who have loved and supported me every step of the way.

I would like to acknowledge those in my life who have been sources of both inspiration and motivation.

I would like to express my profound gratitude to my supervisor Donna Arnold for the guidance and support they have shown me in the past year and encouraged me to never give up.

I would like to thank the previous academics at the University of Kent who have taught me not only Chemistry throughout my Undergraduate years but who have also taught me about perseverance and resilience.

Lastly, I would like to thank my fellow peers who have been colleagues and friends to me over the past few years and have helped me develop on my journey at the University of Kent.

CHAPTER 5   **72**

ACOPO$_4$ SERIES   **72**

Chapter 1

Introduction

New materials are important as they pave the way for modern day innovation. Materials science and condensed matter physics investigate the structure-property correlations of novel materials. Through these evaluations one can see how new technologies are able to improve and facilitate everyday life through means unseen by the unknowing eye. Improved material properties can lead to better devices with, for example, increased energy storage,[1] longer battery life,[2] better battery efficiency,[3] increased data storage, and decreased power consumption.[4]

A material is characterised by both its intrinsic and extrinsic properties. Intrinsic properties are based on the structural and chemical compositions which a crystal displays and are independent of the size and mass of the crystal i.e. its intramolecular bonding. Contrary to this, extrinsic properties are dependent on the amount of the material present *i.e* it's weight. Electricity and Magnetism are common intrinsic properties which occur due to the transport and orientation of electrons within a system.[5] These two properties will be the focus of this next section.

1.1 Electronic properties

The earliest mention of electricity is of the electric fish, referred to as *"thunderer of the nile"*, Reports of these fish span through millennia, in ancient Greek, Roman and Arabic societies.[6] The earliest known researcher of this effect is Thales of Miletus an ancient Greek philosopher. Circa 600 BC, he found that when amber is rubbed with animal fur, the friction produces an electrical effect, later referred to as static electricity.[7, 8] Millenia following this, electricity remained mostly undiscovered until an English scientist, William Gilbert, distinguished static electricity from the lodestone effect.[8] Lodestone is a magnetic form of the mineral magnetite, and in the past the Chinese have used the natural magnetic abilities of lodestones for use in a divination compass.[9] This led to investigations into new materials and what happens inside them on a microscopic level to give rise to their unique properties.

On the microscopic scale electrons are essentially a cloud of negatively charged energy, which inhabit the immediate space surrounding a positively charged atomic nucleus. When an external electric field is introduced, there is a separation, δ, of charges, q; this is named an induced dipole (μ), denoted as:

$$\mu = \delta q \qquad\qquad \text{Eqn. 1}$$

Bulk alignment of induced or permanent electric dipole moments parallel to the applied field results in a polarisation. This property allows these materials to store charge and electrical energy. However, prior to applying an external electric field, these materials contain randomly oriented dipole moments and are termed as electrical insulating dielectrics.

There are three classes of dielectric materials which exhibit electrical properties: piezoelectrics, pyroelectrics and ferroelectrics, each one belonging to a subdivision of the prior group, Figure 1.1.[5]
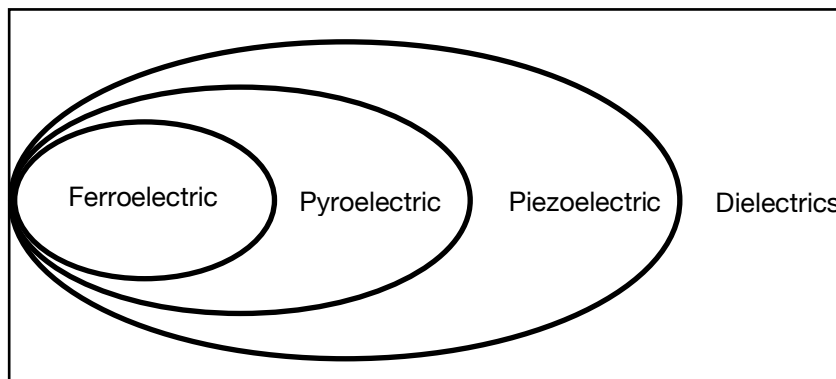
Figure 1.1 - Venn diagram showing the family of dielectric materials. Demonstrating the relationship between piezoelectric, pyroelectric, and ferroelectric. Ferroelectric materials will also exhibit properties of pyroelectrics and piezoelecrics.[5]

Firstly, dielectric materials exhibit no transport of electrons between the conduction and valence bands, in other-words the excited electrons do not move between a higher or lower energy state. They have no electrical conduction and are therefore classed as insulators. When an external electric field is applied, the dielectric material becomes polarised due to induced dipoles orienting themselves in the same direction as the field. Piezoelectrics are the largest subgroup of dielectrics, classified by materials which produce an electrical charge as a result of an applied mechanical stress. The reverse can also be seen, where an applied electric field can produce a mechanical strain within the material. The next subclass are pyroelectrics, the main feature of these materials is that they have a spontaneous dipole moment, which are shown to be sensitive to temperature. Essentially, they produce an

electrical charge as a result of a temperature change, this occurs due to the orientation of the spontaneous dipole moments, the more random the orientation, the lower the voltage of the material. This leads to the introduction of the Curie temperature (T_c), at this temperature there is a phase transition; in pyroelectrics between a state where the dipoles are arranged in a fully random manner, and consequently have a low voltage (high temperature), and state where the dipoles are highly ordered (low temperature). Lastly, ferroelectrics are a class of materials which, similarly to pyroelectrics, have spontaneous dipole moments which are temperature dependent. One key difference between them, however, is that ferroelectrics are able to undergo a reversible polarisation as a result of an applied electric field; above T_c they behave as normal dielectric materials.[5]

Due to the reversibility of the ferroelectric polarisation a hysteresis occurs, when plotting polarisation, P, against electric field (E). Ferroic materials have the ability to '*remember*' previous states, this allows them to show the history of the materials domains *via* a hysteresis profile, Figure 1.2.

Domains are sub-structures of unaligned (random) poles / spins, which align and orient themselves in the same direction after the application of an applied external field: electric or magnetic field.[5]
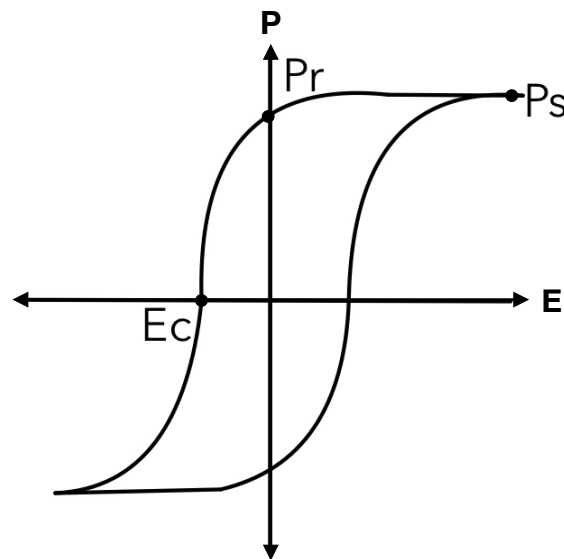
Figure 1.2 - A ferroelectric Hysteresis loop, demonstrating saturation polarisation, P_S, remnant polarisation, P_r, and the coercivity field, E_C.[5]

This profile demonstrates the relationship between the polarisation, *P*, of a material as a function of the applied electric field, *E*. On increasing *E*, the domains within the material

become aligned in the same direction in which E is propagating. When all domains are aligned it is said the material has saturation polarisation, P_S. When E is removed, the domains become randomly oriented, but still retain some polarisation in the propagating field direction. This is classified as the remnant polarisation, P_r. Furthermore, to nullify the polarisation a coercive field, E_c, is introduced so that $P=0$.[10] Eventually a high enough reverse field is applied such that the dipoles reorient in the opposite direction

1.2   Magnetic properties

Magnetism, as a whole, is more complex than electricity to define due to there being more contributions which lead to the effect. On the microscopic scale, the orbital angular momentum, L, denotes how an electron orbits the central atomic nucleus. The spin angular momentum, S, depicts how an electron spins on its axis; these two components are summed to equal the net angular moment, J, this is expressed as:

$$J = S + L$$

Eqn. 2

Using this equation, we can further explain that the magnetic moment, μ_m, of a single electron atom, e, with mass, m, is defined by:

$$\mu_m = \frac{e}{2m}J$$

Eqn. 3

Where, on the macroscopic scale, magnetisation (M) is denoted by:

$$M = x_m H$$

Eqn. 4

The magnetic susceptibility, x_m, of a material is a measure of how much the material will be magnetised by the applied magnetic field, H, expressed as:

$$x_m = \frac{M}{H}$$

Eqn. 5

Magnetisation is seen to be a somewhat similar phenomenon to polarisation, the main differences being that magnetic dipoles precess in a magnetic field whereas electric dipoles align with the electric field. This is not to say that the magnetic dipoles will not eventually tend to align with the field. For a ferromagnet the angle of precession will tend to decrease when the potential of the magnetic dipoles decreases. However, because of energy contributions from the thermal vibrations of the system they will not align completely. At lower temperatures the dipoles will be prone to align with the field because the thermal energy contribution is offset.[5]

There are two main types of induced magnetic phenomena: diamagnetism and paramagnetism, these occur due to electron contributions in the *d* and *f* orbitals of metal ions. Diamagnetic materials have no unpaired electrons in their respective *d* orbitals. The Pauli exclusion principle dictates that paired electrons must have opposite spins, therefore they cancel each other out in an applied field and no net magnetic dipole moment is seen. Hence, they are repelled by an external magnetic field.[11] Paramagnetic materials have unpaired electrons of parallel spins in accordance with Hunds rule (all orbitals must be singly occupied before electrons can pair). In the presence of an applied magnetic field the electrons tend to align in the same direction and the material is attracted to the field.[11] Further instances of magnetism are expanded on below.

Permanent magnets are able to function without the application of an external magnetic field, they are used to form an applied field for other materials. However, they can only maintain function below a certain temperature; this happens because some domains become unaligned on increasing temperatures and therefore the net magnetisation of the material decreases.

Ferromagnets are species with a spontaneous magnetisation and have a reversible magnetisation on the introduction of an applied magnetic field. Increasing the temperature above the T_C results in a paramagnetic state in the species which decreases on an increasing temperature. Similar to ferromagnets, other magnetic states exist such as antiferromagnets and ferrimagnets. Antiferromagnets have neighbouring magnetic ions with anti-parallel spins of the same magnitude which produces no net magnetisation in any direction. Expanding on this, anti-ferromagnetic materials have three possible configurations in a unit cell: A, C, and G which correspond to which neighbouring atoms have anti-parallel spins, in relation to each other,[12] Figure 1.3. Ferrimagnets behave similarly, however, the anti-parallel spins are of different magnitudes giving rise to a net magnetisation in the direction of the applied field, Figure 1.4.
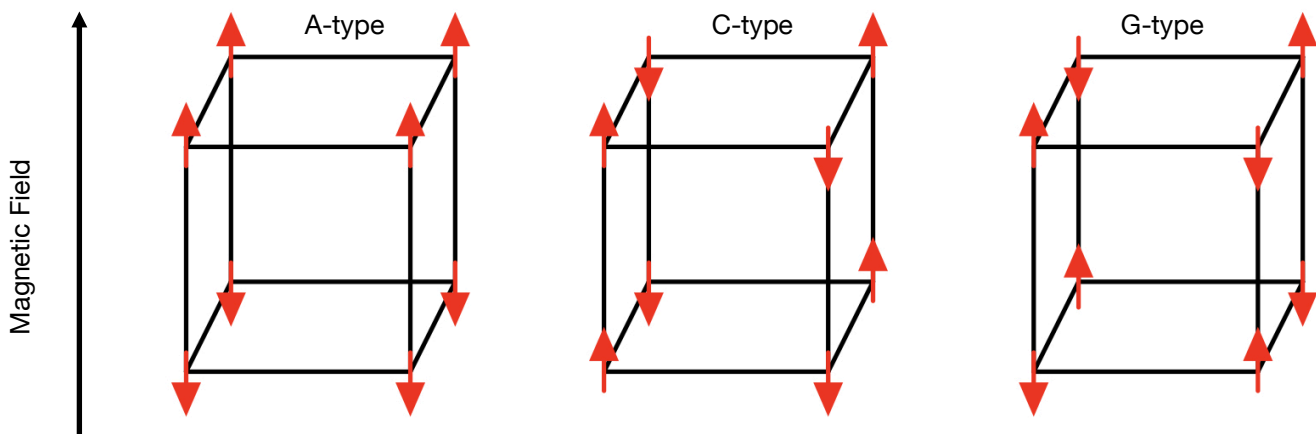
Figure 1.3 - A 3D diagram showing the different antiferromagnetic arrangements, assuming all vertices are magnetic ions.
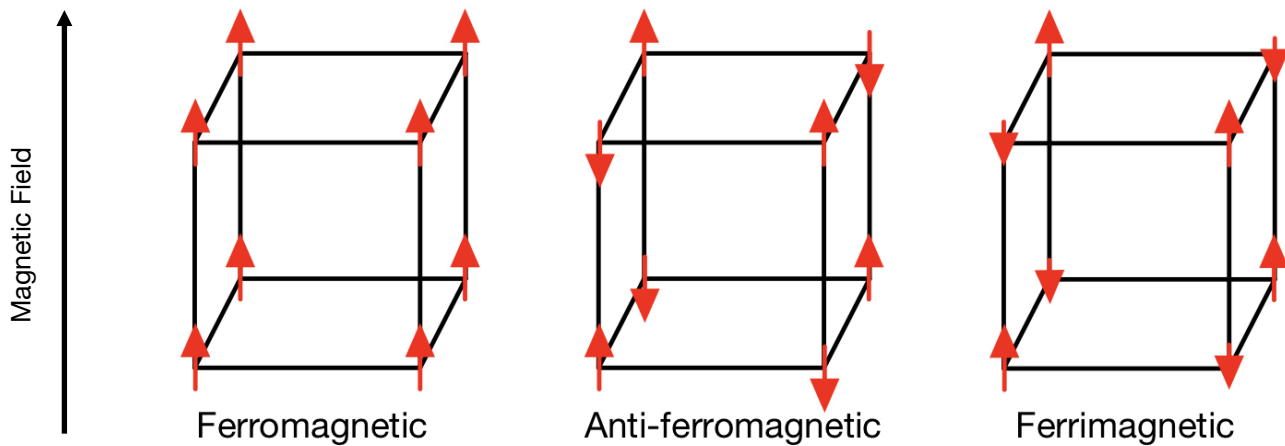
Figure 1.4 - A 3D diagram showing the different spin arrangements, assuming all vertices are magnetic ions.

Magnetic interactions are often more complicated and can be realised through specific mechanisms, for example, super exchange.

In 1957, Dzyaloshinskii theorised that a ferromagnetic response can be observed in a crystal lattice which displays antiferromagnetism. Crystal lattices, such as Fe_2O_3 or certain transition metal carbonates, Mn or Co, with changes in the unit cell symmetry give rise to different spin arrangements of the magnetic moment. He found that in Fe_2O_3 there are two antiferromagnetic states with different spin arrangements. The first state where the spins align along the crystal lattice, and the second state where the spins lie in the (111) plane of the unit cell. The first shows no ferromagnetic character, but the second state shows a small

ferromagnetic moment. This is because the ions are rotated minimally with respect to each other and are therefore not wholly anti-parallel.[13]

Later, in 1960, Moriya further expanded on this spin-only phenomenological theory, by including spin-orbit coupling with the super exchange phenomenon.[14] This was introduced by Kramers in 1934,[15] and was further expanded by Anderson in 1950.[16]

Super exchange details how anisotropic magnetic interactions were observed between orthogonal magnetic cations. This occurred even though non-magnetic anions, O^{2-}, were separating them. This is due to the electron contribution from the magnetic cation's orbital overlap with the central anion's orbitals. This interaction provides weak ferromagnetism in the system. This led to the ferromagnetic response being named '*Antisymmetric exchange*', also known as the Dzyaloshinskii-Moriya (DM) interaction.[17]

Magnetocrystalline anisotropy details how the electron orbitals are coupled to the crystal structure. It further explains how the electron spins prefer to orient in one direction than another. Therefore, there are directions in space in which it is easier to spontaneously magnetise a material, the easy axis, and directions which are more difficult to produce a spontaneous magnetisation, the hard axis.[18,19]

1.3   Ferroelastic properties

Ferroic properties are found in materials which display a specific combination of structural and electronic contributions. In addition to the previously discussed ferroelectric and ferromagnetic properties, materials can also exhibit ferroelasticity. Ferroelasticity is described as a spontaneous strain in a material which allows for switching between remnant states *via* the application of mechanical stress, this property will not be explained further as it beyond the scope of this project.

1.4   Multiferroics

Multiferroics are classified by the combination of two or more ferroic order parameters combined in a single phase of a material. If coupling is observed between the two order parameters this allows the material to exhibit both ferroic properties. Some multiferroic materials, under certain conditions, allow expression of one property over another. This is termed the magnetoelectric effect, which allows the material to behave differently under one applied field than another, magnetic vs electric.[20]

The magnetoelectric (ME) effect was first discovered and introduced by Wilhelm Conrad Röntgen in the late 19th century (1888).[21] It was found that introducing a moving dielectric into

an electric field, magnetised the dielectric material.[22] In 1894, Marie Curie suggested that the ME response in crystalline media was correlated to symmetry-based operations.[23] Despite Curie's realisation of symmetry considerations in ME behaviour, it was not until decades afterwards that the effect was found to only occur in time-asymmetric media.[24] In 1905, some 17 years following the original discovery, the reverse of the effect was observed by Harold Albert Wilson, who found that applying a magnetic field to the moving dielectric produced a polarisation in the material.[25]

This effect has gained lots of attention which has led to increased research and an increase perspective of how a polarisation is seen as a result of an external magnetic field. Similarly, how a magnetisation occurs as result of an external electric field.

The ME effect is the coupling seen between the magnetic and electronic behaviours of a material. The ME effect is a linear response which can be seen by the vacuum permeability, μ_0, and the magnetisation, M_j, of a material through an applied electric field, E_i, linked by the magnetoelectric coefficient, a_{ji}:[26]

$$\mu_0 M_j = \alpha_{ji} E_i \qquad\qquad \text{Eqn. 6}$$

The conception of materials which exhibit multiferroicity, such as $BiFeO_3$, have been theorised to have applications in modern devices such as spintronics, and new electronics.[27-28]

In 2009, Khomski determined that there exists type I and type II multiferroics.[29] Type I multiferroics have been known for longer and usually have better ferroelectric properties. They are normally ferroelectric species which happen to have antiferromagnetic character. These two properties arise individually of each other, using different mechanisms and at different temperatures.[29, 30] Type II multiferroics are a more recent discovery. The ferroelectric response is a direct causation of a magnetic transition, as such the transition temperatures coincide. It can be said that strong magneto-electric coupling can be expected in type II multiferroics. [30]

Due to these attractive properties, applications of these classes of materials are ranged from data storage,[31] spintronics,[32] and sensors.[33]

In recent years, many researchers have delved deeper to uncover a novel, theorised property termed ferrotoroidicity (FT), which would allow one to combine both magnetic and electric order parameters with strong coupling between the two. FT is described by a spontaneous toroidisation, which occurs because of aligned vortices, through an applied toroidal field.[34-38] It is produced by the corkscrew-like orientation of the dipoles, which produces a toroidal moment up or down depending on if the current is clockwise or anti-clockwise in the

torus. For this to occur, the material has to have antiferromagnetic (AFM) ordering. AFM ordering does not give rise to the same inherent properties or symmetry violations as ferromagnetism, i.e., there is no magnetisation produced from a phase change. According to Tolédano and Fiebig,[37] it was suggested that when using AFM ordering in a vortex-like manner, a toroidal moment will be produced. At present, it is further hypothesised that the toroidal moment may not be a primary ferroic order itself but instead, a by-product of the AFM crystal structure which drives the phase transition.[37] This is a similar mechanism to that which can be found in type II multiferroics.

The Magnetoelectric effect is said to be a good way to indirectly measure the ferrotoroidic response due to the asymmetric nature of the ME contributions. However, only the existence of an order parameter is able to denote the characteristic ferroic response of ferrotoroidicity.[38]

1.5   Symmetry

Symmetry takes root in many areas of importance in modern science, the origin of which dates back as far as ancient Greece. However, the basics of group theory were first introduced to modern life in the early 19th century (1811-1832) by Evariste Galois who used the symmetry properties of n-th order polynomials to show that basic mathematical operations cannot be used to solve the quintic polynomial equation.[39] In 1830, the introduction of group theory allowed Johan Hessel to derive 32 morphological crystalline symmetries (crystallographic point groups) which correspond to a geometric crystal class, and are indicators of the crystal's properties; based on crystal structure. Tavger and Zaitsev expanded on staple work done by Heinrich Heesch who established the idea of antisymmetry in 1929.[40] In essence, the application of the antisymmetry operation to the previous 32 point groups derived a further 122 magnetic point groups.[41] The initial work laid out by Heesch, and subsequent expansion by Tavger and Zaitsev, was further improved by Lev Schubnikov who referred to these 122 point groups in terms of colour symmetry.[46, 47]

Ferroic properties arise due to a break or invariance in two types of symmetry: space and time, Figure 1.6. A break of space symmetry and an invariance of time symmetry gives rise to a ferroelectric response, the opposite is true for a ferromagnetic response. An invariance of both space and time symmetry gives rise to a ferroelastic response. However, a change in both space and time symmetry gives rise to the fourth, theoretical property: ferrotoroidicity.

Figure 1.6 - Shows which Ferroic property occurs as a result of a change or invariance in space and time symmetry. *P* denotes a spontaneous polarisation. *S* denotes the magnetic spin of an electron, *e*⁻. *T* shows the toroidal moment of a torus with radius, *r*.[38]

From Figure 1.6, we can see that breaking spacial symmetry ($\overline{1}$) but not time symmetry (1') of an electric field (E) gives rise to ferroelectricity. The opposite is true for ferromagnetism, which breaks time symmetry but not space symmetry in a magnetic field (H), this can be written as:

$$\overline{1}E = -E,\ 1'E \neq -E \qquad\qquad \text{Eqn. 7}$$

$$\overline{1}H \neq -H,\ 1'H = -H \qquad\qquad \text{Eqn. 8}$$

This can be more easily envisioned through Figure 1.7, where a mirror is used to demonstrate the symmetry breaking.[44]
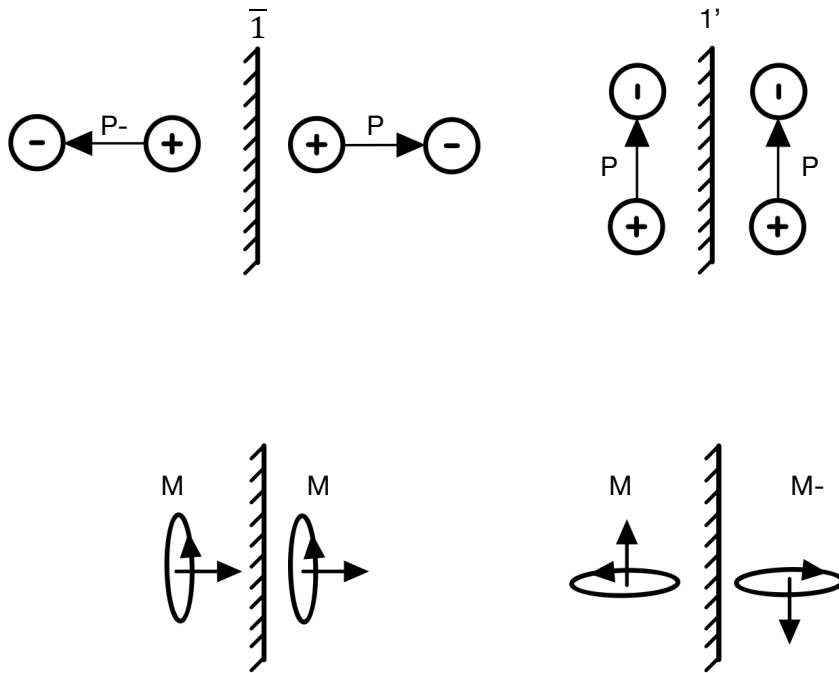
Figure 1.7 - Where the effect of time and spatial symmetry breaking, 1' and $\bar{1}$ respectively, is represented by polarisation (P) and Magnetisation (M) seen through a mirrors reflection.[48]

Ferrotoroidicity occurs from a perturbation of both space and time symmetry in a toroidal field (T) and can be expressed as:

$$\bar{1}T = -T, \, 1'T = -T \qquad \text{Eqn. 9}$$

Thus, it can be said that the toroidization, which is analogous to magnetisation and polarisation, is affected by an electric and magnetic field in the same manner.[45]

In order to understand material behaviour, it is important to also understand symmetry considerations. As a result, in order to exploit new materials, it is necessary to carefully probe structure-property considerations.

1.6 Aims

The aim of this research is to further expand studies detailing multiferroic behaviour as well as discussing the potential for ferrotoroidic nature in antiferromagnetic materials.

The background theory for ferrotoroidicity is quite obscure due to this phenomenon being relatively new. It was not found decades ago like ferromagnetism; therefore little work has been done to understand this effect experimentally.

In this thesis we aim to discuss the structure-property contributions of ferrotoroidicity in crystal structures, through means of synthesising two series of materials: $Li_{1-x}Na_xCoPO_4$ (x = 0, 0.1, 0.2, 0.3, 0.4), and $Dy_{1-x}Sm_xFeO_3$ (x = 0, 0.25, 0.5, 0.75, 1). Further analysis of multiferroic behaviour is discussed through the analysis of a 5% Dysprosium doped BFO sample, $Bi_{0.95}Dy_{0.05}FeO_3$.

Chapter 3 details previous studies on BFO and the effect of doping with the isovalent rare earth ion Dy^{3+}. The materials synthesis is described which was conducted by Arnold *et al.*[46] The structural composition is investigated over a temperature range of 5 - 1023 K using neutron diffraction, alongside ambient and low temperature (12 K) XRD. The multiferroic nature of the doped sample is confirmed by ferroelectric and antiferromagnetic responses. Characterisation was additionally performed using Raman spectroscopy, SEM, SQUID magnetometry and Polarisation-Electric field (PE) loops.

Chapter 4 details previous studies on parent materials of $DyFeO_3$ and $SmFeO_3$ and the solid solution of $Dy_1Sm_{1-x}FeO_3$. The synthesis of this family of materials is also described. The investigation probed the structural analysis of changes that occur over a composition range of: x = 0, 0.25, 0.5, 0.75, 1. Magnetic responses are also measured over this composition range. Room temperature XRD and Raman spectroscopy as well as low temperature XRD analysis and SQUID magnetometry are reported. From this, the mulitferrocity and ferrotoroidicity capabilities are discussed.

Chapter 5 details the previous studies on $LiCoPO_4$. The synthesis of this class of ceramics is also described. The investigation probes the structural composition and ferromagnetic responses of the material. This chapter also explains the effect of Na doping in the ceramic up to compositions of 40% Na, $Li_{1-x}Na_xCoPO_4$ (x = 0, 0.1, 0.2, 0.3, 0.4). The multiferroic nature is analysed alongside the suggestion of ferrotoroidic behaviour.

Initial findings are presented through structural analysis of room temperature XRD, SEM, and Raman spectroscopy. Antiferromagnetic responses are shown *via* the use of SQUID magnetometry.

Each chapter contains its introduction, experimental section, results and discussion, and conclusions. A summarising end chapter as well as references and appendices at the end of the thesis.

Chapter 2

Experimental Methods

2.1   Synthesis routes

All synthesis routes and characterisation details for the materials discussed in this thesis are shown in their individual chapters.

This chapter focuses on the experimental theory behind the characterisation techniques used for the data discussed in subsequent chapters.

2.2   Characterisation Techniques

A variety of techniques were used during these investigations. The techniques used determine the chemical crystal structure, as well as the ferroelectric and antiferromagnetic responses.

X-Ray Diffraction and Powder Neutron Diffraction were used to investigate the structure of the synthesised materials and their crystallinity. Their phase purity can be determined quantitively by comparing the observed reflections and the reflections expected for the crystal's space group. Raman spectrometry was used to analyse the vibrational modes of the materials which can tell us their symmetry. The chemical structure can be obtained qualitatively by observing specific bonding interactions.   Thermogravimetric Analysis alongside Differential Scanning Calorimetry were used to test material decomposition and observe phase changes as a function of temperature, respectively.

The ferroelectric response was measured with the use of Polarisation-Electric field Loops. The magnetic response was recorded using DC SQUID magnetometry.

Scanning Electron Microscopy was used to visually observe potential grain boundaries and surface defects on pre-made pellets.

2.2.1 X-Ray Diffraction

X-Ray Diffraction (XRD) is a non-destructive technique and is a useful analysis tool to determine the structure of a crystalline material. It can detect the crystalline phases within and reveal a materials chemical composition.

X-Rays are an electromagnetic wave of radiation with wavelength (λ) range = 0.1-100 Å, comparable to the inter-atomic distance in materials. Unit cells usually have dimensions of several Angstroms, Å. Implying that crystals with large sizes consist of many repeating unit cells in all three Cartesian coordinate directions. In other words, these crystals possess long-range order. Some crystals have repeating units that span over a shorter range which is interrupted by disordered atomic units, named amorphous crystals. Hence, the quality of diffraction is dependent on the crystallinity of the material and the non-interruption of the periodicity of long-range order.

X-Rays interact with the electrons in an atom in the crystal lattice of the analyte material. This excitation is not enough to release the electron, but instead elastic scattering is observed. A somewhat spherical wave is diffracted which has the same wavelength as the incident X-Ray. The amplitude is correspondent to the number of electrons in the atom and therefore the atomic number. This is to say this characterisation is element specific. Lighter elements diffract less and heavier elements diffract more.

When an atom is hit, the diffraction occurs as a spherical wave, but due to diffraction effects the scattering sphere redistributes intensity into specific directions, which produce peaks. These peaks also named '*reflections*' occur on lattice planes as introduced by Bragg.[47] From his discovery, Bragg's law is able to be distinguished, Eqn 10.

$$n\lambda = 2dsin\theta \qquad \text{Eqn. 10}$$

Where *n* is an integer, λ is the X-Ray wavelength, usually 1.5406 Å / (Cu sources), *d* is the inter-plane distance, θ is the angle of incidence. Bragg's law denotes how parallel incident X-Rays are reflected by parallel atomic planes. The angle of reflection is measured as 2θ and is the angle between the oncoming incident X-Ray and the reflected X-Ray as denoted in Figure 2.1.
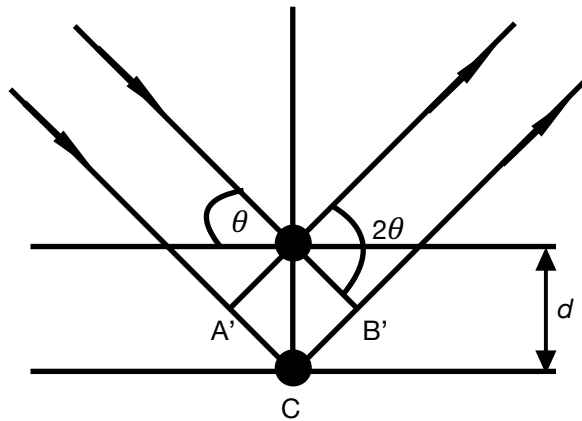
Figure 2.1 - A schematic diagram showing the reflective process as described by Bragg's Law, Eqn 10. Where the vector A'CB' = n.[51]

When n is a non-zero integer, the two parallel rays have constructive interference, and a Bragg peak is obtained. The peaks and troughs of the parallel wavelengths combine to increase the wavelength intensity. When n is not a non-zero integer, such a fraction, then a destructive interference is obtained, and no Bragg peak is seen.[48] This can be further expanded to analyse how there can be structural defects in the analyte material. An interruption of the unit cell periodicity through atomic impurities or phase perturbations, *i.e.* non phase pure materials. The Cu target accounts for the $\lambda \sim 1.54189$ radiation. However, because of the splitting of $2p$ energy levels there are two X-Ray wavelengths observed experimentally: $k\alpha_1 = 1.5456$ Å and $k\alpha_2 = 1.5439$ Å.

A typical X-Ray Diffractometer uses a $\theta : 2\theta$ method for analysis. The zero-background plate with analyte is rotated at angle θ, with respect to the X-Ray source. The detector is rotated similarly by angle 2θ. The output is measured by a connected computer which plots the intensity of the reflected Bragg peaks as a function of 2θ.

Other X-ray diffractometers use a fixed sample holder with a $\theta : \theta$ geometry, otherwise termed Bragg-Brentano geometry. The source and detector are rotated around the sample in a goniometer circle (fixed radius) and placed at the intersection of the focusing circle, Figure 2.2. The focusing circles radius is varied as a function of the goniometer angle and increases the higher the θ becomes. This geometry type helps to retain peak intensity.[49]
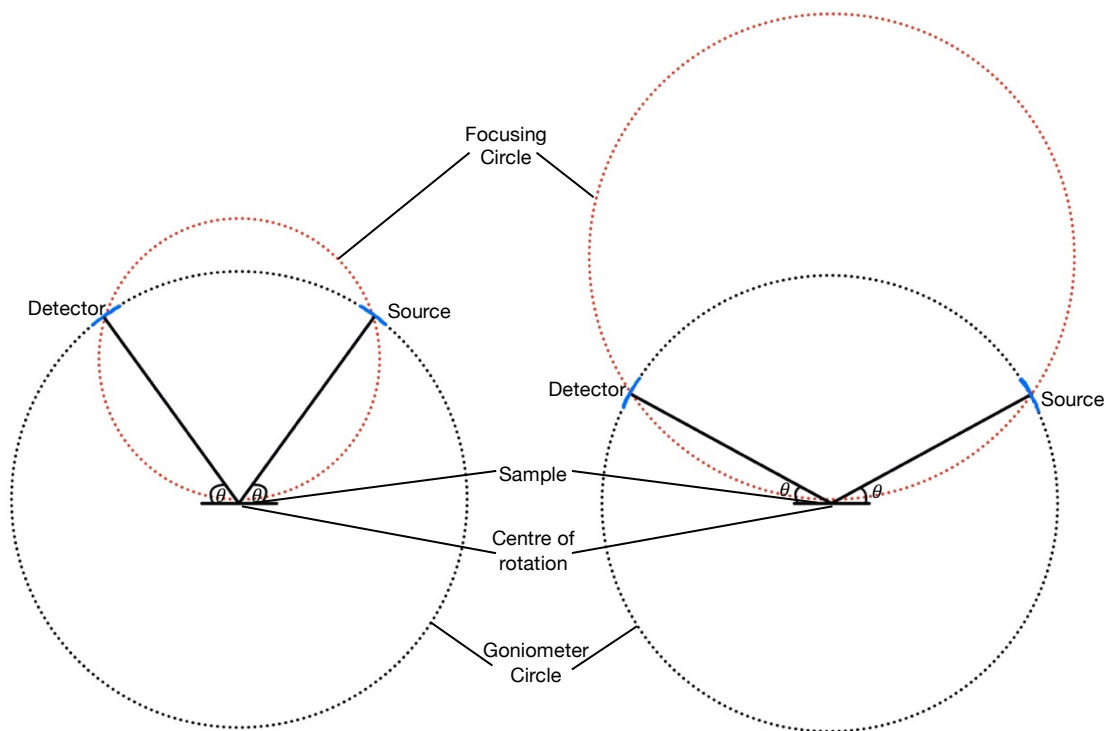
Figure 2.2 – A diagram denoting the change in focusing circle radii as a function of angle θ in the Bragg-Brentano geometry using a fixed sample placement and $\theta{:}\theta$ measurement.[52]

2.2.2 Powder Neutron Diffraction

Powder Neutron Diffraction (PND) is similar non-destructive technique to XRD but uses neutrons instead of X-rays. There are two ways to generate neutrons, one comes from atomic fission, the second comes from a spallation source. Spallation techniques don't produce neutrons from chain reactions unlike fission processes. Neutrons that pass through a monochromator can be fixed in a specific wavelength. Time Of Flight (TOF) neutrons, neutrons with a fixed wavelength, are fired at a sample and scattered. The change in velocity and final position of the scattered neutron compared to the initial can be used to observe how the sample has effected the neutron, this change is sample dependent.

To achieve neutron diffraction, one must have a neutron which has a similar wavelength to the inter-atomic distance. This occurs through the use of high-speed neutrons, the relationship can be seen with the de Broglie relationship, Eqn 11.

$$\lambda = \frac{h}{mv} \qquad \qquad \text{Eqn. 11}$$

Where the wavelength, λ, is dependent on the Planck's constant, h, divided by the momentum. The momentum is equal to the mass of the neutron, m = 1.675×10^{-27} kg, multiplied by the neutron's speed, v.

The measurement of this diffraction method is not based on θ values, but instead on TOF. Eqn. 11 can be re-written in this case to show TOF, Eqn 12. TOF uses different wavelengths of neutrons instead of changing the angle of incidence.

$$\lambda = \frac{ht}{ml} \qquad\qquad \text{Eqn. 12}$$

Where t is TOF, and l equates to the neutron's travel distance. This relationship shows how the TOF dictates the neutrons wavelength.

The neutrons are generated by a high intensity beam of hydride ions, H$^-$, being accelerated towards a spallation target. Hydride ions are produced by electrical discharge and accelerated by electromagnets to form a beam. After acceleration the hydride ions are stripped of their electrons by a thin alumina film and are converted to protons. These protons are accumulated and then are fired at the spallation target, a tungsten brick. Neutrons are ejected which fire in short, quick, high-energy pulses.[50]

Neutrons are able to identify the magnetic structure of the material due to the interaction of the neutron's spin with the magnetic field of unpaired electrons present in the material.

2.2.2.1 HRPD

The High-Resolution Powder Diffractometer (HRPD) is one instrument which can be used to analyse the neutron diffraction of the analyte material. It is able to accurately measure small changes in lattice parameters and structural distortions that occur in materials.

The HRPD instrument has three detectors at differing angles to the neutron source. The first is a '*backscattering*' 168° detector. The second is a 90° detector. The third is a 30° '*low angle*' detector. As this instrumentation uses TOF instead of θ values the detectors, '*Banks*', are in fixed positions, Figure 2.3. As previously mentioned the neutron source is at a fixed angle and the wavelength of neutrons is altered by TOF to afford the Bragg reflections in d-spacing.[51, 52]
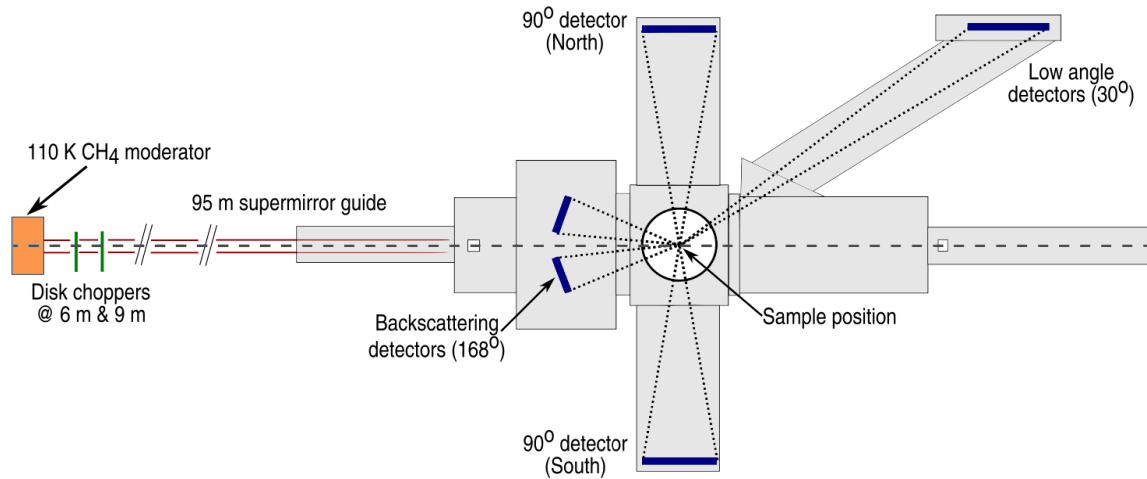
Figure 2.3 - A diagram of the HRPD instrument displaying the sample positioning, the neutron beam (dotted line) and the three detector banks: 168˚ detector, 90˚ detector, and the low angle 30˚ detector.[51]

2.2.2.2 WISH

Wide angle In a Single Histogram (WISH) is a long wavelength diffractometer used for polycrystalline diffraction. Similar to the HRPD instrument it is a high-resolution neutron powder diffractometer. It works by observing a range of almost overlapping magnetic and nuclear Bragg peaks at long d-spacing. Due to high-resolution over a large range, weak Bragg reflections can be visible and it is used to solve complex magnetic structures. Instead of three detector banks at fixed angles. An almost 360˚ array of detectors is used, 10˚ - 175˚ on both sides, surrounding the diffracting sample to measure the scattering pattern.[53]
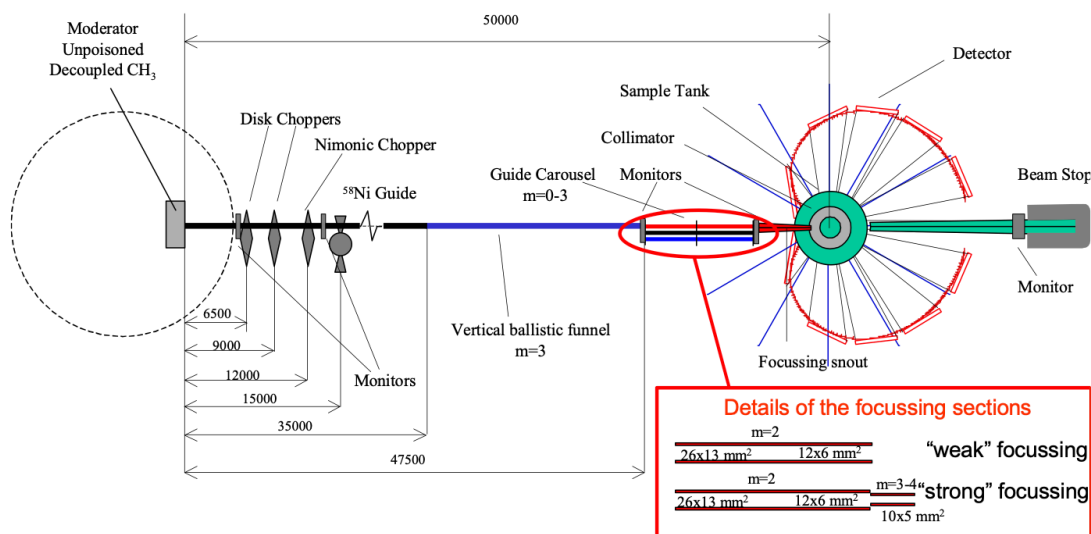
Figure 2.4 - A diagram showing the WISH diffractometer at the ISIS neutron source, UK.[53]

2.2.3 Rietveld Refinement

Once diffraction data has been collected the data must be refined in order to determine the crystal structure.

This is done to reduce the discrepancies between the applied model for the fit and the experimental data. The model used is dependent on the crystallographic space group the material crystallises with, *i.e.* BFO uses *R*3*c*.

Refinement usually occurs with the least squares method. With this method, the user alters the structural parameters obtained by the measurement in order to minimise the discrepancies in the structure.[47]

General Structure Analysis Software (GSAS) I and II are used to refine the patterns. Background parameters are refined in order to find the baseline of the measurement which can further be used to identify and refine the Bragg reflections. The commonly used background parameter is a shifted Chebyshev polynomial.[54] In determining the peak shape, a pseudo-Voigt approximation is used. This approximation takes into account both Gaussian (*X, Y, Z*) and Lorentzian (*U, V, W*) mathematical functions.

The parameters used in this determination are most commonly the atomic position parameters: *x, y, z*, the unit cell parameters, as well as the thermal displacement parameter *U*. These are refined until convergence, where the perturbations in the parameters are negligible.[55]

Once convergence is achieved, the '*goodness of fit*' can be attained by observing the Chi squared, χ^2, value.

χ^2 is a value given to the relationship between the weighted profile R-factor, R_{wp}, and the expected R-factor, R_{exp}. These are shown through Eqns 13, 14, and 15 respectively.[56, 57]

$$\chi^2 = \frac{R_{wp}}{R_{exp}} \qquad \text{Eqn. 13}$$

$$R_{wp} = [\frac{\Sigma_j w_j (y_{obs_j} - y_{calc_j})^2}{\Sigma_j w_j y_{obs_j}^2}]^{\frac{1}{2}} \qquad \text{Eqn. 14}$$

$$R_{exp} = [\frac{(j - v)}{\Sigma_j w_j y_{obs_j}^2}] \qquad \text{Eqn. 15}$$

Where the terms: j is the number of data points. y equals the intensity for any calculated or observed (experimental) j value. w equals the weight for any j value and is further defined by $1/\sigma^2[y_j]$ where σ is the uncertainty value for the intensity seen at the given j value. v is number of refined parameters. R_{wp} should tend towards the statistically expected R_{exp} value. Comparing these two, one observes the '*goodness of fit*' and quality of the refined data.

FullProf suite is another program which is used for Rietveld refinements. The magnetic structure of a material is determined through analysis of the PND of a sample. Using this method, the nuclear phase is able to be refined separately to the magnetic phase. A refinement without the magnetic phase allows one to clearly see the magnetic contributions present in diffraction pattern. The magnetic structure can be identified through use of symmetry information found in the samples crystallographic space group. A .PCR file is used to generate a refinement, the file includes all the necessary information which FullProf can use to determine both the nuclear and magnetic contributions to the diffraction pattern.

2.2.4 Scanning Electron Microscopy

Scanning Electron Microscopy (SEM) is used to analyse the surface of an analyte material. It is a non-destructive technique useful for 2-dimensional imaging of the topography of the analyte. Observing any apparent defects on the surface, as well as the material composition (through EDX mapping).

This technique works by illuminating a sample with a beam of electrons. The sample, on contact with the electron beam, will inelastically scatter and produce secondary electrons (SE's). These are electrons which are ejected from the valence shell of the atoms in the material due to weak binding energies. They have a lower energy than the primary electron, electrons from the electron beam, due to the weak exchange of kinetic energy. Due to this decrease in energy, the consequent electron is only able to travel a few nanometers. SE's are produced the throughout the material, but due to their low kinetic energy the photoelectric effect comes into practice. Only a small amount of the SE's have the required energy to be able to escape the surface energy of the material. Hence why only the surface of the material is able to be observed. The SE's are very localised from the point of impact and it is therefore able to successfully image the material with a resolution as small as <1 nm. These electrons are detected from detectors in the chamber of the election microscope.[58] Back Scattered Electron's (BSE's) are also produced upon sample illumination. These have the same energy as the same primary electrons which strike the material. They elastically scatter having the same energy but the reverse trajectory and are therefpre able to escape the material's surface. It has been reported that the number of BSE's from the sample increase proportionally with the atomic number, z.[59] Similarly it has been reported that on tilting of the sample, so that the beam is not perpendicular, the number of BSE's increase. Due to the atomic number dependence of the BSE's one is able to determine the phase distribution within the sample.[58]

When an inner, core-shell electron is ejected, an outer shell electron relaxes and fills the positive hole, h^+, created. During this process an X-ray is released on relaxation which is characteristic of the element analysed. This allows for Energy-Dispersive X-Ray Microscopy otherwise termed EDX mapping which can be used to map the dispersion of the different elements in an analyte material. [58]

Coupling the use of BSE's produced through SEM, and EDX mapping. One is able to identify the homogeneity of the analysed sample.

2.2.5 Raman spectroscopy

Raman spectroscopy is a non-destructive technique, commonly used for structural analysis in the field of materials chemistry. One is able to extract the vibrational information

which is characteristic of a material providing the vibration is Raman active. This means that the vibrational and rotational energy of the molecule can be observed *via* the Raman spectrum. The vibrational information depends on: the chemical bond, sample crystallinity, and polymorphy of said material. [60]

Raman spectroscopy is a light scattering technique and shows how a molecule interacts with differing wavelengths of light, scattering the incident beam of photons. Traditionally, four different wavelengths are used: 473 nm, 532 nm, 632 nm, and 784 nm. These correspond to blue, green, red and Infra-Red, IR, light respectively. When the photons hit the sample, they can be reflected elastically or inelastically.

Elastic (Rayleigh) scattering is most commonly observed which is not useful in structural analysis. This is because the reflected photons have the same energy as the incident photon, therefore, no interaction with the analyte is seen.

Inelastic (Raman) scattering is less common and is categorised in two ways: Stokes and anti-Stokes. Stokes scattering shows the emitted photon has less energy than the incident photon. Whilst anti-Stokes scattering shows the emitted photon has more energy than the incident photon,[61] Figure 2.5.

Due to the difference in magnitude of the reflected photons, Rayleigh > Raman, the elastic scattered Rayleigh photons have to be filtered out. Edge and Notch filters rejecting specific wavelengths have been used for this purpose.[60]

The scattered light is plotted as Intensity vs Raman shift, which is plotted in wavenumbers (the inverse of wavelength $1/\lambda$).
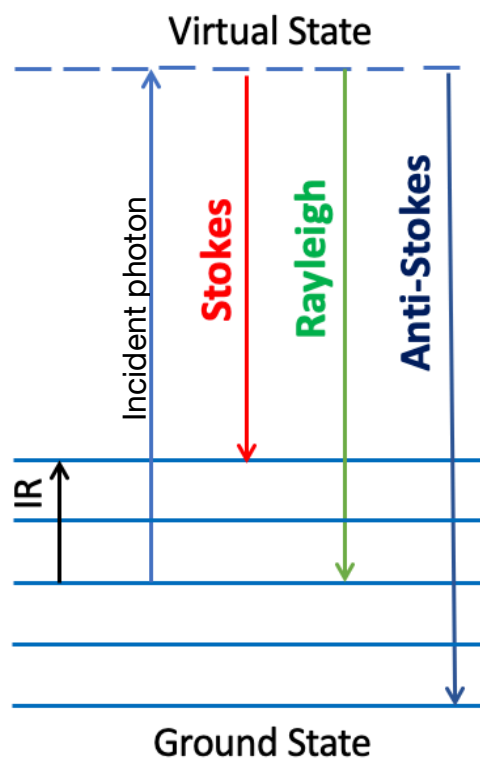
Figure 2.5 - A diagram showing Rayleigh and Raman scattering as well as the IR absorption of an arbitrary sample.[65]

Scattering occurs due to the vibrational modes of the sample. If the sample observed is linear, such as carbon monoxide, then there are 3n-5 vibrational modes. If the sample is non-linear, such as water, there are 3n-6 vibrational modes. The incoming light is used to excite the sample to a higher, virtual energy level in which these vibrational modes are seen. The sample then relaxes to the ground state where elastic or inelastic scattering is observed. These excited states can be symmetric or asymmetric stretches of bond vibration or rotation. A sample can be both IR and Raman active but due to the rule of mutual exclusion only one effect is seen. Mutual exclusion states that if a molecule has a centre of symmetry, it is Raman active but not IR active. This correlates to whether the vibrational mode observed has a change in dipole or a change in polarisability. A molecule with a centre of symmetry which is retained during a vibration is Raman active as there is no change in dipole moment, but a change in the molecules polarisability. Conversely, when the vibration alters the dipole moment by an asymmetric vibration then the molecule is said to be IR active.[64]

Therefore, the molecules symmetry is able to determine how many of these vibrational / rotational modes are observed. As explained in the previous chapter, Group theory is used to describe the symmetry of a molecule. Through further derivation of Group theory, irreducible

representations are used to see which vibrational / rotational modes are IR active versus which ones are Raman active.

2.2.6 SQUID magnetometry

Superconducting quantum interference device (SQUID) magnetometry is used to observe the magnetic properties of a sample.

SQUIDs are used based on their application of two physical phenomena. The first is flux quantisation. This is where the flux, Φ, is quantised when introduced into a closed superconducting loop.[62] The units of this quantisation are given in Eqn 16:

$$\Phi_0 = \frac{h}{2e} \equiv 2.07 x 10^{-15} Wb \qquad \text{Eqn. 16}$$

Where h is the Planck's constant, and e is the electron charge.

The second phenomenon is Josephson tunnelling. This describes the translational effect of electron Cooper pairs moving between two superconductors through a thin insulating material.[63, 64]
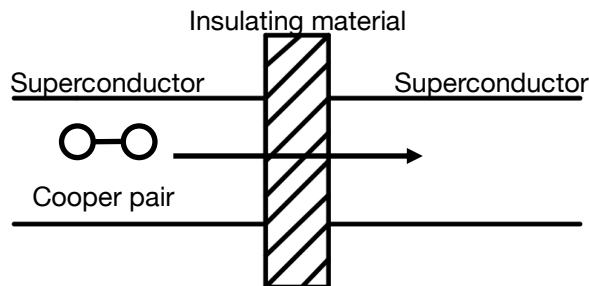
Figure 2.6 - A diagram showing a Josephson junction and the movement of Cooper pairs which describes Josephson tunnelling.[68]

The superconductor apparatus described above is known as a Josephson junction, Figure 2.6. There exist two different types of SQUIDs based on the Josephson junction arrangement. A direct current (dc) SQUID which shows two Josephson junctions in a parallel circuit within a superconducting loop over a steady bias field. The second is a radio frequency (rf) SQUID in which there is a single Josephson junction within a superconducting loop and operates over an interrupting flux bias. It has been reported that dc SQUIDs are more sensitive than their

flux bias counterpart. This is because they are able to detect small changes in flux, smaller than the Φ unit.[65]

The magnetic properties of materials are measured by the distortion of the magnetic field in relation to a sample of known mass.[66] In (anti) ferromagnetic materials, a spontaneous magnetisation occurs below T_C (T_N). Usually this is far below room temperature, therefore, cooling with liquid helium is used to reach temperatures of ~2 K. The temperature is increased and the change in magnetisation can be observed as a function of temperature. Allowing one to experimentally determine the magnetic transition temperature.

In general, two analyses are used, a zero field cooled (ZFC), and a field cooled (FC) analysis. ZFC analysis cools the sample in the absence of the applied field. The magnetic spins are pinned in random directions for polycrystalline materials. For highly magnetic anisotropic materials the subsequent application of an applied field is not enough to align these spins. Therefore, a small magnetisation is produced. This is contrary to materials with a small magnetic anisotropy, in which a larger magnetisation is produced in the same applied field. FC analysis cools the sample alongside the applied field. The spins are aligned and pinned when cooled below the ordering temperature. The magnetisation observed is practically the same for materials with a small anisotropy. However, when the material has a large anisotropy, decreasing the temperature allows one to see a steady increase in magnetisation.[67]

A SQUID magnometer allows for the magnetic profile to be seen as a hysteresis loop. It shows the change in magnetisation over a range of the varying applied magnetic field strengths. As the applied magnetic field is altered, the temperature must remain constant. This allows one to see the difference in magnetic behaviour at different temperatures, *i.e.* above and below T_c.

2.2.7 Ferroelectric PE Loop

Polarisation-Electric Field (PE) loops are a useful method to extract the electrical data of the analyte material, which is pelletised. Hysteresis profiles are collected by measuring the polarisation of the material as a function of the applied electric field. A range of the electric field strength $\pm E$ are used, which measures the voltage applied across the diameter of the pellet in units kV/cm, at a known frequency.

The spontaneous polarisation direction of the ferroelectric material is able to be re-oriented through the use of the applied electric field. On changing the sign of E, the polarisation direction is reversed through reversal of the electric dipoles. This allows a hysteresis profile to be plotted as seen in Figure 1.2.[68]

2.2.8 Thermogravimetric Analysis

Thermogravimetric Analysis (TGA) is a method to show how the mass of a sample is measured over a temperature range, this is normally seen through material decomposition or through moisture loss. The sample is heated at a constant rate, in an oxidising, or inert atmosphere of either O_2 or N_2.

A top-loading thermobalance is used to measure the weight change of the analyte sample as a function of temperature. Plotting a curve of mass change as percentage loss or gain over the temperature range. This allows one to see the thermal stability of the analyte.

A correction profile is initially run, whereby two empty alumina crucibles are placed on the thermobalance and a program is run. The program contains the temperature range, heating rate, and the atmosphere with which the analyte sample will be measured in. The second crucible is used as the reference crucible in future measurements, using the same correction profile.

A sample of known mass is then placed in the first crucible which is placed beside the reference crucible. The measurement works by determining the difference in heating the sample requires in comparison to the empty reference crucible.[69]

2.2.9 Differential Scanning Calorimetry

Differential Scanning Calorimetry (DSC) was first introduced in the 1960's.[70] It is a useful tool to determine the phase change of a material as a function of temperature. DSC is normally run over the same temperature range as the TGA, therefore they can be run alongside each other.

DSC measures the energy perturbations which occur over the aforementioned temperature range. The energy is either exothermic or endothermic depending on the phase change, seen by positive or negative values. Changes are measured in megawatts per milligram (mW/mg). The energy changes are seen quantitively and the exact temperature at which these changes occur can be seen, and the temperature of the phase change can be seen. The raw data can hide some shouldering peaks which can contain useful information. Therefore, the second derivative of these measurements are used which allow for facile measurement analysis.[70,71]

Chapter 3

Dy-BiFeO$_3$

3.0   Introduction

BiFeO$_3$ (BFO) is the most studied type I multiferroic to date.[44,72] At room temperature, BFO is characterised by a polar *R*3*c* rhombohedral symmetry and crystallises with a distorted perovskite structure.[46] This material is well studied due to its multiferroicity at room temperature; it has ferroelectric characteristics with a Curie transition temperature (T_c) observed at ~1083-1103 K. and antiferromagnetic (AFM) ordering (G-type) with a Néel temperature (T_N) observed at ~623-643 K.[72]

The G-type AFM ordering occurs due to the Fe^{3+} ions being surrounded by six neighbouring atoms of anti-parallel spins. However, there is canting of these atoms giving rise to a weak ferromagnetic moment due to the Dzyaloshinksii-Moriya (DM) Interaction.[73] The long range AFM ordering is also compromised due to the material giving rise to a spin cycloid with an incommensurate periodicity measured to be ~62 nm which can be seen at temperatures up to T_N.[74, 75]

There has been literature reporting the use of BiFeO$_3$ in gas sensors. Phase-pure nanoparticles were used to detect organic gases due to the p-like semiconductivity displayed by the material.[76-77] On top of this, a BiFeO$_3$ nanocomposite with carbon fibers has been mentioned to have humidity sensing applications due to the high oxygen vacancies introduced by the high volatility of Bi^{3+} ions.[78] The multiferroicity of BiFeO$_3$ gives application to spintronic devices. These have uses in non-volatile memory storage which allow one to write bytes electronically and read them magnetically.[78] Doping with a rare-earth magnetic ion such as Dysprosium (Dy^{3+}) as a replacement of some of the A-site Bismuth (Bi^{3+}) ions is monitored to see how doping affects the multiferroic character of BFO. The currently published research suggests that it improves the ferroelectric and (antiferro-) magnetic properties.[46]

The change in magnetism observed could be due to the disruption of the spin cycloid upon Dysprosium doping. Due to the aforementioned strain and increases of spin canting.[79] Improved ferroelectric character could be attributed to less oxygen vacancies and increased lattice perturbations.[80]

In literature, it is suggested that there is a phase change to non-polar, orthorhombic *Pbnm* on increasing Dy^{3+} content, (> 15%).[50] However the sample analysed for the purpose of this

thesis as described in section 3.1 contained only 5% Dy^{3+} and therefore it is expected to see only rhombohedral *R3c* symmetry at this dopant level. However, due to the large disproportionate ion radii of these ions, it may be seen that Dy^{3+} is more favourable to exist in a secondary phase of $DyFeO_3$ alongside the primary phase of $BiFeO_3$. These distinct materials exist in different symmetries with $DyFeO_3$ crystallising with orthorhombic *Pbnm* symmetry, Figure 3.1. As previously mentioned, there is a phase change on high Dy^{3+} content this can be linked to an increase in lattice strain, whereby the symmetry changes from *R3c* to the more favourable *Pbnm* symmetry. *R3c* is classed as a unit cell whereby the 3 *'a,b,c'* axes are equal and are separated by oblique angles. *Pbnm* has unequal axes at right angles to eachother.[81]

At higher temperatures, 5% Dy-BFO undergoes a phase change due to the orthorhombic β-*Pbnm* symmetry becoming more stabilised.
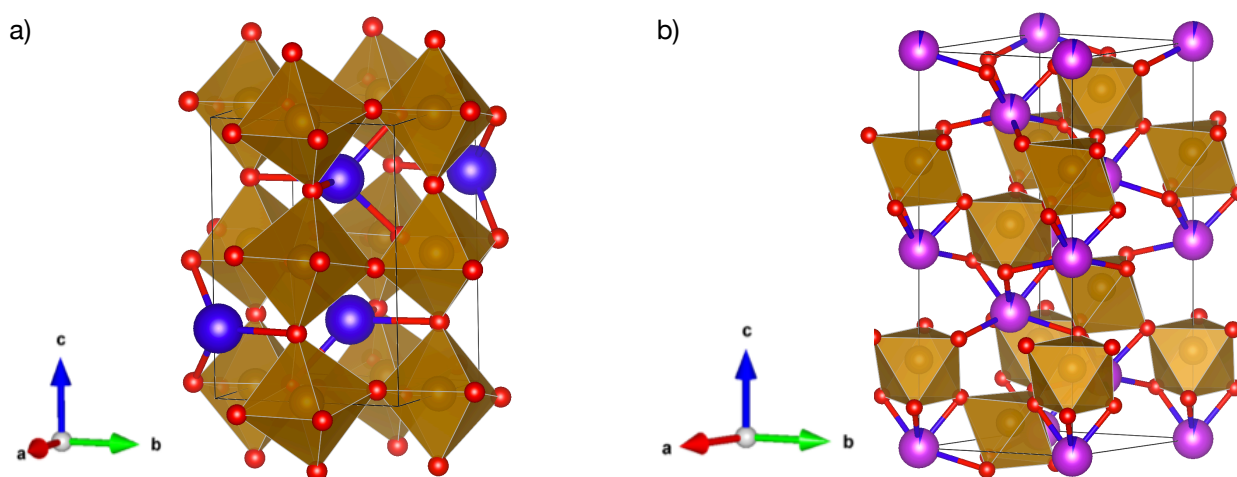
Figure 3.1 - a VESTA image of two crystallographic unit cells of Dy^{3+} substituted $BiFeO_3$.
a) shows Pbnm symmetry b) shows R3c symmetry with Dy^{3+} and Bi^{3+} on the same site.
Red spheres demonstrate oxygen atoms. Brown octahedra show FeO_6 Octahedra with the Fe^{3+} in the centre. Blue spheres demonstrate Dy^{3+} ions, and pink spheres showing Bi^{3+} ions.

3.1   Synthesis

The synthesis of this material was done *via* a '*shake and bake*' method completed by Arnold.[50]

The raw materials for Dy-$BiFeO_3$ are: Bi_2O_3, Dy_2O_3, Fe_2O_3 (all Sigma Aldrich, ≥99%). The following reaction describes the compounds synthesis:

$$\frac{1}{40}Dy_2O_3 + \frac{19}{40}Bi_2O_3 + \frac{1}{2}Fe_2O_3 \rightarrow Bi_{0.95}Dy_{0.05}FeO_3$$
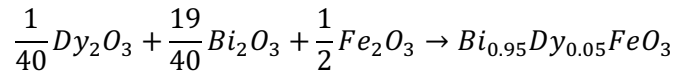
Phase purity of 5% Dy-BFO was analysed with a Bruker D8 Advance diffractometer with Cu Kα_1 (40 kV and 40 mA, λ = 1.54056 Å) with a 2θ range of 10-70°.

Variable temperature powder neutron diffraction patterns were obtained on the high-resolution powder diffractometer (HRPD) between 10-1023 K and on the WISH diffractometer, ISIS, UK, between 5-718 K. The material was loaded into 6 mm diameter vanadium cans for both experiments. HRPD is sensitive to perturbations in structure and is able to give us detailed structural information. However, due to the long periodicity of the spin cycloid for BFO, the magnetic peaks are ~4.6 Å; this is detected at the 45° bank which has bad resolution. Whilst WISH is not as detailed, it maintains a good resolution over a larger range and therefore is able to detect the incommensurate spin cycloid, allowing one to analyse the magnetic contributions more conclusively. In turn, WISH is able to give more accurate magnetic information compared to HRPD and therefore both are used in the analysis.

The refinements were completed using the General Structure Analysis Suite (GSAS) and the Fullprof suite to allow analysis of nuclear and magnetic scattering.

A pellet was made for use in Raman spectroscopy as well as SEM imaging and Dielectric measurements. The pellet was pressed into a 10 mm diameter and sintered at 1123 K for three hours. The pellet was polished until a near mirror smooth surface was achieved for analysis.

SEM imaging was obtained using a Hitachi S-3400 machine, SE imaging was done with 5 ekV. EDX mapping was obtained using BSE imaging at 20 ekV, images were collected at 250x and 500x.

Raman spectra were collected on a Horiba Yvon Jobin LabRAM instrument. Room temperature mapping was performed using a 633 nm laser over a ~50-50 μm area. Two second acquisitions were used on ten integrations with a x50 objective lens and 600 lines per mm grating. The Raman shift range occurred between 80-1280 cm^{-1}.
Variable temperature Raman spectra were collected over a range of 77 – 307 K.

Electrical measurements for Polarisation-electric field loops were made using an Agilent 4294A impedance analyser over a range of ~100 – 5000 Hz over a temperature range of 50 – 340 K and an applied alternate current of 500 mV.

SQUID magnetometry was conducted using a Magnetic Property Measurement System (MPMS) XL-7 instrument. Hysteresis character was observed at 120 K and 300 K in a variable applied magnetic field of ± 7 T with a step size of 0.01 T between 0-0.1 T, a 0.05 T step

between 0.1-0.5 T, and 0.5 T step between 0.5-7 T. High temperature SQUID measurements were conducted with a ZFC/FC analysis between 300-800 K.

TGA/DSC measurements were collected *via* a NETZSCH STA 409PC/PG Thermogravimetric analyser combined with a differential scanning calorimeter.

This material was not synthesised for this project, but the data collected by Donna *et al.* was further analysed. The data corresponds to the multiferroic discussion laid out throughout this thesis.

3.2 Results and Discussion

3.2.1 XRD

XRD analysis of this material at low temperature (12 K) and room temperature (298 K) show there is no change in symmetry with temperature. Full Rietveld refinements were conducted on the diffraction data collected using General Structure Analysis Software (GSAS) II. The data was refined using an *R*3*c* model to fit the data.

The refined parameters were W, Y, Z instrument parameters. The sample X and Y displacement sample parameters. The unit cell, and the x, y, z atomic positions and displacement parameter U.

The refinement data can be seen in Table 3.1. The increase in cell volume is consistent with the data seen.[50] The increase of the parameters can be attributed to the thermal expansion of the material.

Furthermore, with the patterns in Figure 3.2, we can see the data is a good visual fit with the observed model for *R*3*c* symmetry. It can be deduced that at temperatures below 298 K the material exists with this symmetry. The pattern shows the best fit achieved with some peaks not fitting perfectly due to strain effects of the dysprosium ion. Another factor could be the preferred orientation as the sample holder is not able to spin in the Phenix sample holder.
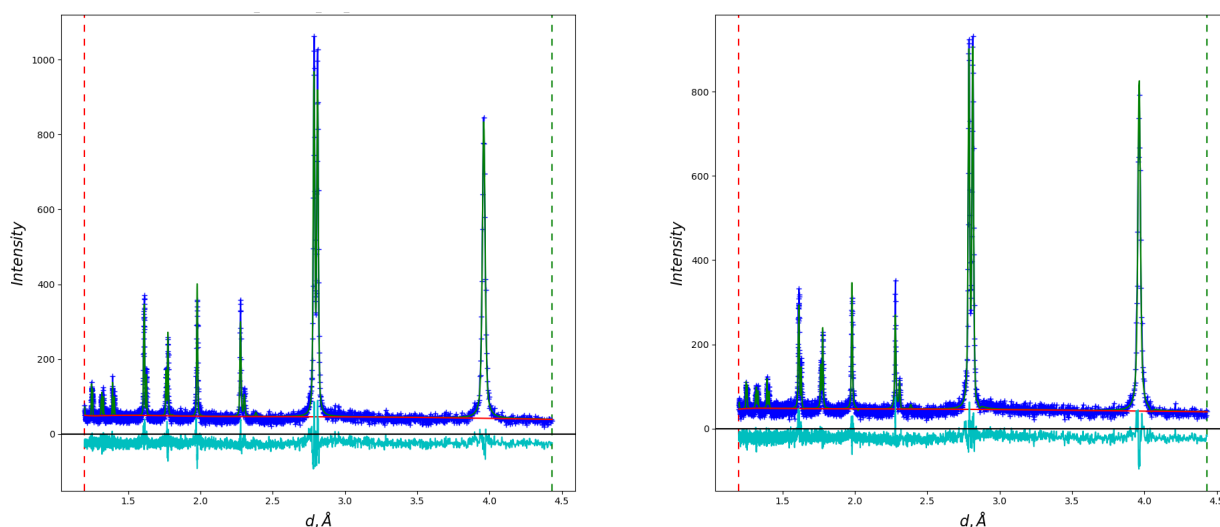
Figure 3.2 - Low temperature 12K (left) and Room temperature 298K (right) Rietveld refinements using GSAS II. The dark blue line showing the experimental data, the green line showing the calculated data fit to the model CIF file, and the light blue showing the difference in the patterns, shown in d-spacing along the x-axis.

Table 3.1 – Refined XRD data for 5% Dy-BFO in $R3c$ at 298 K and 12 K using GSAS II

Temp	Rwp %	χ^2	Cell volume Å	Lattice Parameters Å	
				A	C
12 K	16.949	1.776	370.83(20)	5.567(12)	13.818(2)
298 K	17.617	1.882	376.510(30)	5.5933(4)	13.8968(8)

Table 3.2 – Refined atomic positions and thermal paramaters for 5% Dy-BFO in $R3c$ at 12 K and 298 K using GSAS II.

	12 K				298 K			
	Dy	Bi	Fe	O	Dy	Bi	Fe	O
X	0	0	0	0.445(56)	0	0	0	0.436(78)
Y	0	0	0	0.020(44)	0	0	0	0.018(55)
Z	0	0	0.222(73)	0.954(17)	0.0092(49)	0.0092(49)	0.2327(60)	0.956(25)
Uiso	0.015(10)	0.015(10)	0.012(36)	0.03(11)	0.0462(96)	0.0462(96)	0.029(49)	0.05(15)

In literature, it is stated that on introduction of the rare earth trivalent ion Dy^{3+}, in replacement of the current A-site Bi^{3+} ion, it suppresses the formation of impurity phases and stabilises the rhombohedral structure.[82] This is confirmed by the lack of impurity phase peaks.

However, it is also suggested that the contrary is true, that due to the introduction of Dy^{3+} ions at the Bi^{3+} A-site it could result in some lattice strain, because of the large ion radius disparity: Bi^{3+} = 1.17 Å and Dy^{3+} = 1.03 Å, Ionic radii data taken form the Shannon database of both ions having a coordination of 8.[83] The lattice is destabilised and could produce a Pbnm symmetry in a doped sample as low as 5% Dy^{3+}. It has also been suggested that a monoclinic polar Cc space group is present alongside the suggested Pbnm symmetry.[50]

It was reasoned that XRD analysis alone is not enough to fully probe the symmetry and phase perturbations that arise due to the doping at this magnitude. Therefore, further analysis of variable temperature Powder Neutron Diffraction (PND) data can tell us symmetry changes that could occur as a function of temperatures. PND measurements attained from HRPD and the WISH diffractometer allow further inspection at a higher resolution. One problem is that Dysprosium is known to absorb neutrons.

The patterns attained from these diffractometers allow complex analysis of overlapping Bragg peaks that contain structural information as well magnetic information. These are discussed later in the chapter.

3.2.3   SEM

SEM imaging with Backscattering Electrons at 20 keV along with EDX mapping was conducted to analyse the distributions of the Dy, Bi, Fe, and O atoms within the pellet, Figure 3.3. From this, one can see a clear homogenous distribution of the atoms throughout, and there are no clusters in a single area. SEM with Secondary Electrons at 5 keV were used to detect the topography of the pellet. Images were taken at 500x magnification, with hopes to observe any structural defects or grain boundaries that were present, Figure 3.4.
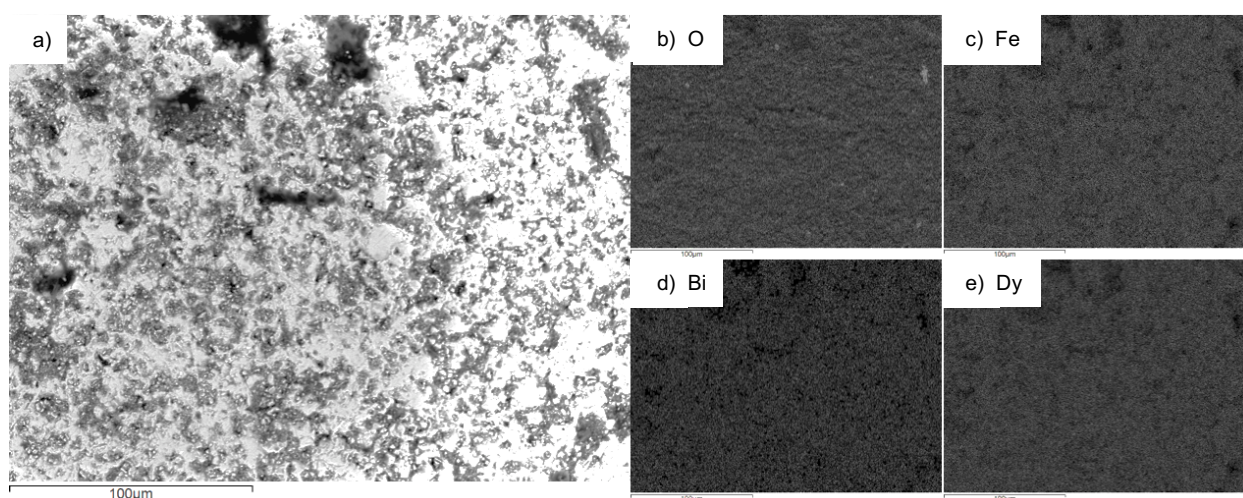
Figure 3.3 – greyscale imaging of atomic distribution of a 5% Dy-BFO pellet. a) BSE imaging at 500x magnification of the surface of the pellet, b) EDX map of Oxygen distribution, c) EDX map of Iron distribution, d) EDX map of Bismuth distribution, e) EDX map of Dysprosium distribution.
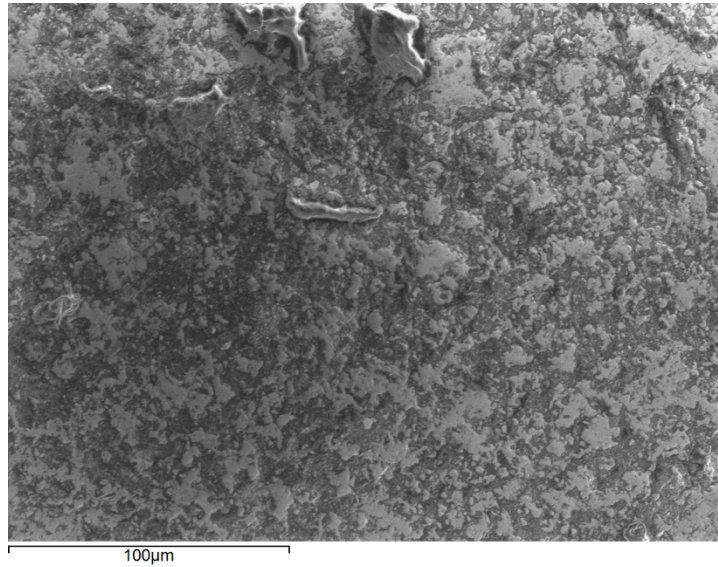
Figure 3.4 – SE imaging of the pellet surface at 500x magnification

It was found that at this magnification, grain boundaries were still unable to be observed. This could be due to the roughness of the sample surface. Although the pellet was polished, complete mirror smoothness was difficult to attain. Figure 3.4 shows the roughness of the pellet surface. In correlation with the EDX mapped image, Figure 3.3, we can see there is an even distribution across the mapped area consistent with homogenous samples.

The pellet was fragmented in order to see the atomic distribution inside. Further SEM imaging with backscattering electrons at 20 keV alongside EDX mapping at the 250x magnification was analysed, Figure 3.5.
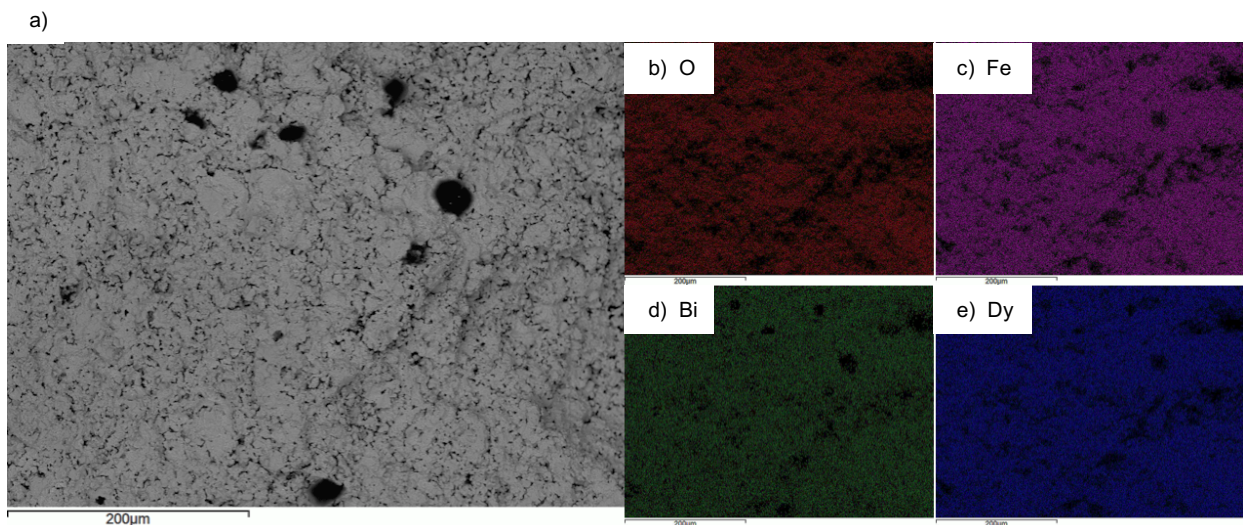
Figure 3.5 - greyscale imaging of atomic distribution of a 5% Dy-BFO pellet. a) BSE imaging at 250x magnification of the pellet side, b) EDX map of Oxygen distribution in red, c) EDX map of Iron distribution in magenta, d) EDX map of Bismuth distribution in green, e) EDX map of Dysprosium distribution in blue.

The EDX map was colourised to see the homogenous distribution of the atoms more clearly, within the area analysed. Some of the areas appear black due to pores within the pellet. The surface of this sample was not very smooth so some of the imaging shows poor BSE detection. A clear homogenous distribution of the 4 atoms is visible.

Figure 3.6 shows the SE image at 5 keV and magnification of 250x of the broken pellet side. No grain boundaries were seen due to the roughness of the sample and smaller grain size.
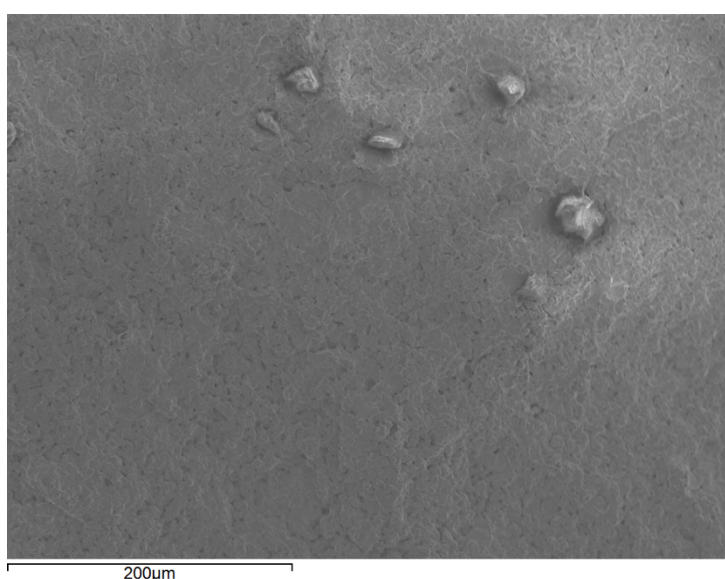
Figure 3.6– SE imaging of the fragmented pellet side at 250x magnification

3.2.4   SQUID

SQUID magnetometry was conducted on the sample at both room temperature (300 K) and low temperature (120 K). The magnetisation seen is a straight line with a small hysteresis loop magnified, Figure 3.7, These are reproduced from data presented in Lennox *et al.*[50]

The hysteresis loop shows that at both 120 K and 300 K, the sample has poor saturation which correlates to the G-type antiferromagnetic behaviour stated in the literature for Dy-BFO.[50] It is also suggested that the poor magnetisation is a result of the iron oxide sub lattice providing a molecular magnetic moment, which magnetises the paramagnetic rare earth ion.[84] The spin-canted iron atoms on the iron oxide octahedra allow for weak ferromagnetism in the bulk antiferromagnetic ordering due to the Dzyaloshinskii-Moriya interactions.

Furthermore, due to this change in magnetic spins leading to ferromagnetic character, it has led to the possibility of uncompensated spins in the bulk AFM ordering. This arises due to the anti-parallel spin pairing becoming unbalanced; there are more spins in one direction than the other which reduces the antiferromagnetism.
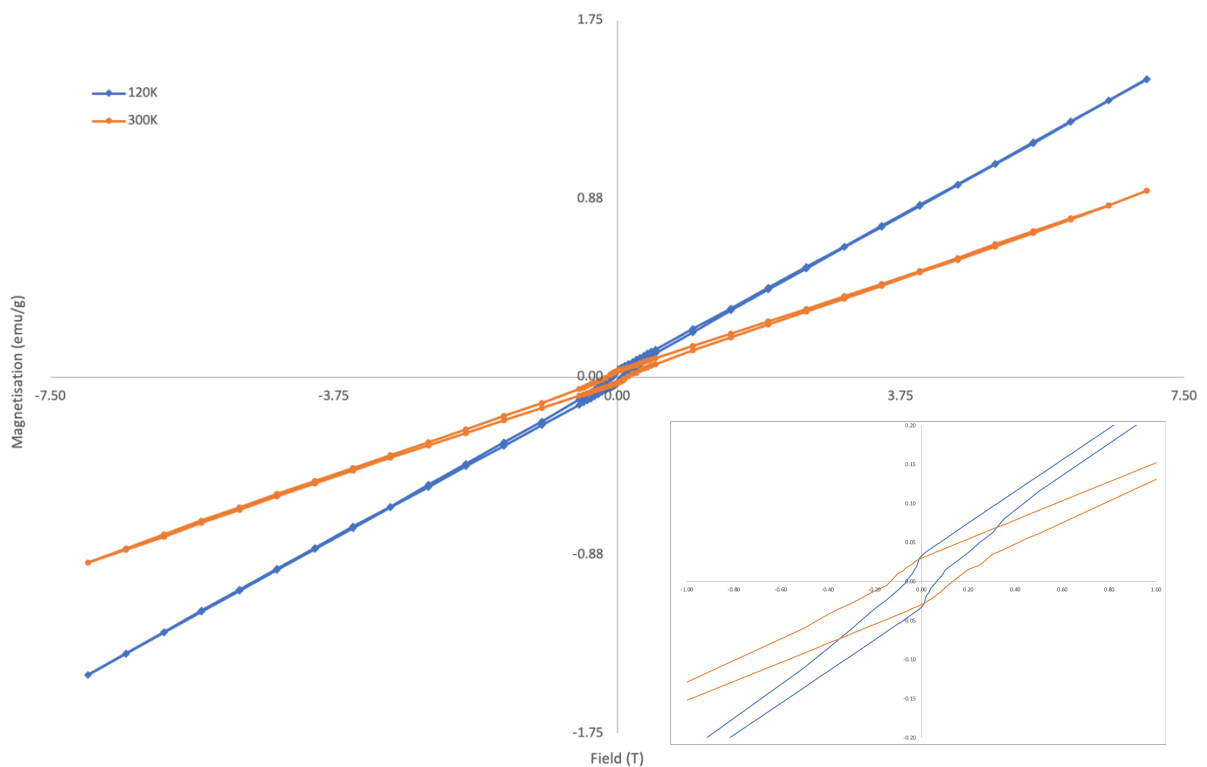
Figure 3.7 - A graph to show the magnetisation of Dy-BFO as a function of field strength in T, showing hysteretic behaviour

On closer inspection of the inset in Figure 3.7, we can see a small difference in remnant magnetisation of 0.0331 emu/g and 0.0297 emu/g for 120 K and 300 K respectively. There is a much larger difference for the coercivity field which is ~0.07 T and ~0.15 T for 120 K and 300 K respectively.

A high temperature (HT) SQUID analysis of the material was conducted, and it was found that there is a phase transition roughly around 675 K, Figure 3.8, which is an increase from

the expected value of pure BFO (~633 K). This is consistent with the T_N found in literature for other RE doped BFO materials.[50, 85, 86]
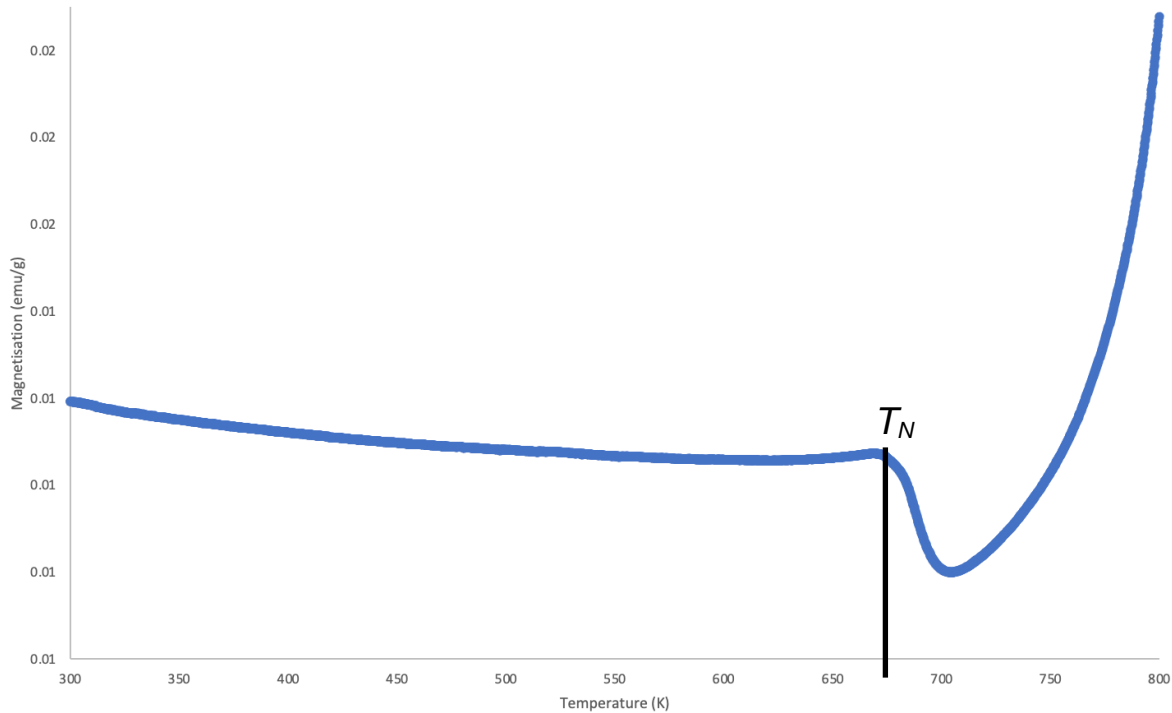
Figure 3.8 - A graph to show the magnetisation of Dy-BFO as a function of temperature.

3.2.5   P-E Loop

Utilising a Polarisation-electric (PE) field loop, one can see how changing the voltage and current can change the electric hysteresis of the material. Most commonly, hysteresis loops are shaped in a sigmoidal '*s*' shape. The shape given to this Hysteresis can be said to be somewhat '*lemon*' shaped. The Hysteresis loop of this ferroelectric material shows no saturation polarisation. This correlates to similar hysteresis loops reported by Zhang *et al.,* Zheng *et al.*, Kumar *et al.*, Arnold *et al.* [50, 80, 86, 87]

This can be attributed to high leakage currents which are associated with the variable oxidation states of Fe ions (II and III) in the BFO material. Alongside oxygen defects which are caused by the volatile nature of the Bi^{3+}. Doping with Dy^{3+} is a strategy which has been said to overcome these high leakage currents.[86] This is because it reduces the oxygen defects by replacing the volatile Bi^{3+} and further stabilises the ferroelectric character.[80]

From Figure 3.9, we can see a clear relationship with switch in polarisation and a switch in current on increasing the applied voltage. This suggests some ability to switch, consistent

with FE behaviour. However, the data is consistent with a lossy dielectric and shows a similar profile to a hysteresis loop presented by J. F. Scott,[88] meaning that FE behaviour cannot be confirmed.

There is also some potential loss in ferroelectric character as the ferroelectricity in BFO arises from the lone pair $6s^2$ electrons hybridising with the p orbital. This creates a high polarisability and their orientation will create a local dipole leading to polarisation.[86, 89] This will become more diffuse in the rare earth ion electron cloud.
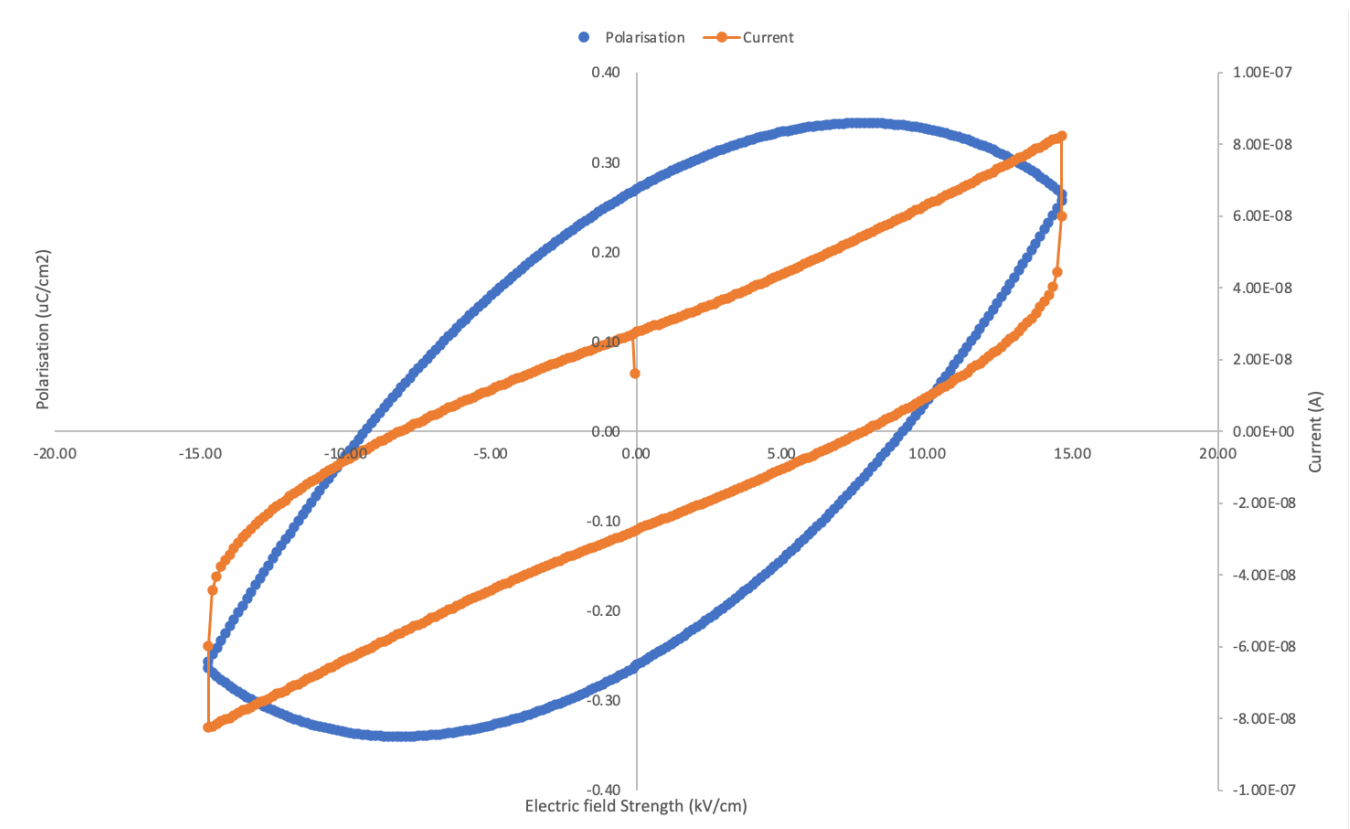
Figure 3.9 - A P-E Loop of a Dy-BFO pellet with gold adhered onto the top and bottom

3.2.6 TGA / DSC

Thermogravimetric Analysis (TGA) was used to analyse the thermal stability of the material. This combined with Differential Scanning Calorimetry (DSC) was used to probe into potential phase changes that could occur over a temperature range (296-1223 K), Figure 3.10. 60.2 mg of Dy-BFO was used for analysis and was found that after analysis, 60.2 mg of the sample remained. It can be said that the thermal stability of Dy-BFO is high as it did not change

on increasing temperature, it remained at 100% mass up to and including 1223 K. This is inconsistent with studies of pure BFO which show dielectric decomposition above 1173 K.[90]

The first derivative of the DSC curve is plotted. We can see a small drop in mW/mg around 926 K and a second, drop of mW/mg at 1055 K. The two drops potentially belong to the two temperature phase changes of T_N and T_C respectively. This further correlates to the T_N found in the HT SQUID discussed above.
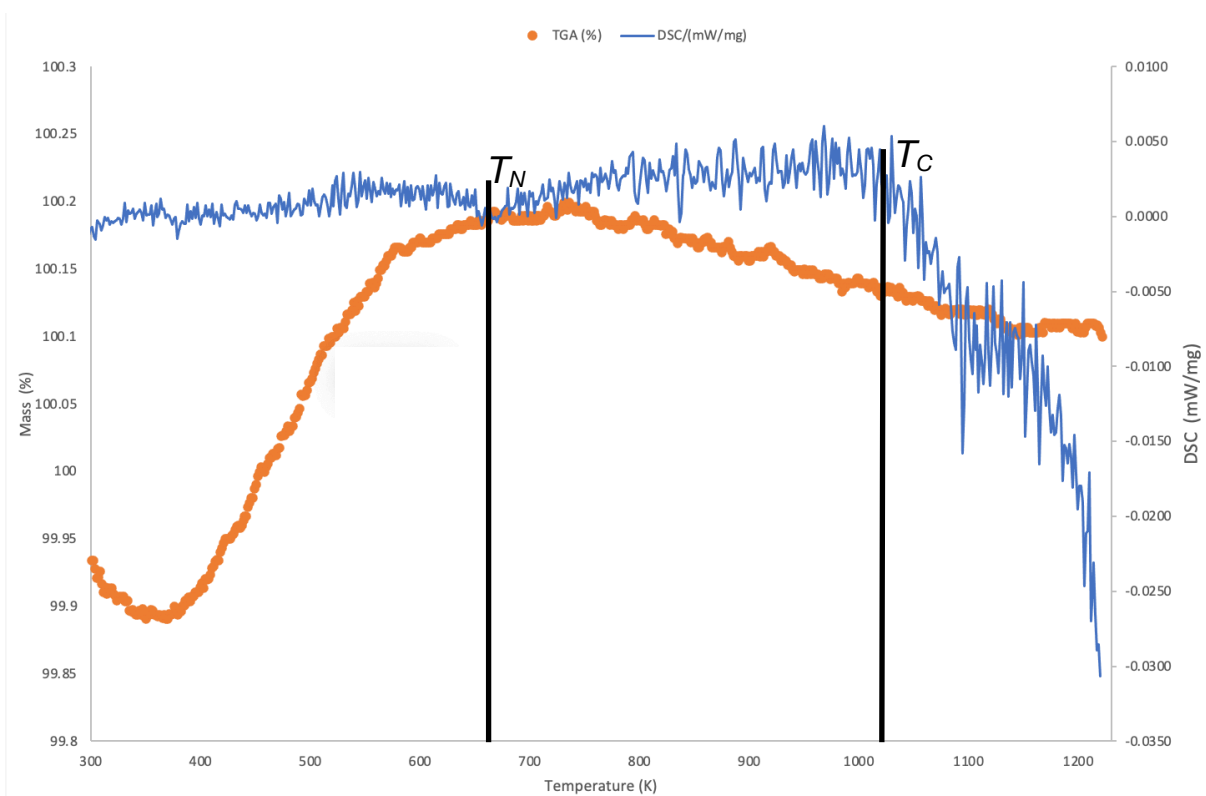
Figure 3.10 – A graph showing the TGA curve (orange, x-axis) alongside the first derivative of the DSC curve (blue, z-axis) as a function of temperature

The stated FE phase changes for pure BFO T_c occurs between 1083-1103 K. Showing some variation due to the incorporation of Dy^{3+}.

There is a decrease in the expected phase transition from ~1083 K to 1055 K this could be due to the introduction of orthorhombic phase around this temperature, which can be seen in literature.[87, 91] This shows that at this temperature there is enough energy, combined with increased lattice strain from the large ion radius disparity of Bi^{3+} and Dy^{3+} for phase transition of the α-phase to the β-phase.[92] Furthermore, it can be seen that even a small addition of Dy is enough to perturb the FE behaviour.

3.2.7   WISH

Wide angle In a Single Histogram (WISH) diffraction data from the ISIS Neutron source is analysed over a range of temperatures from 5 K to 718 K. Magnetic Rietveld refinements of the diffraction data were carried out to see the change in magnetic contribution over the temperature range. Table 3.3 shows a preview of the change in lattice positions of '*a*' and '*c*', the propagation vector, as well as the magnetic moment of 5% Dy-BFO for 7 temperatures. (For full Data sets see <mark>Appendix 3.1</mark>)

Table 3.3 – WISH diffractometer data of lattice parameters, magnetic moment and propagation vector, showing accompanying errors

Temperature (K)	Lattice Parameters (Å)		Magnetic Moment (emu/g)	Propagation Vector
	'*a*'	'*c*'		
5	5.5875(808)	13.872(368)	4.13(26)	0.00395(636)
110	5.5886(806)	13.877(367)	4.08(26)	0.00397(679)
230	5.5925(827)	13.893(375)	3.88(27)	0.00389(728)
353	5.5965(863)	13.908(390)	3.61(27)	0.00379(770)
473	5.6030(903)	13.930(406)	3.11(29)	0.00360(956)
583	5.6078(971)	13.945(434)	2.60(34)	0.0035(130)
718	5.616(113)	13.970(502)	0.7(100)	0.003(154)

Refinements of the data with Fullprof analysis software, see appendix 3.1 for refinement data, allowed us to see a clear decrease in the magnetic Bragg peak at 4.6 Å, Figure 3.11. At 5 K we can see a magnetic moment of 4.13(26) emu/g on increasing the temperature, there remains a weak magnetic Bragg peak 0.7(1) emu/g at 718 K which is consistent with the SQUID data presented above.

The data seen in Figure 3.11 also shows two peaks of different intensity at ~2.35 Å at 5 K. At 718 K these two peaks exhibit a 1:1 ratio, this could be due to the change in lattice parameters between *R*3*c* and *Pbnm,* further analysed below. (Full diffraction plots can be seen in the appendices.)
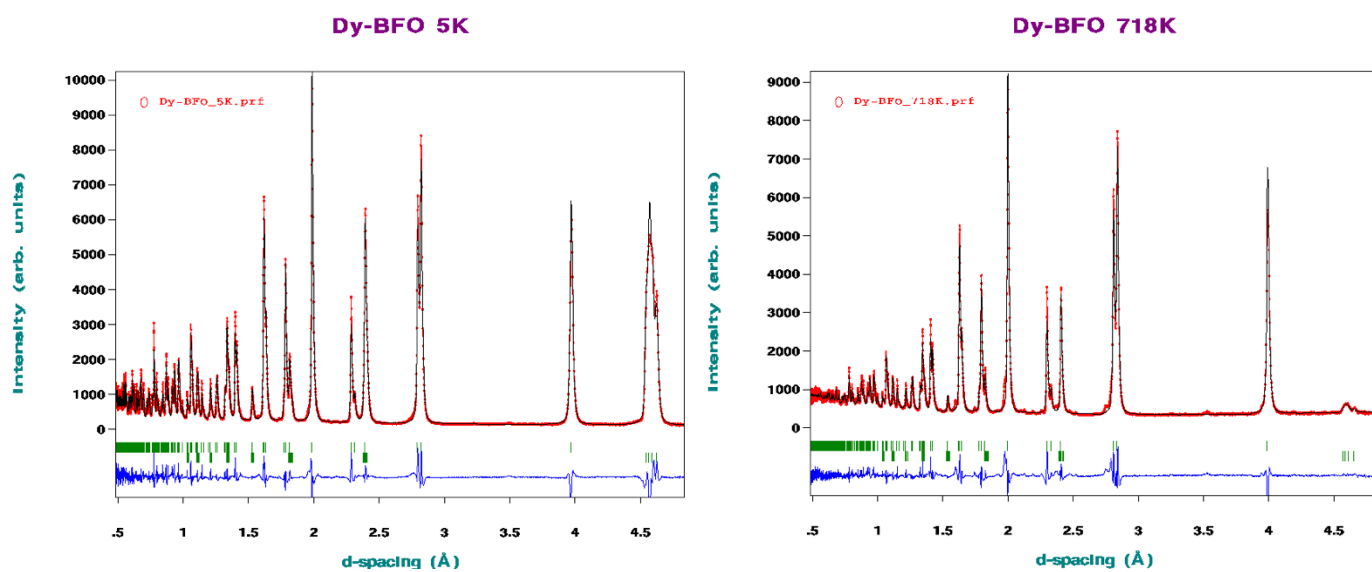
Figure 3.11 – Fullprof Rietveld refinement plots of WISH diffraction data at 5 K and 718 K showing a decrease in the magnetic Bragg peak and intensity changes.

As previously mentioned, the data shows a clear decrease in the magnetic character on increasing the temperature, Figure 3.12. There is a steady decline of the magnetic moment from 4.13 emu/g at 5 K which decreases to 2.30 emu/g at 633 K. At 643 K the magnetic moment is recorded as 2.18 emu/g and there is a dramatic drop to 0.7 emu/g over a 75 K range to 718 K. This is consistent with the Néel temperature expected from SQUID magnetometry.
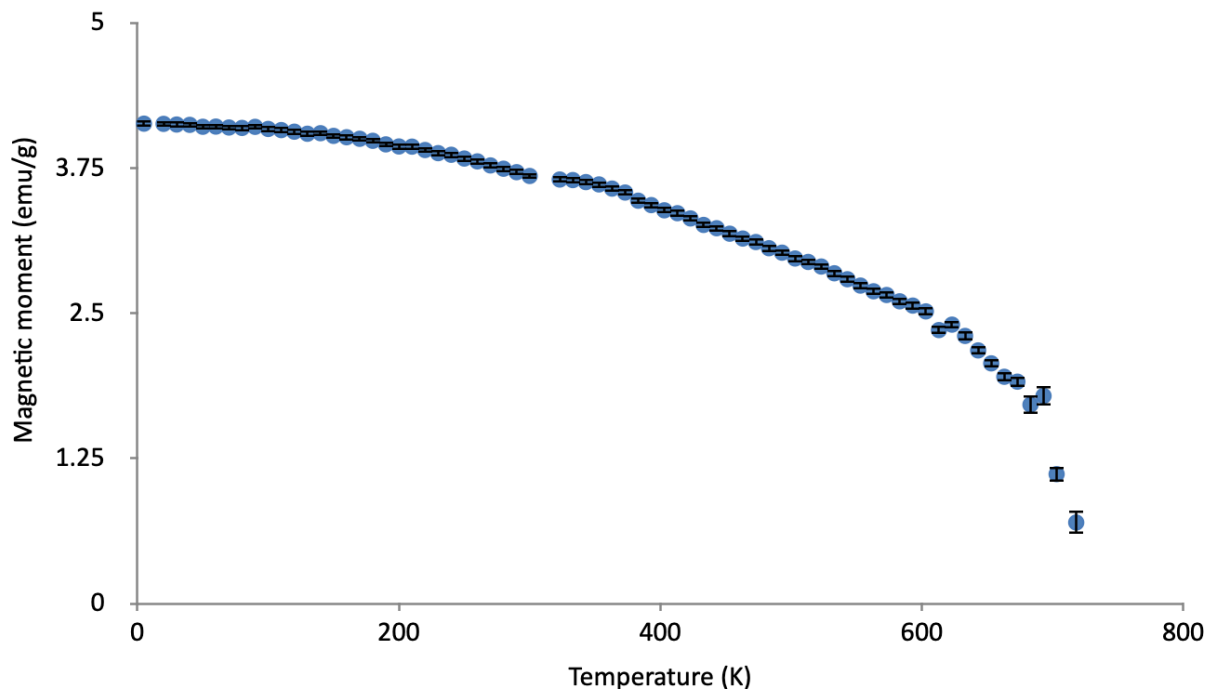
Figure 3.12 – Magnetic moment of 5% Dy-BFO decreasing as a function of temperature, collected via WISH diffractometer. the error bar for each measurement shown.

This has direct correlation with the decrease in the propagation vector (K) which demonstrates a decrease in spin between one magnetic moment relative to the next on increasing temperature, Figure 3.13. This shows that there is increased canting between the Fe^{3+} ions in the FeO_6 octahedra which alludes to the elongation of the spin cycloid, which increases the spontaneous magnetisation.[93] This is contrary to pure BFO which has a shorter spin cycloid as there is less canting in comparison to the Dy doped sample even at room temperature.
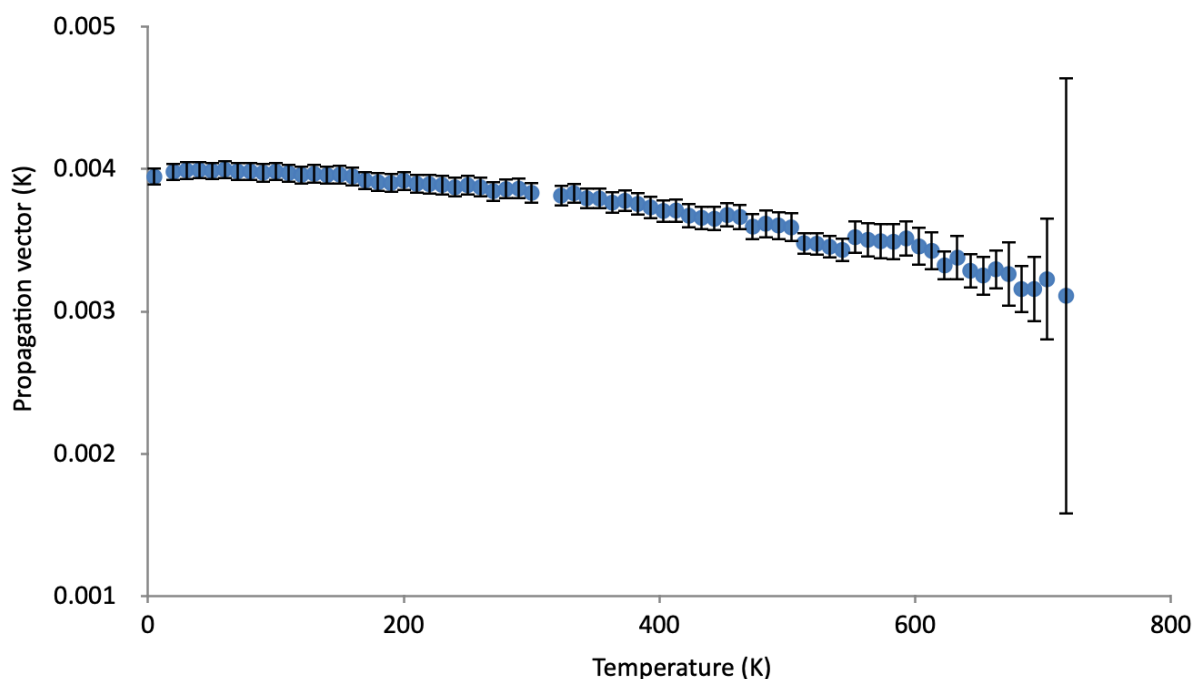
Figure 3.13 – Propagation vector, K, collected *via* the WISH diffractometer, decreasing as a function of temperature with the error bars shown for each measurement.

The WISH data also describes a clear linear increase in lattice parameters: '*a*' and '*c*', on increasing the temperature, Figure 3.14 and Figure 3.15, respectively, and an increase in unit cell volume, Figure 3.16

At 5 K the cell volume is 375.061 $Å^3$ which increases to 381.527 $Å^3$, a range of ~6.5 $Å^3$, figure 27. This can be attributed to the thermal expansion of the crystal lattice on increasing temperatures and can further be supported by the VT-XRD data analysed above.

In all of the WISH data analysed there is an anomaly around 300-323 K in each measurement. This is due to a change of sample environment, and subsequently where heating occurred. Therefore, there is a gap in the measurement from room temperature to the initial heating temperature, 323 K. An anomaly at low temperature is due to a jump from 5 K to 20 K.
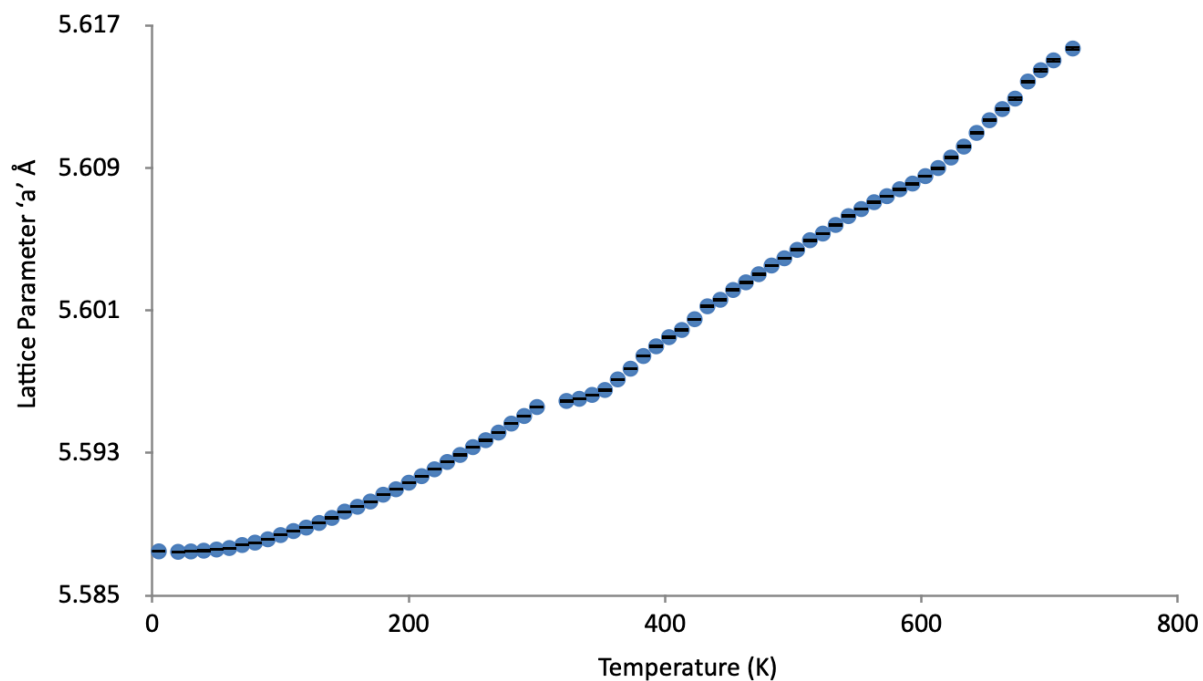
Figure 3.14 – Lattice parameter '*a*', collected *via* the WISH diffractometer, increasing in Ångstrom, as a function of temperature. with the error bars for each measurement shown.
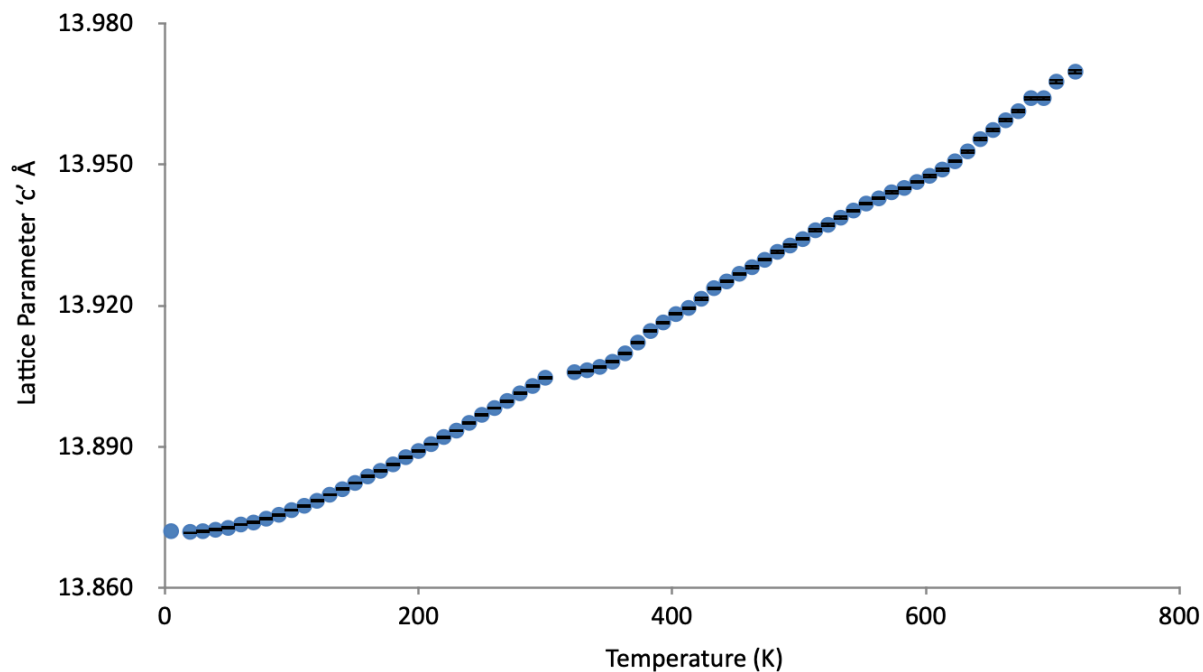
Figure 3.15 – Lattice parameter '*c*', collected *via* the WISH diffractometer, increasing in Ångstrom, as a function of temperature. with the error bars for each measurement shown.
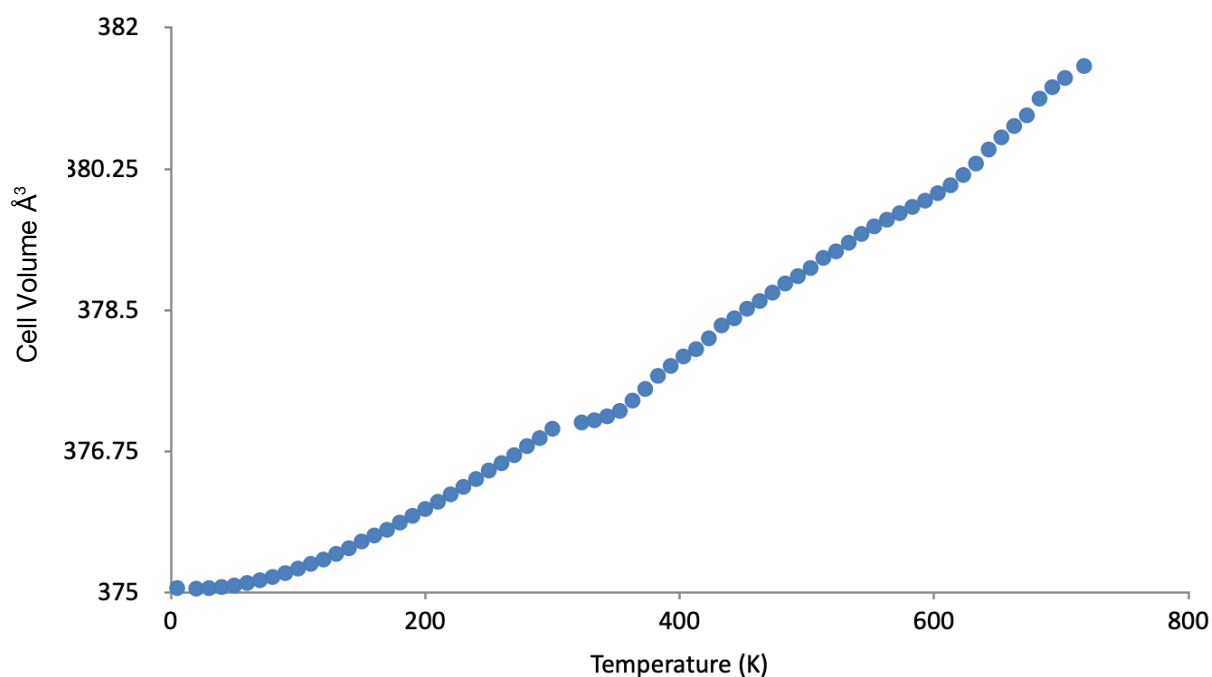
Figure 3.16 – Cell volume, collected via the WISH diffractometer, increasing in Å³, as a function of temperature.

3.2.8   HRPD

High resolution powder diffraction (HRPD) data from the ISIS Neutron source is analysed over a range of temperatures from 10 K to 1023 K. Rietveld refinements of the diffraction data were carried out to see changes of lattice parameters and their correlation between the phase fractions of *R*3*c* and *Pbnm* space groups. Refinements were carried out between 30 – 1023 K as there was a problem in refining the 10 K data set. General structure analysis software (GSAS) was used to refine these data sets using 37 variables including: lattice parameters, atom positions, (with XYZU constraints on the Bi^{3+} and Dy^{3+} atoms ensuring equivalence) peak shape, and background. The Background was fitted with 12 terms, using a shifted Chebyschev polynomial function. The peak shape was modelled *via* a pseudo-Voigt function. A damping factor of 9 was also used throughout to minimise perturbations during the refinement. *R*3*c* symmetry was used to fit the data.

Increasing the temperature, one can see a clear increase in lattice parameters '*a*' and '*c*', Table 3.2. This is expected due to the increase in thermal energy. This can also be correlated to the previously presented WISH data. There is a peak in the pattern at 2.1 Å which cannot be refined. This corresponds to an impure phase being present in the material, most likely a

BiO rich phase. This peak diminishes at 773 K showing that on further heating impurity phases can be removed. (see appendix for refined patterns).

From 573 K there is an emergence of a secondary phase in the material, on increasing temperatures this phase becomes more intense and can be correlated to the β-phase, *Pbnm*, becoming more stabilised. From 573-673 K the secondary phase is too small to refine. Therefore, multi-phase refinements were conducted on temperatures of 773 – 1023 K. The *R*3*c* phase of the material decreases on increasing temperature, at the same time the *Pbnm* phase is becoming more prevalent. This can be seen more clearly though Figure 3.17. The final temperature, 1023 K, showed a very low primary *R*3*c* phase, the bond lengths for this temperature were able to be extracted but the bond angle was too negligible. The bond lengths and angles are seen in appendix 3.72.

The HRPD data analysed doesn't account for the magnetism as it is week in the backscattering detector. It is much stronger and be seen more clearly in the WISH data. However, one is still able to see the change in phase symmetry at higher temperatures changing from the *R*3*c* group to the *Pbnm* space group. This is to say the lattice becomes centro-symmetric (orthorhombic) from a previously non-centrosymmetric (rhombohedral) orientation. Due to the lack of the inversion centre, there can be no time inversion, therefore no FE character. This can be seen through Figure 3.17 which correlates with the DSC phase change seen in Figure 3.10.
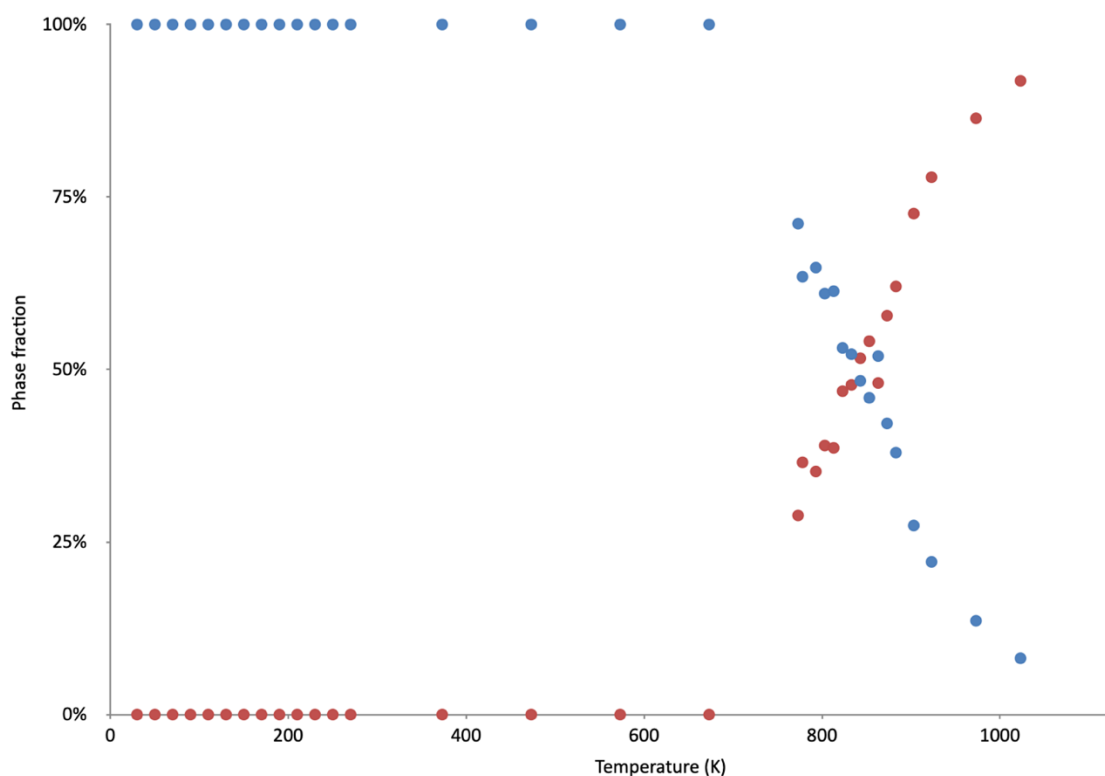
Figure 3.17 – A graph to show the phase fraction of *R*3*c* (blue dots) and *Pbnm* (red dots) as a function of temperature. Error bars are too small to be seen but the errors included in Table 3.4.

Table 3.4 – Showing the refined lattice parameters as well as the χ^2 and R_{exp}, R_{wp} values for the HRPD data. With accompanying errors in brackets.

Temp (K)	Rwp %	Rexp %	Chi squared	R3c Å A	R3c Å C	R3c Å V	Phase fraction % R3c	Phase fraction % Pbnm	Pbnm Å A	Pbnm Å B	Pbnm Å C	Pbnm Å V
30	3.9	3.62	4.674	5.56573(1)	13.81828(4)	370.705(1)	1	0				
50	3.98	3.65	4.821	5.56506(5)	13.81675(2)	370.575(7)	1	0				
70	3.94	3.66	4.733	5.56529(5)	13.81821(2)	370.645(7)	1	0				
90	3.92	4.26	4.719	5.56566(5)	13.81967(2)	370.733(7)	1	0				
110	3.88	3.59	4.593	5.56602(5)	13.82167(2)	370.835(7)	1	0				
130	3.91	3.64	4.694	5.56649(5)	13.82379(2)	370.954(7)	1	0				
150	3.85	3.58	4.559	5.56703(5)	13.82609(2)	371.088(7)	1	0				
170	3.83	3.54	4.505	5.56765(5)	13.82856(2)	371.237(8)	1	0				
190	3.82	3.52	4.458	5.56826(5)	13.83101(2)	371.385(8)	1	0				
210	3.83	3.58	4.515	5.56896(5)	13.83383(2)	371.554(8)	1	0				
230	3.73	3.42	4.279	5.56970(5)	13.83678(2)	371.732(8)	1	0				
250	4.05	3.81	2.763	5.57044(6)	13.83957(3)	371.905(8)	1	0				
270	3.82	3.59	3.438	5.57128(5)	13.84229(2)	372.090(8)	1	0				
373	3.06	2.93	2.773	5.57681(5)	13.86136(2)	373.344(8)	1	0				
473	3.33	3.27	1.686	5.58246(6)	13.87864(3)	374.567(9)	1	0				
573	3.25	3.16	1.618	5.58907(6)	13.89820(3)	375.983(1)	1	0				
673	3.26	3.09	1.65	5.59636(6)	13.91847(3)	377.514(1)	1	0				
773	2.16	1.91	2.463	5.6042(1)	13.93760(4)	379.090(2)	71.1(18)	28.9(18)	5.5118(4)	5.6471(4)	7.8786(6)	245.227(3)
778	2.89	2.81	1.302	5.6046(2)	13.93850(5)	379.164(2)	63.5(23)	36.5(28)	5.5127(5)	5.6475(4)	7.8794(7)	245.310(4)
793	2.93	2.82	1.359	5.6054(2)	13.94030(5)	379.332(2)	64.8(22)	35.2(22)	5.5158(5)	5.6479(4)	7.8824(6)	245.558(3)
803	2.82	2.68	1.474	5.60538(6)	13.9395(3)	379.304(1)	61.0(22)	39.0(22)	5.5169(3)	5.6471(4)	7.8834(6)	245.601(3)
813	2.98	2.87	1.393	5.6068(2)	13.94280(5)	379.581(2)	61.4(21)	38.6(21)	5.5206(4)	5.6484(4)	7.8852(5)	245.879(3)
823	2.97	2.87	1.404	5.6075(2)	13.94430(5)	379.726(2)	53.1(19)	46.9(19)	5.5225(3)	5.6482(4)	7.8874(5)	246.024(3)
833	2.98	2.85	1.399	5.6084(2)	13.94510(5)	379.858(2)	52.2(20)	47.8(20)	5.5255(3)	5.6484(4)	7.8894(5)	246.227(3)
843	2.99	2.9	1.417	5.6092(2)	13.94720(5)	380.033(2)	48.4(12)	51.6(12)	5.5274(3)	5.6482(3)	7.8942(5)	246.457(3)
853	3.07	2.89	1.491	5.5297(2)	13.94820(6)	380.115(2)	45.9(17)	54.1(17)	5.5297(3)	5.6481(3)	7.8957(5)	246.601(3)
863	3.14	2.99	1.563	5.6102(2)	13.94860(6)	380.200(2)	51.9(17)	48.1(17)	5.5324(3)	5.6474(3)	7.8980(4)	246.762(2)
873	3.19	3.303	1.658	5.6112(2)	13.95120(6)	380.410(0)	42.2(15)	57.8(15)	5.5330(3)	5.6462(3)	7.9051(4)	246.961(2)
883	3.25	3.04	1.691	5.6121(2)	13.95350(6)	380.599(0)	37.9(14)	62.1(14)	5.5359(3)	5.6463(3)	7.9075(4)	247.168(2)
903	3.49	3.27	1.935	5.6138(3)	13.95550(7)	380.885(0)	27.4(12)	72.6(12)	5.5410(3)	5.6458(3)	7.9116(5)	247.499(3)
923	3.91	3.68	1.826	5.6154(1)	13.95980(6)	381.212(0)	22.1(10)	77.9(10)	5.5463(2)	5.6453(2)	7.9159(4)	247.851(2)
973	4.23	3.85	2.142	5.6209(4)	13.97280(2)	382.320(1)	13.59(93)	86.41(93)	5.5608(4)	5.6469(3)	7.9237(5)	248.818(3)
1023	3.86	3.3	6.093	5.6268(5)	13.99300(4)	383.670(0)	9.82(87)	90.18(87)	5.5740(3)	5.6482(3)	7.9351(5)	249.821(2)

3.2.9 Raman

In pure BFO, there is stated to be 13 vibrational modes which correlate with the group theory suggested for *R*3*c* symmetry.[94] Dy-BFO demonstrates the same symmetry as represented with the XRD data presented. These 13 vibrational modes have been visible in experimental Raman data, which are overlaid in appendix 3.105. In previous studies of this material, it is stated that there are 2 intense peaks visible at ~140 cm^{-1} and ~175cm^{-1} which corresponds to the vibrational modes of the irreducible representations of A_1-1 and A_1-2 respectively.[50, 95, 96, 97]

Analysis of variable-temperature Raman spectra (77 - 307 K) shows clear intensity changes as well as some wavenumber variation of the two main peaks situated at wavenumbers between: 139-145 cm^{-1}, and 167-172 cm^{-1}, Figure 3.18 and Figure 3.19 respectively. These correspond to the wavenumbers seen in literature.[94, 100] The wavenumber peak position variance can be attributed to higher temperatures. In both cases, the A_1-1 and A_1-2 vibrational modes decrease in wavenumber when the temperature increases. This could correlate to lattice parameter changes seen on increasing temperature consistent with powder neutron diffraction (PND) data.
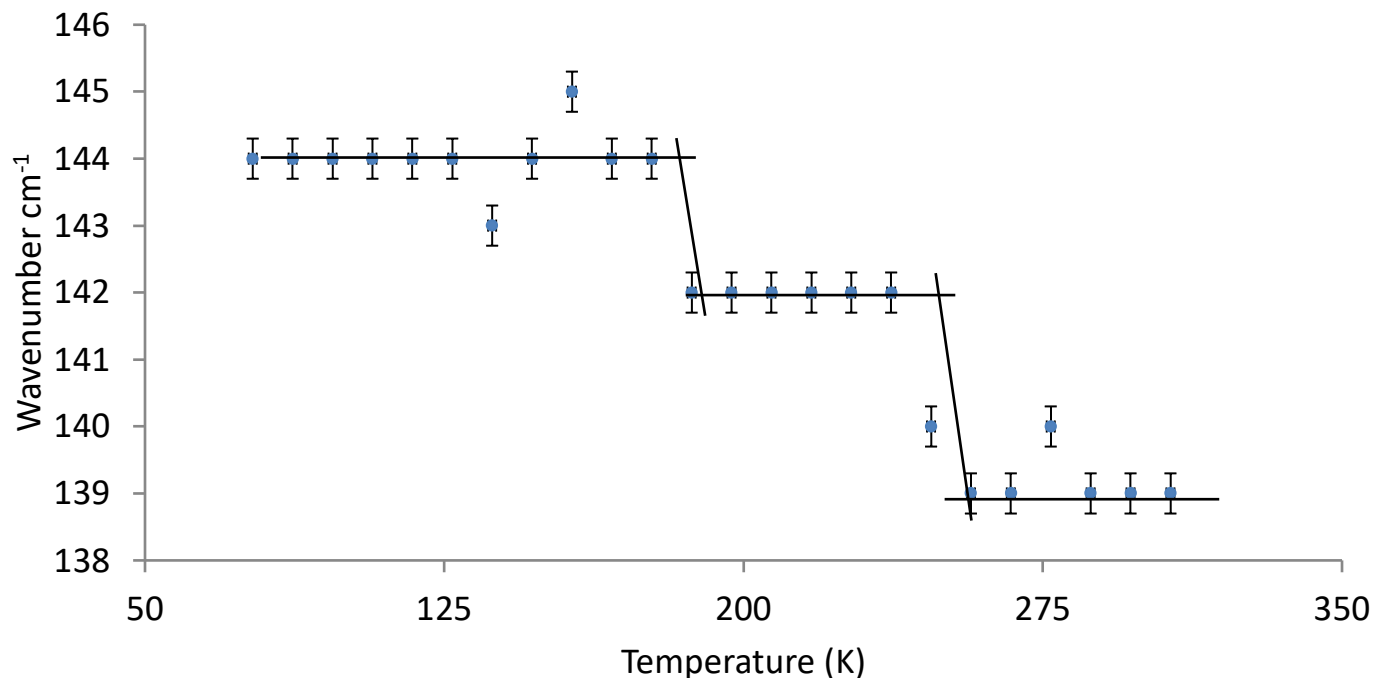
Figure 3.18 - Position of the Raman peaks at variable temperatures which correspond to the A_1-1 vibrational mode in Dy-BFO. Data was extracted manually *via* cursor peak pick, therefore, errors of 0.3 cm^{-1} are used for each measurement.
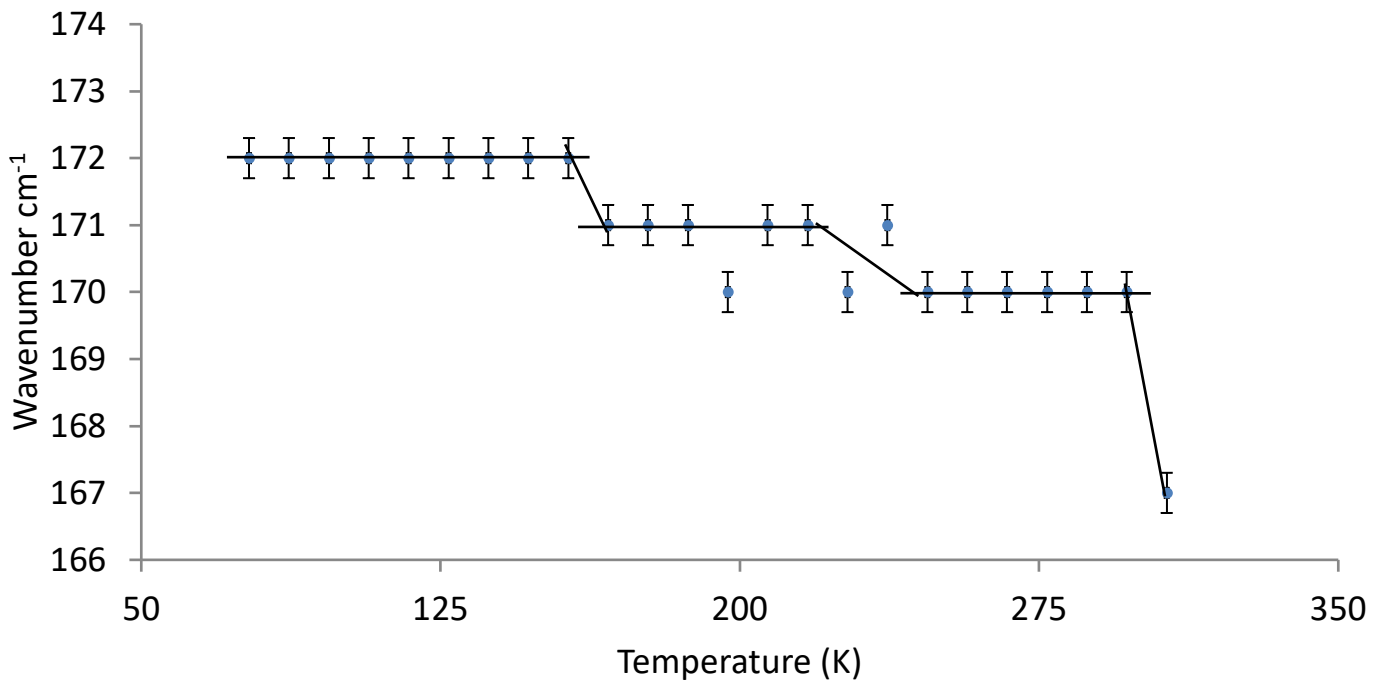
Figure 3.19 - Position of the Raman peaks at variable temperatures which correspond to the A_1-2 vibrational mode in Dy-BFO. Data was extracted manually *via* cursor peak pick, therefore, errors of 0.3 cm^{-1} are used for each measurement.

On increasing temperatures, the higher kinetic energy allow for more densely populated vibrational states which give higher intensity Raman peaks. Vibrational stretches of the Fe-O bond and Bi-O bond are subdued at lower temperatures T << 217 K due to lack of thermal energy. At increasing temperatures T ≥ 227 K, the bonds have a higher energy and become more intense - the optical phonons, which are the reason for the more intense peaks, can further be seen through the displacement parameters seen in the WISH data. However, to fully test this theory, higher temperature Raman spectroscopy (T > 307 K) will be needed to probe into the vibrational effects which take place. The lower temperatures can also attest for the peak broadening of the Raman spectra. There are fewer thermal influences at lower temperatures, so the bond vibrations arise purely from the excitation of the laser beam. On increasing temperatures, the bonds have more energy, therefore the peaks have the excitation energy not only from the laser beam but also from the lattice vibrations.

The difference in peak height and shape also correlates to the orientation of the lattice cell in the pellet analysed. The homogeneity of the recursive crystal lattice can be disrupted by grain boundaries, changing the morphological orientation of these crystallites; not only this but a secondary phase becoming prominent at higher temperatures will also change the Raman peaks. This suggests there maybe surface defects consistent with literature.[98] There are also

large variations in point spectra due to domain related effects as discussed by Hlinka *et al.*[97] However, at the temperatures used for Raman analysis there has been no observed *Pbnm* symmetry or change in symmetry which is reinforced by the previous data analysed.

Raman mapping was conducted of the pellet over an area of 50 μm^2. This allows us to further see discrepancies in the crystallite orientation and observe any potential structural defects. From the spectra range collected, one can see a slight change in relative peak intensity of A_1-1 and A_1-2, seen from Figure 3.20. This could be attributed to a change in domain sizes and other domain effects as previously mentioned above.[99] Other map spectra can be seen in appendix 3.106 and 3.107.
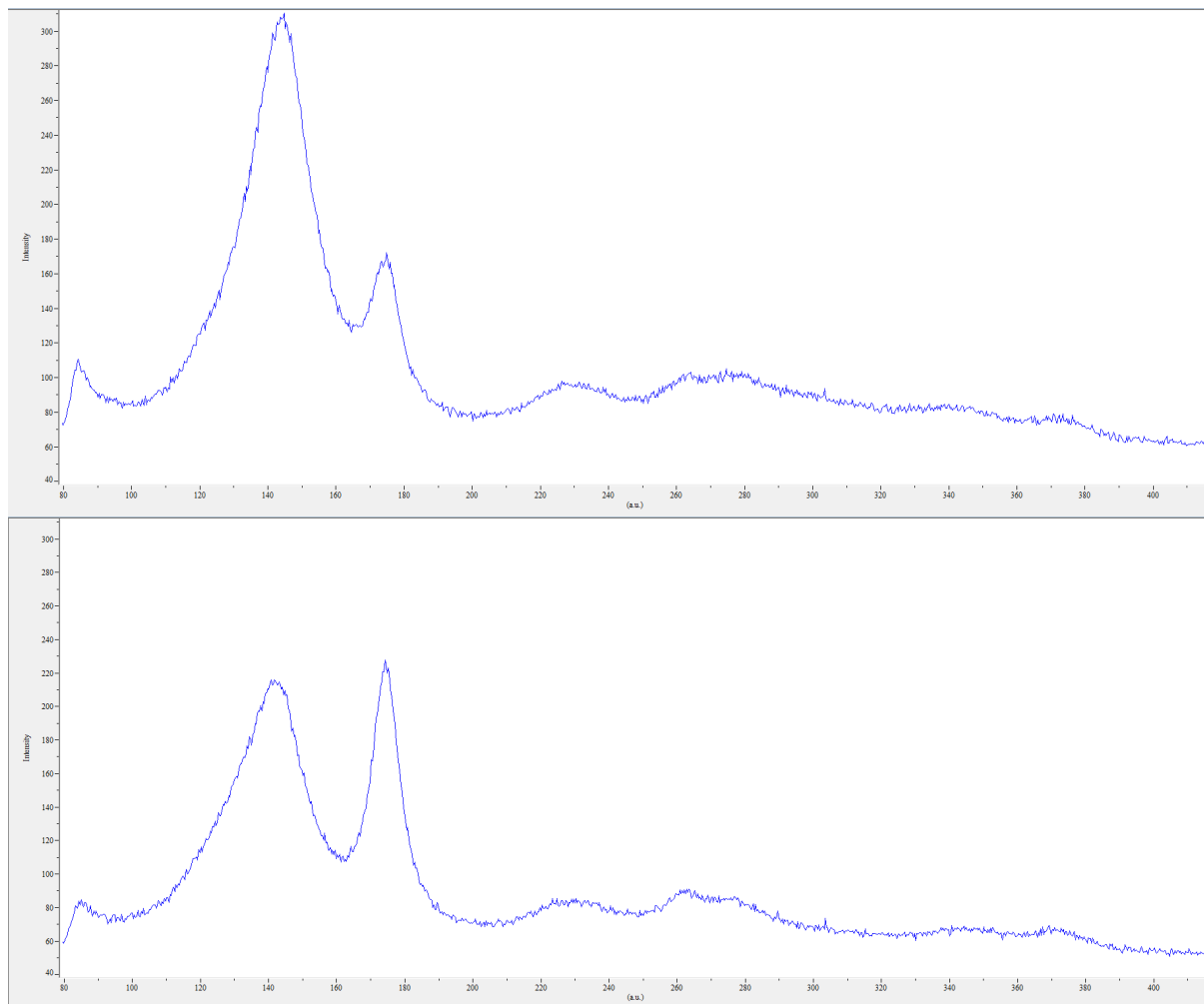
Figure 3.20 – Raman map Spectra of 5% Dy-BFO showing the intensity changes of A_1-1 and A_1-2 modes between a wavenumber range of 80-420 cm^{-1} over two points in the 50 μm^2 area.

Comparing a red/green map of the A_1-1 and A_1-2 peak intensities of 5% Dy-BFO and pure BFO, Figure 3.21. One can see a clear change in domain sizes, the doped sample having smaller domains with less variation in size compared to the pure counterpart. This could suggest weaker ferroelectric character in the doped sample. As discussed previously, the spin cycloid has increased in length. Within each domain we can say that the cycloid has a non-zero average, leading to the hysteresis observed in the magnetic hysteresis discussion above.
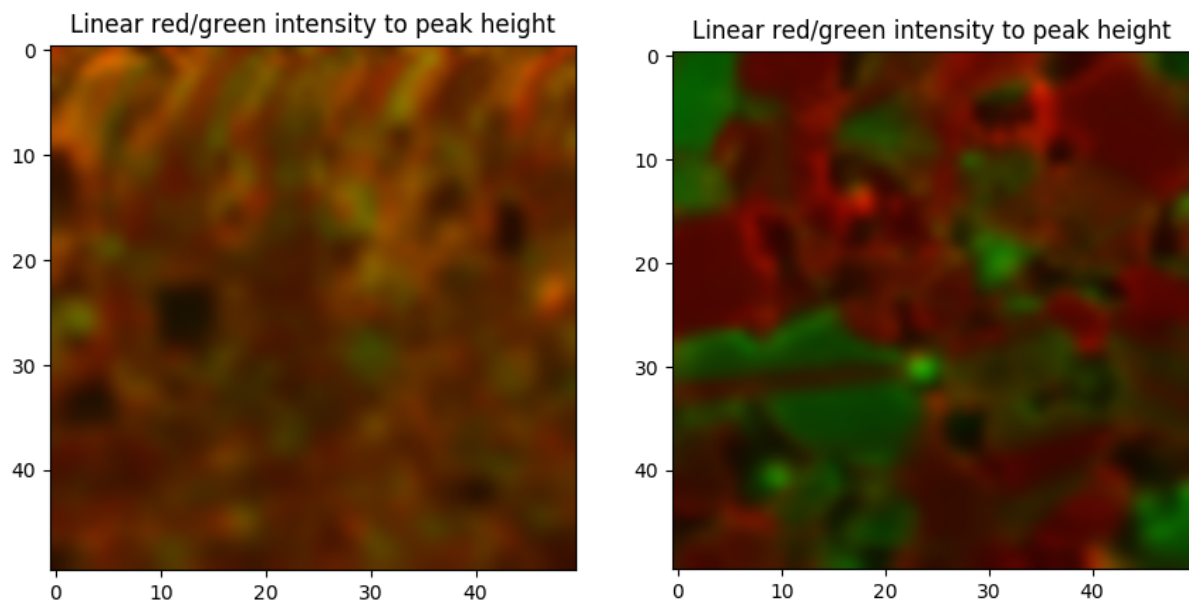
Figure 3.21 – Red/Green intensity map of A_1-1 and A_1-2 modes of 5% Dy-BFO (left) and pure BFO (right).

3.3 Conclusion

In conclusion, it can be seen through structural refinement that at temperatures below 773 K the data can be fitted to the *R3c* model. Above this temperature multiphase refinements are need with *R3c* and *Pbnm* symmetry as the material exists in both phases simultaneously.

Through SEM imaging and EDX mapping, both at 250x and 500x no grain boundaries were able to be observed. However, this was most likely due to the surface roughness of the sample analysed. EDX mapping showed a clear homogenous distribution of the elements expected both at a surface level and throughout the pellet.

SQUID magnetometry showed a clear magnetic hysteresis of antiferromagnetic character which decreased on increasing temperature which is expected. Furthermore, HT SQUID showed an increase in the expected 643 K T_N to 675 K. This is consistent with what has been observed for other RE doped $BiFeO_3$ materials.

The PE loop of the material showed a poor hysteresis with no saturation polarisation but a clear switching of polarisation with the current. Further analysis of the material will be needed to determine whether it is ferroelectric at this doping level.

TGA/DSC analysis showed a very high stability of the material with 100% mass being retained at the 1223 K limit. The DSC showed two peaks which correlate to the T_N, 653 K, which further correlates to the T_N found with the HT SQUID analysis. A second peak around 1053 K which correlates to a potential phase change at a lower temperature than the expected 1083 K.

The WISH data further shows that at increasing temperatures, there is a loss of magnetic character similar to that seen before at 653 K. The propagation vector, K, can also be seen to decrease which explains the increase in the magnetic transition temperature. On top of this, there is an expected increase in the lattice parameters consistent with thermal expansion.

This *Pbnm* introduction can more clearly be seen in the HRPD data where the secondary phase is seen in temperatures as low as 573 K, but is not refined until 773 K. This data further shows the secondary phase becoming more present at high temperatures.

Lastly, Raman spectroscopy shows a change in peak intensity over the temperature range used but not much variation in the Raman shift. This can be summarised that this material has a homogenous distribution of the dysprosium dopant throughout. As there is no change in Raman peak patterns over the temperature range, it can be concluded that *R*3*c* symmetry is present at 307 K and below.

Further work needed for this project is to more closely analyse the FE behaviour through use of optical second harmonic generation (SHG).

In essence, from the data analysed in the chapter above we can see that doping has improved the temperature at which we observe the magnetic character which allows the multiferroic character to be seen at a higher degree of temperatures. If more work can be done to experimentally stabilise a dysprosium or rare earth doped BFO phase pure sample, then being able to use this material at higher temperatures can be accomplished. This paves the way for more temperature dependent devices such as sensors, or for further use in data storage devices which require less energy for the reading / writing processes.

Chapter 4

ReFeO$_3$ Series

4.0   Introduction

Rare Earth Orthoferrites have the general formula RFeO$_3$ (with a rare earth such as Dy, and Sm). They crystallise with a distorted perovskite structure with *Pbnm* symmetry, Figure 4.1. They have an arrangement of FeO$_6$ octahedra with rare earth ion neighbours. The orthogonal Fe-O-Fe bond digresses from 180˚ on smaller R^{3+} cations. That is to say, with larger cations, the bond angle tends towards 180˚. The change in this angle dictates the electronic properties of the system as it alters the distance between the O *2p* orbital and the Fe *3d* orbital.[99]

RFeO$_3$ have two magnetic sublattices. The first sublattice is comprised of the *3d*-electrons from the Fe^{3+} ions. The second sublattice consists of the *4f*-electrons from the R^{3+} ions. G-type antiferromagnetic character arises from the spin canting of FeO$_6$ octahedra which also produces weak ferromagnetism.[100] The rare earth orthoferrite family have a reviewed Neél temperature between 650-700 K. DyFeO$_3$ and SmFeO$_3$ have a T$_N$ of 645 K and ~675 K respectively.[101, 102]

Other than the strong Fe-Fe interactions, RFeO$_3$ shows ferromagnetic R-Fe interactions of spin orientation along the *c*-axis which is preferred for the Fe ions. DyFeO$_3$ has a Dy-Fe interaction parallel to the Fe-Fe interaction which below ~38 K shows no net ferromagnetism and has ordered R-R interactions below 4 K. Unlike DyFeO$_3$, SmFeO$_3$ has a spin reorientation around 450-480 K.[100] Below this temperature the Sm-Fe moment is ordered along the a-axis and shows anti-parallel Sm spins below 5 K.[103, 104] RFeO$_3$ compounds have been a large area of interest due to their suggested multiferroic properties.[105, 106]

These materials have such applications in memory storage due to their multiferroic ability, allowing one to write data electronically and read it magnetically.[107, 108] Further applications include: magneto-optics,[109, 110] catalysts,[111] sensors.[112, 113]

The aim of this project was to dope DyFeO$_3$ with Sm with increasing amounts to see if we could alter the magnetic and electronic properties. This could lead to improvements in T$_N$ and T$_c$ which could allow for the magnetic and electronic properties to exist at higher temperatures.
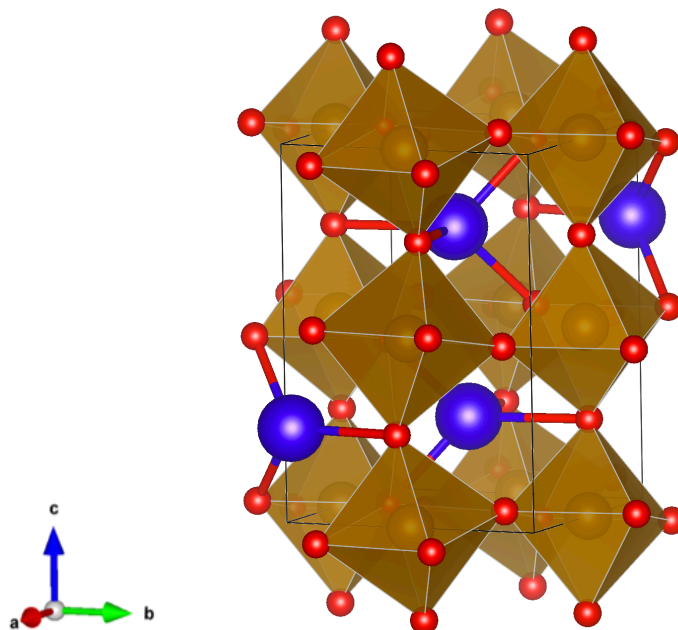
Figure 4.1 – a VESTA image of an $RFeO_3$ (R = Dy, Sm) *Pbnm* crystallographic unit cell. Red spheres show Oxygen atoms. Brown octahedra show FeO_6 octahedra with Fe^{3+} in the centre. Blue spheres denote rare earth atoms, in this instance: Dy^{3+}, Sm^{3+}.

4.1   Synthesis

The preparation and synthesis of the second series of materials $RFeO_3$ (R = Sm, Dy) were completed via a '*shake and bake*' method similar to the method completed by Efrain Rodriguez for $LiCoPO_4$, which is discussed in chapter 5.[114]

The solid solution of $Dy_{1-x}Sm_xFeO_3$ (x = 0, 0.25, 0.5, 0.75, 1) was prepared using stoichiometric amounts of: Dy_2O_3 (Sigma Aldrich, ≥99.9%), Sm_2O_3 (Sigma Aldrich, ≥99.9%), and Fe_2O_3 (Sigma Aldrich, ≥99%). The following reaction describes the compounds synthesis:

$$1 - xDy_2O_3 + xSm_2O_3 + Fe_2O_3 \rightarrow 2Dy_{1-x}Sm_xFeO_3$$
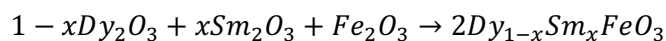
Before synthesis of these materials could begin, the rare-earth metal oxides were dried for 2 hours at 1273 K.

Appropriate amounts of the reagents were weighed out in a stoichiometric ratio and hand ground into a fine powder, in an agate mortar. Minimal amounts of acetone were used to ensure a homogenous mix. The subsequent powders were heated in a furnace, initially for 12 hours at a temperature of 1273 K at 5 K/minute. After the first heating, the powders were

allowed to cool down to room temperature, and reground. The fine powders were then reheated for a further 12 hours at 1273 K at 5 K/minute, affording the products $Dy_{1-x}Sm_xFeO_3$ (x = 0, 0.25, 0.5, 0.75, 1).

For Raman spectroscopy pellets of the materials were made. The pellets were of a 10 mm diameter and sintered at 1273 K for 12 hours at 5 K/minute. It was difficult to make these pellets as the materials were too soft to compress and subsequent sintering didn't harden the pellet. In the future, higher temperatures will be used for sintering to see if that improves the structural integrity of the pellet.

Polishing these pellets was difficult as they were too soft, and the material was easily worn away, so a mirror smooth finish was near impossible to achieve. However, these pellets were able to be analysed *via* Raman spectroscopy without a mirror smooth surface.

Raman spectra were collected on a Horiba Yvon Jobin LabRAM instrument. Room temperature mapping was performed using a 633 nm laser over a ~50-50 μm area. Two second acquisitions were used on ten integrations with a x50 objective lens and 1800 lines per mm grating. The Raman shift range occurred between 100-400 cm^{-1}.

SQUID magnetometry was conducted using a Magnetic Property Measurement System (MPMS) XL-7 instrument. Hysteresis character was observed at 2 K and 300 K in a variable applied magnetic field of ± 7 T with a step size of 0.01 T between 0-0.1 T, a 0.05 T step between 0.1-0.5 T, and 0.5 T step between 0.5-7 T. Low temperature to Room temperature SQUID measurements were conducted with a ZFC/FC analysis between 2-300 K.

4.2 Results & Discussion

4.2.1 DyFeO₃

4.2.1.1 XRD

XRD data was collected at 12 K and 298 K for this material to show potential structural differences which occur at these temperatures.

The parent material DyFeO₃ was refined at both temperatures, it was found that at both temperatures there is very little variance of the lattice parameters and the '*goodness of fit*' parameters were fairly similar, Table 4.1. (Bond length and angle data in the appendix). The synthesised material shows a very good match at both temperatures to the *Pbnm* model used and the observed diffraction data, Figures 4.2 and 4.3. However, a minute difference in the

observed model and the observed data can be seen for the 12 K diffraction patten at 1.95 Å and 3.3 Å. The differences could be due to an unequal ratio of Dy:Fe atoms therefore a slight defect in the crystal lattice. One further difference could be due to noise from the machine at low temperature which is resolved at higher temperatures, which can attest for the lack of these impurity peaks at 298 K.
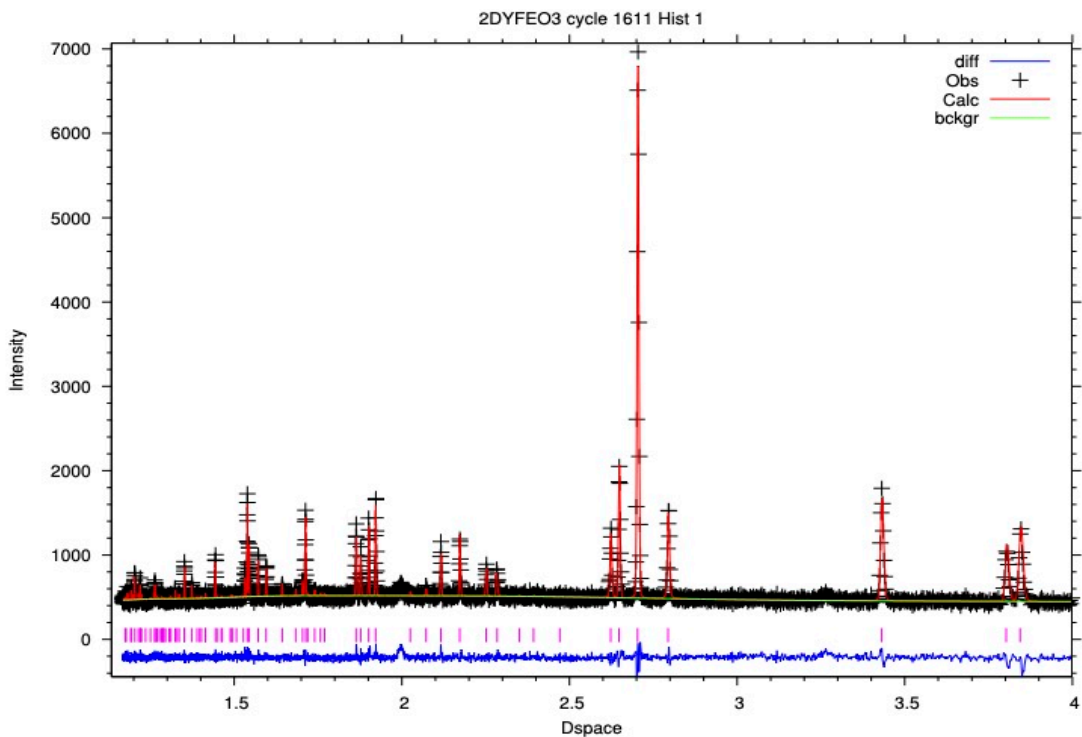
Figure 4.2 – Rietveld refinement of DyFeO$_3$ XRD pattern at 12 K using GSAS.
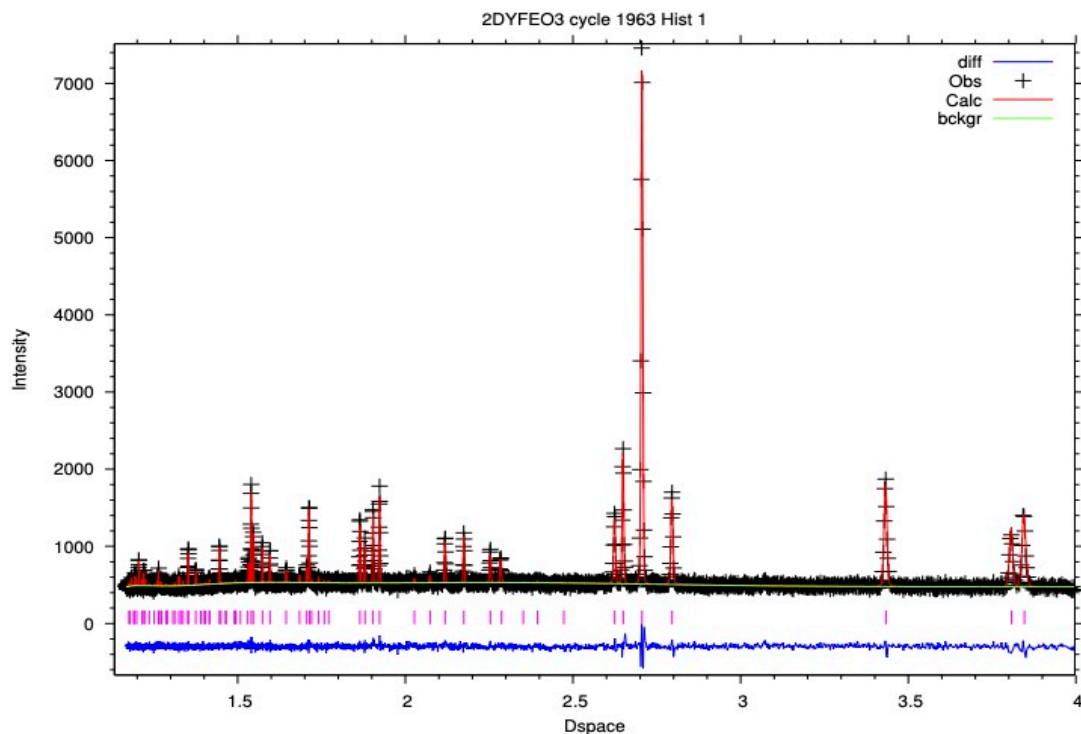
Figure 4.3 – Rietveld refinement of DyFeO$_3$ XRD pattern at 298 K using GSAS.

Table 4.1 – Rietveld refinement lattice parameter data from GSAS for $DyFeO_3$ at 12 K and 298 K showing the accompanying errors.

Temp	R_w	R_{wp}	χ^2	A	B	C	Volume
12 K	4.26	5.48	1.559	5.58826(14)	7.60464(19)	5.29550(13)	225.041(1)
298 K	3.98	5.04	1.368	5.59156(23)	7.61576(31)	5.29927(21)	225.664(16)

4.2.2.2 Raman

Raman spectroscopy studies of orthoferrites by Weber *et al*. show 24 Raman active modes with *Pbnm* symmetry.[115] The Raman map was taken of $DyFeO_3$ at room temperature, over a wavenumber range of 100-400 cm^{-1} at 1800 grating with a 633 nm laser.

$DyFeO_3$ shows five main peaks at 115 cm^{-1}, 138 cm^{-1}, 159 cm^{-1}, 260 cm^{-1}, and 335 cm^{-1}, over the stated range, Figure 4.4. These wavenumbers correspond to: an A_g Dy vibration on the x axis which is out-of-phase in y, an A_g Dy vibration on the z-axis which is out of phase, a B_{2g} Dy vibration on the x-axis which is out of phase, an A_g FeO_6 octahedra rotation in phase, and an A_g O vibration on the x-z plane, respectively. As the peaks of the Raman map do not vary in relative intensity over the 50 μm^2 area it shows that the sample has a homogeneous distribution of the atoms throughout the pellet. Further showing that the synthesis of the material *via* this synthesis route is viable to make the material for a variety of applications if the expected multiferroic effect can be observed. This is discussed in the proceeding chapters.
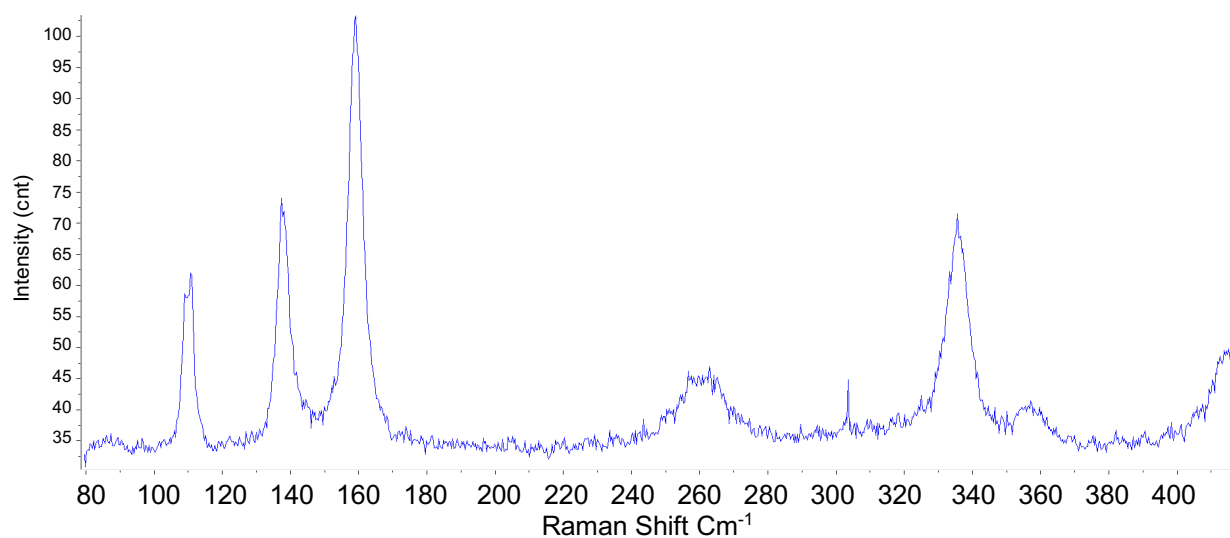
Figure 4.4 – $DyFeO_3$ Raman spectrum over 80-400 cm^{-1}. Showing 5 main Raman peaks in wavenumbers cm^{-1}.

4.2.2.3 SQUID

DyFeO$_3$ has been stated to demonstrate weak ferromagnetic character below the T_N of ~645 K, this dissipates below 50 K as there is a spin reorientation. Below ~5 K there is an ordering of the Dy^{3+} ions.[116]

Figure 4.5, shows the magnetisation as a function of field strength of the material at 2 K and 300 K. At 2 K there is a sigmoidal curve with an anomaly of the applied field around 1.6/1.7 T due to issues with the SQUID magnetometer at low temperatures. Furthermore, the curve shows no M$_r$ or H$_c$ showing that it has antiferromagnetic characteristic. There is step-like behaviour shown by the profile at ~0.4 T, which can be attributed to the ordering of the Dy^{3+} ions at low temperatures. On increasing field strength >0.4 T these become ordered parallel to the antiferromagnetic FeO$_6$ direction. This is due to the applied field overcoming the magnetocrystalline anisotropy of the low temperature Dy^{3+} ordering.

At 300 K there is no ordering of the Dy^{3+} ions, and a straight line is observed showing antiferromagnetism. On closer inspection of the origin, with the inset of the hysteresis profile, we can see a very weak M$_r$ and H$_C$ of ~0.35 emu/g and -0.2 T respectively. A small hysteresis is observed due to the weak ferromagnetic character.
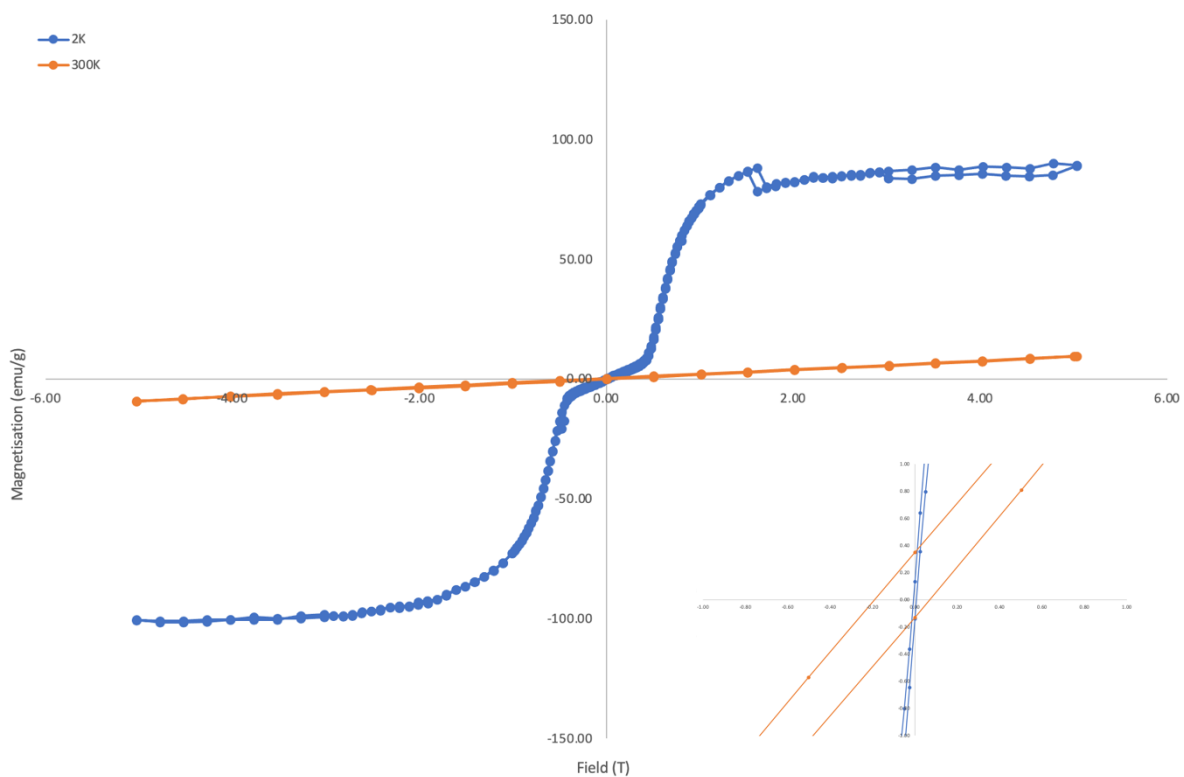
Figure 4.5 – DyFeO$_3$ SQUID analysis at 2 - 300 K with a magnified inset showing the hysteretic behaviour.

The Zero-Field Cooled / Field Cooled (ZFC/FC) SQUID profile displayed in Figure 4.6 below shows the magnetic profile of the $DyFeO_3$ material as described.[116] The profile shows that the spin reorientation, T_{SR}, is higher than the stated value of 50 K and exists experimentally at 0.1 T at ~60 K. The ordering of Dy^{3+} ions, T_N^2, is also higher than the expected, existing at 6 K. There is no major difference in magnetisation between the ZFC/FC profiles which overlap. The latter being slightly higher as expected due to the facilitation of magnetisation caused by the external magnetic field.
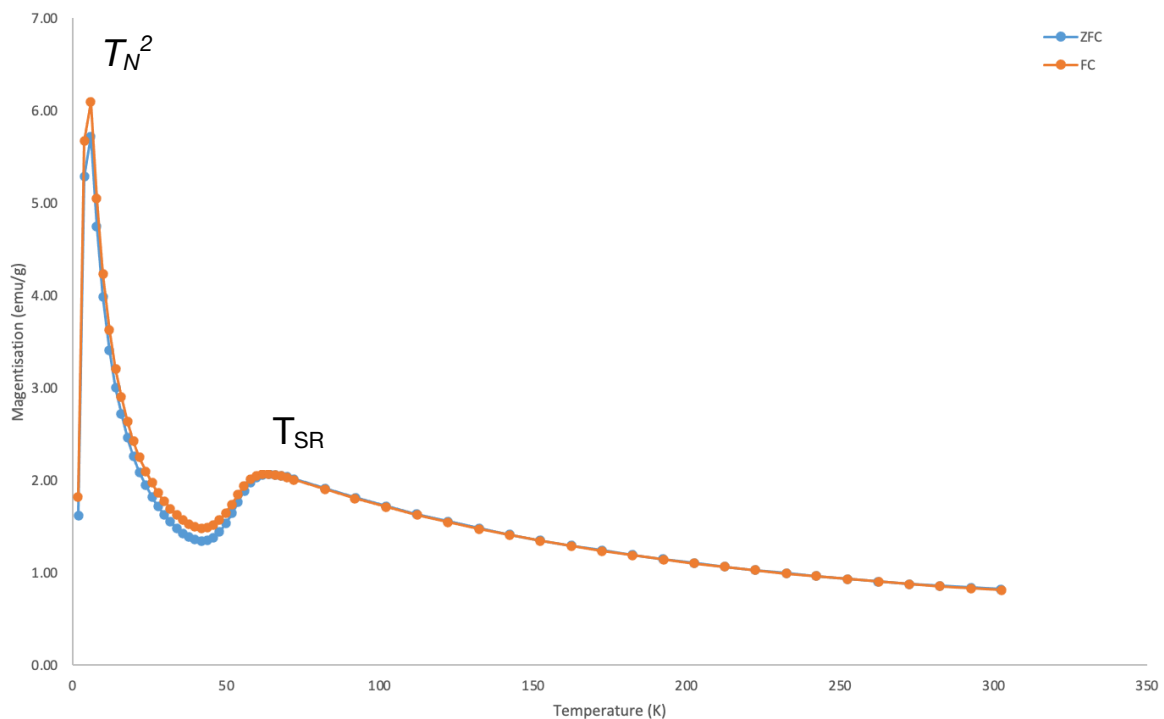
Figure 4.6 – $DyFeO_3$ Zero-Field Cooled / Field Cooled SQUID analysis at 0.1 T over a 2 – 300 K temperature range.

4.2.3 SmFeO₃

4.2.3.1 XRD

XRD data were collected at 12 K and 298 K for this material to show potential structural differences which occur at these temperatures.

The parent material $SmFeO_3$ was refined at both temperatures. It was found that at both temperatures there is very little variance of the lattice parameters and the '*goodness of fit*'

parameters were fairly similar seen in Table 4.2. (Bond length and angle data in the appendix). The samples synthesised show a very good holistic match between the used *Pbnm* model and the observed data, Figure 4.7 and 4.8. This is further confirmed by the lack of impurity peaks in the pattern. From the data given we can say that there is no change in symmetry from low temperature to room temperature.

Table 4.2 – Rietveld refinement lattice parameter data from GSAS for $SmFeO_3$ at 12 K and 298 K showing the accompanying errors.

Temp	R_w	R_{wp}	χ^2	A	B	C	Volume
12 K	3.61	4.61	1.569	5.58780(13)	7.69429(18)	5.39427(13)	231.92(1)
298 K	3.51	4.51	1.581	5.59479(12)	7.70846(17)	5.39984(12)	232.880(9)
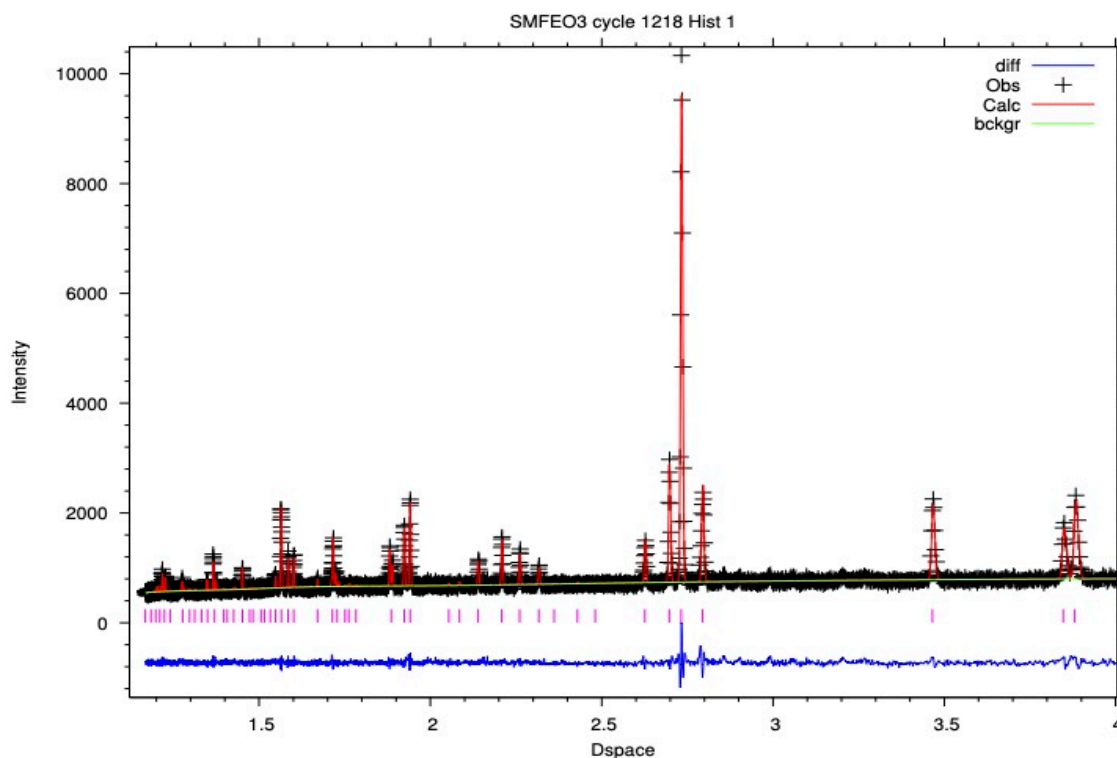
Figure 4.7 – Rietveld refinement of $SmFeO_3$ XRD pattern at 12 K using GSAS.
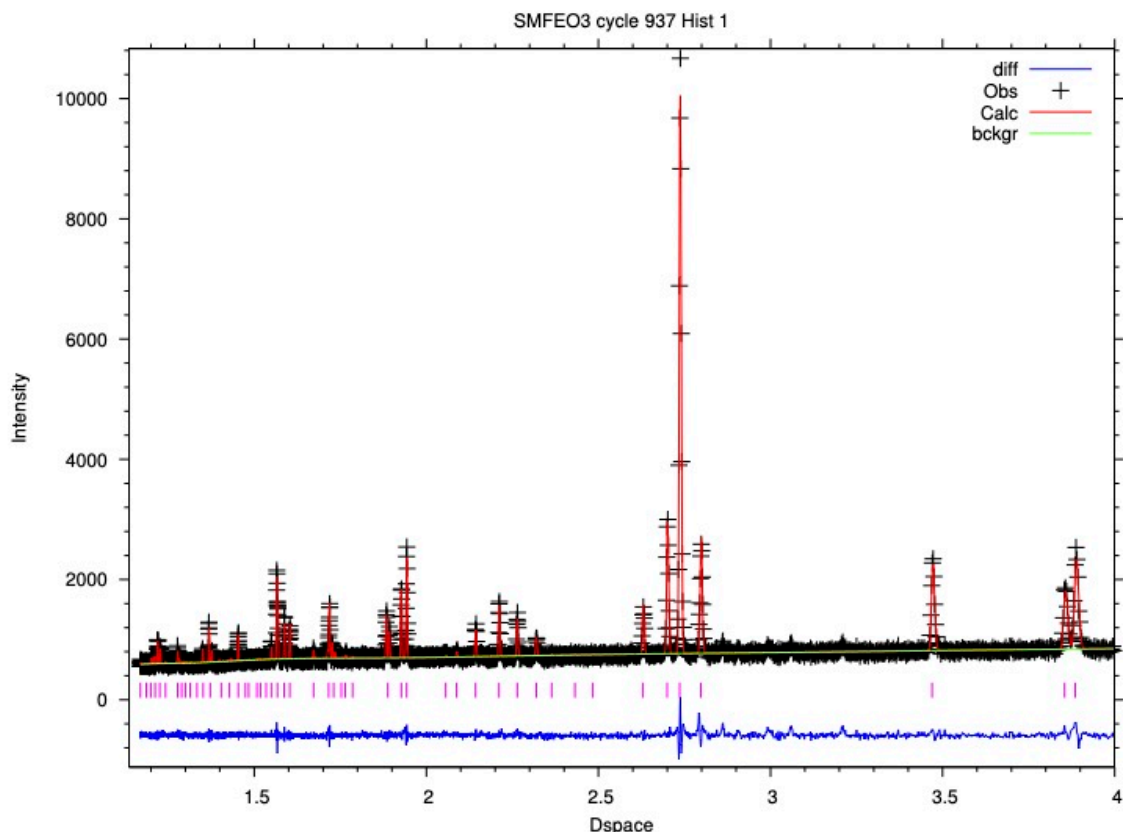
Figure 4.8 – Rietveld refinement of SmFeO$_3$ XRD pattern at 298 K using GSAS.

4.2.3.2 Raman

SmFeO$_3$ shows a similar profile to DyFeO$_3$ (mode assignments completed with Weber *et al.*)[115] which is Raman shifted due to the larger Sm ion. In addition to the Raman shift, the first three peaks located at: 107 cm^{-1}, 139 cm^{-1}, 154 cm^{-1}, correspond to the same vibration/rotation allocations. Peaks present at: 231 cm^{-1}, 314 cm^{-1}, correspond to previous allocations of a FeO$_6$ octahedra in phase rotation, and an O vibration on the x-z plane. A Raman peak at 257 cm^{-1} could correspond to a B$_{2g}$ FeO$_6$ octahedra in phase rotation. Furthermore, two smaller, broad peaks are present around 347 cm^{-1} and 373 cm^{-1} which could correspond to a B$_{2g}$ O vibration in the x-z plane, and an A$_g$ FeO$_6$ in phase rotation, respectively. SmFeO$_3$ shows no major changes in relative peak intensity over the 50 μm^2 area. This could indicate a homogenous sample with identical crystallite orientations.

Three iron oxide octahedra rotation peaks are visible in SmFeO$_3$ compared to the single peak in DyFeO$_3$. This could be due to the decreased canting, or a change in crystallite orientation. This could further be due to the arbitrary mode assignments in correlation with Weber *et al.* and Gupta *et al.*[117, 118]
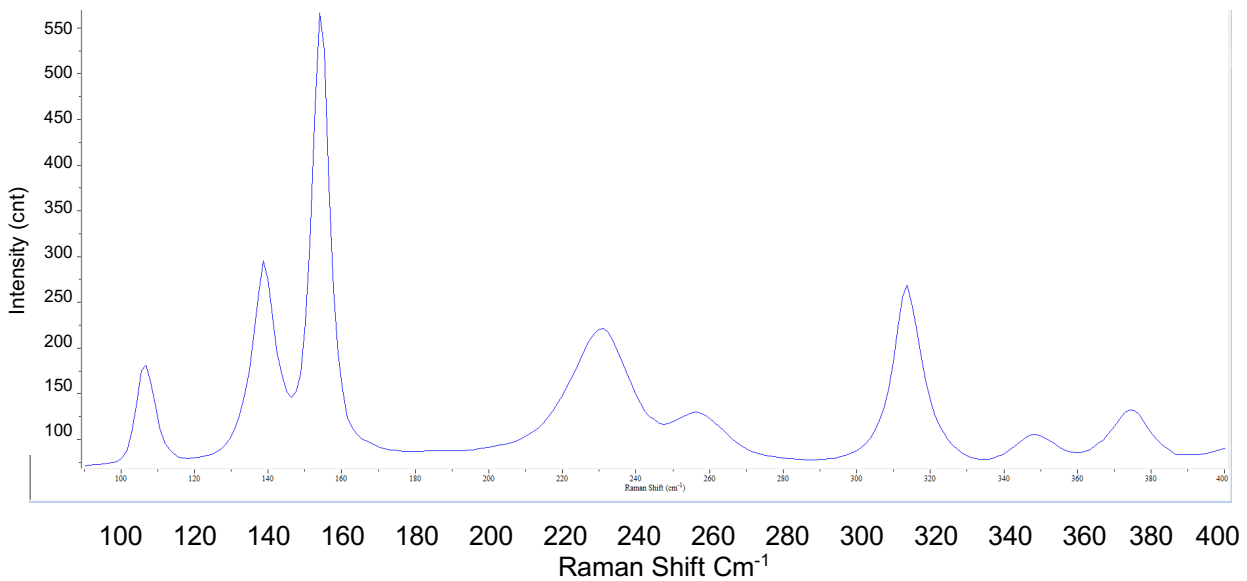
Figure 4.9 – SmFeO$_3$ Raman spectrum over 80-400 cm^{-1}. Showing 8 main Raman peaks in wavenumbers cm^{-1}.

4.2.3.3 SQUID

SmFeO$_3$ shows weak ferromagnetism due to the canting of the FeO$_6$ octahedra. However, at low temperatures of 2 K, SmFeO$_3$ displays ideal antiferromagnetic behaviour as seen in Figure 4.10. The anomaly seen at an applied field of 3 – 4 T is due to cooling problems that occurred with the SQUID Magnetometer.

At 300 K, a poor hysteresis profile can be seen with an M$_r$ and H$_C$ of ~0.44 emu/g and 1 T respectively. In contrast no hysteresis is seen at 2 K. This could be due to the incompatibility of the DM interaction at low temperatures on top of the rare-earth ordering.

The parent material SmFeO$_3$ shows no spin transition at temperatures below 300 K, previous literature states that a spin reorientation occurs between ~450-480 K.[100] On increasing temperatures, above 250 K, there is a gradual increase in magnetisation, seen in Figure 4.11. This could correlate to the expected spin flip as described above.[103,119]

From the ZFC/FC profile shown in Figure 4.11, the magnetisation is much lower than the Dy^{3+} species, this could be due to the canting of the Iron oxide octahedra.
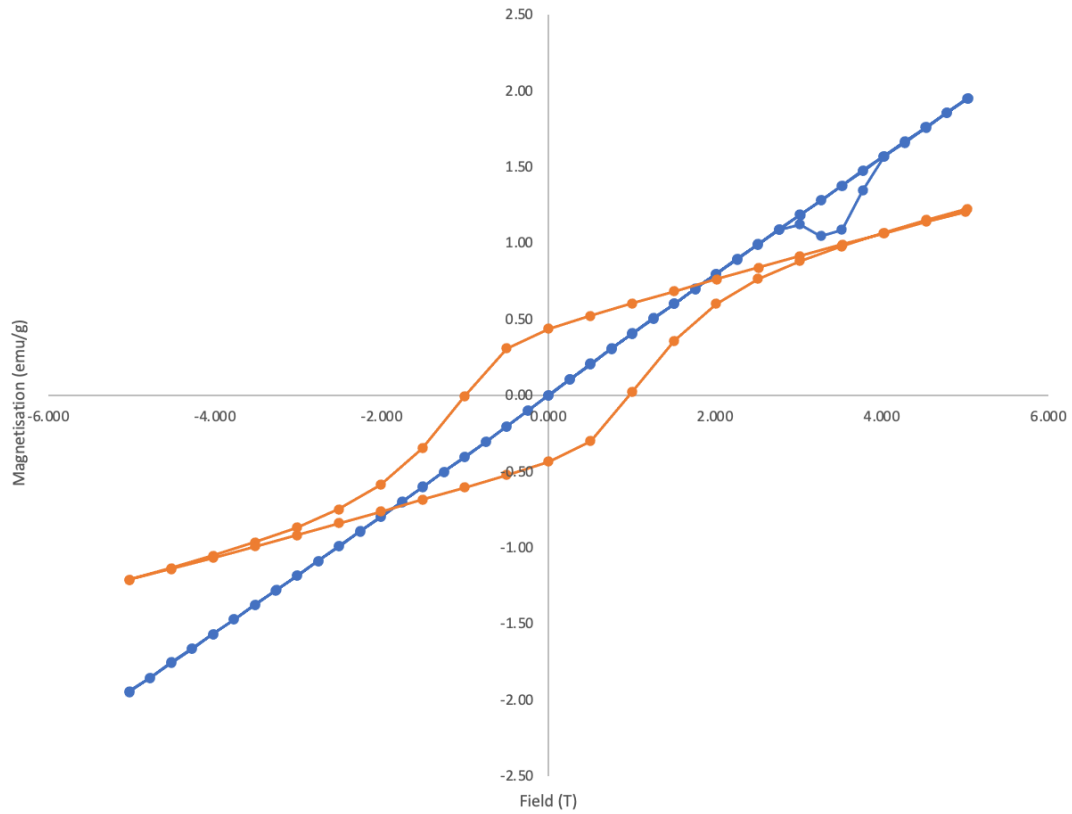
Figure 4.10 – Magnetic behaviour of SmFeO$_3$ *via* SQUID analysis at 120 K (blue) and 300 K (orange).
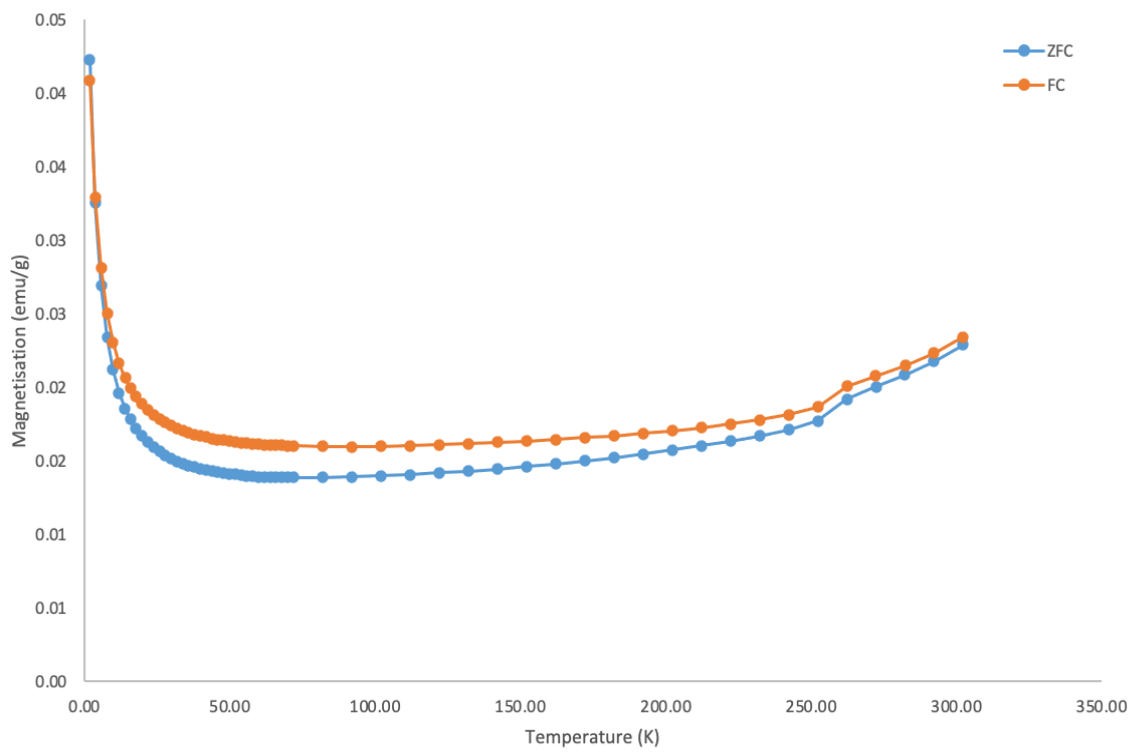
Figure 4.11 – SmFeO$_3$ ZFC/FC SQUID analysis at 0.1 T over a 2 – 300 K temperature range.

4.2.4 $Dy_{1-x}Sm_xFeO_3$

4.2.4.1 XRD

Crude comparisons of the composition patterns at 12 K were analysed to assess the incorporation of the Sm isovalent ion in the Dy^{3+} A-site of the lattice. It was found that there were mixed phases in the composition, seen by the shouldering peaks observed in Figure 4.12.

In $DyFeO_3$ there is a large peak present at 32.8 Å. This peak shifts to 32.6 Å in $SmFeO_3$. In the intermediate compositions, it is expected for this peak to shift linearly with respect to an increase in Sm content. If there was any Sm content incorporated into the A-site of the lattice there would be a shift in d-spacing observed by Zhao *et al.*[120] However, these patterns are from single crystals therefore there could be some disparity between the polycrystalline materials and the single crystals.

In Figure 4.12, the unrefined patterns are compared. It can be seen that there are $SmFeO_3$ peaks in the intermediate compositions as well as $DyFeO_3$ peaks. The Bragg peaks situated between 32-33 Å show a change in intensity of the respective peaks on increase of the Sm content. Therefore, it can be said that there is an $SmFeO_3$ rich phase and a $DyFeO_3$ rich phase in the intermediate solid solutions. These phases vary when varying the respective parent material.

Analysing the room temperature patterns, Figure 4.13, shows the same peak profile as above. Therefore, it can be said that there are no structural changes between the 12 – 298 K temperatures during analysis consistent with the observations for the parent materials.
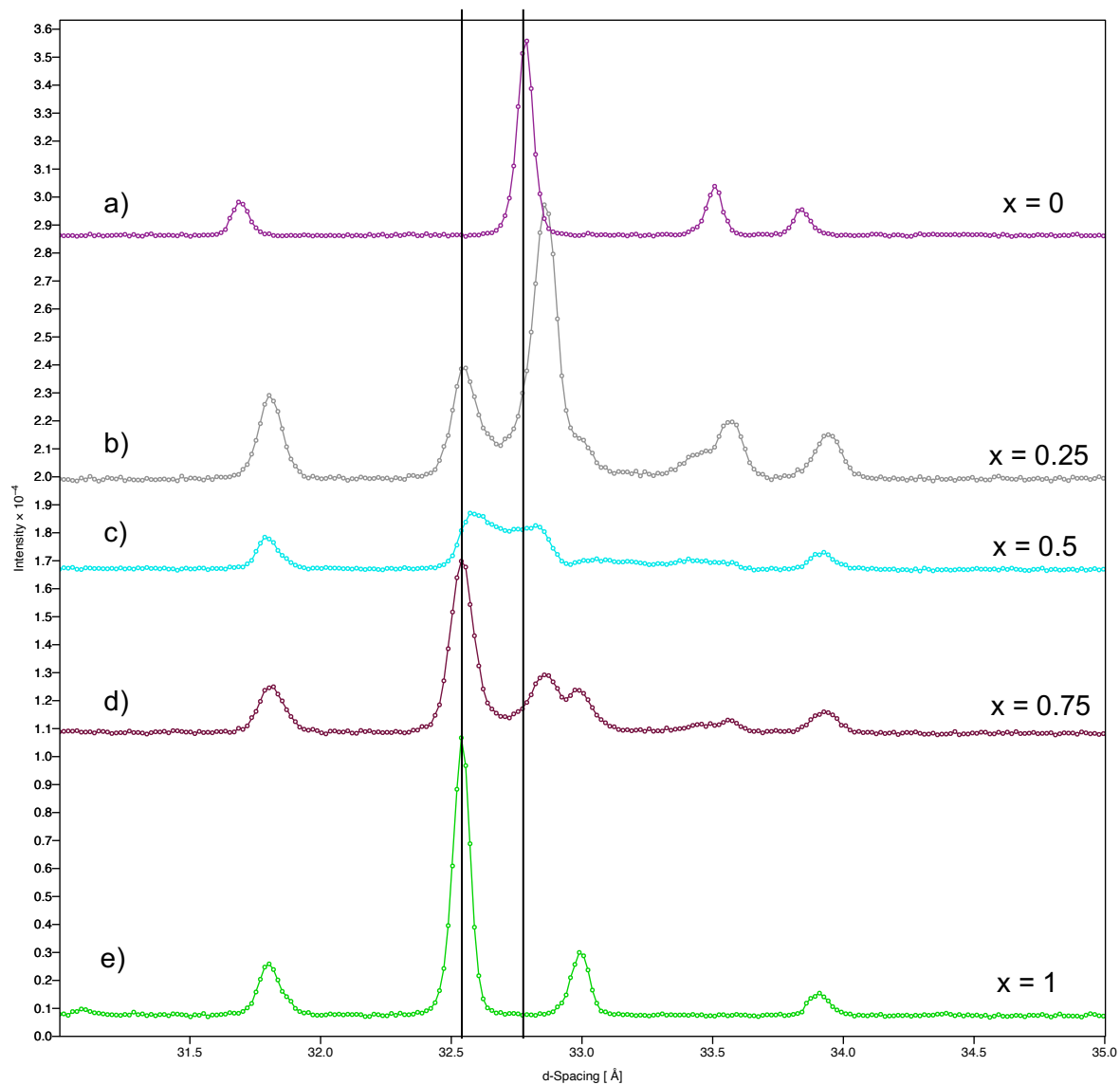
Figure 4.12 – Stacked 12 K diffraction patterns between 31 – 35 d-spacing of the $Dy_{1-x}Sm_xFeO_3$ series. a) x=0, b) x=0.25, c) x=0.5, d) x=0.75, e) x=1.
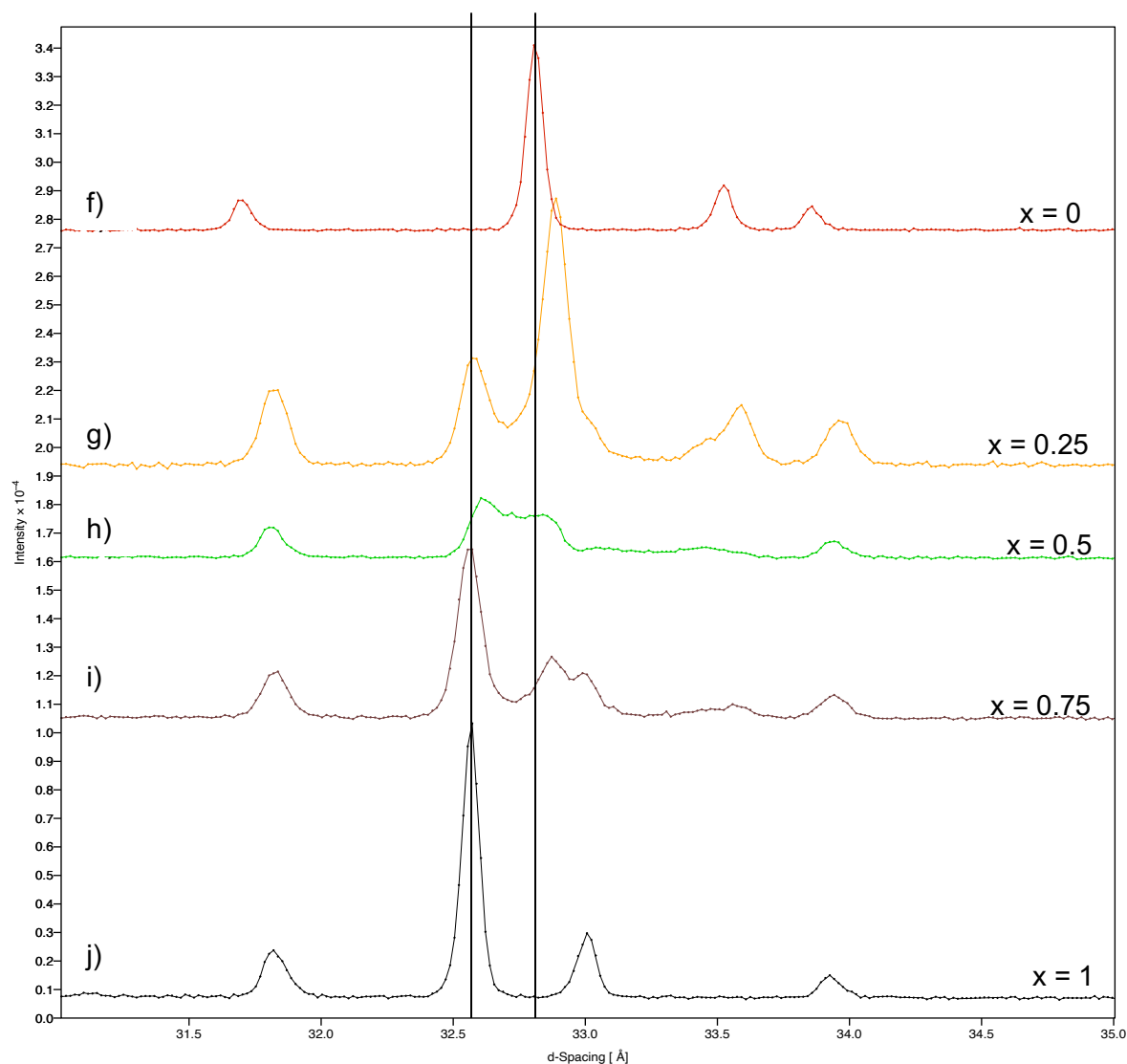
Figure 4.13 – Stacked 298 K diffraction patterns between 31 – 35 d-spacing of the
$Dy_{1-x}Sm_xFeO_3$ series. f) x=0, g) x=0.25, h) x=0.5, i) x=0.75, j) x=1.

4.2.4.2 Raman

Raman Spectroscopy of the solid solution samples was conducted to observe phase differences that could occur in throughout the samples *via* differences in bond vibrations throughout the fabricated pellet.

On addition of Sm to the $DyFeO_3$ parent material, there is increasing rotation of the FeO_6 octahedra which alters the Raman profile. Therefore, it is expected to see a more $SmFeO_3$ like profile on higher Sm content.

On addition of 25 % Sm to the $DyFeO_3$ parent material, a similar profile to the parent material is seen with a Raman shift, as expected, Figure 4.14. The first three peaks are now seen at 107 cm^{-1}, 137 cm^{-1}, and 154 cm^{-1}. These correspond to the previously mentioned mode assignments. The following peaks at 223 cm^{-1}, 257 cm^{-1}, 330 cm^{-1}. These correspond to a potential A_g FeO_6 in-phase rotation, a B_{2g} FeO_6 in-phase rotation, and an A_g O vibration in the x-z plane. A peak at 290 cm^{-1} cannot be assigned a mode. This could be due to the mixing of the two potential parent phases. This could also be the reason for the dramatic changes in peak intensity and the presence of many spectra which are just high intensity noise. This could be attributed to peak overlaps.
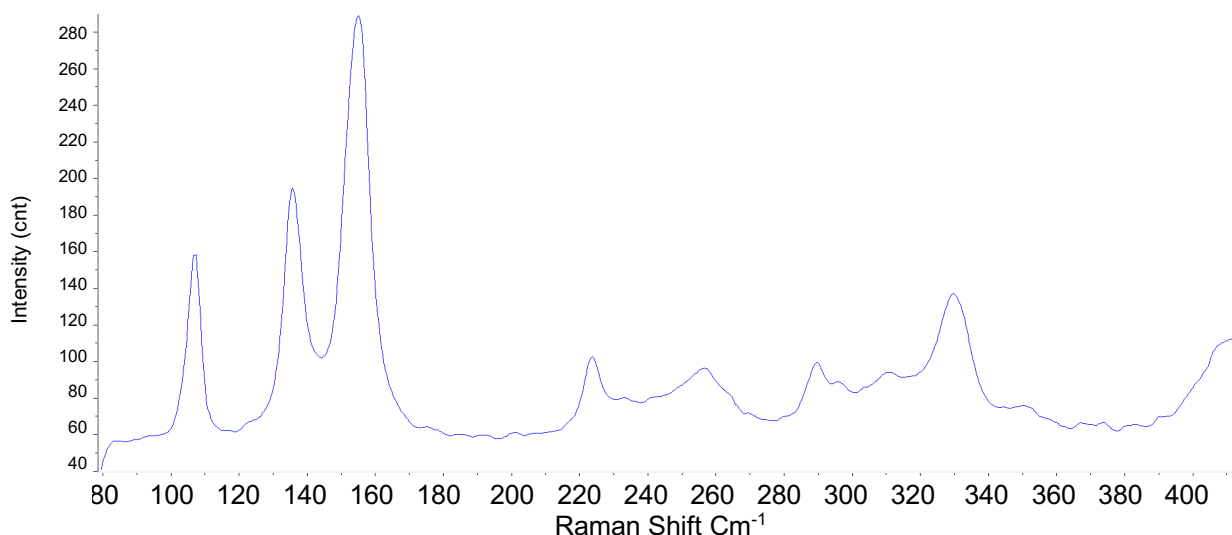
Figure 4.14 – $Dy_{0.75}Sm_{0.25}FeO_3$ Raman spectrum over 80-400 cm^{-1}. Showing 7 main Raman peaks in wavenumbers cm^{-1}.

Analysing the 50:50 composition, it shows a very similar profile to the $DyFeO_3$ parent material, Figure 4.15. The same characteristic 3 peaks are displayed at 115 cm^{-1}, 140 cm^{-1}, and 159 cm^{-1}. These peaks don't change in relative intensity. There are only two peaks following at: 238 cm^{-1}, and 318 cm^{-1}. These could correspond to a B_{1g} FeO_6 out-of-phase rotation, and an A_g O vibration on the x-z plane or a B_{3g} O-Fe-O in-phase vibration. This could have two mode assignments due to the multiphase nature of this sample. However, more analysis will be required for absolute mode assignment. Similar, to the previous composition, there are many spectra with high intensity. It can also be reasonably argued that the broad peaks are the overlap of single peaks.
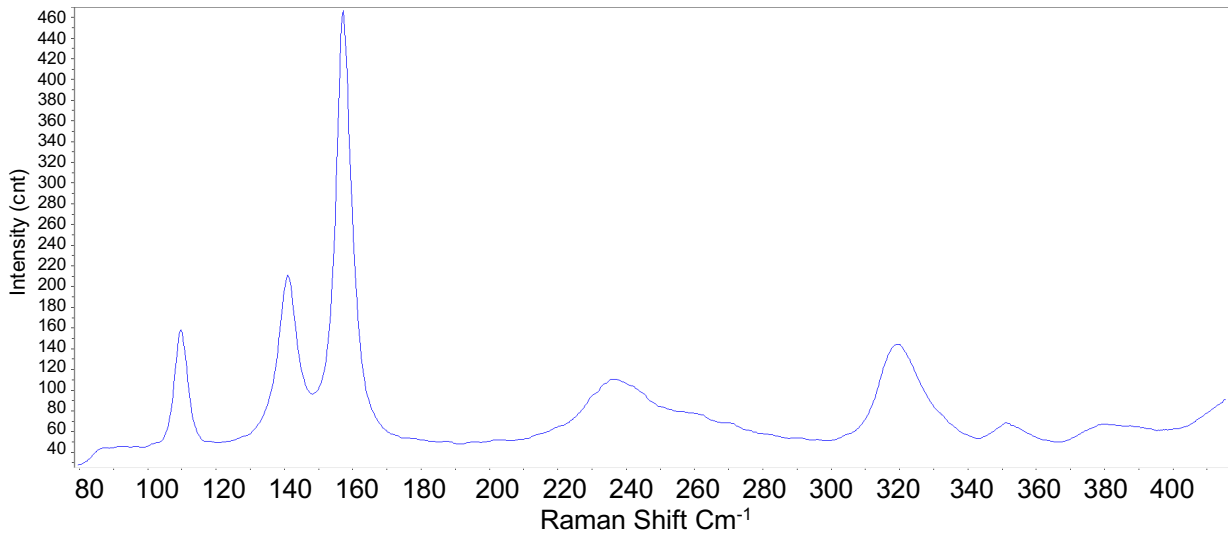
Figure 4.15 – $Dy_{0.5}Sm_{0.5}FeO_3$ Raman spectrum over 80-400 cm^{-1}. Showing 5 main Raman peaks in wavenumbers cm^{-1}.

Finally, the 75 % Sm contribution to the $DyFeO_3$ parent material was analysed, Figure 4.16. It proved difficult to analyse as this sample showed the most amount of spectra with high intensity noise, therefore no peaks were able to be seen over a lot of the 50 μm^2 range. This could be due to the poor incorporation of Sm into $DyFeO_6$ consistent with the XRD analysis. The first three peaks at 109 cm^{-1}, 137 cm^{-1}, 156 cm^{-1} similar correspond to previous mode allocations at similar wavenumbers. The following Raman peaks are present at a Raman shift of: 224 cm^{-1}, 258 cm^{-1}, 289 cm^{-1}, 330 cm^{-1} which have the same mode allocations as seen with similar wavenumbers above. The difference in wavenumber can be attributed to a higher Sm contribution. The change in wavenumber could also be alluded to a difference in crystallite orientation, which is more probable, due to the poor mixing of the parent materials as previously mentioned. This poor mixing could arise from the difference in spin orientation of the two R^{3+} ions. This could show incompatibility of the two lattices from a magnetic spin perspective.
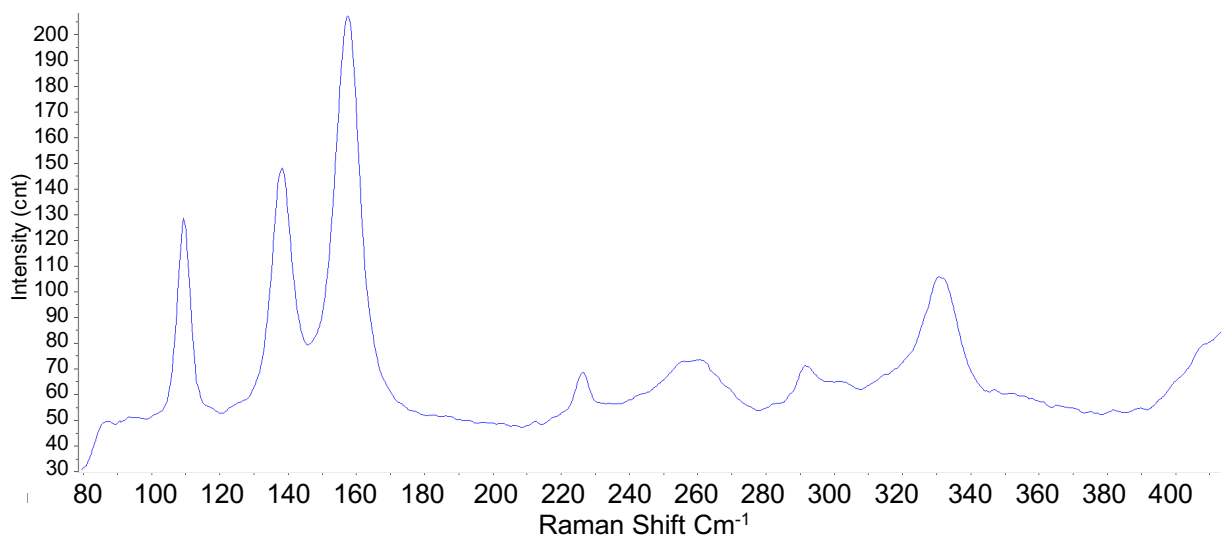
Figure 4.16 – $Dy_{0.25}Sm_{0.75}FeO_3$ Raman spectrum over 80-400 cm^{-1}. Showing 7 main Raman peaks in wavenumbers cm^{-1}.

4.2.4.3 SQUID

SQUID Magnetometry was used to analyse the magnetic character of the 3 intermediate $Dy_{1-x}Sm_xFeO_3$ samples, x = 0.25, x = 0.5, x = 0.75, Figures 4.17, 4.18, 4.19, respectively.

Addition of Sm content to the $DyFeO_3$ parent material shows a depletion in the ferromagnetic characteristic whilst also showing a decrease in the rare earth ion ordering temperature. This could correspond to the multiphase nature of the materials diminishing the ferromagnetic response based on the overpowering strength of the antiferromagnetic contribution from the SmFeO3 phase. This is not to say that the ferromagnetic nature does not exist, but the magnetism is difficult to analyse with the multiphase behaviour of the materials. Looking at the magnetic profiles of x=0.25 and x=0.75, there is a small 'bump' present at ~70 K. This could be due to the presence of parent $DyFeO_3$ phase throughout the material giving rise to the spin reorientation as seen in Figure 4.6.

Throughout the solid solution, the rare-earth ordering temperature is maintained at 3.8 K. However, there are changes in the magnetisation seen, this effect can be attributed to the previously discussed separation of phases. The Dy^{3+} ion is able to order at low temperatures but T_N^2 is reduced from the synthesised parent material seen in Figure 4.6. The new T_N^2 is more similar to the literature value seen by Rajeswaran *et al.*[116] This could be due to the complex magnetic behaviour exhibited by the mixed phases of the solid solution. Further magnetic characterisation will be need for a full analysis.
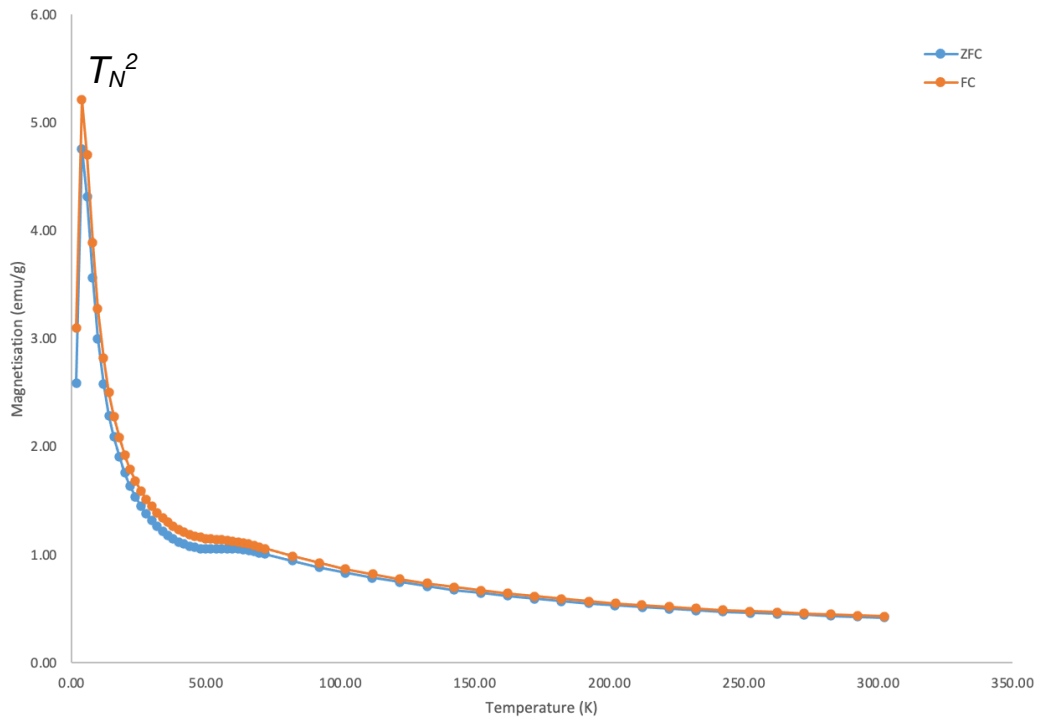
Figure 4.17 - $Dy_{0.75}Sm_{0.25}FeO_3$ ZFC/FC SQUID analysis at 0.1 T over a 2 – 300 K temperature range.
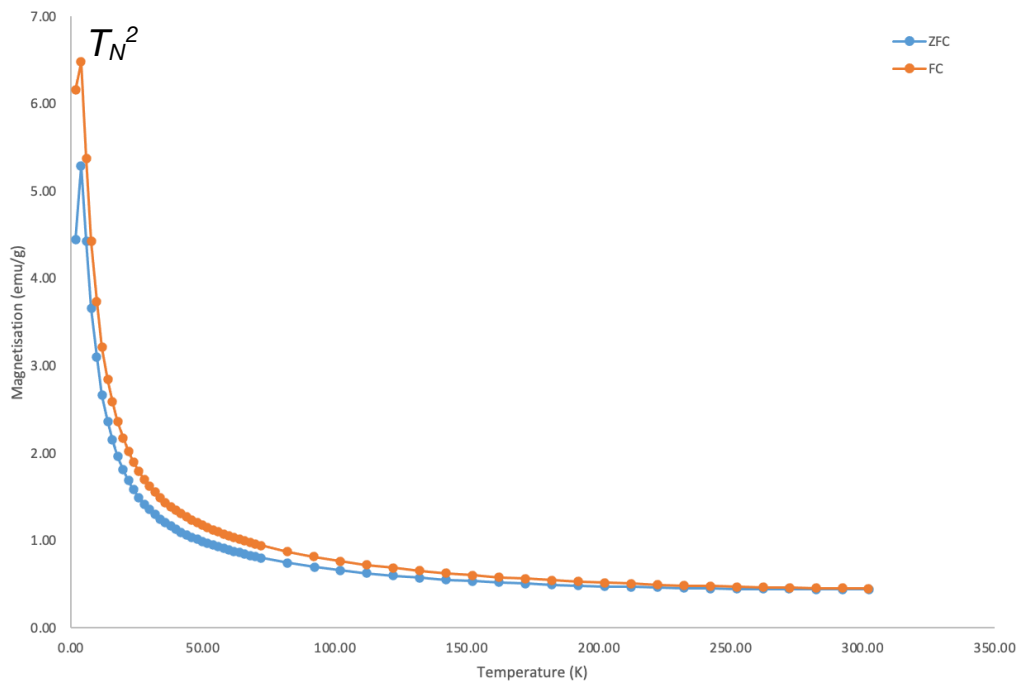
Figure 4.18 - $Dy_{0.5}Sm_{0.5}FeO_3$ ZFC/FC SQUID analysis at 0.1 T over a 2 – 300 K temperature range.
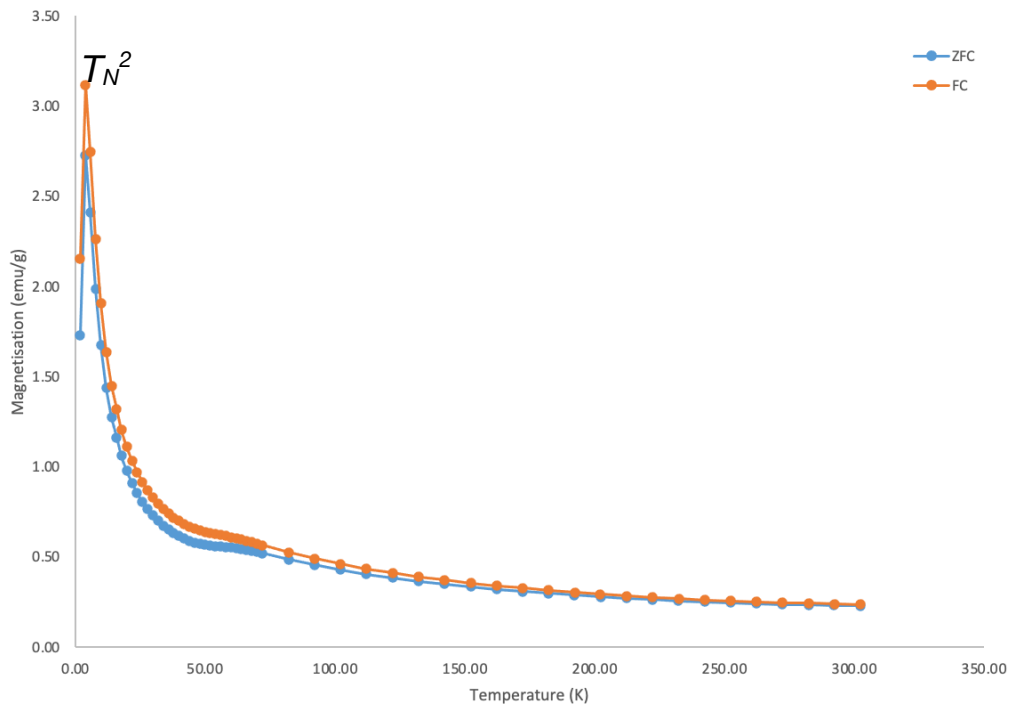
Figure 4.19 - $Dy_{0.25}Sm_{0.75}FeO_3$ ZFC/FC SQUID analysis at 0.1 T over a 2 – 300 K temperature range.

Previously reported by Zhao *et al.* single crystals of Sm doped $DyFeO_3$ were synthesised to assess the spin reorientation transition.[120] They found that doping the parent material with Sm allowed one to control the spin reorientation. However, as previously mentioned the materials produced are polycrystalline. They formed different rare earth rich phases based on the content % of the parent materials.

4.3 Conclusion

Initial synthesis of the parent materials ($DyFeO_3$ and $SmFeO_3$) was found to be simple and produced clean powders with no impure phases. Both were able to be refined to the expected *Pbnm* structure. On synthesis of the mixed rare earth solid solution $Dy_{1-x}Sm_xFeO_3$ (x = 0.15, 0.5, 0.75), it was found that the synthetic route didn't incorporate the rare earth ions onto the same lattice A-site in the distorted perovskite structure. This shows us that there is no variance in the A-site cation exchange and therefore only mixed phases with rich $DyFeO_3$ and rich $SmFeO_3$ phases.

The magnetism of the parent materials proved to be fairly similar to that seen in literature,[116] with a change in the magnetic ordering temperature of the Dy^{3+} ions existing at 6.5 K instead of 4 K. The $SmFeO_3$ parent material has magnetism which is expected.[103] The ZFC/FC data for this family of materials show that there is not much change in the measurements between the two data sets. The ZFC data show more $DyFeO_3$ like behaviour which can be seen with the 'bump' around 70 K which is attributed to the spin reorientation. However, this characteristic is diminished in the FC data. One further difference is that the magnetic moment for all materials is larger with the FC measurements which is expected due to the interaction with the external field. A trend of decreased magnetisation can be seen on introduction of more Sm^{3+} content into the $DyFeO_3$ parent material. This could be due to the higher degree of canting of the Iron oxide octahedra which is introduced to the system with the Sm^{3+} material, Existing more similarly to the $SmFeO_3$ parent material.

Due to the mixed phase nature of the solid solution, the magnetism was hard to determine. A phase pure solid solution would need to be fabricated, such as the work done by Zhao *et al*.[123] In order to observe the magnetism of the Sm doped $DyFeO_3$ samples which was unable to be identified presently but intended for the purpose for further understanding the multiferroicity in this species.

Furthermore, to fully understand the electronic and magnetic properties of this family of materials and their impact on the modern world, and their role in improving energy efficiency in electrical storage devices such as hard drives and solid state drives. PND data of phase pure materials is needed, in addition to using higher temperatures to see phase changes and lattice parameter perturbations which cannot be seen in-house. The electrical properties were unable to be measured due to technical difficulties, therefore, it is also necessary to look at the polarisation-electric field loops to fully prone the electronic properties.

ACoPO$_4$ Series

5.0   Introduction

There have been many studies relating to the synthesis and analysis of the lithium cobalt phosphate (LiCoPO$_4$) compound. This material has been extensively studied due to its large magnetoelectric coefficient,[114,121] which could potentially lead the way to new interesting multiferroic materials and new fascinating properties. One such property is the fourth ferroic order: ferrotoroidicity. This arises from the culmination of the symmetry breaking of spatial and time inversion so that antiferromagnetism (AFM) and ferroelectricity (FE) are present in the same phase of the material and can occur through one order parameter, a toroidal field.[34,35]

In literature, the structure of this material is said to have distorted CoO$_6$ octahedra which edge share along the '*b-c*' plane, stacking themselves in the '*a*' plane. Co-O rows contain the magnetic moment and couple by super exchange. [122]

P atoms exist in tetrahedral sites in adjacent layers, creating PO$_4$ tetrahedra leaving the Li atoms to occupy remaining octahedral sites. LiCoPO$_4$ crystallises in an orthorhombic olivine structure with *Pbnm* (*Pnma*) symmetry, Figure 5.1. Complex oxyanions of PO$_4$ surround the Li and Co ions. Rodriguez *et al.* suggested these tetrahedra play two vital roles; they allow for facile intercalation of the lithium ions during oxidation and reduction of the transition metal cobalt ion. On top of this, they also allow for super-exchange to occur between the Cobalt ions and the non-magnetic oxygen anions.[118] In recent years, this compound has been investigated for battery fabrication in energy storage along with B-site analogues, LiMPO$_4$ (M=Fe, Mn, Ni).[123]
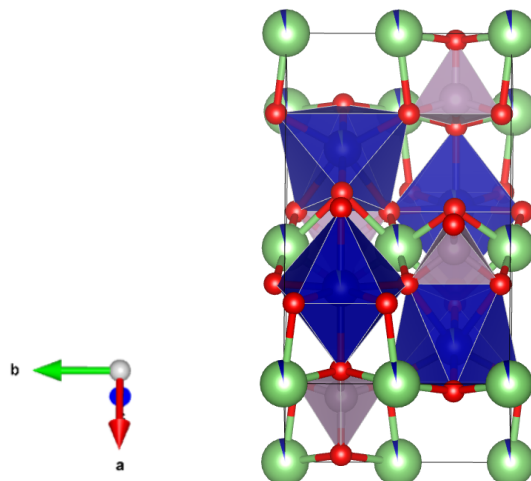
Figure 5.1 - a VESTA image of a $LiCoPO_4$ Crystal unit cell in *Pbnm* symmetry. Oxygen atoms in red. Light pink tetrahedra show PO_4^{3-} with P^{5+} in the centre. Blue octahedra show CoO_6 octahedra with Co^{2+} in the centre. Green spheres show Lithium atoms.

Macroscopically, four domain states have been observed in previous studies of this material. In single crystals, two antiferromagnetic and two ferrotoroidic domains have been found, however, it was found that these are degenerate. The difference between them is the orientation of their net magnetic moment.[124]

$LiCoPO_4$ was synthesised to assess the magnetic and electric behaviour exhibited by the material. Doping the material with different levels of sodium was conducted to observe if there are any changes to the material properties, such as a variance in T_N. This would potentially allow for facile identification of the FT behaviour which is mentioned to exist within this material due to its high magnetoelectric coeffiecient.[34]

Sodium and Potassium analogues were also synthesised to see if the variance of the A-site cation had any further effect on the magnetic properties observed.

5.1   Synthesis

The preparation and synthesis of this series of materials: $ACoPO_4$ (A = Li, Na, K) was based off of two 'Shake and Bake' methods proposed by Rodriguez *et al*,[114] and Hector *et al.*[125]

The raw materials for $ACoPO_4$ are, A = Li: Li_2CO_3 (Honeywell, ≥ 99%), A = Na: Na_2CO_3 (Sigma Aldrich, ≥99%), A = K: K_2CO_3 (Sigma Aldrich, >99%), Co_3O_4 (Sigma Aldrich, >99%),

$NH_4H_2PO_4$ (ACROS organics, ≥ 98%). The following reaction describes the compounds synthesis:

$$A_2CO_3 + Co_3O_4 + NH_4H_2PO_4 \rightarrow LiCoPO_4 + NH_3 + CO_2 + H_2O$$
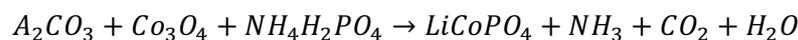
Before synthesis of these materials could begin, the metal carbonates were dried for 2 hours at 543 K.

Both methods required the same precursor materials but used different temperatures and dwelling times. Appropriate amounts of the reagents were weighed out in a stoichiometric ratio for the desired mass of the product (~5 g) and hand ground into a fine powder, in an agate mortar.

For the method proposed by Rodriguez *et al.* minimal amounts of ethanol were used initially to ensure a homogenous mix.[118] This method was also repeated using minimum amounts of acetone in lieu of ethanol, to see solvent effects. After ~20 minutes of mechanical grinding, the mixed reagents were placed in an alumina boat and the subsequent powders were heated in a furnace. Heating occurred initially for 2 hours at a temperature of 648 K at 5 K/minute. Heating at this temperature affords the by-products: NH_3, CO_2, H_2O, to be removed. After the first heating, the powders were naturally cooled down to room temperature, and reground. The resulting crude, fine powder was then reheated for 12 hours at 1073 K at 5 K/minute, affording the product $ACoPO_4$ (A = Li, Na, K).

For the method proposed by Hector *et al.* the only change was the heating section.[129] A reduction in the initial heating temperature from 648 K to 573 K was used maintaining the same 2-hour dwelling time instead of the proposed 6 hours. The second heating was reduced from 1073 K to 1053 K and the dwelling time increased from 8 hours to 36 hours.

For Raman spectroscopy and SEM imaging, pellets of the materials were made. The pellets were of a 10 mm diameter and sintered at 1073 K for 12 hours. After sintering the pellets were polished to a near mirror smooth surface. However, it was found that polishing the ceramic gave a poor mirror surface, as there were regions of smoothness surrounded by rough, uneven regions.

XRD data was collected using a Rigaku Benchtop miniflex 600 diffractometer over a 10-70 2θ range with a step size of 0.02° and a time per step of INSET this (Cu add wavelength 40 kV, 15mA).

SEM imaging was obtained using a Hitachi S-3400 machine, SE imaging was done with 5 kV. EDX mapping was obtained using BSE imaging at 20 kV, images were collected at 250x and 500x.

Raman spectra was obtained use a Horiba Jobin Yvon Labram HR spectrometer using a 633 nm laser at 600 grating. A Raman map was obtained using 1800 grating analysing a 50 μm^2 range over a wavenumber range of 180-500 cm^{-1}.

SQUID magnetometry was conducted using a Magnetic Property Measurement System (MPMS) XL-7 instrument. Hysteresis character was observed at 120 K and 300 K in a variable applied magnetic field of ± 7 T with a step size of 0.01 T between 0-0.1 T, a 0.05 T step between 0.1-0.5 T, and 0.5 T step between 0.5-7 T. High temperature SQUID measurements were conducted with a ZFC/FC analysis between 300-800 K.

TGA/DSC measurements were collected *via* a NETZSCH STA 409PC/PG Thermogravimetric analyser combined with a differential scanning calorimeter.

5.2 Results & Discussion

The initial process produced a light pink, fine powder, for $LiCoPO_4$ (a) which aligns with the product observed by Rodriguez *et al.*[114] However, the exact same process was repeated a further three times (b, c, d), affording a varying range of purple, powders, Figure 5.2.

There could be many factors that attribute to the difference in colour. For example potential impurities or loss of Li in the sample which can alter the oxidation state of the cobalt ions, which is the origin of the intense colour seen. Alternatively, this could signify a secondary phase becoming more prevalent, which was further analysed by X-Ray Diffraction. The texture of the powders also seemed to have changed, from a fine powder to a powder which had some 'static'-nature. The second synthesis (b) used acetone and it can be seen in Figure 5.2, that the texture of the product is different to the remaining powders. This could be due to the reagents having poor solubility in acetone when compared to their solubility in ethanol.

One further difference in synthesis methods throughout the experiment was the variation of the Cobalt source. Initially CoO was used to produce (a) but subsequent repeats of the method with this source showed poor reproducibility. (b) and (c) were synthesised with CoO whilst (d) and (e) were synthesised with Co_3O_4. This was done as it was unsure why there were physical colour changes in the material with exactly the same synthesis routes (a and c). The colour change for (b) as previously mentioned can be attributed to solvent change. On top of this, due to the colour change observed, one could argue that there is a change in the Co oxidation state which therefore has an effect on the contents of Li and P within the samples.
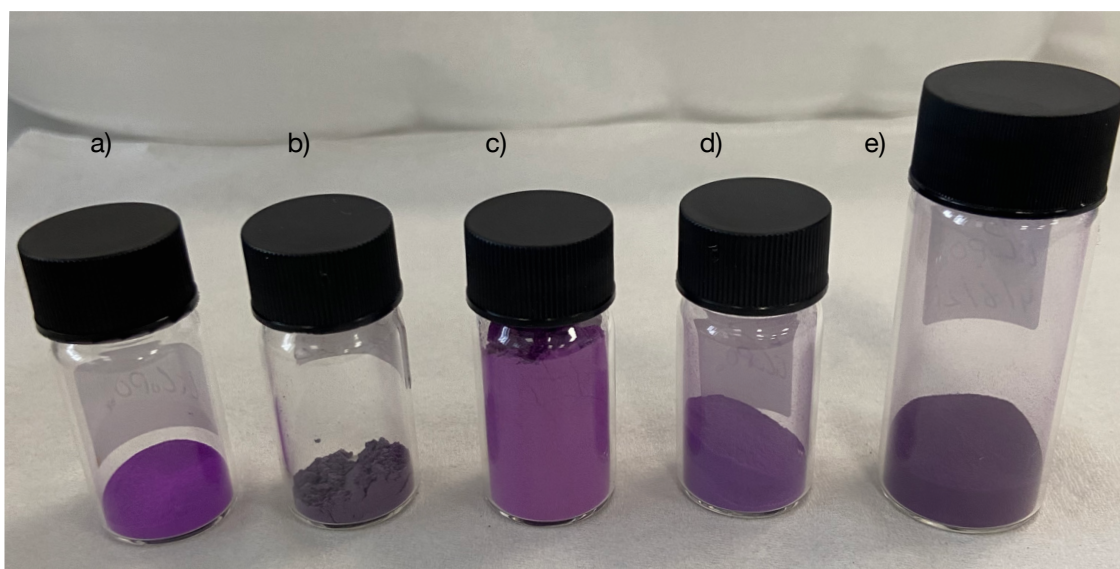
Figure 5.2 - A photo comparing the varying colours which have been produced from two LiCoPO$_4$ synthesis methods. a-d) synthesised via the method proposed by Efrain *et al.* e) synthesised by Hector *et al.*

After the method from Rodriguez *et al.* was found to be failing on reproducibility, another method by Hector *et al*. was found using the same precursors but changing the heating time. [118, 129] This method was used to see if the change in heating time has any effect on the thermal stability of the potential phases has, to favour one over the other. The change in heating time could be one further reason for the different colours seen in the materials (d and e) which were heated differently. The main difference as seen is the colours of the powders, further comparison of XRD patterns were analysed to show crystalline differences and potential phase differences.

5.2.1 XRD

All of the LiCoPO$_4$ materials pictured in Figure 5.2 above were compared in a side-by-side analysis to observe changes in the XRD patterns, Figure 5.3. We can see that materials a and e show the most similarity and are analysed in greater depth later on. Materials *b* and *c* contain a large range of Bragg peaks which are not expected in the *Pbnm* diffraction pattern. Therefore, we can say that there are impurities in the samples which are most likely unreacted starting materials. Sample d shows similar peaks to a and e but also contains an impurity peak around a d-spacing of 38 Å. This is similar to an impurity peak present in both sample b and

c. Due to the presence of these impurities samples 'b', 'c', 'd' are not analysed further. Figure 5.3 shows the stacked diffraction pattern of samples '*a-e*' imaged in Figure 5.2 above.

XRD analysis of 'a' and 'e' showed a large fluorescence of the material during analysis due to the Cu incident X-ray being of a similar wavelength to the Co reflected X-ray.
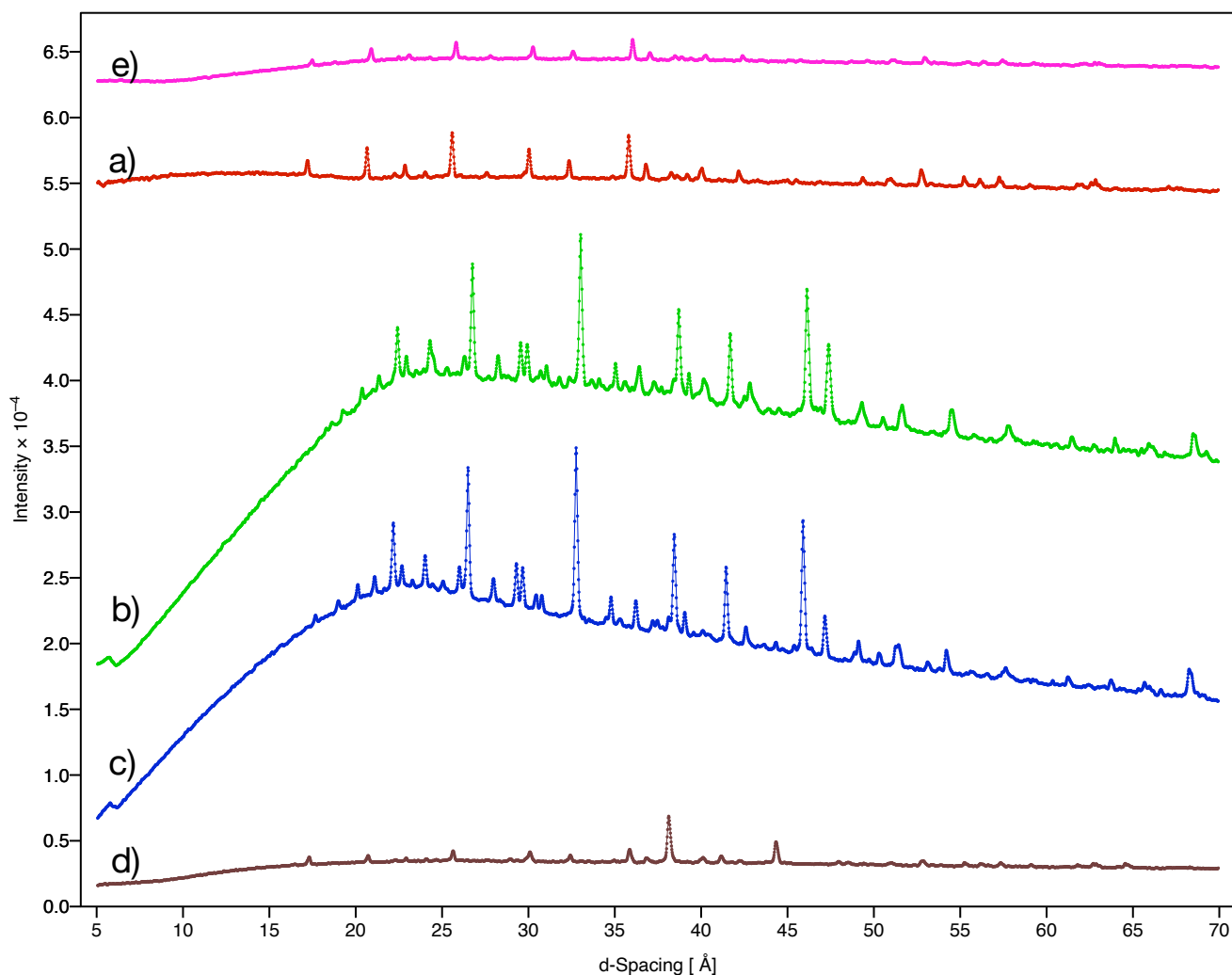
Figure 5.3 – A stacked plot of the LiCoPO$_4$ samples '*a-e*' showing samples '*a*' and '*e*' together for ease of comparison. Shown in d-spacing along the x-axis.

XRD patterns of '*a*' and '*e*' were refined using GSAS II. The refined parameters included: background, X, Y, Z, U, V, W, the scale factor and the atomic positions and thermal parameters. The refined patterns, Figure 5.4, are analysed to show potential changes in lattice parameters. From the data of the refined XRD patterns shown in Table 5.1, we can see that the χ^2 is larger and the Residual weighting (Rw) is lower for (a) than (e). It can be said that

the first synthesis of this material using Rodriguez method produced a more crystalline material that fits the expected CIF pattern used for $LiCoPO_4$.[118]
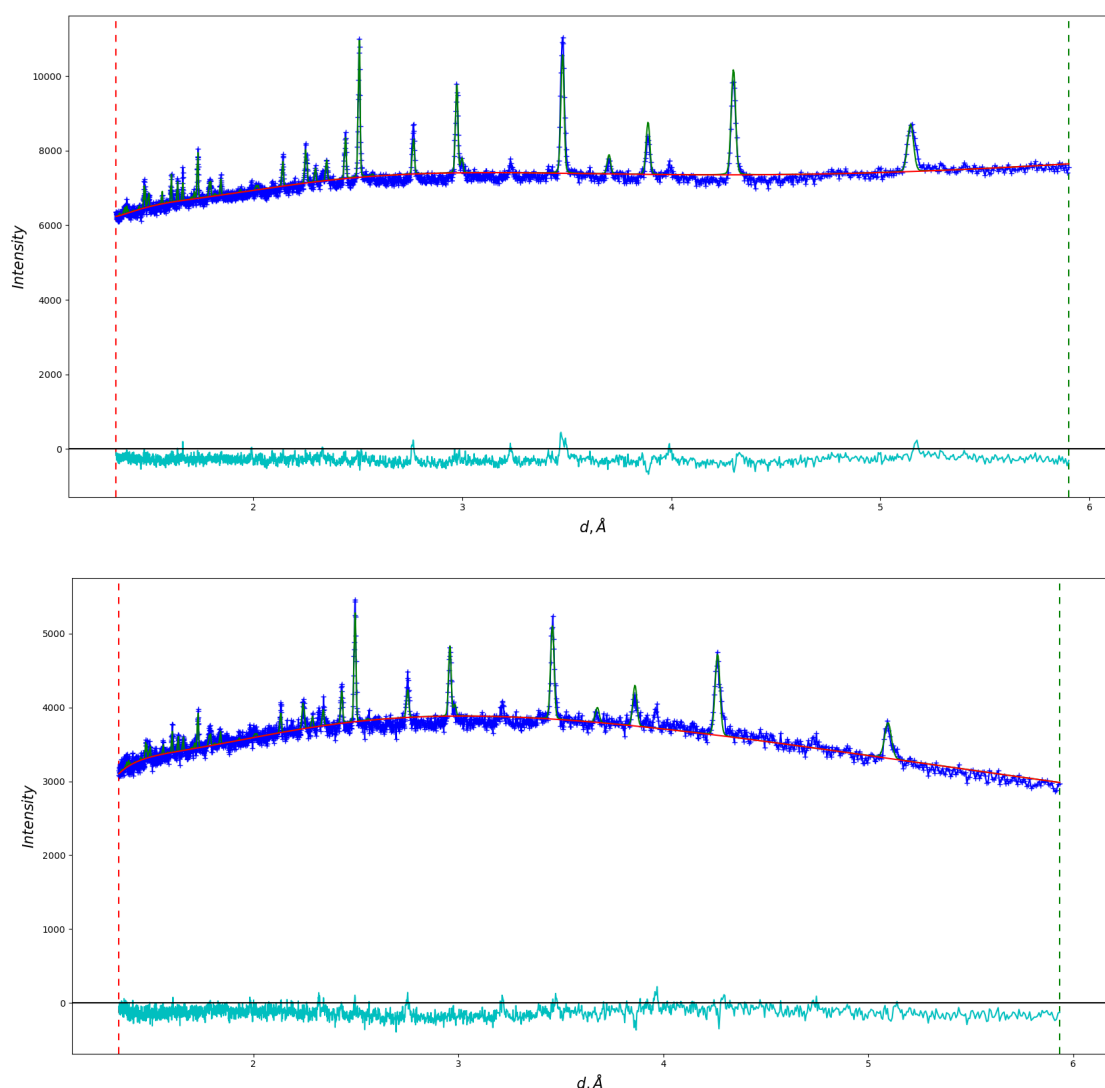
Figure 5.4 – $LiCoPO_4$ sample '*a*' (top) and sample '*e*' (bottom) diffraction pattern's Rietveld refinements using GSAS II. The dark blue line showing the experimental data, the green line showing the calculated data fit to the model CIF file, and the light blue showing the difference in the patterns, shown in *d*-spacing.

Table 5.1 - A table showing the lattice parameters of the Rietveld refined $LiCoPO_4$ materials synthesised by Rodriguez *et al.* and Hector *et al.* sample '*a*' and sample '*e*' respectively.[118, 129]

Sample	R_w	χ^2	Lattice Parameters Å			Cell Volume Å
			a	b	c	
$LiCoPO_4$ (a)	1.679	1.98	10.1992(6)	5.9185(3)	4.6968(3)	283.518(18)
$LiCoPO_4$ (e)	1.983	1.407	10.2007(9)	5.9216(5)	4.6991(4)	283.847(28)

The material produced by Hector's method has a higher R_w and lower χ^2 which demonstrates a more correlating fit to the CIF file used. As both materials were able to be refined using the *Pbnm* symmetry to a high degree, we can suggest that both synthesis methods produced the required material.

The lattice parameters of these two differently synthesised materials show very close similarities and the differences can be put down to the crystallinity of the powders and the surface roughness of the materials. Further differences can be related to impurities in the sample analysed.

5.2.3 SEM

SEM imaging was used to visually observe the topography of the $LiCoPO_4$ (sample '*e*') Pellet. Backscattering electrons were used at 20 keV at a magnification of 300x to observe structural defects, Figure 5.5. Not much information was able to be extracted at the magnification used for observation. However, one is able to clearly tell the surface of the pellet was not as smooth as desired. There are clear changes in surface topography seen by darker and lighter regions.

The brighter regions which are largely homogenous could suggest a secondary phase at the surface. Alternatively, the darker regions could show a loss of Li content.
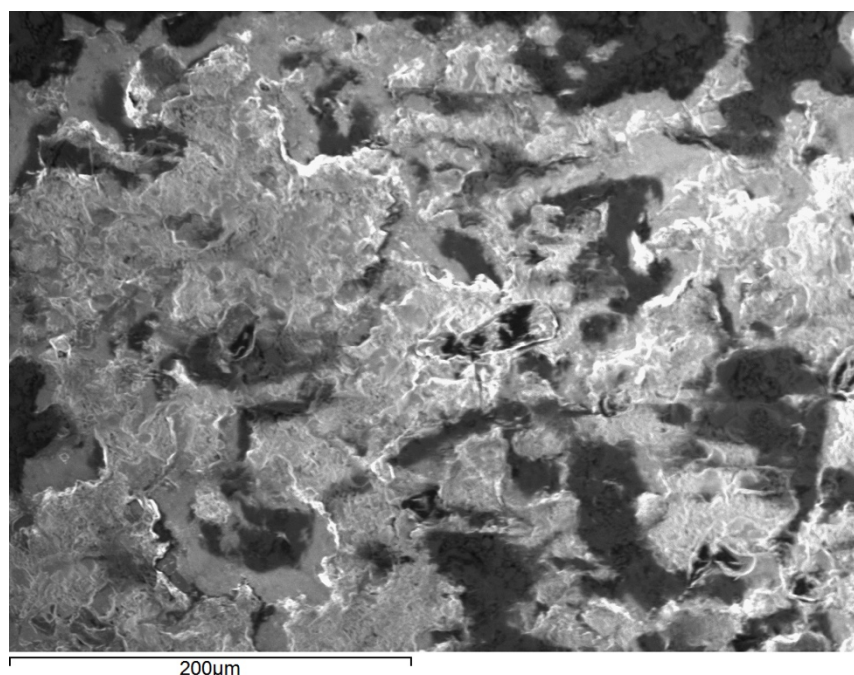
Figure 5.5 – SEM image of the surface of a $LiCoPO_4$ pellet, using backscattering electrons

5.2.4 SQUID

SQUID Magnetometry was used to analyse the magnetic nature of this material during a zero-field cooled (ZFC) analysis. It has been previously reported that LiCoPO$_4$ is an antiferromagnet with a T_N of 23 K.[114,126] From the SQUID data analysed, Figure 5.6, there is clear antiferromagnetic ordering in the material seen with the transition temperature around 21.8 K which correlates to the T_N of 21.6 K found experimentally by Ludwig et al.[127]
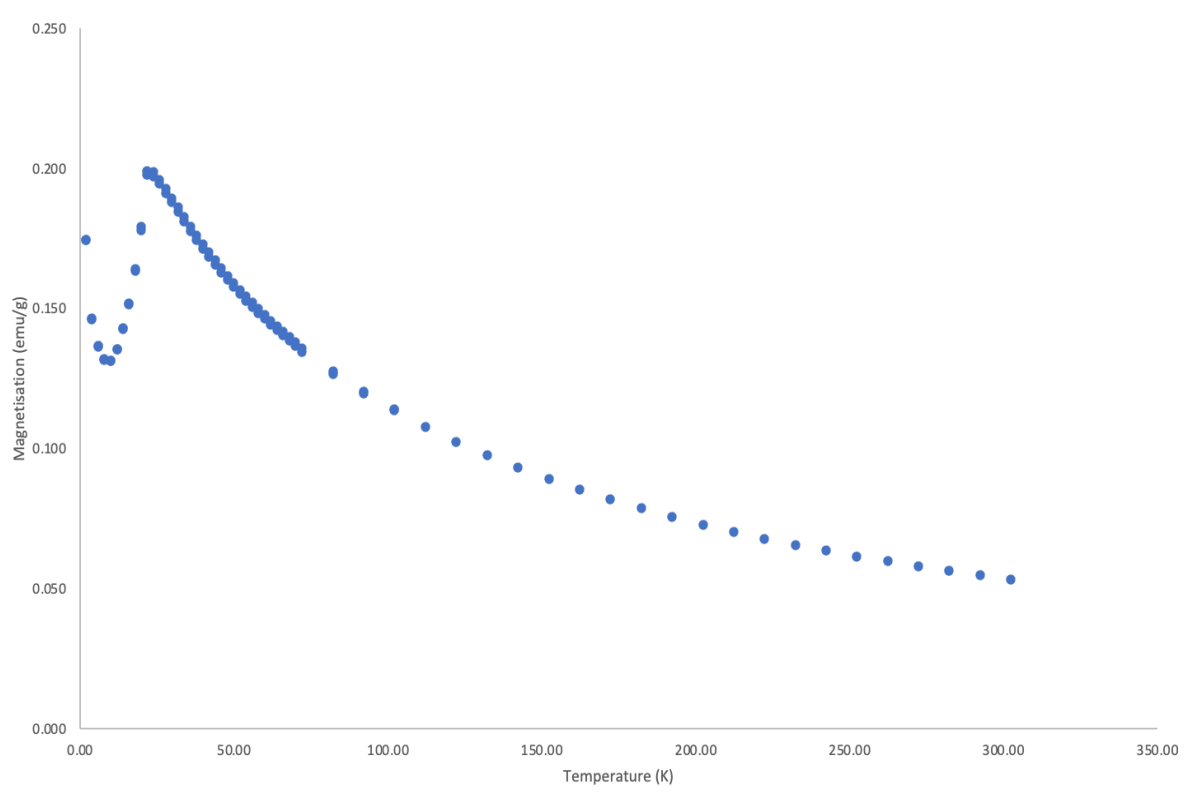
Figure 5.6 - SQUID magnetometry data of a ZFC sample of LiCoPO$_4$ (sample 'e') (54.75 mg) demonstrating antiferromagnetism.

5.2.5 TGA / DSC

TGA analysis was conducted on LiCoPO$_4$ (sample 'e') of temperatures between 296-1223 K. It can be seen that there is a decrease in weight % of the material, ~2.2%.

Ludwig et al. reviewed three polymorphs of this material. Pna2$_1$ with a Co^{2+} in a tetrahedral environment. Pbnm and Cmcm with octahedral Co environments.[127] They deduced that Pbnm is stable up to 1173 K. Cmcm undergoes two transitions to Pbnm and then to Pna2$_1$ at 848 K and 948 K respectively. Pna2$_1$ undergoes a single transition to Pbnm at 800 K. In Figure 5.7,

it is difficult to see any of the described peak's due to one broad peak being recorded from 723 K onwards until decomposition.

Not many other studies have been conducted on the thermal stability of this phosphate material. However, the sodium analogue, $NaCoPO_4$, has been studied due to its polymorphic nature.[128] Therefore, it may be reasoned $LiCoPO_4$ could show similar polymorphic characteristics on heating. This polymorphic nature described could attest for the difference in the product afforded during the repeat experiments as explained above. This could further explain the colour difference in the afforded powders.

Senguttuvan *et al.* described different phases of the sodium analogue afforded at different temperatures, however they used different precursors to get the desired product.[132] The DSC curve shows two exothermic peaks at roughly 623 K and ~998 K. This corresponds to two phases which are recorded by Senguttuvan *et al.* the $P6_5$ and the $Pna2_1$ space groups respectively. After ~998 K there is a decrease in thermal stability leading to decomposition.
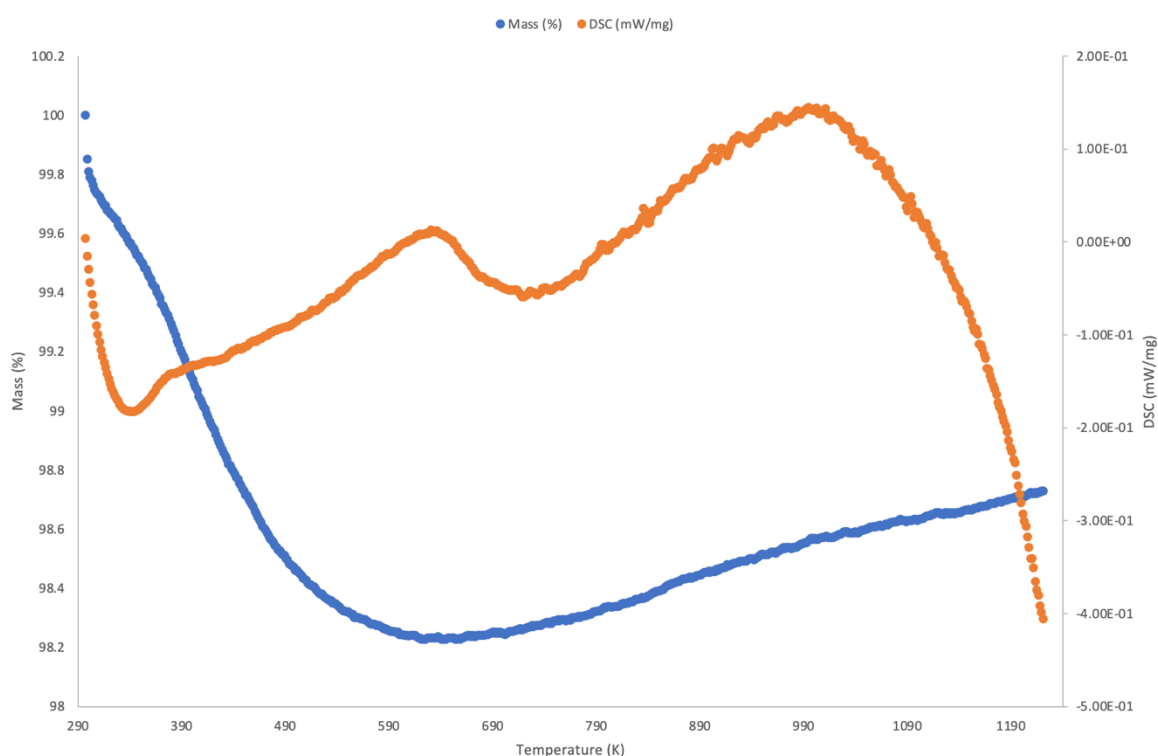
Figure 5.7 - TGA curve (blue) plotted alongside DSC curve (orange) as a function of temperature for 52.4 mg of $LiCoPO_4$

5.2.6 Raman

Raman analysis was conducted on a polished pellet of $LiCoPO_4$ (sample '*e*'). This was done in order to observe the vibrational modes present in the material, and further allow us to see correlate this to previous data.

A Raman spectrum was analysed, Figure 5.8. The most intense, and sharpest peak corresponds to a phosphate (PO_4^{3-}) symmetric vibration at 945 cm^{-1}. The two following weaker peaks at 983 cm^{-1} and 1074 cm^{-1} correspond to asymmetric bond vibrations of the PO_4^{3-} anion. Wavenumbers between 400 and 800 cm^{-1} have been said to correlate to PO_4^{3-} bending modes. Similarly seen by Markevich *et al.*[129]
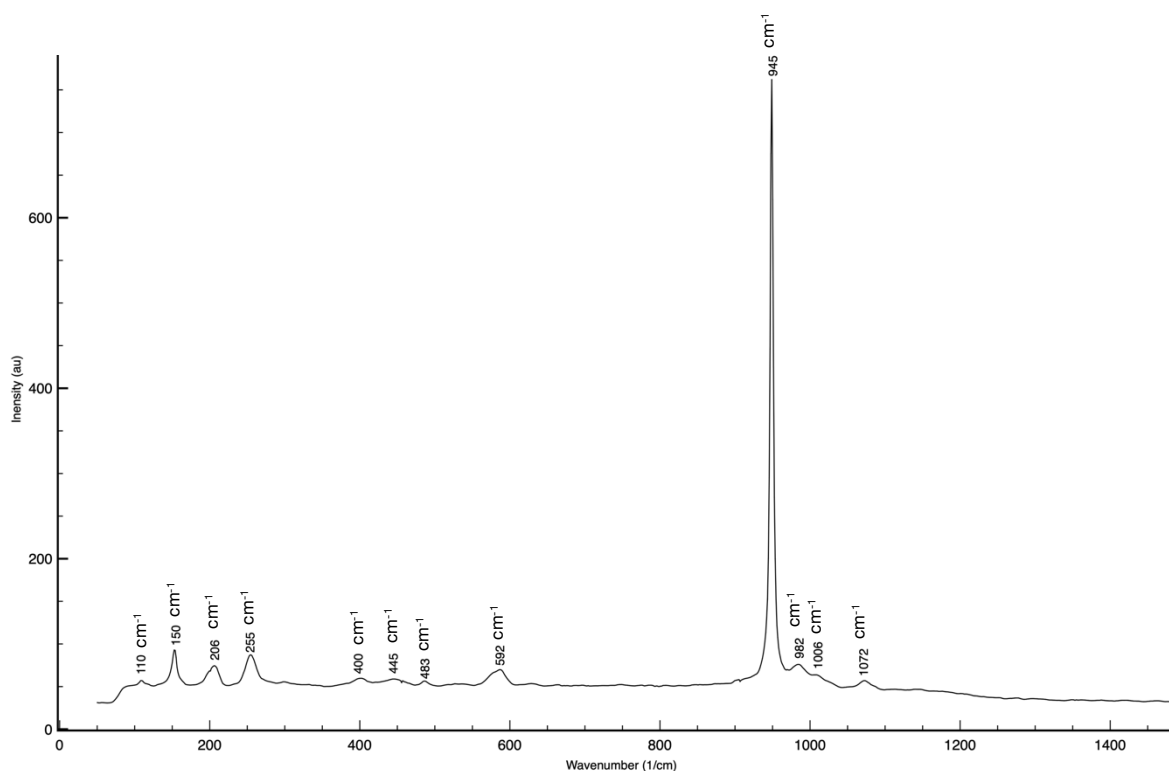
Figure 5.8 – Raman spectrum of $LiCoPO_4$ showing with significant peaks labelled.

Taking a map of the material over a 50 μm^2 range, observing data over 180 – 500 cm^{-1}, clear deviations can be seen in the peak intensities. This can be attributed to a change in crystal orientation across the pellet surface. This can further be seen by the surface roughness of the pellet, seen *via* SEM.

Observing a range of spectra taken throughout the map (see appendices) allows us to further see which bonds are present in the area mapped, which can tell us phase differences. At the origin point, appendix 5.1, 5 peaks can be seen: 198 cm^{-1}, 207 cm^{-1}, 255 cm^{-1}, 271 cm^{-1}, 483 cm^{-1}. Observing a different data point 40 μm above the origin, appendix 5.2, and therefore a different spectrum, one is able to see most of the prior peaks disappear, leaving the first and the last peak. This could be due to the crystallite analysed on the pellet potentially being directed in a different orientation. Therefore, the laser is not able to excite the bond as it cannot illuminate it.

Over the range of spectra, one is able to see the same peaks at the same or similar wavenumbers to that analysed in the point spectrum above. The large noise difference that can be seen over the spectra range can be attributed to the surface roughness of the pellet. Alternatively, this could suggest a lack of homogeneity in the sample which may suggest that Li content varies and may link to the different colours observed in the different samples.

5.2.7 Na Doping

The LiCoPO$_4$ analogue was doped with varying amounts of Na content, x = 0.1, 0.2, 0.3, 0.4. This was done by limiting Li$_2$CO$_3$ and replacing it with stoichiometric amounts of Na$_2$CO$_3$. It followed the same synthesis method as before and following this reaction profile:

$$1 - xLi_2CO_3 + xNa_2CO_3 + Co_3O_4 + NH_4H_2PO_4 \rightarrow Li_{1-x}Na_xCoPO_4 + NH_3 + CO_2 + H_2O$$
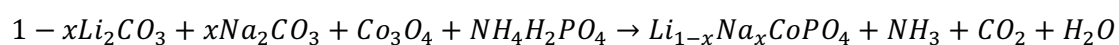
These materials has been doped to see if one can increase the Neél temperature.[118, 130]

Sodium was used in increasing concentrations of 10%-40%, in 10% intervals, to see the difference the dopant has on changing the structural and magnetic properties. Sodium has a larger ionic radius than Lithium, Na$^+$ = 1.02 Å, Li$^+$ = 0.76 Å. Ionic radii data taken form the Shannon database of both ions having a coordination of 6.[83] Therefore, it is expected to see lattice strain when (and if) the sodium ion is successfully introduced to the system.

Similar to the synthesis of the un-doped sample. These materials were also synthesised via both methods. Pellets were also prepared for subsequent Raman spectroscopy and SEM

imaging. It was found that polishing the pellets to afford a smooth mirror surface became more difficult at higher Na %.

On sintering of the 40% Na pellet, air bubbles were produced which disrupted the structural integrity of the pellet, these had to be smoothed to allow for a flat surface for Raman spectroscopy. The air bubbles could be due to some residual solvent remaining, or some gases, CO_2 and NH_3, still being produced.

5.2.7.1 XRD

The synthesis of this family of materials produced some unclean products, and the reproducibility of this method was poor. Attaining a clean product was found to be difficult each time the process was conducted, as reported in the synthesis section, 5.1, above. This could be down to the unreliability of the heating time and not allowing sufficient venting of the reducing atmosphere away from the sample to allow for full oxidation. Furthermore, this could suggest an incompatibility between Na and Li ions in this material.

Secondary phases also become present in the material on increasing sodium doping (x ≥ 0.2) this could be due to the material only having a doping threshold of ~10% or, on longer heating methods, secondary phases are becoming more kinetically allowed.

Figure 5.9 below shows the pattern overlay of the parent $LiCoPO_4$ material and the 10% Na doped sample. The only difference being a shifting in *d*-space which is expected due to the introduction of the larger isovalent ion, decreasing interplanar distances.
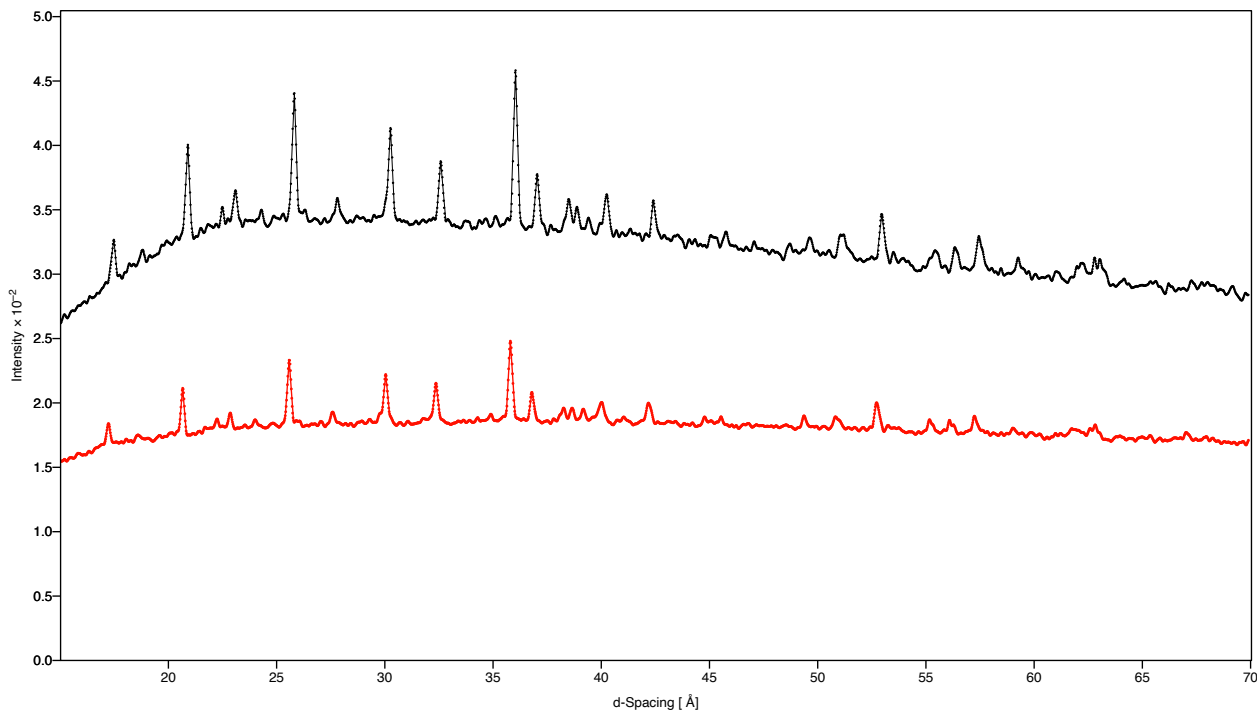
Figure 5.9 – XRD patterns of LiCoPO$_4$ (black) and Li$_{0.9}$Na$_{0.1}$CoPO$_4$ (red) overlaid, shown in d-spacing along the x-axis over a range of 15-70 Å.

As mentioned above the x=0.1 pattern is shifted in *d*-spacing which shows the incorporation of the Na ion. In subsequent compositions, x = 0.2, 0.3, 0.4 the peaks have the same d-spacing in relation to the parent material, Figure 5.10. They also show two impure phase peaks arising at 33.5 2θ and 35.25 2θ which do not correspond to any known phase changes that arise from LiCoPO$_4$. Therefore, it can be deduced that the inception of these peaks occurs from the addition of the Na$_2$CO$_3$ precursor.
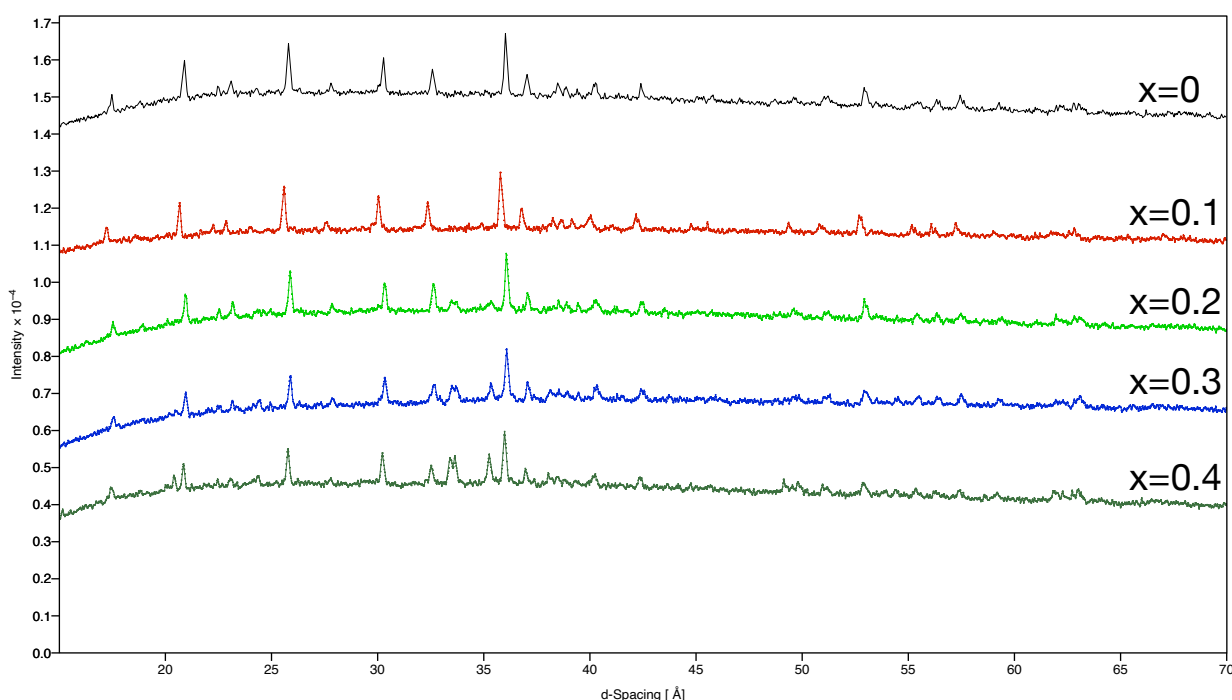
Figure 5.10 – XRD patterns of $LiCoPO_4$ (black), $Li_{0.9}Na_{0.1}CoPO_4$ (red), $Li_{0.8}Na_{0.2}CoPO_4$ (light green), $Li_{0.7}Na_{0.3}CoPO_4$ (blue), $Li_{0.6}Na_{0.4}CoPO_4$ (dark green), stacked and shown in d-spacing along the x-axis over a range of 15 – 70 Å.

The peak ~32 Å decreases on higher Na content whilst the two impure succeeding peaks are increasing, therefore these phases are becoming more prevalent. Through search matching, the potential impurity phase peaks could correspond to a potential LiO phase (33.5 Å) and a Na_3P (35.25 Å) phase. This could further be probed through SEM imaging to visually observe changes in grain boundaries and structural deformations.

5.2.7.2   SEM

SEM imaging of $Li_{1-x}Na_xCoPO_4$, x = 0.1, 0.2, 0.3, pellets were taken using BSE's at 20 keV and 300x magnification. The x = 0.4 composition was unable to be photographed due to time constraints.

From the images of the pellet surfaces, Figures 5.11, 5.13, it can be seen that there are bright regions which are a stark contrast when compared to the surroundings. These correlate to charging effects seen in the non-conductive material. A fairly homogenous distribution of ions can be seen, as well as surface defects present on the pellet. Figure 5.12 shows clear changes in surface topography indicated by darker and lighter regions. Similar to the parent

material, this could be due to a secondary phase, potentially correlating to a loss in Li content. To better analyse these materials a near mirror smooth surface will need to be achieved.

The homogeneity of the atomic distribution of $Li_{0.9}Na_{0.1}CoPO_4$ can be attributed to a phase pure sample seen in the XRD pattern above. The darker and lighter regions seen in Figure 5.12 can be due to an area of the pellet analysed where there is a clear phase difference between the $LiCoPO_4$ and the potential $NaCoPo_4$ phases. Seen by the impure XRD pattern. Figure 5.13 shows a homogenous distribution despite the impure diffraction pattern. This could be due to the area of the pellet analysed showing a phase pure distribution of either $LiCoPO_4$ or $NaCoPO_4$.

200µm
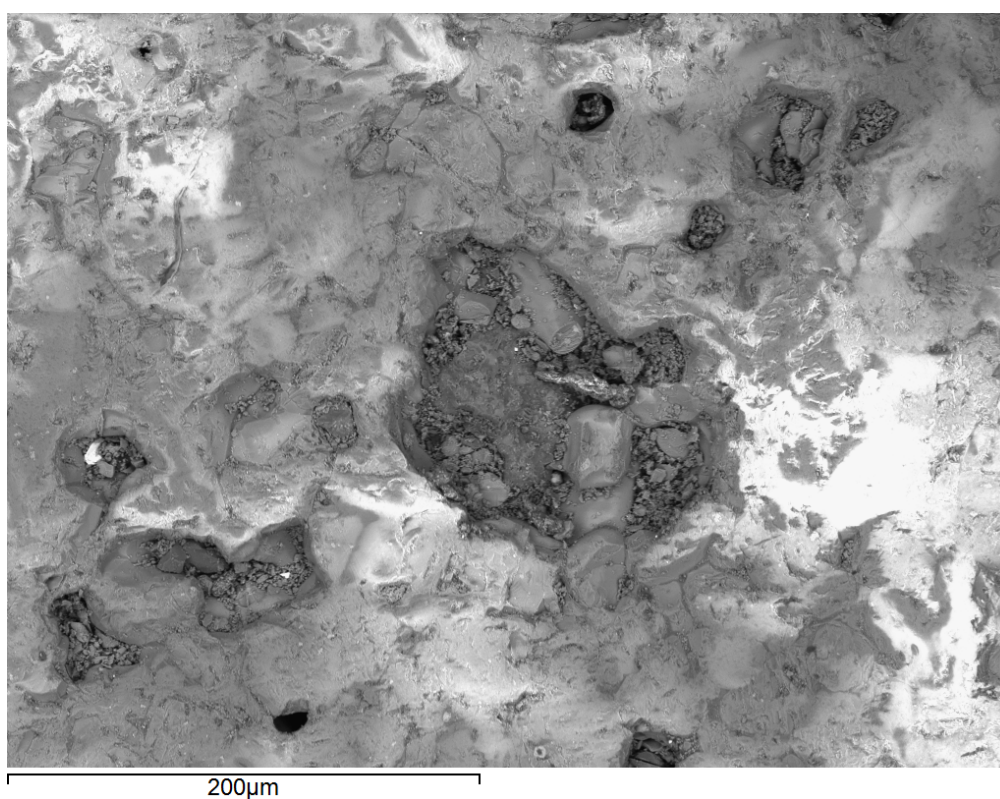
Figure 5.11 – SEM image at 300x magnification of the surface of the $Li_{0.9}Na_{0.1}CoPO_4$ pellet.
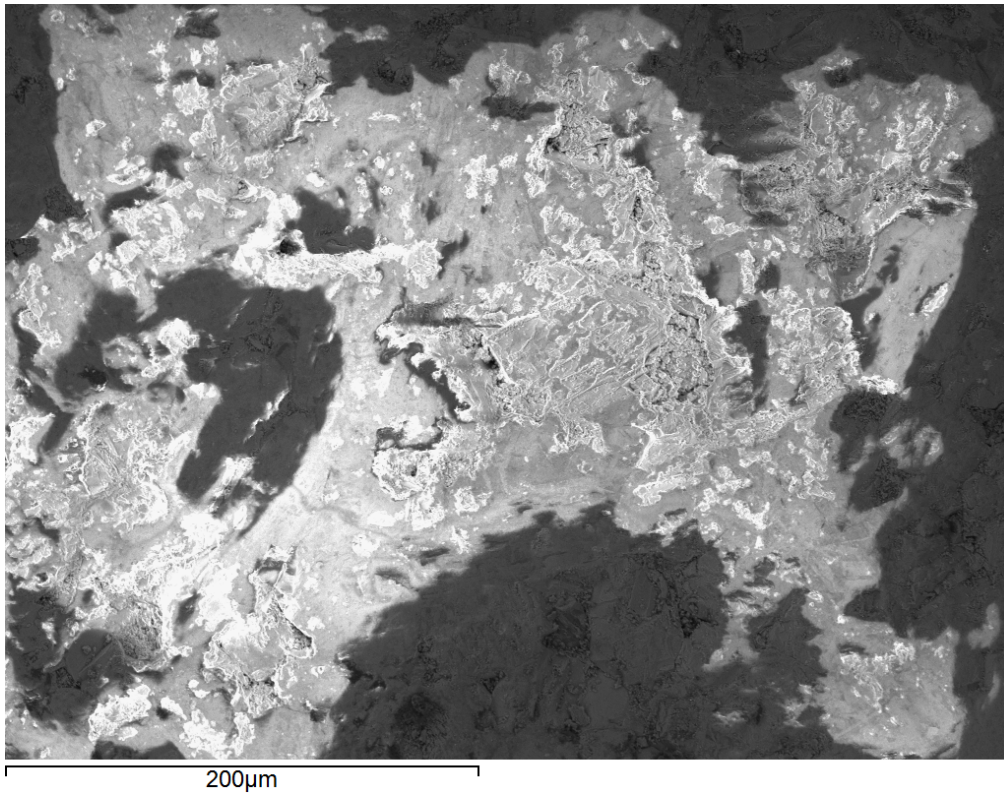
Figure 5.12 – SEM image at 300x magnification of the surface of the $Li_{0.8}Na_{0.2}CoPO_4$ pellet.
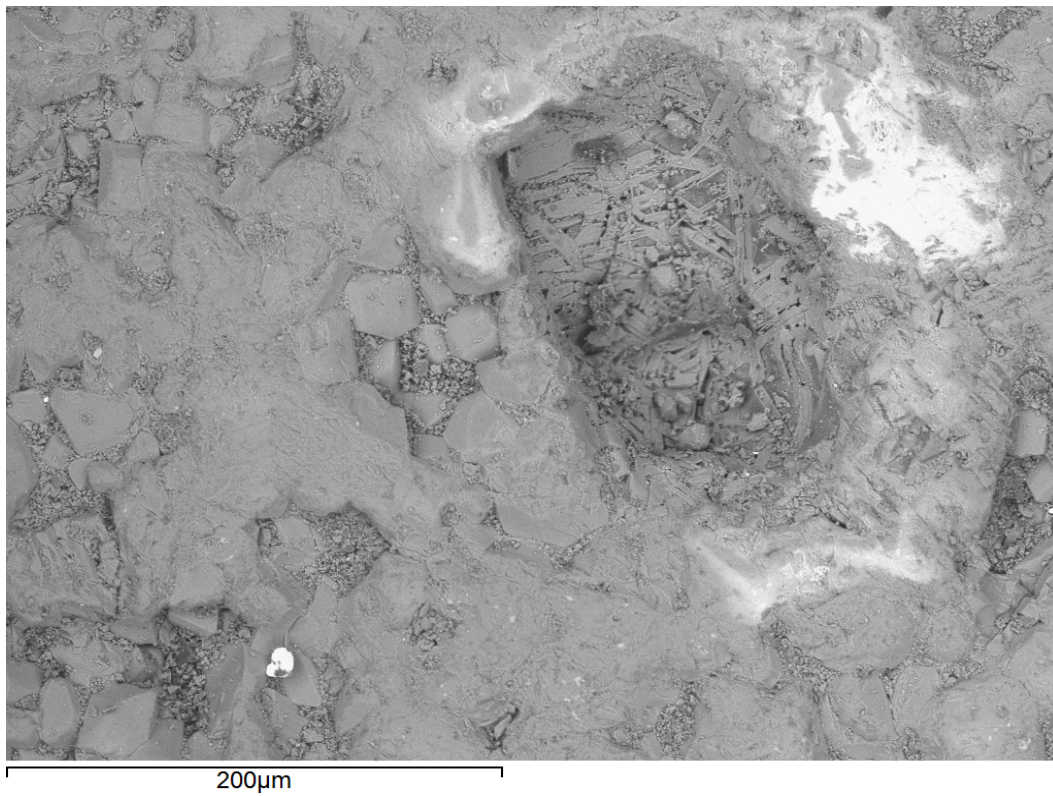
Figure 5.13 – SEM image at 300x magnification of the surface of the $Li_{0.7}Na_{0.3}CoPO_4$ pellet.

5.2.7.3 SQUID

SQUID magnetometry was used to analyse the magnetic character of $Li_{0.9}Na_{0.1}CoPO_4$. Only this composition was analysed as it was found that sodium was only able to be incorporated into the lattice at this dopant level. On increasing dopant % it was found to have impure phases and therefore a poor magnetic profile would have been attained.

Similar to the previously discussed $LiCoPO_4$ parent compound, there is a clear antiferromagnetic character seen with this composition. A T_N of ~21.8 K was found experimentally using the SQUID apparatus, Figure 5.14. Showing no increase of magnetic transition temperature with sodium doping as low as 10%. This could be due to the minute change in ion radius between sodium and lithium not having the desired effect to increase or decrease the lattice strain Alternatively this could suggest that Na has not be incorporated into to the material as desired.

In literature of $LiCoPO_4$, the Co-O bond lengths range from 2.07-2.21 Å, and the P-O bond lengths range from 1.53-1.58 Å.[130] The Co-O-Co bond angle = ~128° with O-P-O bond angles ranging between 103°-114°.[114, 131] In literature of $NaCoPO_4$, the same bond lengths are 1.99-2.38 Å and 1.55-1.58 Å, respectively.[132] The Co-O-Co bond angle = ~180° with O-P-O bond angles ranging from 107°-112°.[133] If the Na ion was incorporated as desired, we hopefully would be able to see a change in magnetism due to the large difference in bond lengths of Co-O and the Co-O-Co bond angle. There is not much change in the P-O bond lengths of O-P-O bond angles between the two analogues.
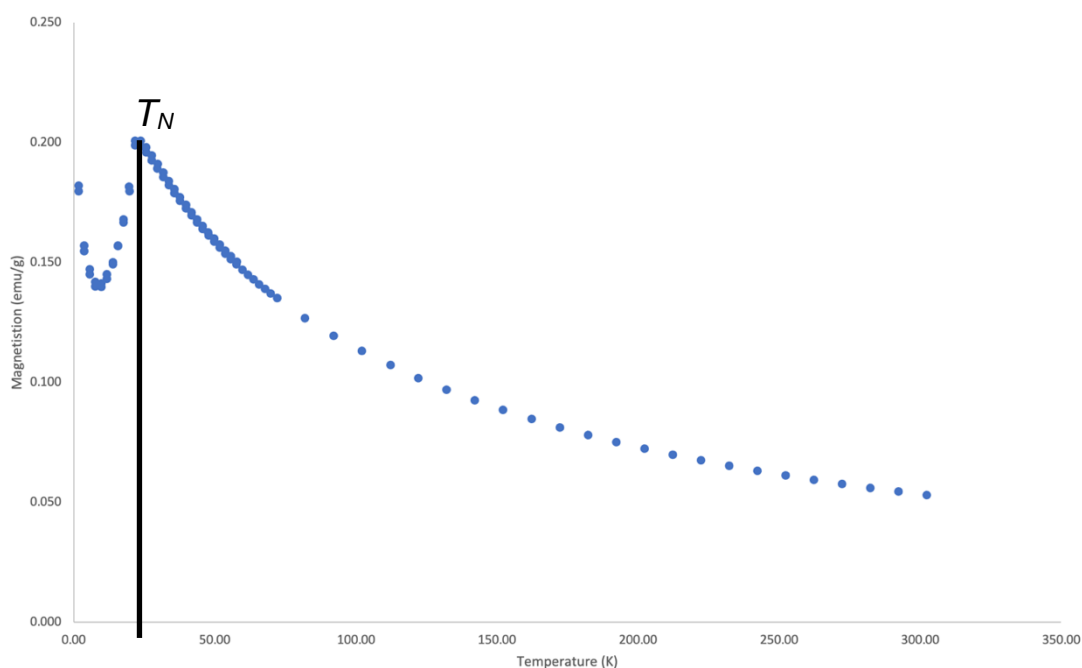
Figure 5.14 – a SQUID ZFC/FC measurement of $Li_{0.9}Na_{0.1}CoPO_4$ (53.96 mg) showing antiferromagnetic character.

5.2.7.4 TGA / DSC

The compounds, x = 0.1, 0.2, 0.3, 0.4, were all analysed via TGA and DSC to observe the thermal stability and potential energy changes which occur.

$Li_{0.9}Na_{0.1}CoPO_4$, Figure 5.15, has a differing thermal stability to that of the pure analogue. Where the pure sample was seen to decrease in mass by ~2.2% the 10% Na sample shows a minute increase in mass. 66.9 mg of analyte was measured, and 67.1 mg was recorded after the heating occurred.

The DSC curve plotted shows the energy output of the sample over the temperature range. There are 3 crystallisation peaks, the first peak could correspond to the previously mentioned *P*6$_5$ space group at 623 K. The second could correspond to the *Pbnm* symmetry which is more pronounced in this profile than the parent material. After 998 K there is a decrease in thermal stability leading to decomposition.

The succeeding compositions, Figures 5.16, 5.17 and 5.18, show more erratic DSC curves to that described previously. Small peaks around ~623 K are consistent in all the curves, which can be attributed to polymorphic behaviour similar to that seen from the Na analogue.[128] Above 773 K it is more difficult to discern peaks. There is a peak around ~803 K which could correlate to the phase change of *Pna*2$_1$ to *Pbnm* as reviewed by Ludwig *et al*.[127] Another peak at 903 K could correlate to a *Cmcm* to *Pna*2$_1$ transition. Further analysis shows another peak at ~1028 K which shows a $NaCoPO_4$ *Pbnm* to *Pna$_1$* transition. Due to the wide variety and ambiguity of the peaks seen in the DSC curves, one could conclude that there are more than one phases present in the polycrystalline material. This is further re-enforced by the increase in the impure peaks seen in the XRD patterns analysed above.

At higher Na content, x = 0.3, 0.4, Figures 5.17 and 5.18, the DSC curve shows a more erratic decrease in mW/mg and further in-depth analysis of these materials will have to be conducted to conclude phase information.

There is a change in the % mass of the x = 0.2 sample by ~0.9 % to 79.78 mg. The x = 0.3 sample shows a miniscule % increase of ~0.06 – 0.05 % to 93.05 mg. The x = 0.4 sample shows a % decrease of 0.8%. to 94.44 mg. The TGA curves shows irregular mass changes on increasing sodium content. This could be due to poor incorporation of Na into the $LiCoPO_4$ lattice creating the variety of phases present as previously discussed. It could also be due to unreacted reagents, for example Na_2CO_3 has a higher thermal stability than Li_2CO_3 so it could be expected that potential impurities increase the thermal stability recorded.
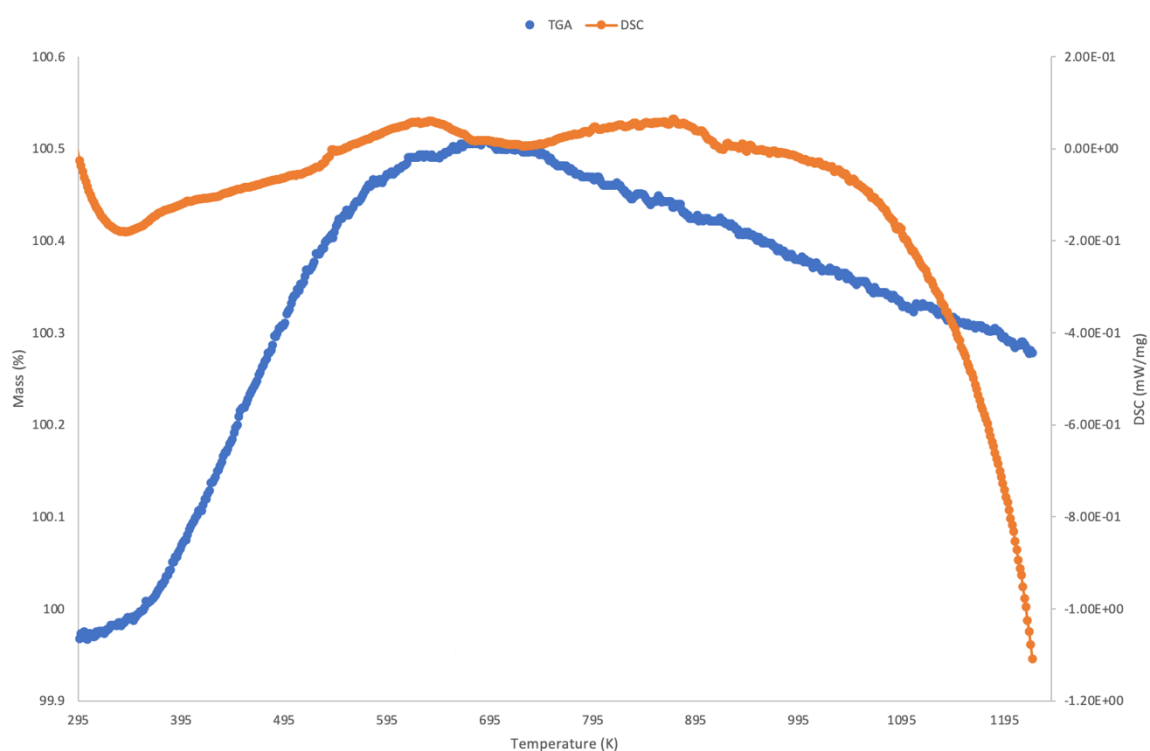
Figure 5.15 - TGA curve (blue) plotted alongside the DSC curve (orange) as function of temperature for 66.9 mg of $Li_{0.9}Na_{0.1}CoPO_4$.
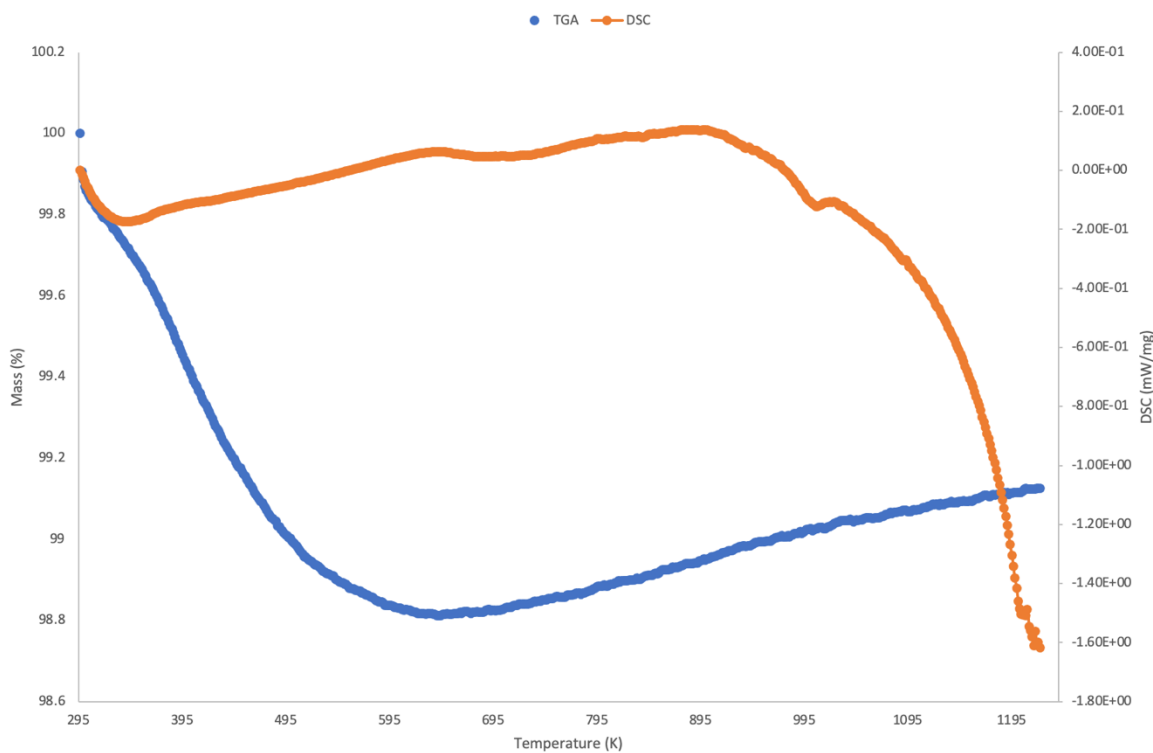
Figure 5.16 - TGA curve (blue) plotted alongside the DSC curve (orange) as function of temperature for 80.5 mg of $Li_{0.8}Na_{0.2}CoPO_4$.
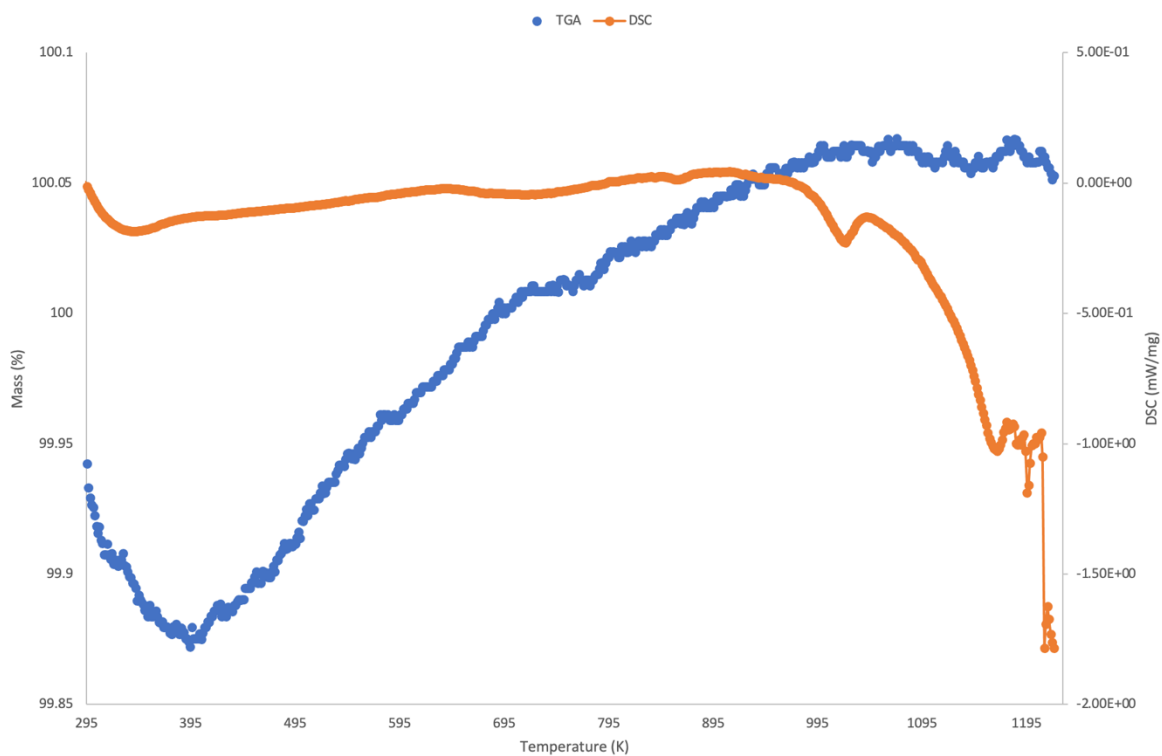
Figure 5.17 - TGA curve (blue) plotted alongside the DSC curve (orange) as function of temperature for 93 mg of $Li_{0.7}Na_{0.3}CoPO_4$.
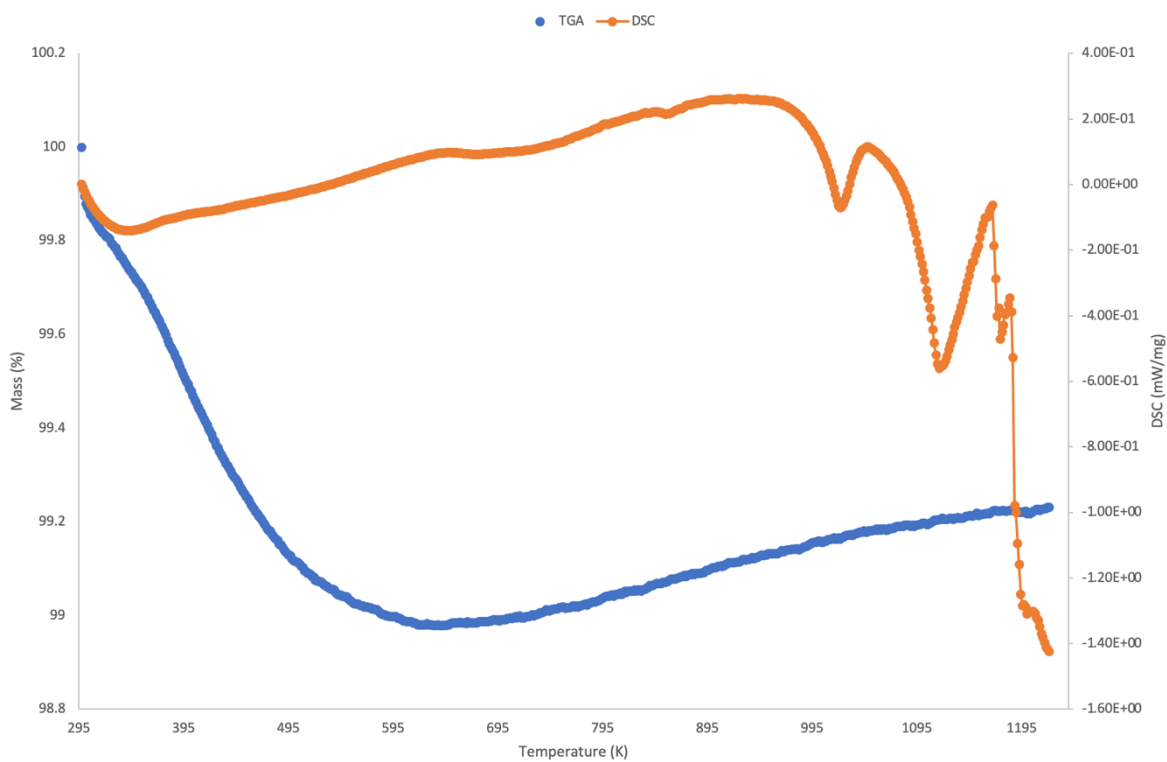
Figure 5.18 - TGA curve (blue) plotted alongside the DSC curve (orange) as function of temperature for 95.2 mg of $Li_{0.6}Na_{0.4}CoPO_4$.

5.2.7.5 Raman

Raman maps were acquired of all compositions and analysed over a 50 μm^2 range between 180 – 550 cm^{-1} with a 633 nm laser at 1800 grating. Similar to the parent material, peaks arose at similar wavenumbers showing the same bonds present in the material. For $Li_{0.8}Na_{0.2}CoPO_4$, Figure 5.20, the wavenumber range occurred over 240 - 560 cm^{-1} and the majority of the spectra within the 50 μm^2 range showed noise. Therefore, not many peaks were able to be determined, only a single peak at ~443 cm^{-1} was measured. This could correlate to the surface roughness of the sample pellet, which is further seen *via* the SEM images above.

The noise seen could be due to the mixed phase nature of the materials causing problems in the lattice periodicity and crystallite orientation.
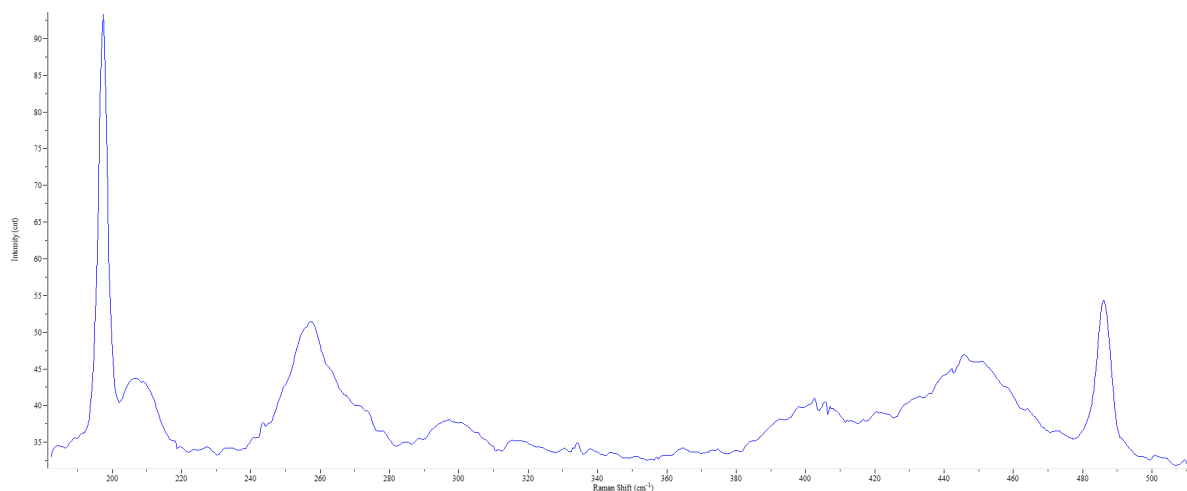
Figure 5.19 – Raman map spectrum of $Li_{0.9}Na_{0.1}CoPO_4$.
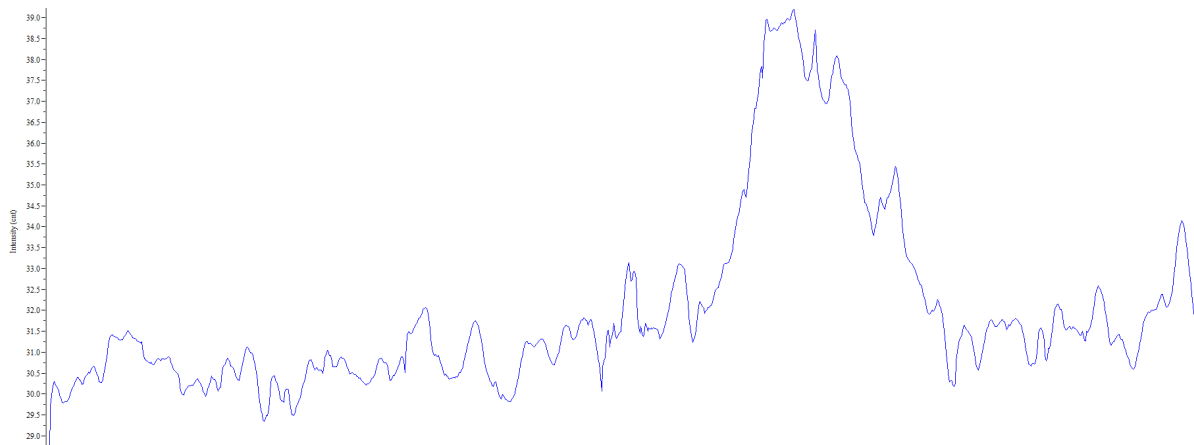
Figure 5.20 – Raman map spectrum of $Li_{0.8}Na_{0.2}CoPO_4$.
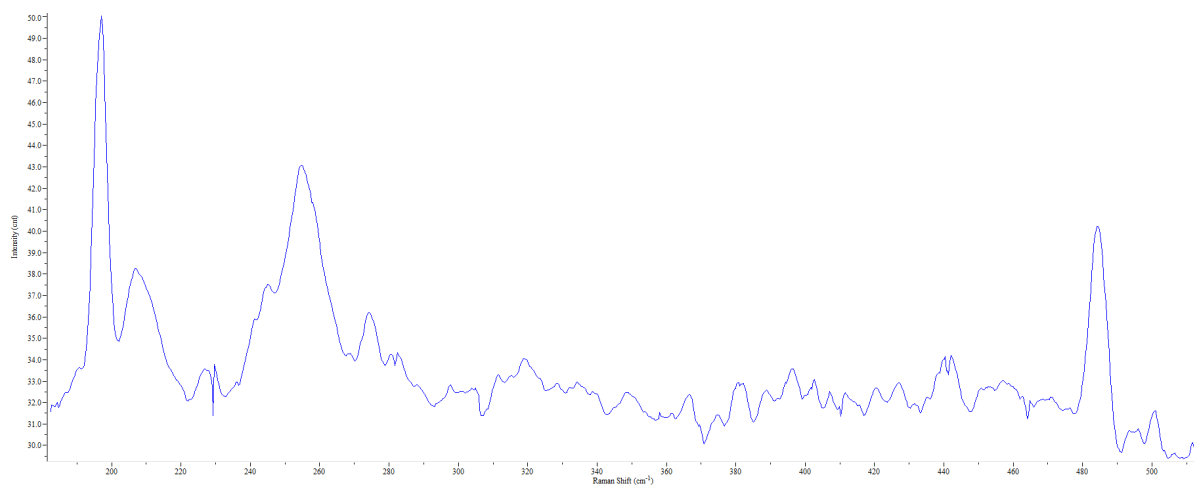
Figure 5.21 – Raman map spectrum of $Li_{0.7}Na_{0.3}CoPO_4$.
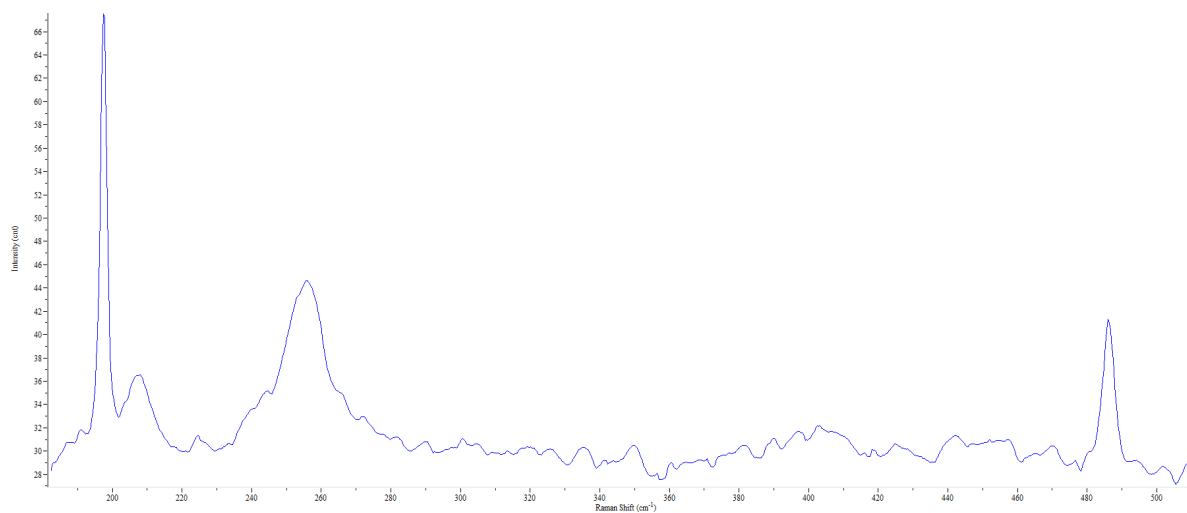
Figure 5.22 – Raman map spectrum of $Li_{0.6}Na_{0.4}CoPO_4$.

5.2.8 ACoPO₄ Analogues

NaCoPO$_4$ and KCoPO$_4$ were synthesised due to the thought that they would change magnetic behaviour of the CoPO$_4$ family. However, due to the multi-phase nature of the materials, they were not refined or analysed further due to time constraints. Furthermore, due to NaCoPO$_4$ having polymorphic behaviour it was difficult to isolate the required phase.[128] KCoPO$_4$ does not crystallise in the *Pbnm* symmetry. Comparing the XRD patterns of the analysed analogues, they all very clearly crystallised with different symmetries. Figure 5.23 shows a stacked plot of the unrefined diffraction patterns.
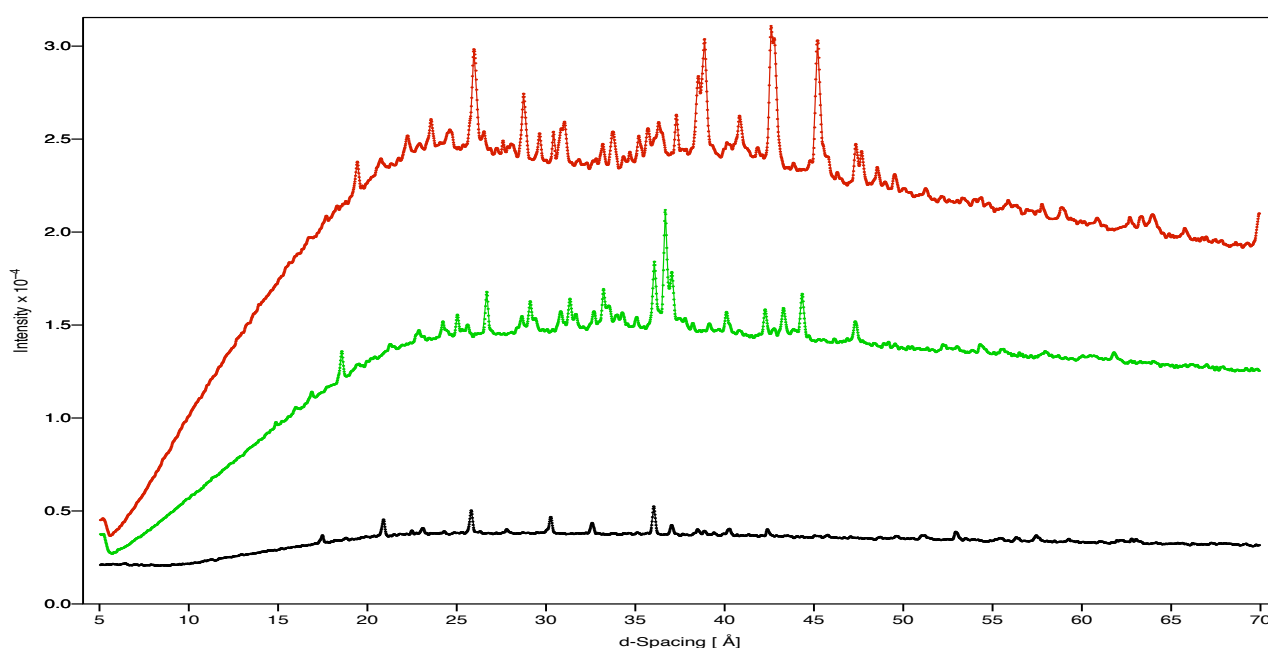
Figure 5.23 – XRD patterns of LiCoPO$_4$ (black) KCoPO$_4$ (green), and NaCoPO$_4$ (red).

5.3 Conclusion

In conclusion, it was found that synthesis the LiCoPO$_4$ analogue proved to be difficult due to the poor reproducibility of the methods discussed. It was also found that: solvent used, heating rate, the source of Cobalt ions as well as the oxidation state, played a part in the phase purity of the sample. It was discovered that the furnace used for sintering had damaged heating elements after synthesis of the materials. Therefore, it is uncertain if the desired temperature was reached during production of these materials.

However, once a phase pure sample had been synthesised it showed properties similar to that seen in literature. With a T_N of 21.8 K, similar to that observed by Ludwig *et al.*[127]

Doping the parent material with increasing Na content also proved difficult due to the potential incompatibility of the ions in the A-site of the lattice. A doping limit of 10% is hypothesised as higher % contributions showed impurity peaks and potentially impure phases ($NaCoPO_4$) becoming prevalent. T_N of the phase pure $Li_{0.9}Na_{0.1}CoPO_4$ sample measured to be 21.8 K similar to the parent material potentially showing no change in transition temperature upon doping, or no incorporation of the dopant into the material as desired.

In the future, phase pure samples at each of the doping levels will need to be synthesised (if possible) and analysed *via* PND measurements. This will provide more precise diffraction data over a potentially higher temperature range and allow one to more clearly see phase changes and lattice perturbations.

Once phase pure samples are synthesised, electrical properties need to be measured *via* polarisation electric-field loops. They have not been measured thus far due to phase purity problems as well as problems that arose with the analyse machine.

Chapter 6

Summary

In essence, the multiferroic properties of materials have been noticed to change *via* the introduction of a dopant ion. Observing and understanding these changes are key to fine-tuning materials with the ability to perform electrically and magnetically at room temperature. This can improve energy efficiency and power consumption, providing sustainable devices. Structural-property correlations seen in novel multiferroics can allow for the rational design of new materials and the experimental realisation of ferrotoroidicity.

Doping $BiFeO_3$ with Dysprosium at levels as low as 5%, one is able to see dramatic changes to domain size T_N, and T_C. The ferroelectric transition is seen to decrease in temperature whilst in contrast the antiferromagnetic transition is seen in increase slightly as a result of a lengthening of the spin cycloid propagation vector. This coupled with small domains results in the weak magnetic hysteresis observed for this material. Additionally, polar character in this material is weak (as seen by PE loops and Raman mapping) suggesting that the material is only weakly ferroelectric, and this requires further investigation. In the future, second harmonic generation is needed to observe the polarity of the material in comparison to pure BFO to see potential differences. Furthermore, improved electrical testing of the doped sample is required by increasing the pellet integrity *via* changing the synthesis method of the pellet. Using an isostatic press instead of a uniaxial press under different atmospheric conditions, i.e., under oxygen / argon instead of air to remove defects such as oxygen vacancies and to improve pellet density. Additionally, a more careful consideration of the polar displacements needs to be extracted from the PND data which was outside the scope of this thesis.

The doping observed for the rare-earth ferrites ($Dy_{1-x}Sm_xFeO_3$) produced a mixed phase solid solution suggesting that there is an incompatibility of the isovalent ions and/or structure. This could potentially be due to the discussed difference in the magnetic ordering of the two A-site cations. In the future, quenching above the T_N could allow for the successful synthesis of phase pure compositions. This would allow for facile magnetic and electronic measurements, enabling more in-depth discussions about the multiferroicity of these orthoferrites and their A-site cation doping.

$LiCoPO_4$ was successfully synthesised, however, there were clear barriers in reproducibility which need to be further investigated. It was not possible to explore ferrotoroidic domains in this material due to the limitation in laboratory based techniques. Raman mapping has been shown to be an effective way of probing ferroelectric domains in chapter 3 for Dy

doped $BiFeO_3$. Previously, polarised SHG was used to confirm ferrotoroidicity in $LiCoPO_4$. showed no obvious ferrotoroidic domains with conventional Raman mapping. It has been suggested that in order to observe ferrotoroidic domains, polarised Raman mapping is key. In the future, understanding the polymorphism of the Na analogue, $NaCoPO_4$, is necessary to isolate the pure ferrotoroidic phase. This knowledge of polymorphy can be subsequently used in identifying and isolating phase pure samples of Na doped $LiCoPO_4$. This could further lead to observing how doping can affect the ferrotoroidic nature of materials.

If ferrotoroidism is able to be achieved it can pave the way for a new range of magnetoelectric devices, primarily in data storage which can allow the facile movement of data. Secondly it could allow for less resources used in the production and manufacture of such devices by decreasing the amounts of material needed for storing large amounts of data.

References

1 C. Liu, F. Li, M. Lai-Peng and H. M. Cheng, *Adv. Mater.*, 2010, **22**, 28–62.

2 Y. Fang, L. Xiao, Z. Chen, X. Ai, Y. Cao and H. Yang, *Electrochem. Energy Rev.*, 2018, **1**, 294–323.

3 E. Sánchez-Díez, E. Ventosa, M. Guarnieri, A. Trovò, C. Flox, R. Marcilla, F. Soavi, P. Mazur, E. Aranzabe and R. Ferret, *J. Power Sources*, 2021, **481,** 228804.

4 X. Bin Li, N. K. Chen, X. P. Wang and H. B. Sun, *Adv. Funct. Mater.*, 2018, **28**, 1–21.

5 L. Solymar, D. Walsh and R. R. A. Syms, *Electrical Properties of Materials*, Oxford University Press, Ninth Edit., 2014.

6 P. Moller, *Bioscience*, 1991, **41**, 794–796.

7 D. Laertius and M. H. U. P. Cambridge, *Lives of Eminent Philosophers Volume I, Book I, Chapter I. Translated by R. D. Hicks*, 1925, 22-45.

8 J. V Stewart, *Intermediate Electromagnetic Theory*, WORLD SCIENTIFIC, 2001.

9 K. S. Tom 1915-, *Echoes from old China: life, legends, and lore of the Middle Kingdom / K.S. Tom*, Hawaii Chinese History Centre: Distributed by University of Hawaii Press, Honolulu, 1989.

10 E. Engineers, *IEEE Standard Definitions of Primary Ferroelectric Terms*, The Institute of Electrical and Electronics Engineers, New York, 1988, vol. 986.

11 R. L. Carlin, *Magnetochemistry,* Springer-Verlag, Berlin; New York, 1986.

12 E. F. Bertaut, R. Pauthenet and M. Mercier, *Phys. Lett.*, 1963, **7**, 110–111.

13 I. Dzyaloshinksii, *Phys. Status Solidi*, 1971, **46**, 763–772.

14 T. Moriya, *Phys. Rev.*, 1960, **120**, 91–98.

15 H. A. Kramers, *Physica*, 1934, **1**, 182-192.

16 P. W. Anderson, *Phys. Rev.*, 1950, **79**, 350–356.

17 S. W. Ambler, *Dr. Dobb's J.*, 2006, **31**, 64–67.

18 A. Aharoni, *Introduction to the Theory of Ferromagnetism (International Series of Monographs on Physics)*, 1996.

19 M. S. Dresselhaus, *Solid State Physics Part III.*, 2001.

20   C. Lee, J. Liu, M. H. Whangbo, H. J. Koo, R. K. Kremer and A. Simon, *Phys. Rev. B - Condens. Matter Mater. Phys.*, 2012, **86**, 1–5.

21   M. Fiebig, *J. Phys. D. Appl. Phys.*, 2005, **38**, 123-152.

22   W. C. Rontqen, *Ann. Phys.*, 1888, **35**, 264.

23   P. Curie, *J. Phys. Théorique Appliquée*, 1894, **3**, 393–415.

24   L. D. Landau Lifshits, E. M., *Electrodynamics of continuous media*, Pergamon Press, Oxford; New York, 1960.

25   H. A. Wilson, P. Trans and R. S. Lond, *Philos. Trans. R. Soc. London. Ser. A, Contain. Pap. a Math. or Phys. Character*, 1905, **204**, 121–137.

26   J. M. Hu, C. G. Duan, C. W. Nan and L. Q. Chen, *npj Comput. Mater.*, 2017, **3**, 1–20.

27   Z. H. U. Jian-Gang, *Proc. IEEE*, 2008, **96**, 1786–1798.

28   S. Fusil, V. Garcia, A. Barthélémy and M. Bibes, *Annu. Rev. Mater. Res.*, 2014, **44**, 91–116.

29   C. Chappert, A. Fert and F. N. Van Dau, *Nanosci. Technol. A Collect. Rev. from Nat. Journals*, 2009, 147–157.

30   M. Bibes, J. E. Villegas and A. Barthélèmy, *Adv. Phys.*, 2011, **60**, 5–84.

31   D. Khomskii, *J. Physics,* 2009, **2**, 20.

32   M. M. Vopson, *Crit. Rev. Solid State Mater. Sci.*, 2015, **40**, 223–250.

33   J. F. Scott, *Nat. Mater.*, 2007, **6**, 256–257.

34   M. Trassin, E. Gradauskaite, P. Meisenheimer, M. Müller and J. Heron, *Phys. Sci. Rev.*, 2021, **6**.

35   J. Gao, Z. Jiang, S. Zhang, Z. Mao, Y. Shen and Z. Chu, *Actuators*, 2021, **10**, 1–23.

36   S. Gnewuch and E. E. Rodriguez, *J. Solid State Chem.*, 2019, **271**, 175–190.

37   A. S. Zimmermann, D. Meier and M. Fiebig, *Nat. Commun.*, 2014, **5**, 2–7.

38   D. B. Litvin, *Acta Crystallogr. Sect. A Found. Crystallogr.*, 2008, **64**, 316–320.

39   P. Tolédano, M. Ackermann, L. Bohatý, P. Becker, T. Lorenz, N. Leo and M. Fiebig, *Phys. Rev. B - Condens. Matter Mater. Phys.*, 2015, **92**, 1–7.

40   N. A. Spaldin, M. Fiebig and M. Mostovoy, *J. Phys. Condens. Matter*, 2008, **20**.

41   M. De Graef, *Materials Sci.*, 2009, **1**,1–32.

42   B. A. Tavger and V. M. Zaitsev, *Appl. Gr. Theory*, 1968, **3**, 379–391.

43   H. Schmid, *J. Phys. Condens. Matter*, 2008, **20,** 434201

44   M. Senechal, *Comput. Math. with Appl.*, 1988, **16**, 545–553.

45   P. V. Pantulu and S. Radhakrishna, *Proc. Indian Acad. Sci. - Sect. A*, 1967, **66**, 107–111.

46   J. Wang, D. Khomskii, Multiferroic materials: properties, techniques, and applications, 2017.

47   H. Schmid, *Ferroelectrics*, 2001, **252**, 41–50.

48   R. C. Lennox, M. C. Price, W. Jamieson, M. Jura, A. Daoud-Aladine, C. A. Murray, C. Tang and D. C. Arnold, *J. Mater. Chem*, 2020, **1**, 3777.

49   J. Wormald, P. W, Atkins, J. S.E Holker, A. K. Holliday, *Diffraction Methods*, 1973.

50   H. H. W. Stanjek, Hyperfine Interactions, 2004, **154**, 107–119.

51   D. Kriegner, Z. Matěj, R. Kužel and V. Holý, *J. Appl. Crystallogr.*, 2015, **48**, 613–618.

52   ISIS Neutron and Muon Source, How ISIS Works, https://www.isis.stfc.ac.uk/Pages/How-ISIS-works.aspx, (accessed 13 September 2021).

53   ISIS Neutron and Muon Source, HRPD, https://www.isis.stfc.ac.uk/Pages/Hrpd.aspx, (accessed 13 September 2021).

54   C. L. Bull, A. D. Fortes, C. J. Ridley, I. G. Wood, D. P. Dobson, N. P. Funnell, A. S. Gibbs, C. M. Goodway, R. Sadykov and K. S. Knight, *High Press. Res.*, 2017, **37**, 486–494.

55   ISIS Neutron and Muon Source, WISH, https://www.isis.stfc.ac.uk/Pages/wish-science-case.pdf, (accessed 13 September 2021).

56   J. R. Carruthers, D. J. Watkin, Acta Cryst. 1979, **35**,698–699.

57   W. Clegg, *X-Ray Crystallography*, Oxford University Press, Second Edi., 2017, **73**.

58   B. H. Toby, *Powder Diffr.*, 2006, **21**, 67–70.

59   C. J. Gilmore, J. A. Kaduk and H. Schenk, Eds., *International Tables for Crystallography*, 1983, **16**.

60   J. I. Goldstein, D. E. Newbury, J. R. Michael, N. W. M. Ritchie, J. H. J. Scott and D. C. Joy, *Scanning Electron Microscopy and X-Ray Microanalysis*, 2018.

61   K. F. J. Heinrich, *Adv. X-ray Anal.*, 1963, **7**, 325–339.

62   P. Larkin, Infrared and Raman spectroscopy: principles and spectral interpretation 2011.

63   D. Cialla-May, M. Schmitt and J. Popp, *Phys. Sci. Rev.*, 2019, **4**, 1–9.

64   J. Clarke, *Proc. IEEE*, 1989, **77**, 1208–1223.

65   B. D. Josephson, *Adv. Phys.*, 1962, **14**, 419–451.

66   J. Clarke, *Sci. Am,* 1994, **271**, 46-53.

67   H. Weinstcok, *Appl. Sci.*, 1996, **329**, 1-62.

68   S. Foner, *IEEE transactions on magnetics*, 1981, **17**, 3358–3363.

69   P. A. Joy, P. S. Anil Kumar and S. K. Date, *J. Phys. Condens. Matter*, 1998, **10**, 11049–11054.

70   B. A. Strukov and A. P. Levanyuk, *Ferroelectric Phenomena in Crystals*, 1998.

71   P. Gabbott, R. Bottom, *Principles and Applications of Thermal Analysis*, 2008, 87–118.

72   M. Chiu and E. Prenner, *J. Pharm. Bioallied Sci.*, 2011, **3**, 39–59.

73   P. Gabbott, *Principles and Applications of Thermal Analysis*, 2008, 1–49.

74   L. Thansanga, A. Shukla, N. Kumar and R. N. P. Choudhary, *J. Mater. Sci. Mater. Electron.*, 2020, **31**, 10006–10017.

75   J. M. Hu, L. Q. Chen and C. W. Nan, *Adv. Mater.*, 2016, **28**, 15–39.

76   I. Sosnowska, M. Loewenhaupt, W. I. F. David and R. M. Ibberson, *Phys. B Phys. Condens. Matter*, 1992, **180**–**181**, 117–118.

77   I. Sosnowska and A. K. Zvezdin, *J. Magn. Magn. Mater.*, 1995, **140**–**144**, 167–168.

78   A. S. Poghossian, H. V. Abovian, P. B. Avakian, S. H. Mkrtchian and V. M. Haroutunian, *Sensors Actuators B. Chem.*, 1991, **4**, 545–549.

79   X. L. Yu, Y. Wang, Y. M. Hu, C. B. Cao and H. L. W. Chan, *J. Am. Ceram. Soc.*, 2009, **92**, 3105–3107.

80   S. Chakraborty and M. Pal, *New J. Chem.*, 2018, **42**, 7188–7196.

81   Glusker J.P., Lewis M., Rossi M, Journal of chemical education 1995, 72, 38.

82   R. Douani, N. Lamrani, M. Oughanem, M. Saidi, Y. Guhel, A. Chaouchi and B.

Boudart, *Sensors Actuators, A Phys.*, 2020, **307**, 111981.

83   N. V. Srihari, K. B. Vinayakumar and K. K. Nagaraja, *Coatings*, 2020, **10**, 1–19.

84   Y. Li, J. Yu, J. Li, C. Zheng, Y. Wu, Y. Zhao, M. Wang and Y. Wang, *J. Mater. Sci. Mater. Electron.*, 2011, **22**, 323–327.

85   P. Chandra Sati, M. Arora, S. Chauhan, M. Kumar and S. Chhoker, *J. Phys. Chem. Solids*, 2014, **75**, 105–108.

86   R. D. Shannon, Database of Ionic Radii, http://abulafia.mt.ic.ac.uk/shannon/ptable.php, (accessed 23 September 2021).

87   V. A. Khomchenko, D. V. Karpinsky, A. L. Kholkin, N. A. Sobolev, G. N. Kakazei, J. P. Araujo, I. O. Troyanchuk, B. F. O. Costa and J. A. Paixão, *J. Appl. Phys.*, 2010, **108**, 074109.

88   A. T. Apostolov, I. N. Apostolova, S. Trimper and J. M. Wesselinowa, *Solid State Commun.*, 2019, **300**, 113692.

89   S. Zhang, L. Wang, Y. Chen, D. Wang, Y. Yao and Y. Ma, *J. Appl. Phys.*, 2012, **111**, 074105.

90   A. Kumar, P. Sharma and D. Varshney, *J. Ceram.*, 2015, **2015**, 1–8.

91   J. F. Scott, *J. Phys. Condens. Matter*, 2007, **20**, 21001.

92   P. Barone and S. Picozzi, *Comptes Rendus Phys.*, 2015, **1**, 1–10.

93   R. Palai, R. S. Katiyar, H. Schmid, P. Tissot, S. J. Clark, J. Robertson, S. A. T. Redfern, G. Catalan and J. F. Scott, *Phys. Rev. B - Condens. Matter Mater. Phys.*, 2008, **77**, 1–11.

94   W. M. Zhu, L. W. Su, Z. G. Ye and W. Ren, *Appl. Phys. Lett.*, 2009, **94**, 1–4.

95   T. Karthik, D. Rao, A. Srinivas and S. Asthana, *J. Condensed Matter,* 2012, 1206.5606.

96   P. Uniyal and K. L. Yadav, 2009, **012205**, 7–11.

97   J. Bielecki, P. Svedlindh, D. T. Tibebu, S. Cai, S. G. Eriksson, L. Börjesson and C. S. Knee, *Phys. Rev. B - Condens. Matter Mater. Phys.*, 2012, **86**, 16–19.

98   M. S. Bozgeyik, R. K. Katiyar and R. S. Katiyar, *J. Electroceramics*, 2018, **40**, 247–256.

99   S. Gupta, M. Tomar and V. Gupta, *J. Exp. Nanosci.*, 2013, **8**, 261–266.

100 J. Hlinka, J. Pokorny, S. Karimi and I. M. Reaney, *Phys. Rev. B - Condens. Matter Mater. Phys.*, 2011, **83**, 4–7.

101 R. Jarrier, X. Marti, J. Herrero-Albillos, P. Ferrer, R. Haumont, P. Gemeiner, G. Geneste, P. Berthet, T. Schülli, P. Cevc, R. Blinc, S. S. Wong, T. J. Park, M. Alexe, M. A. Carpenter, J. F. Scott, G. Catalan and B. Dkhil, *Phys. Rev. B - Condens. Matter Mater. Phys.*, 2012, **85**, 1–10.

102 E. Haye, F. Capon, S. Barrat, P. Boulet, E. Andre, C. Carteret and S. Bruyere, *J. Alloys Compd.*, 2016, **657**, 631–638.

103 S. Cao, H. Zhao, B. Kang, J. Zhang and W. Ren, *Sci. Rep.*, 2014, **4**, 5.

104 T. Yamaguchi and K. Tsushima, *Phys. Rev. B*, 1973, **8**, 5187–5198.

105 C. Y. Kuo, Y. Drees, M. T. Fernández-Díaz, L. Zhao, L. Vasylechko, D. Sheptyakov, A. M. T. Bell, T. W. Pi, H. J. Lin, M. K. Wu, E. Pellegrin, S. M. Valvidares, Z. W. Li, P. Adler, A. Todorova, R. Küchler, A. Steppke, L. H. Tjeng, Z. Hu and A. C. Komarek, *Phys. Rev. Lett.*, 2014, **113**, 1–5.

106 R. L. White, *J. Appl. Phys.*, 1969, **40**, 1061–1069.

107 J. H. Lee, Y. K. Jeong, J. H. Park, M. A. Oak, H. M. Jang, J. Y. Son and J. F. Scott, *Phys. Rev. Lett.*, 2011, **107**, 1–5.

108 H. J. Zhao, Y. Yang, W. Ren, A. J. Mao, X. M. Chen and L. Bellaiche, *J. Phys. Condens. Matter*, 2014, **26**, 8.

109 Y. Tokunaga, S. Iguchi, T. Arima and Y. Tokura, *Phys. Rev. Lett.*, 2008, **101**, 3–6.

110 A. Panchwanee, V. Raghavendra Reddy, A. Gupta, R. J. Choudhary, D. M. Phase and V. Ganesan, *Thin Solid Films*, 2019, **669**, 301–305.

111 R. Ramesh and N. A. Spaldin, *Nanosci. Technol. A Collect. Rev. from Nat. Journals*, 2009, **3**, 20–28.

112 F. Ahmad Mir, J. A. Banday, C. Chong, P. Dahoo and F. A. Najar, *Eur. Phys. J. Appl. Phys.*, 2013, **61**, 10302.

113 N. Keller, J. Mistrík, Š. Višňovský, D. S. Schmool, Y. Dumont, P. Renaudin, M. Guyot and R. Krishnan, *Eur. Phys. J. B*, 2001, **21**, 67–73.

114 S. T. Shen and H. S. Weng, *Ind. Eng. Chem. Res.*, 1998, **37**, 2654–2661.

115 E. Traversa, S. Matsushima, G. Okada, Y. Sadaoka, Y. Sakai and K. Watanabe, *Elsevier Sci.*, 1995, **25**, 661–664.

116   H. Xu, X. Hu and L. Zhang, *Cryst. Growth Des.*, 2008, **8**, 2061–2065.

117   S. Gnewuch and E. E. Rodriguez, *Inorg. Chem.*, 2020, **59**, 5883–5895.

118   M. C. Weber, M. Guennou, H. J. Zhao, J. Íñiguez, R. Vilarinho, A. Almeida, J. A. Moreira and J. Kreisel, *Phys. Rev. B*, 2016, **94**, 1–8.

119   B. Rajeswaran, D. Sanyal, M. Chakrabarti, Y. Sundarayya, A. Sundaresan and C. N. R. Rao, *Epl*, 2013, **101**, 2–7.

120   M. C. Weber, M. Guennou, H. J. Zhao, J. Íñiguez, R. Vilarinho, A. Almeida, J. A. Moreira and J. Kreisel, *Phys. Rev. B*, 2016, **94**, 1–9.

121   H. C. Gupta, M. K. Singh and L. M. Tiwari, *J. Phys. Condensed matter* 2002, **3**, 67–70.

122   A. Panchwanee, V. R. Reddy and A. Gupta, *J. Magnetism and Magnetic Matter.*, 2018, **448**, 38–42.

123   W. Zhao, S. Cao, R. Huang, Y. Cao, K. Xu, B. Kang, J. Zhang and W. Ren, *Phys. Rev. B - Condense. Matter. Phys.*, 2015, **91**, 1–7.

124   J. P. Rivera, *Ferroelectrics*, 1994, **161**, 37–41.

125   A. Planes, T. Castán and A. Saxena, *Multiferroic Materials*, 2014, **1**, 9-22.

126   C. A. J. Fisher, V. M. H. Prieto and M. S. Islam, 2008, **4**, 5907–5915.

127   A. Szewczyk, M. U. Gutowska, J. Wieckowski, A. Wisniewski, R. Puzniak, R. Diduszko, Y. Kharchenko, M. F. Kharchenko and H. Schmid, *Phys. Rev. B - Condens. Matter Materials Phys.*, 2011, 1-7

128   M. Zhang, N. Garcia-Araez and A. L. Hector, *J. Mater. Chem. A*, 2018, **6**, 14483–14517.

129   C. H. Rhee, S. J. Kim and C. S. Kim, *J. Korean Phys. Soc.*, 2010, **56**, 611–614.

130   J. Ludwig and T. Nilges, *J. Power Sources*, 2018, **382**, 101–115.

131   A. Chiring, M. Mazumder, S. K. Pati, C. S. Johnson and P. Senguttuvan, *J. Solid State Chem.*, 2021, **293**, 121766.

132   E. Markevich, R. Sharabi, O. Haik, V. Borgel, G. Salitra, D. Aurbach, G. Semrau, M. A. Schmidt, N. Schall and C. Stinner, *J. Power Sources*, 2011, **196**, 6433–6439.

133   Materials Data On LiCoPO4 by Materials Project, https://www.osti.gov/dataexplorer/biblio/dataset/1193653, (accessed 16 October

2021).

134   S. Gnewuch and E. E. Rodriguez, Inorg. Chem. 2020, **59**, 5883−5895, 1–10.

135   Materials Data On NaCoPO4 by Materials Project,
https://www.osti.gov/biblio/1194874, (accessed 16 October 2021).

136   R. Hammond and J. Barbier, *Acta Crystallogr. Sect. B Struct. Sci.*, 1996, **52**, 440–449.

Appendix

Appendix 3.1 – Table showing the collated data collected *via* the WISH diffractometer. With the errors shown in parentheses

Temp (K)	Cell volume Å³	Lattice Parameters Å		Propagation Vector	Displacement parameters			Magnetic Moment emu/g	Bond length		Bond angle
		A	C	K	Bi	Fe	O		Fe-O	Fe-O	Fe-O-Fe
5	375.061	5.5875(808)	13.872(368)	0.00395(636)	0.14(47)	0.35(46)	0.56(42)	4.13(26)	1.966(2)	2.103(3)	154.34(14)
20	375.053	5.5874(803)	13.872(366)	0.00398(660)	0.17(47)	0.32(45)	0.54(41)	4.13(26)	1.964(2)	2.105(3)	154.47(13)
30	375.06	5.5875(803)	13.872(367)	0.00399(664)	0.17(47)	0.32(45)	0.54(41)	4.12(26)	1.964(2)	2.105(3)	154.51(13)
40	375.074	5.5875(801)	13.872(366)	0.00399(663)	0.19(47)	0.30(44)	0.53(41)	4.12(26)	1.964(2)	2.104(3)	154.54(13)
50	375.093	5.5876(810)	13.873(369)	0.00399(654)	0.21(48)	0.34(46)	0.55(42)	4.10(26)	1.964(2)	2.104(3)	154.57(13)
60	375.124	5.5877(811)	13.873(369)	0.00400(650)	0.20(49)	0.35(46)	0.56(43)	4.11(26)	1.965(2)	2.104(3)	154.56(13)
70	375.158	5.5878(807)	13.874(368)	0.00398(685)	0.25(48)	0.34(45)	0.56(42)	4.10(26)	1.965(2)	2.104(3)	154.55(13)
80	375.198	5.5880(806)	13.875(367)	0.00398(689)	0.25(48)	0.34(45)	0.55(42)	4.09(26)	1.964(2)	2.105(3)	154.53(13)
90	375.246	5.5882(808)	13.876(368)	0.00397(681)	0.27(49)	0.34(45)	0.57(42)	4.10(26)	1.964(2)	2.105(3)	154.62(13)
100	375.302	5.5884(809)	13.877(369)	0.00398(674)	0.28(49)	0.34(45)	0.58(42)	4.09(26)	1.964(2)	2.105(3)	154.61(13)
110	375.36	5.5886(806)	13.877(367)	0.00397(679)	0.30(49)	0.36(45)	0.58(42)	4.08(26)	1.965(2)	2.104(3)	154.61(13)
120	375.414	5.5888(809)	13.878(369)	0.00396(686)	0.32(49)	0.37(45)	0.59(42)	4.06(26)	1.965(2)	2.104(3)	154.66(13)
130	375.484	5.5891(811)	13.880(369)	0.00397(687)	0.34(50)	0.38(45)	0.60(43)	4.04(26)	1.964(2)	2.106(3)	154.62(13)
140	375.554	5.5894(812)	13.881(369)	0.00396(694)	0.37(50)	0.40(46)	0.64(43)	4.05(26)	1.964(2)	2.106(3)	154.66(13)
150	375.638	5.5897(811)	13.882(369)	0.00396(683)	0.38(51)	0.38(45)	0.62(43)	4.03(26)	1.964(2)	2.106(3)	154.66(13)
160	375.712	5.5900(823)	13.884(374)	0.00395(679)	0.39(52)	0.41(47)	0.66(45)	4.01(26)	1.964(2)	2.106(3)	154.71(13)
170	375.783	5.5903(819)	13.885(373)	0.00392(687)	0.41(52)	0.41(46)	0.66(44)	4.00(26)	1.965(2)	2.105(3)	154.71(13)
180	375.872	5.5907(819)	13.886(372)	0.00391(704)	0.45(52)	0.40(46)	0.68(44)	3.98(26)	1.965(2)	2.105(3)	154.76(13)
190	375.955	5.5910(821)	13.888(373)	0.00390(703)	0.45(52)	0.42(46)	0.69(45)	3.95(26)	1.964(2)	2.106(3)	154.77(13)
200	376.04	5.5913(830)	13.889(377)	0.00392(710)	0.48(53)	0.42(47)	0.72(45)	3.93(27)	1.965(2)	2.105(3)	154.79(13)
210	376.129	5.5917(829)	13.891(376)	0.00390(714)	0.51(53)	0.46(47)	0.75(46)	3.93(27)	1.964(2)	2.107(3)	154.77(13)
220	376.221	5.5921(828)	13.892(375)	0.00389(720)	0.50(53)	0.43(47)	0.73(45)	3.90(27)	1.966(2)	2.104(3)	154.85(13)
230	376.314	5.5925(827)	13.893(375)	0.00389(729)	0.55(54)	0.47(47)	0.76(46)	3.88(27)	1.965(2)	2.106(3)	154.84(13)
240	376.411	5.5929(836)	13.895(379)	0.00387(737)	0.54(54)	0.48(48)	0.78(47)	3.86(27)	1.965(2)	2.107(3)	154.84(13)
250	376.517	5.5933(836)	13.897(379)	0.00389(733)	0.56(55)	0.48(48)	0.80(47)	3.83(27)	1.964(2)	2.108(3)	154.86(13)
260	376.608	5.5937(840)	13.898(381)	0.00387(732)	0.60(55)	0.49(48)	0.82(47)	3.81(27)	1.965(2)	2.106(3)	154.90(13)
270	376.707	5.5941(837)	13.900(379)	0.00384(734)	0.59(55)	0.51(47)	0.82(47)	3.77(27)	1.965(2)	2.107(3)	154.89(13)
280	376.819	5.5946(838)	13.901(379)	0.00386(738)	0.62(56)	0.53(48)	0.87(48)	3.74(27)	1.966(2)	2.105(3)	154.97(13)
290	376.918	5.5951(849)	13.903(384)	0.00386(761)	0.65(57)	0.52(48)	0.87(49)	3.71(27)	1.966(2)	2.106(3)	154.98(13)
300	377.034	5.5956(847)	13.905(383)	0.00383(763)	0.68(57)	0.52(48)	0.90(49)	3.68(27)	1.966(2)	2.107(3)	154.99(13)
323	377.112	5.5959(856)	13.906(386)	0.00381(762)	0.70(59)	0.56(50)	0.95(51)	3.65(27)	1.966(3)	2.106(3)	155.02(13)
333	377.139	5.5960(855)	13.906(386)	0.00383(754)	0.69(59)	0.55(50)	0.92(50)	3.65(27)	1.966(3)	2.107(3)	154.92(13)
343	377.188	5.5963(860)	13.907(389)	0.00379(781)	0.70(59)	0.55(50)	0.92(51)	3.63(27)	1.967(3)	2.106(3)	155.02(14)
353	377.255	5.5965(863)	13.908(390)	0.00379(771)	0.72(59)	0.56(50)	0.97(51)	3.61(27)	1.967(3)	2.105(3)	155.05(14)

363	377.383	5.5971(869)	13.910(392)	0.00376(787)	0.73(60)	0.59(51)	0.98(52)	3.57(27)	1.965(3) 2.108(3) 155.06(14)
373	377.527	5.5977(869)	13.912(392)	0.00378(793)	0.75(60)	0.60(51)	1.02(53)	3.54(28)	1.967(3) 2.107(3) 155.04(14)
383	377.689	5.5984(881)	13.915(398)	0.00375(818)	0.81(62)	0.60(54)	1.03(54)	3.47(28)	1.968(3) 2.106(3) 155.10(15)
393	377.812	5.5990(884)	13.916(398)	0.00373(813)	0.82(63)	0.61(52)	1.06(54)	3.43(28)	1.968(3) 2.107(3) 155.14(15)
403	377.93	5.5995(876)	13.918(395)	0.00371(850)	0.84(62)	0.64(52)	1.08(54)	3.39(28)	1.967(3) 2.107(3) 155.12(15)
413	378.02	5.5999(886)	13.920(399)	0.00371(860)	0.88(63)	0.64(52)	1.10(55)	3.36(28)	1.967(3) 2.109(3) 155.10(15)
423	378.154	5.6005(891)	13.921(401)	0.00367(890)	0.87(64)	0.65(53)	1.11(55)	3.32(29)	1.969(3) 2.106(3) 155.21(15)
433	378.314	5.6012(868)	13.924(397)	0.00366(868)	0.90(64)	0.68(53)	1.15(56)	3.26(28)	1.969(3) 2.107(3) 155.21(15)
443	378.402	5.6016(891)	13.925(401)	0.00365(896)	0.93(64)	0.68(53)	1.17(56)	3.23(29)	1.966(3) 2.109(3) 155.22(15)
453	378.52	5.6021(897)	13.927(403)	0.00368(897)	0.95(65)	0.69(54)	1.19(57)	3.18(29)	1.967(3) 2.109(3) 155.23(15)
463	378.616	5.6026(897)	13.928(403)	0.00366(931)	0.96(65)	0.71(54)	1.20(57)	3.14(29)	1.968(3) 2.108(3) 155.28(15)
473	378.72	5.6030(903)	13.930(406)	0.00360(956)	1.01(67)	0.70(54)	1.24(58)	3.11(29)	1.969(3) 2.108(3) 155.26(15)
483	378.833	5.6035(910)	13.931(406)	0.0036(102)	1.01(69)	0.71(56)	1.23(60)	3.06(31)	1.969(3) 2.108(3) 155.24(15)
493	378.924	5.6039(913)	13.933(408)	0.0036(101)	1.02(70)	0.70(57)	1.20(60)	3.02(31)	1.970(3) 2.108(3) 155.24(15)
503	379.025	5.6044(924)	13.934(413)	0.0036(106)	1.02(72)	0.72(58)	1.22(61)	2.97(31)	1.969(3) 2.108(3) 155.34(17)
513	379.15	5.6049(933)	13.936(415)	0.00348(792)	1.05(72)	0.72(59)	1.27(63)	2.94(31)	1.970(3) 2.108(3) 155.36(17)
523	379.231	5.6053(932)	13.937(415)	0.00347(810)	1.09(73)	0.74(59)	1.30(64)	2.90(31)	1.969(3) 2.109(4) 155.31(17)
533	379.338	5.6058(941)	13.939(418)	0.00345(822)	1.08(74)	0.77(60)	1.32(65)	2.84(31)	1.971(3) 2.108(4) 155.34(17)
543	379.447	5.6063(941)	13.940(419)	0.00343(842)	1.11(74)	0.78(60)	1.33(65)	2.79(31)	1.971(3) 2.107(4) 155.41(17)
553	379.541	5.6067(946)	13.942(422)	0.0035(118)	1.12(79)	0.79(60)	1.36(65)	2.74(33)	1.970(3) 2.108(4) 155.43(17)
563	379.623	5.6071(953)	13.943(425)	0.0035(123)	1.13(75)	0.77(61)	1.36(66)	2.69(33)	1.971(3) 2.108(4) 155.39(17)
573	379.704	5.6074(958)	13.944(427)	0.0035(128)	1.13(76)	0.80(62)	1.38(67)	2.66(34)	1.972(3) 2.107(4) 155.43(18)
583	379.782	5.6078(971)	13.945(434)	0.0035(130)	1.17(77)	0.76(61)	1.38(67)	2.60(34)	1.971(3) 2.109(4) 155.36(18)
593	379.859	5.6081(977)	13.946(435)	0.0035(131)	1.15(77)	0.81(68)	1.40(68)	2.56(35)	1.970(3) 2.109(4) 155.43(18)
603	379.952	5.6085(976)	13.948(435)	0.0035(136)	1.22(83)	0.83(63)	1.44(69)	2.51(35)	1.971(3) 2.109(4) 155.51(18)
613	380.05	5.6090(979)	13.949(438)	0.0034(140)	1.24(79)	0.82(63)	1.47(69)	2.35(35)	1.972(3) 2.107(4) 155.48(18)
623	380.177	5.6096(996)	13.951(443)	0.0033(108)	1.23(84)	0.84(65)	1.48(71)	2.40(34)	1.972(3) 2.108(4) 155.52(18)
633	380.318	5.6101(100)	13.953(447)	0.0034(161)	1.27(82)	0.86(66)	1.53(72)	2.30(37)	1.973(4) 2.108(4) 155.53(19)
643	380.493	5.611(103)	13.955(457)	0.0033(125)	1.30(85)	0.88(68)	1.54(74)	2.18(36)	1.972(4) 2.109(4) 155.55(19)
653	380.643	5.612(104)	13.957(461)	0.0033(141)	1.30(85)	0.88(69)	1.58(75)	2.07(38)	1.972(4) 2.109(4) 155.60(19)
663	380.784	5.612(105)	13.959(467)	0.0033(140)	1.38(88)	0.92(70)	1.64(77)	1.95(39)	1.973(4) 2.109(4) 155.61(19)
673	380.916	5.613(106)	13.961(473)	0.0033(228)	1.40(89)	0.95(72)	1.68(78)	1.91(44)	1.974(4) 2.108(4) 155.66(20)
683	381.123	5.614(109)	13.964(484)	0.0032(167)	1.43(92)	0.97(74)	1.71(80)	1.71(80)	1.974(4) 2.107(4) 155.72(20)
693	381.265	5.614(110)	13.964(488)	0.0032(232)	1.51(94)	1.01(75)	1.79(82)	1.79(81)	1.975(4) 2.108(4) 155.72(20)
703	381.379	5.615(111)	13.968(493)	0.0032(431)	1.49(94)	1.00(76)	1.79(82)	1.11(63)	1.976(4) 2.107(4) 155.73(20)
718	381.527	5.616(113)	13.970(502)	0.003(154)	1.59(98)	1.02(77)	1.89(84)	0.7(100)	1.976(4) 2.107(4) 155.73(20)

Dy-BFO 20K
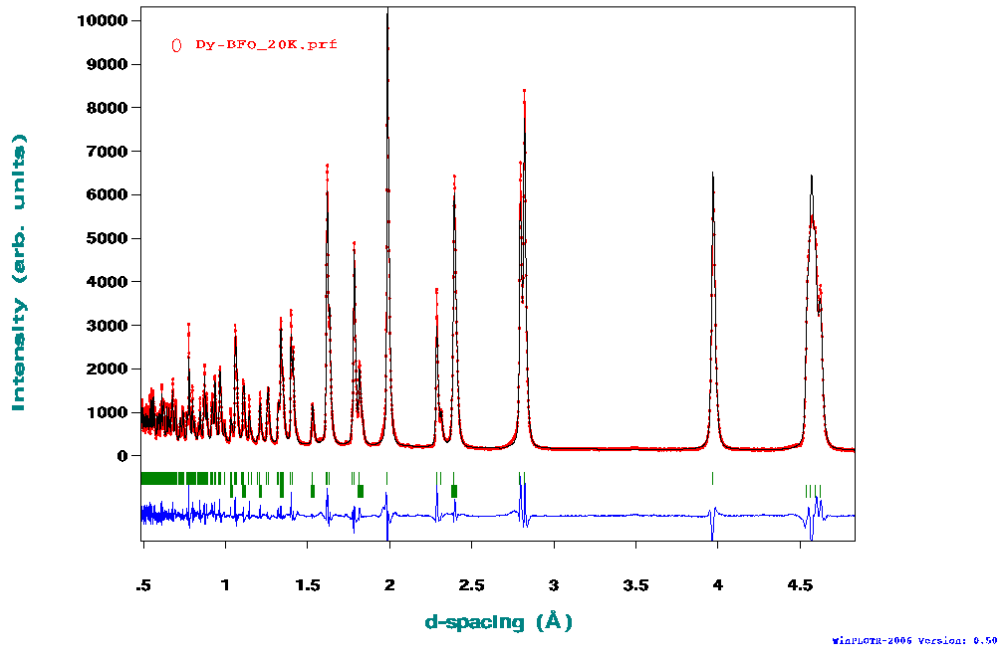
Appendix 3.3 – Rietveld refined WISH diffraction pattern of Dy-BFO at 20 K shown in d-spacing

Dy-BFO 30K
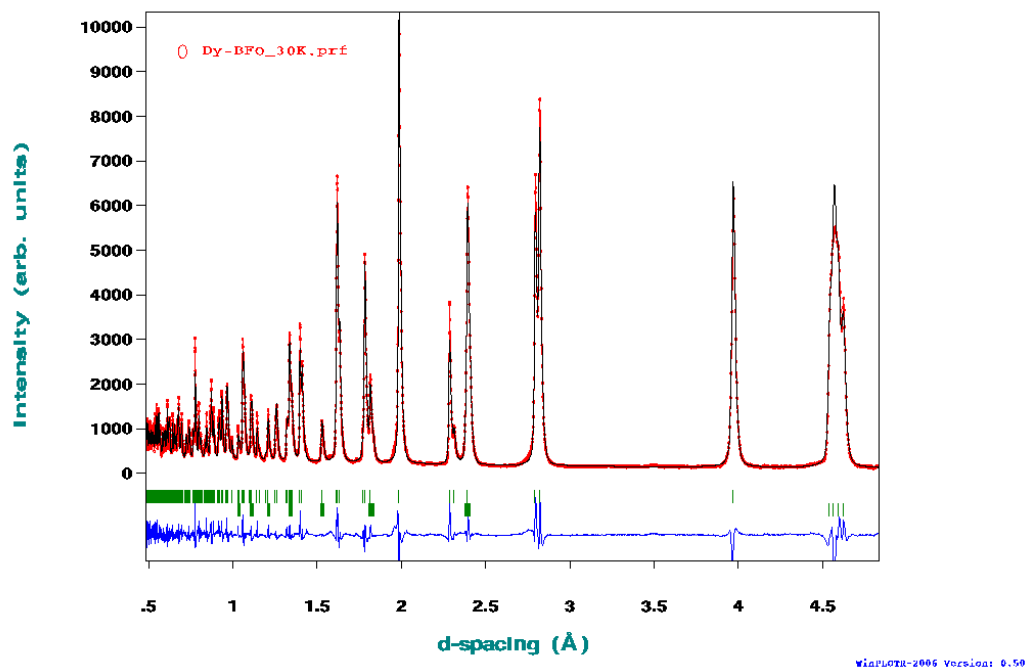
Appendix 3.4 – Rietveld refined WISH diffraction pattern of Dy-BFO at 30 K shown in d-spacing

Dy-BFO 40K
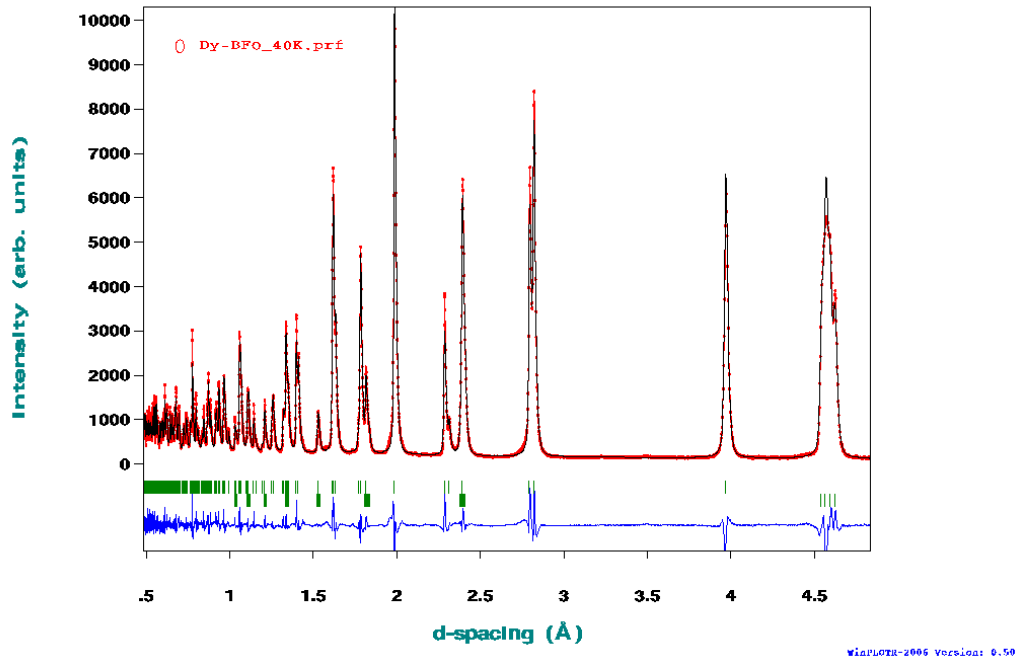
Appendix 3.5 – Rietveld refined WISH diffraction pattern of Dy-BFO at 40 K shown in d-spacing

Dy-BFO 50K
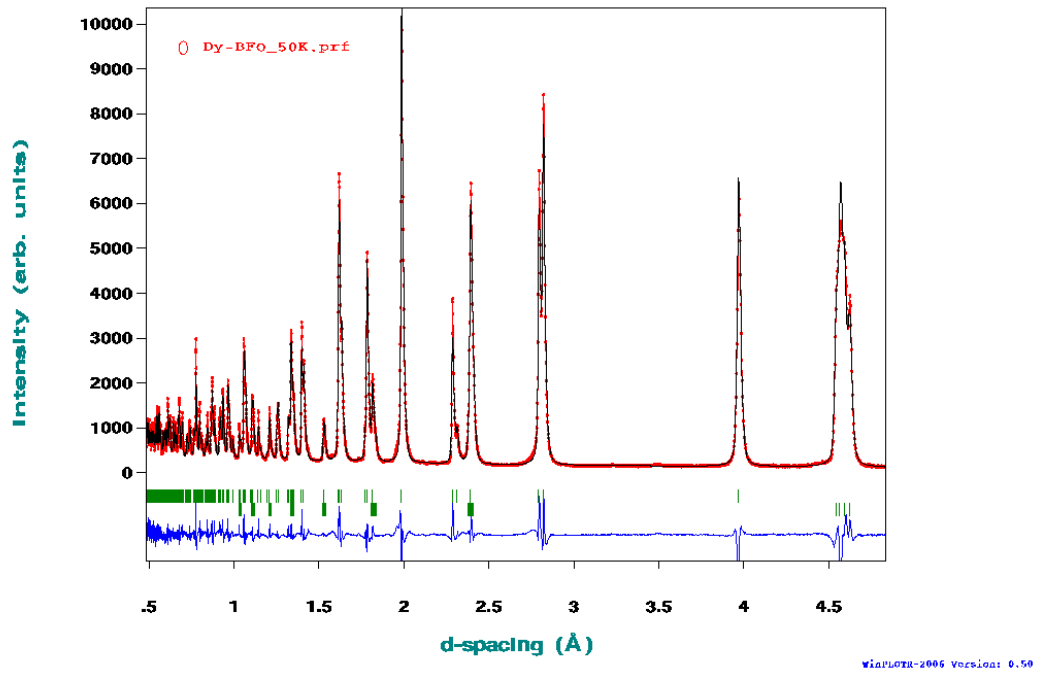
Appendix 3.6 – Rietveld refined WISH diffraction pattern of Dy-BFO at 50 K shown in d-spacing

Dy-BFO 60K
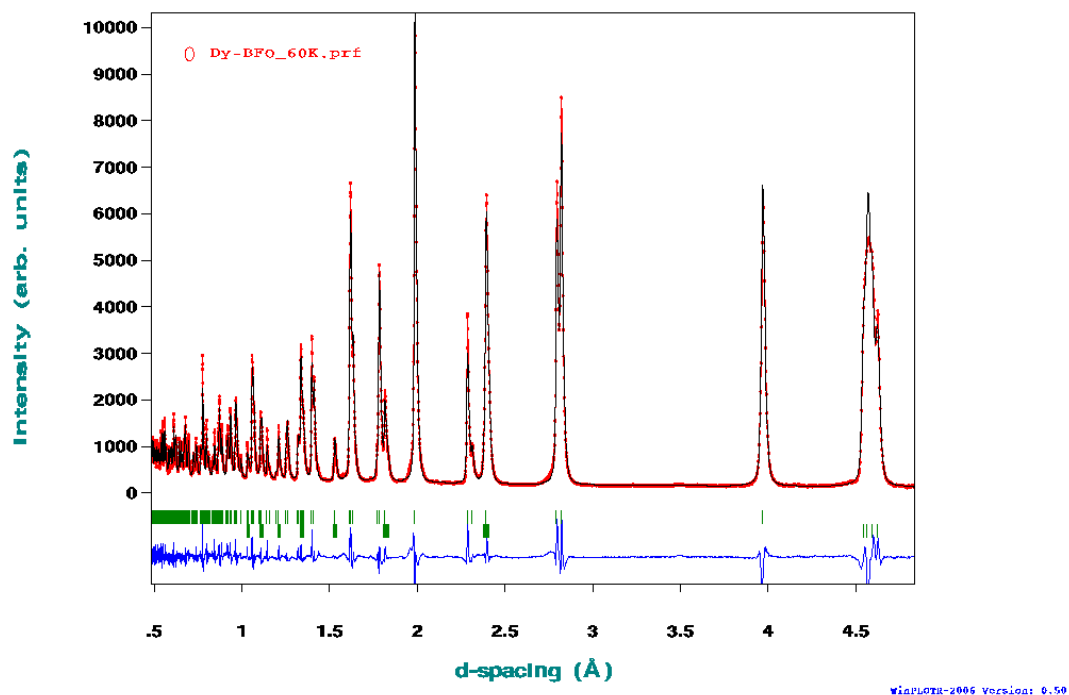
Appendix 3.7 – Rietveld refined WISH diffraction pattern of Dy-BFO at 60 K shown in d-spacing

Dy-BFO 70K
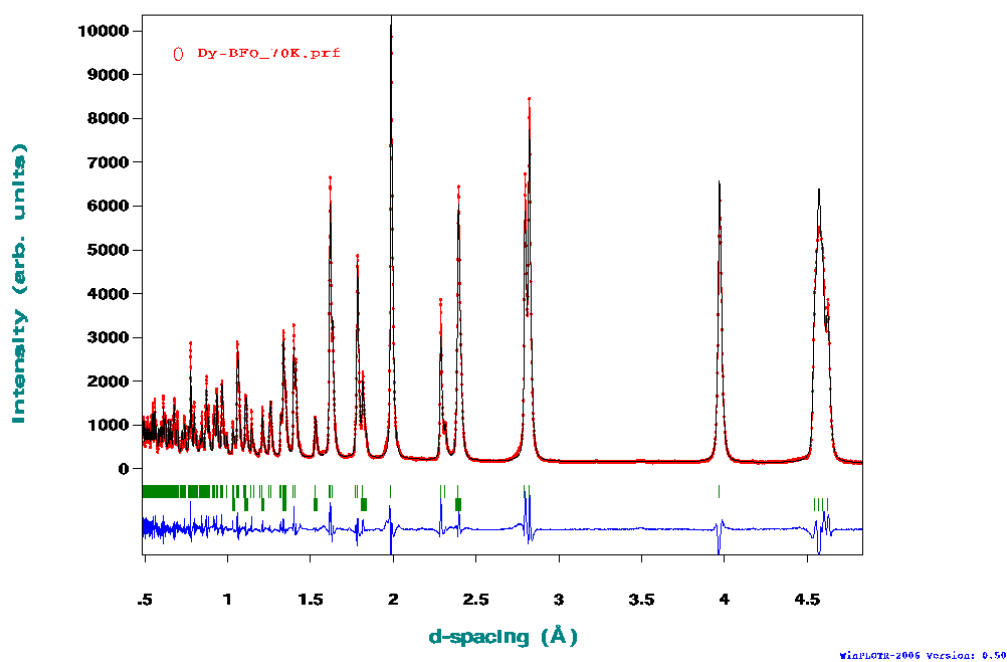
Appendix 3.8 – Rietveld refined WISH diffraction pattern of Dy-BFO at 70 K shown in d-spacing
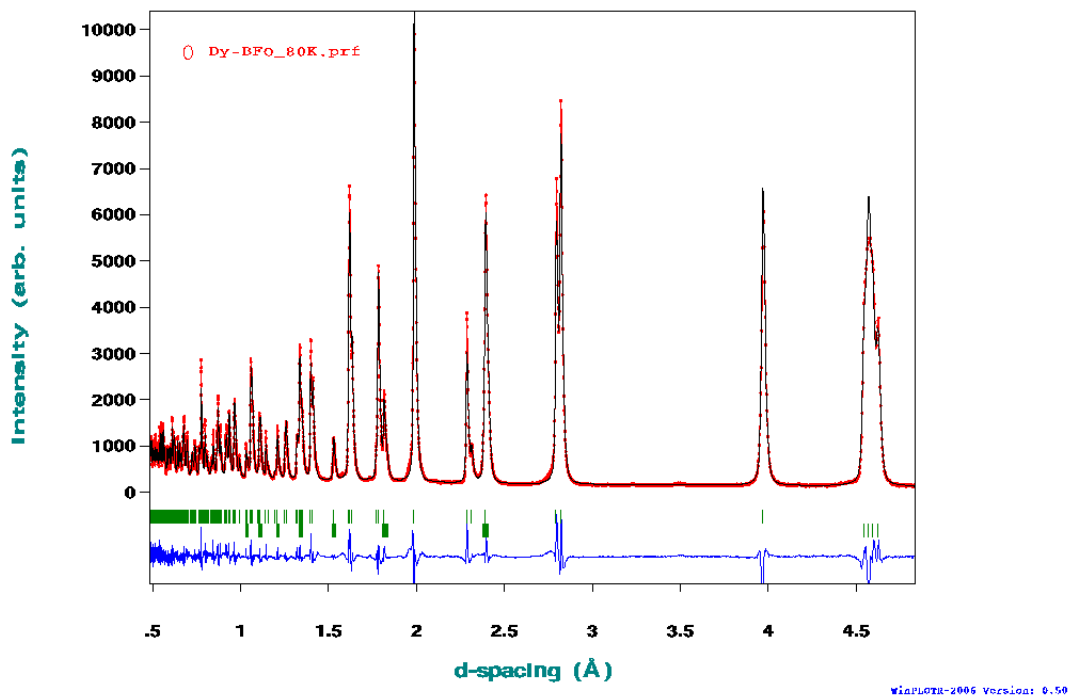
Appendix 3.9 – Rietveld refined WISH diffraction pattern of Dy-BFO at 80 K shown in d-spacing
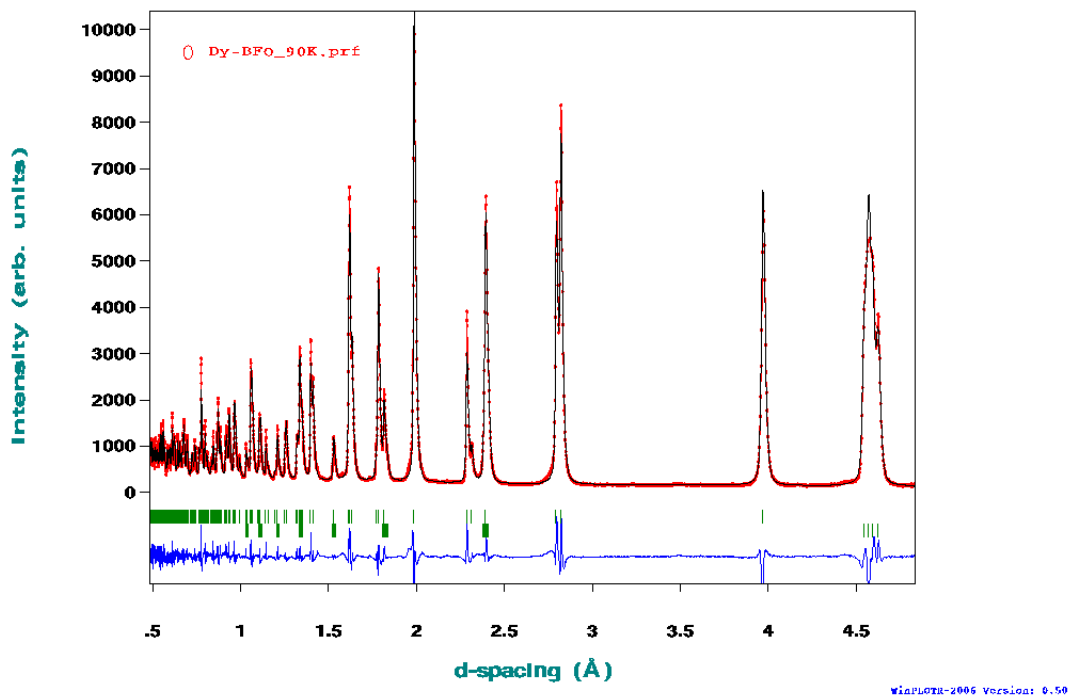
Appendix 3.10 – Rietveld refined WISH diffraction pattern of Dy-BFO at 90 K shown in d-spacing

Dy-BFO 100K
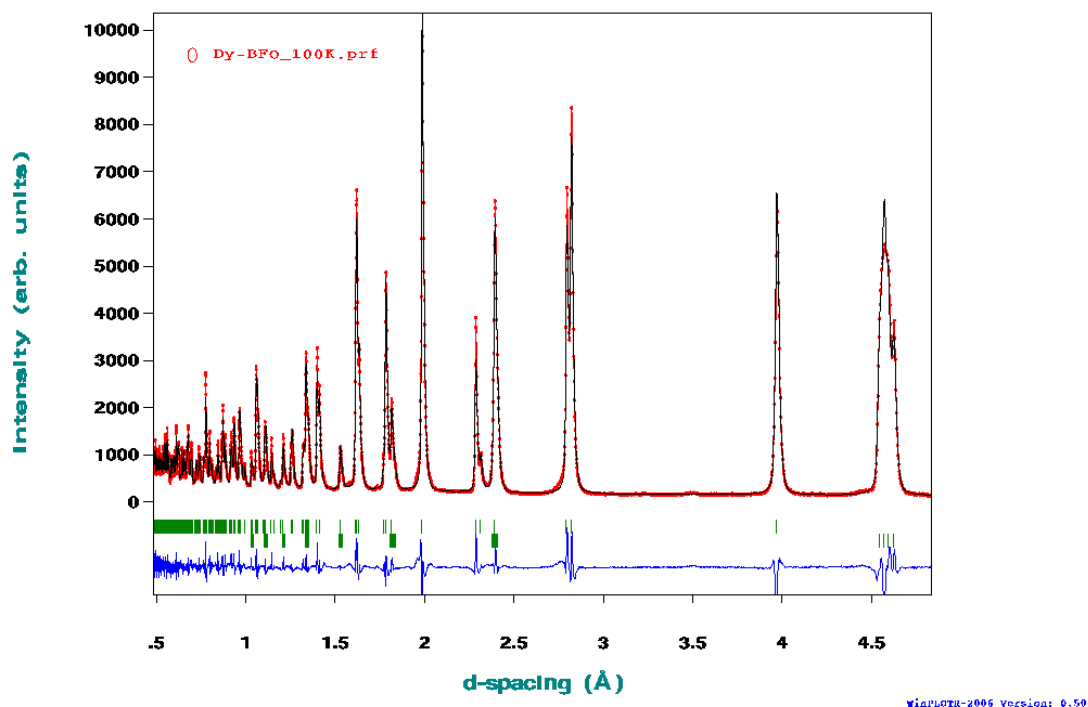
Appendix 3.11 – Rietveld refined WISH diffraction pattern of Dy-BFO at 100 K shown in d-spacing

Dy-BFO 110K
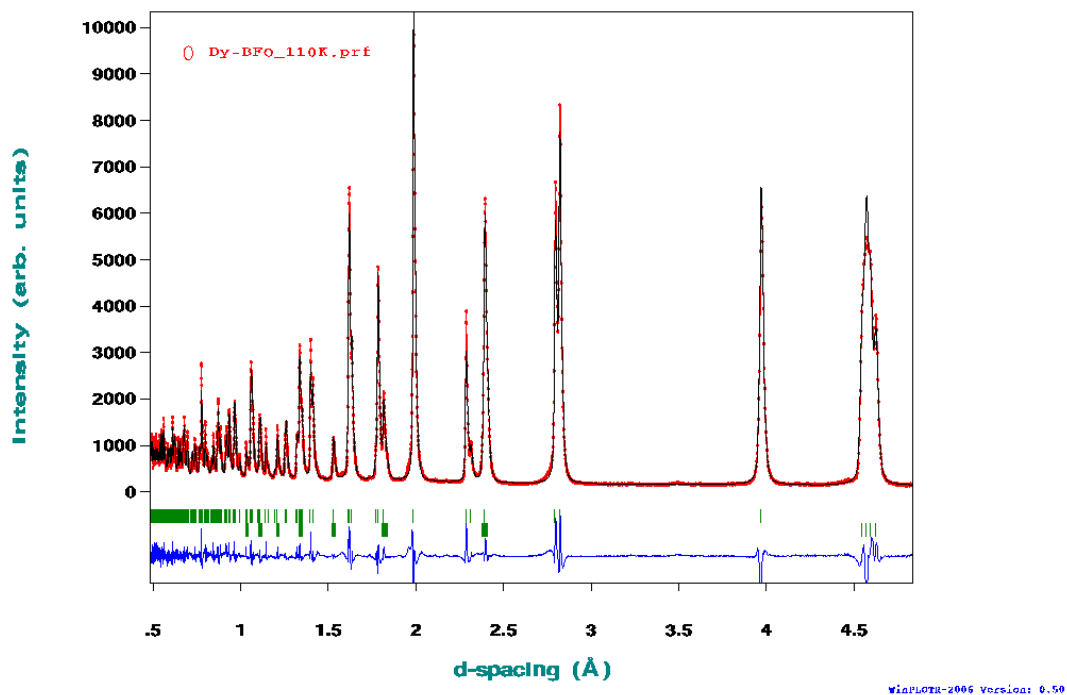
Appendix 3.12 – Rietveld refined WISH diffraction pattern of Dy-BFO at 110 K shown in d-spacing

Dy-BFO 120K
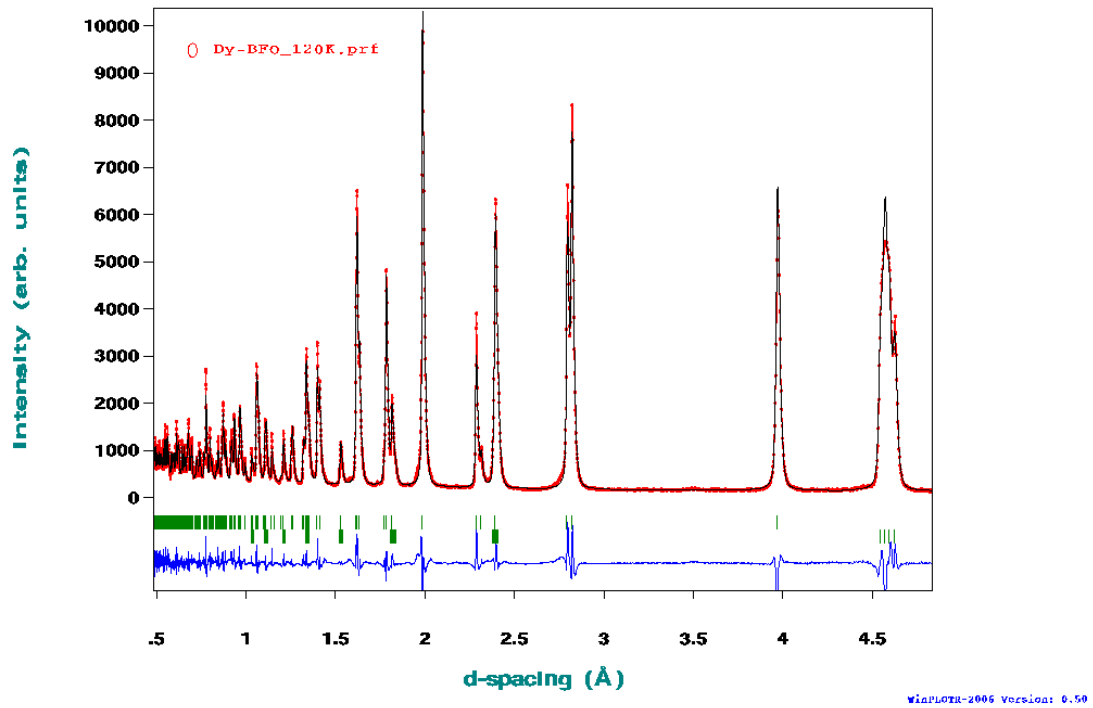
Appendix 3.13 – Rietveld refined WISH diffraction pattern of Dy-BFO at 120 K shown in d-spacing

Dy-BFO 130K
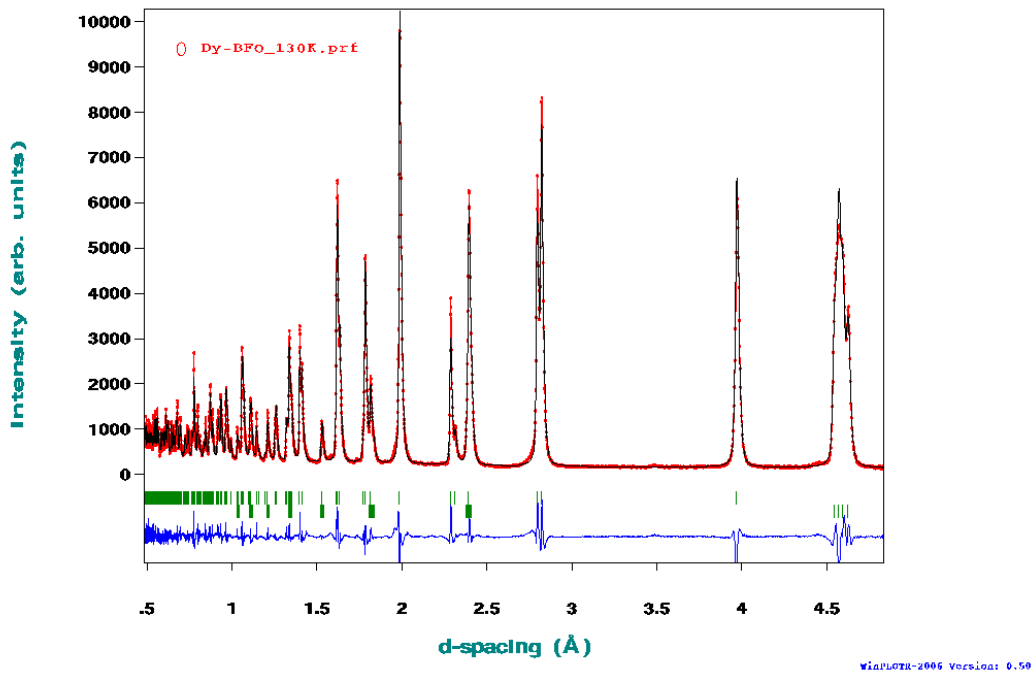
Appendix 3.14 – Rietveld refined WISH diffraction pattern of Dy-BFO at 130 K shown in d-spacing

Dy-BFO 140K
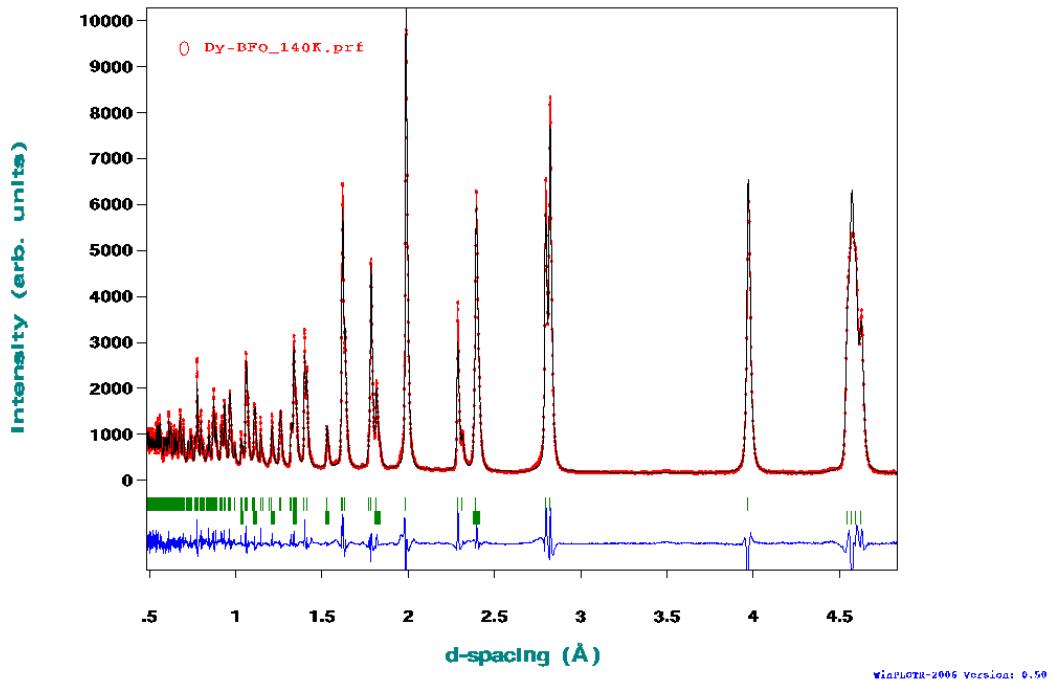
Appendix 3.15 – Rietveld refined WISH diffraction pattern of Dy-BFO at 140 K shown in d-spacing

Dy-BFO 150K
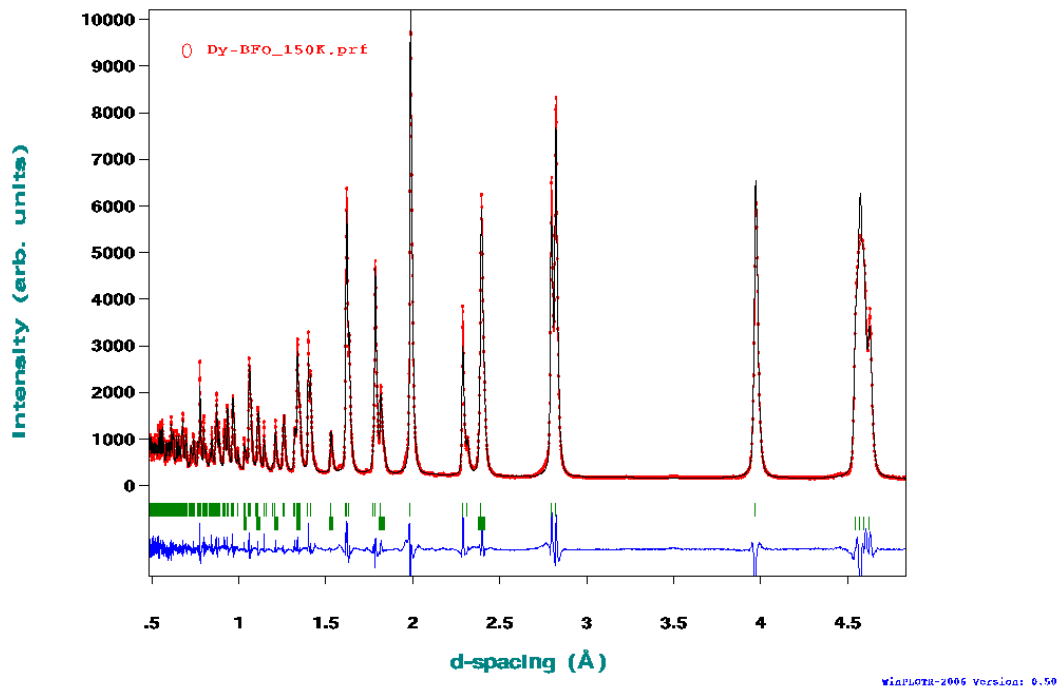
Appendix 3.16 – Rietveld refined WISH diffraction pattern of Dy-BFO at 150 K shown in d-spacing

Dy-BFO 160K
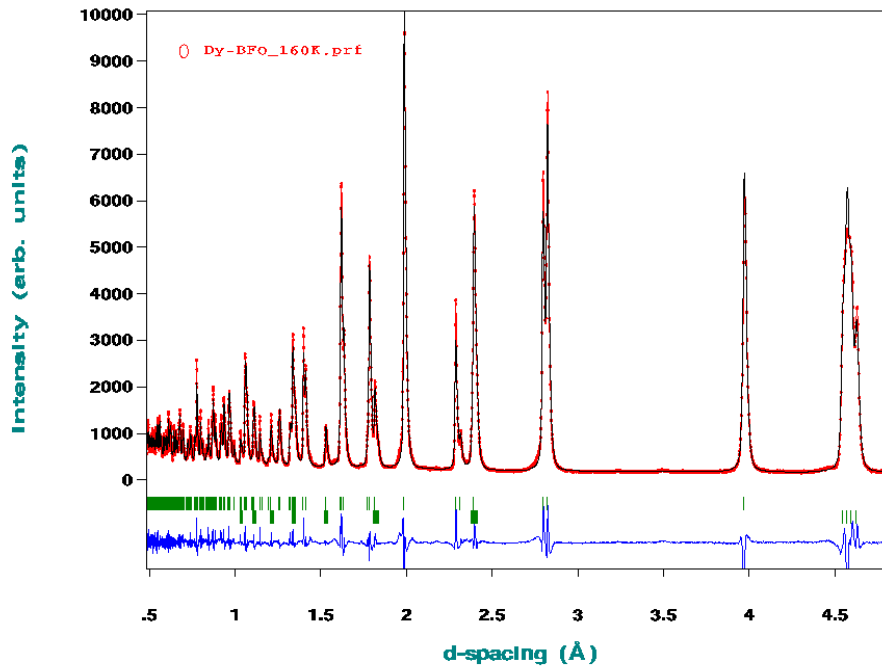
Appendix 3.17 – Rietveld refined WISH diffraction pattern of Dy-BFO at 160 K shown in d-spacing

Dy-BFO 170K
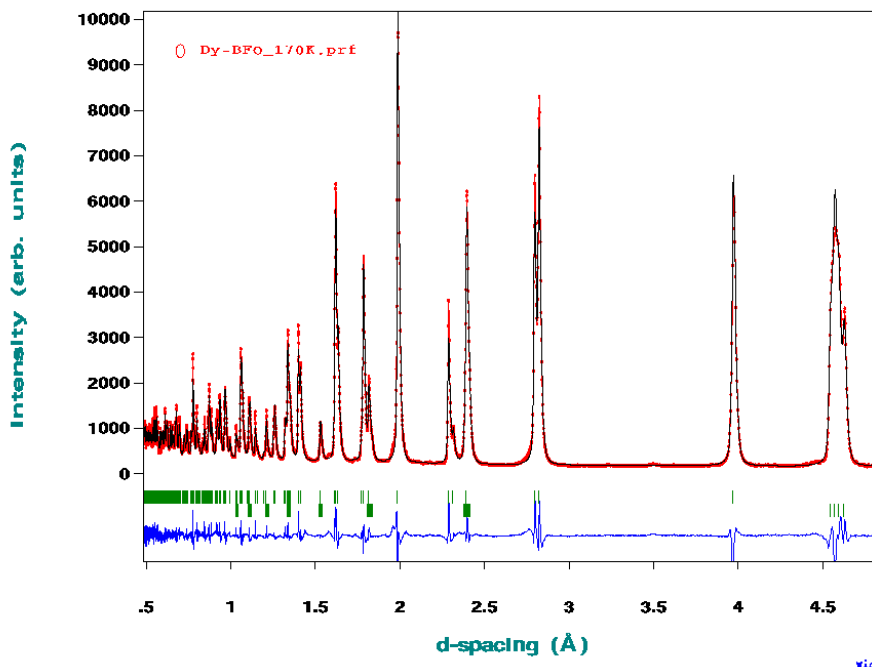
Appendix 3.18 – Rietveld refined WISH diffraction pattern of Dy-BFO at 170 K shown in d-spacing

Dy-BFO 180K
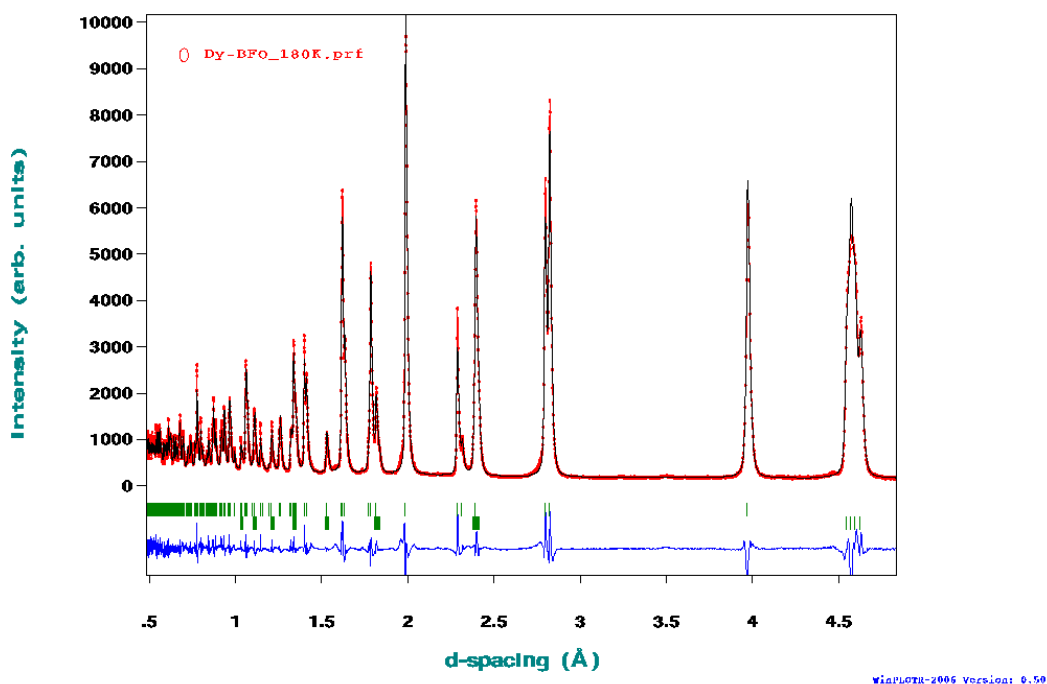
Appendix 3.19 – Rietveld refined WISH diffraction pattern of Dy-BFO at 180 K shown in d-spacing

Dy-BFO 190K
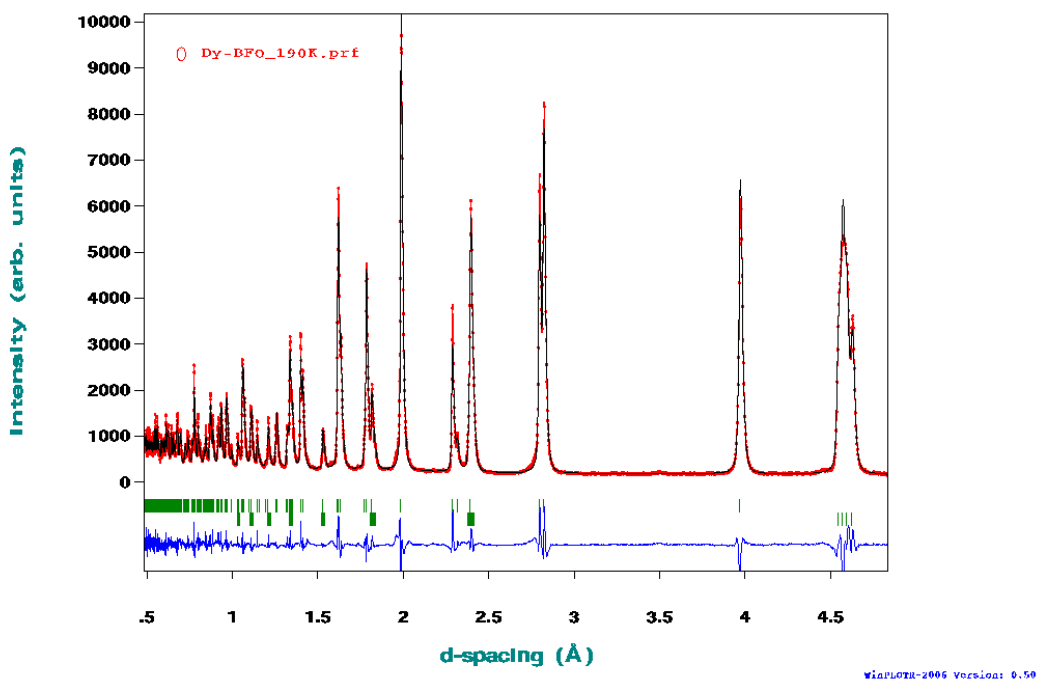
Appendix 3.20 – Rietveld refined WISH diffraction pattern of Dy-BFO at 190 K shown in d-spacing
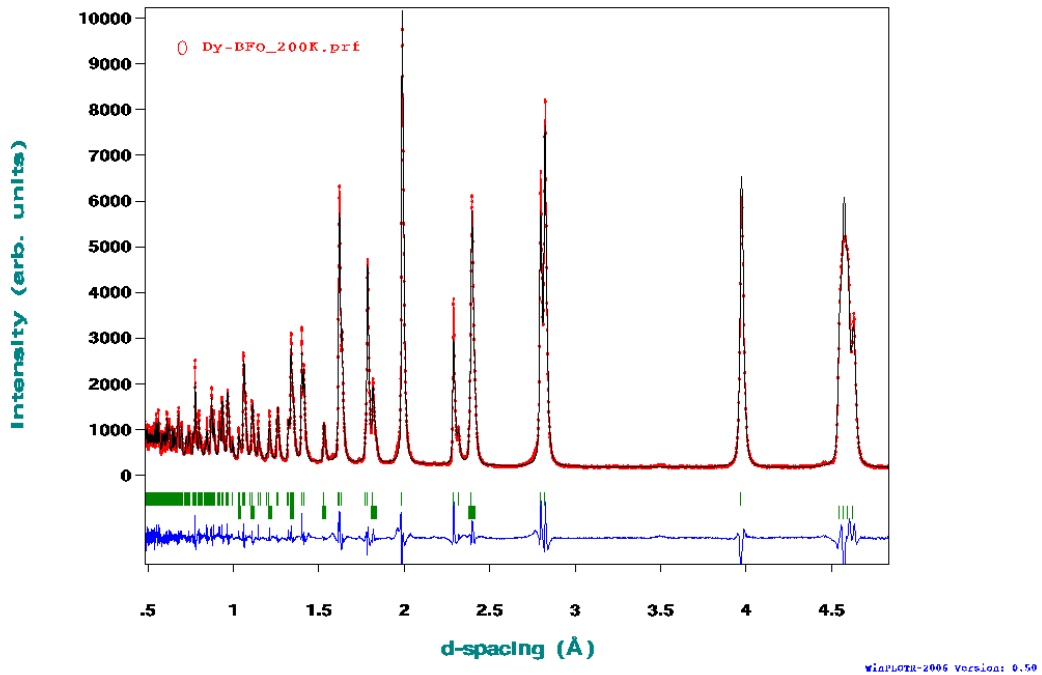
Appendix 3.21 – Rietveld refined WISH diffraction pattern of Dy-BFO at 200 K shown in d-spacing
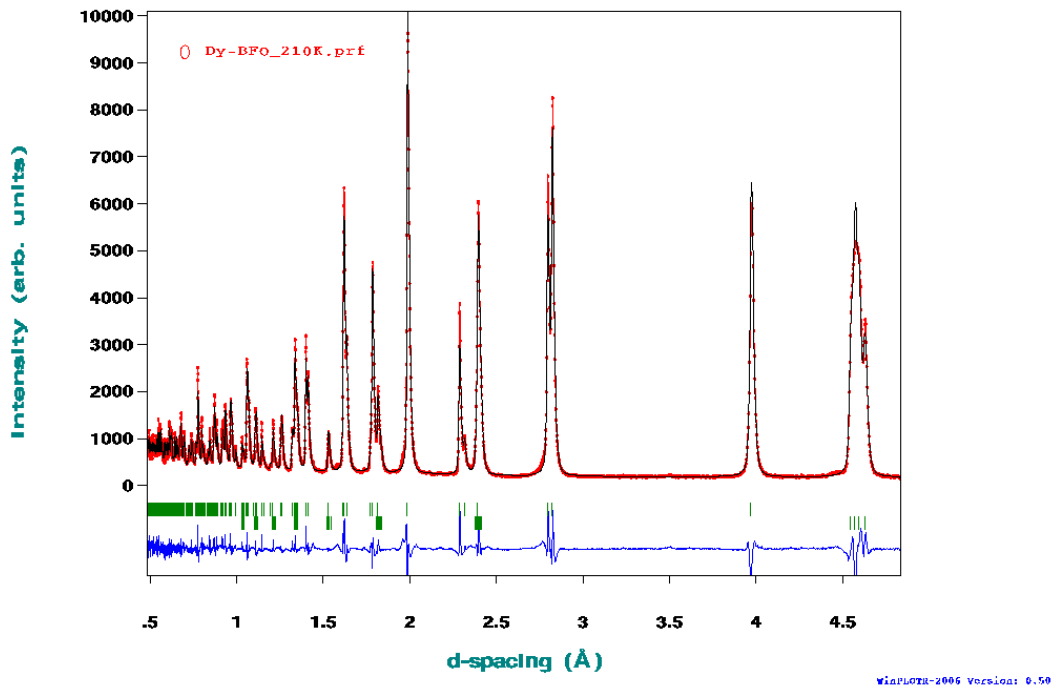
Appendix 3.22 – Rietveld refined WISH diffraction pattern of Dy-BFO at 210 K shown in d-spacing
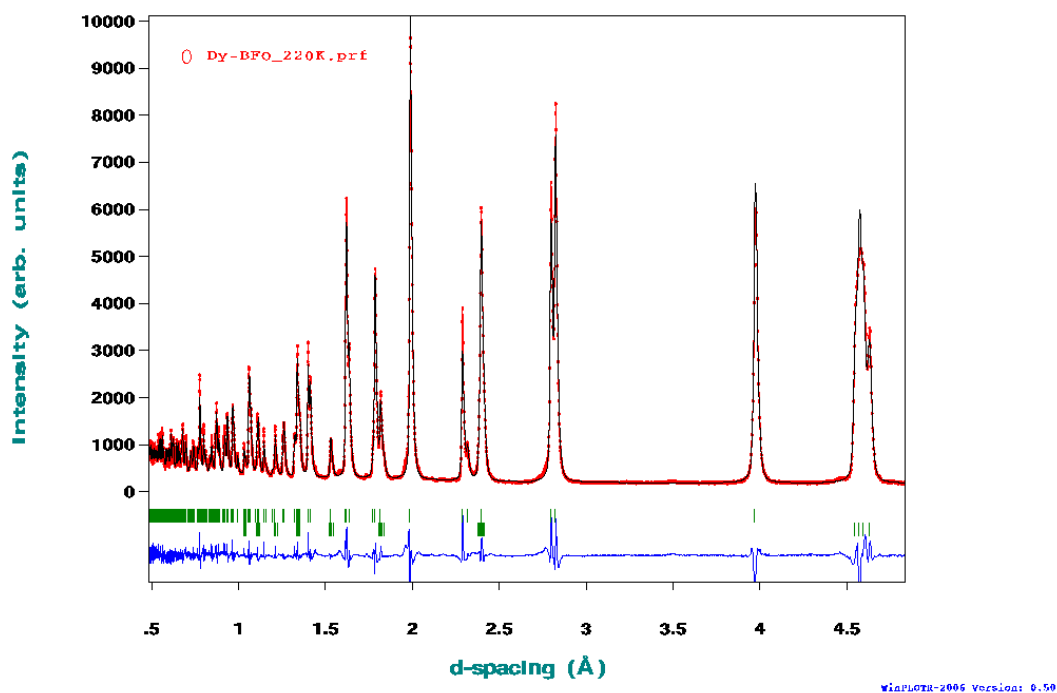
Appendix 3.23 – Rietveld refined WISH diffraction pattern of Dy-BFO at 220 K shown in d-spacing
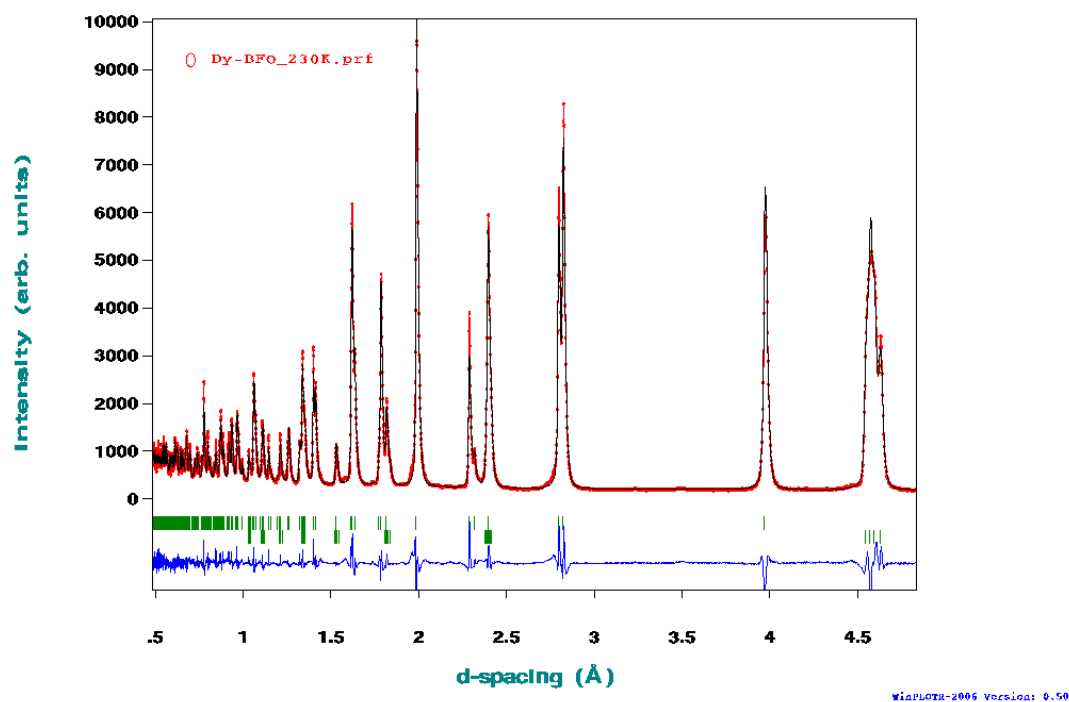
Appendix 3.24 – Rietveld refined WISH diffraction pattern of Dy-BFO at 230 K shown in d-spacing

Dy-BFO 240K
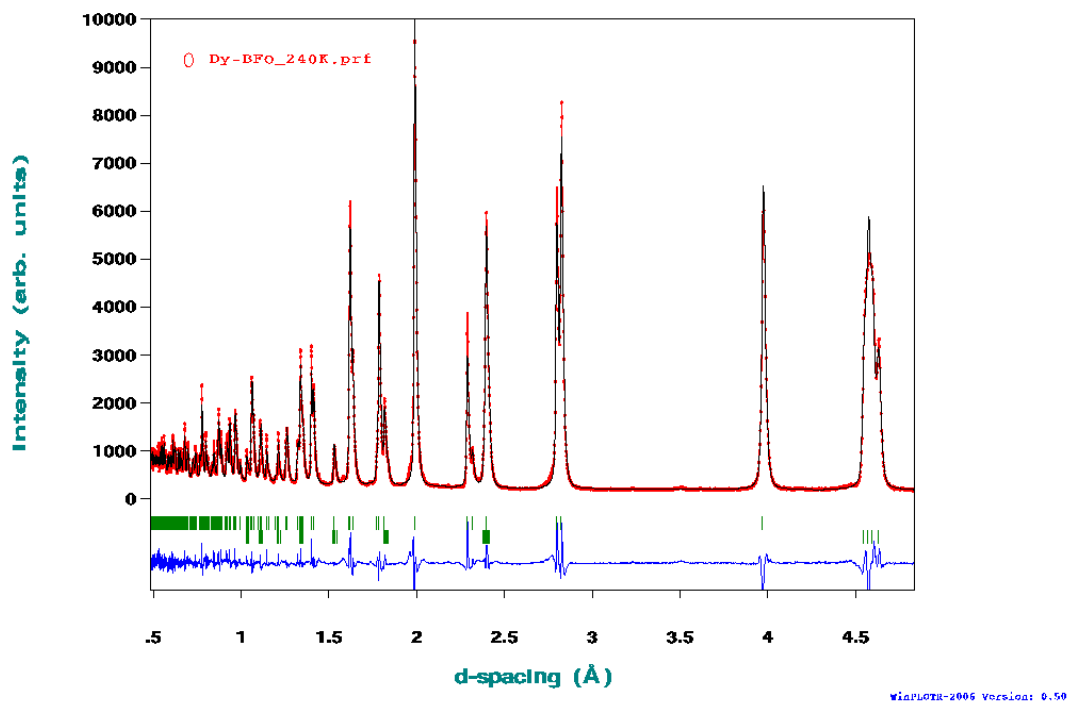
Appendix 3.25 – Rietveld refined WISH diffraction pattern of Dy-BFO at 240 K shown in d-spacing

Dy-BFO 250K
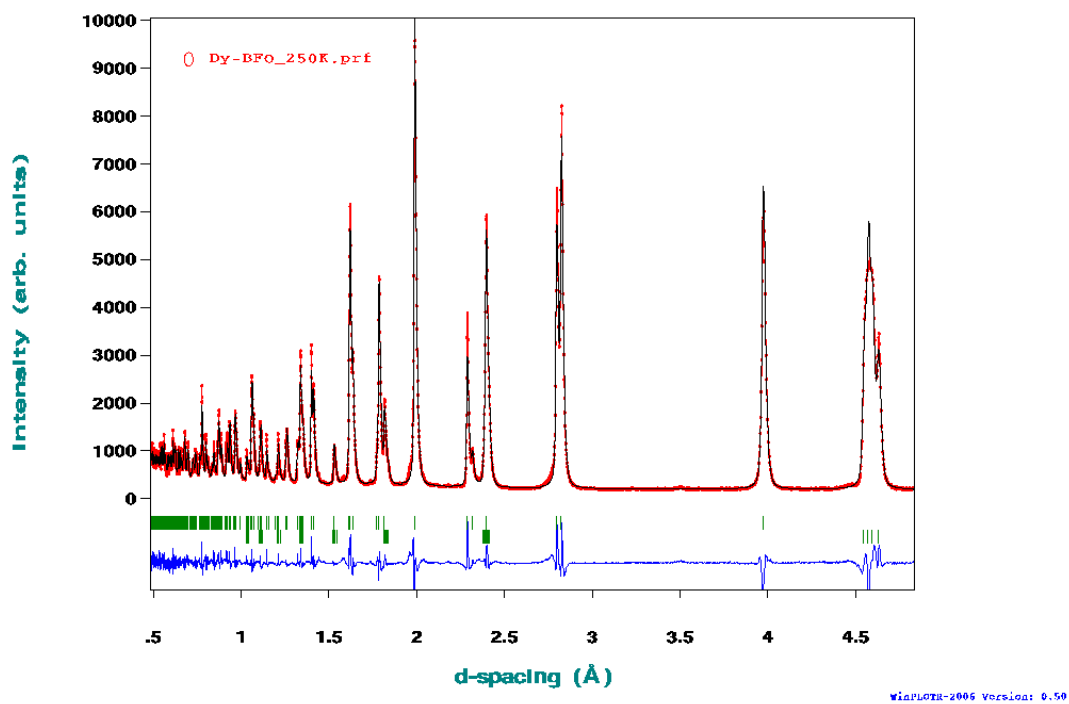
Appendix 3.26 – Rietveld refined WISH diffraction pattern of Dy-BFO at 250 K shown in d-spacing

Dy-BFO 260K
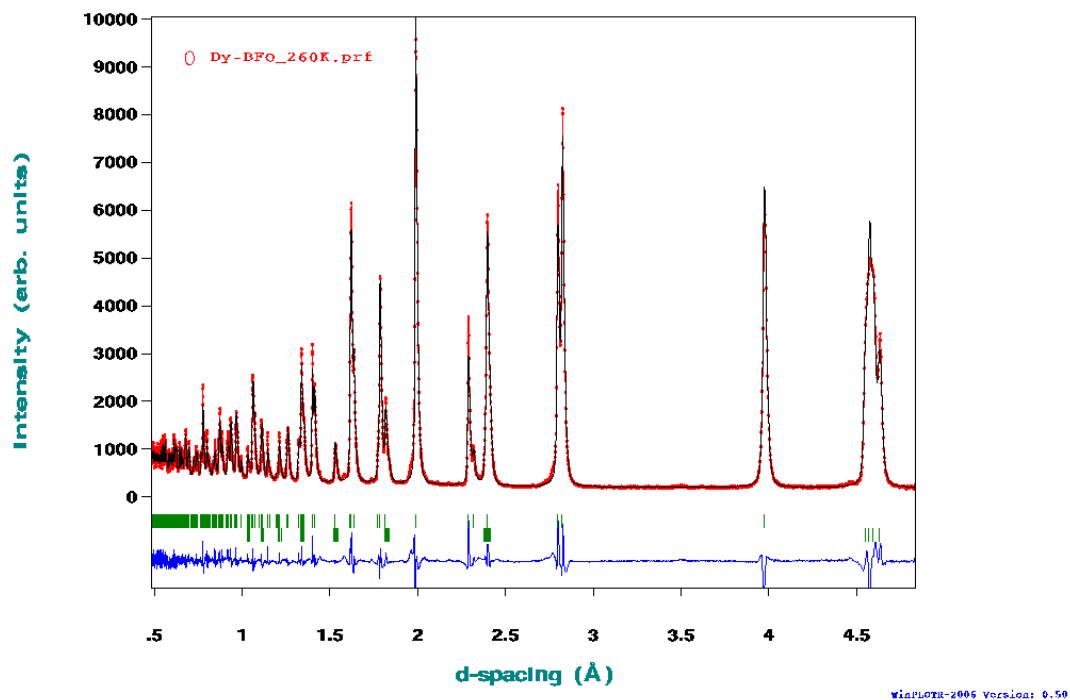
Appendix 3.27 – Rietveld refined WISH diffraction pattern of Dy-BFO at 260 K shown in d-spacing

Dy-BFO 270K
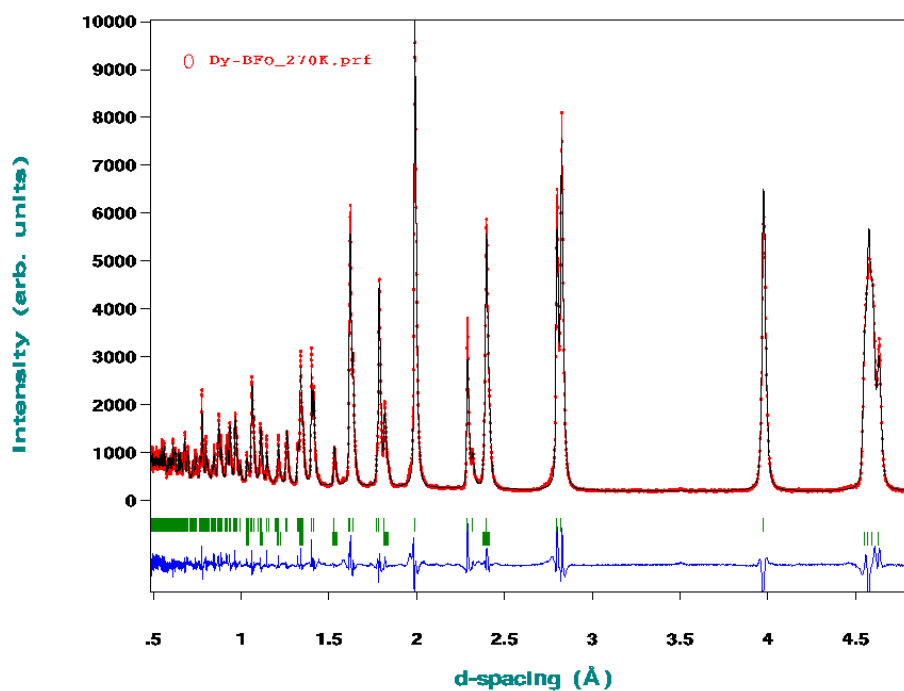
Appendix 3.28 – Rietveld refined WISH diffraction pattern of Dy-BFO at 270 K shown in d-spacing
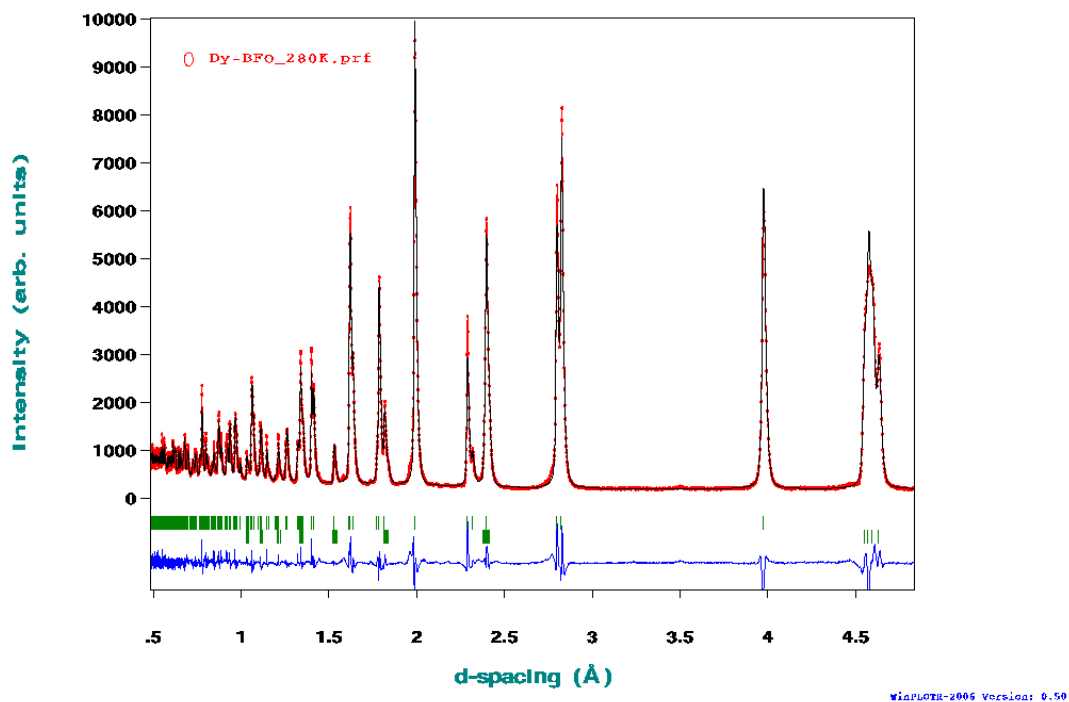
Appendix 3.29 – Rietveld refined WISH diffraction pattern of Dy-BFO at 280 K shown in d-spacing
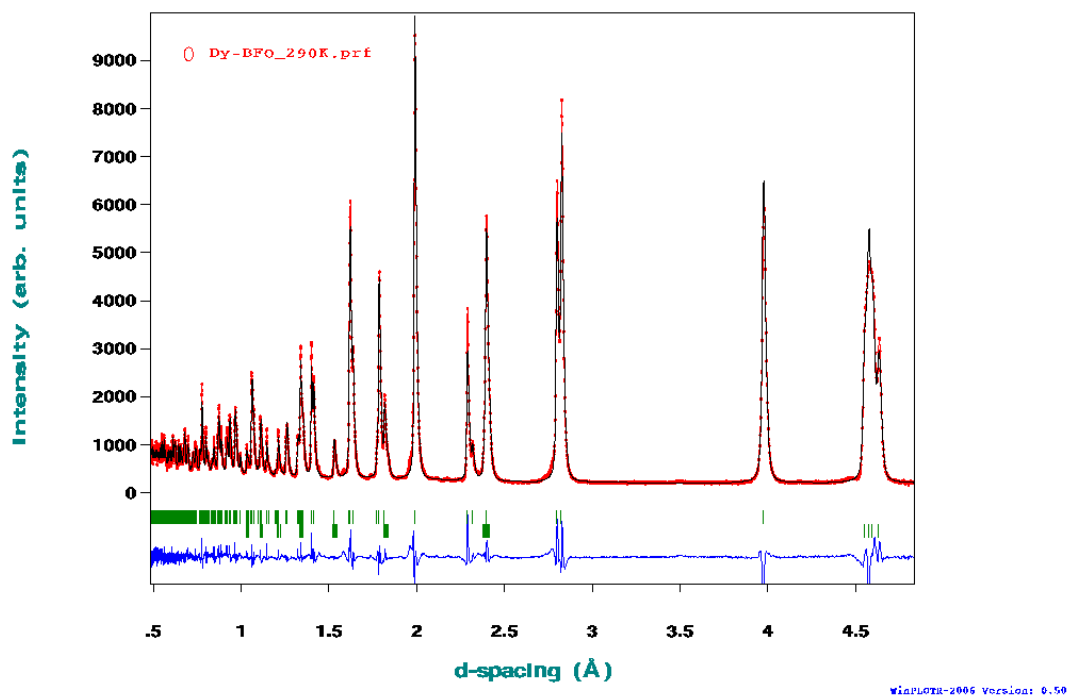
Appendix 3.30 – Rietveld refined WISH diffraction pattern of Dy-BFO at 290 K shown in d-spacing
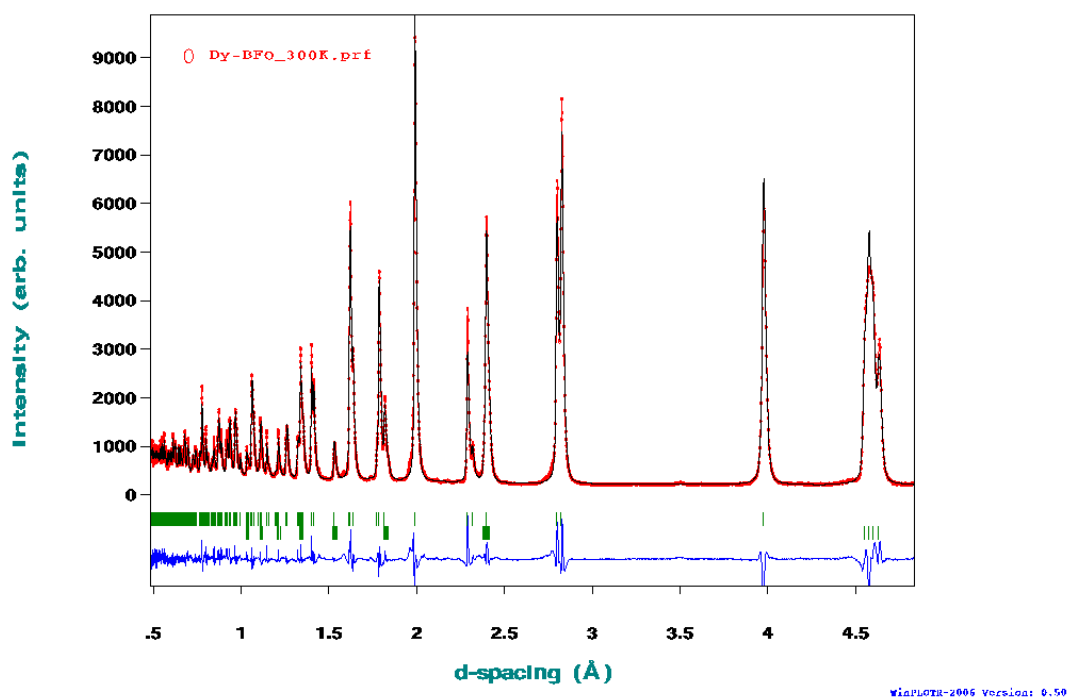
Appendix 3.31 – Rietveld refined WISH diffraction pattern of Dy-BFO at 300 K shown in d-spacing
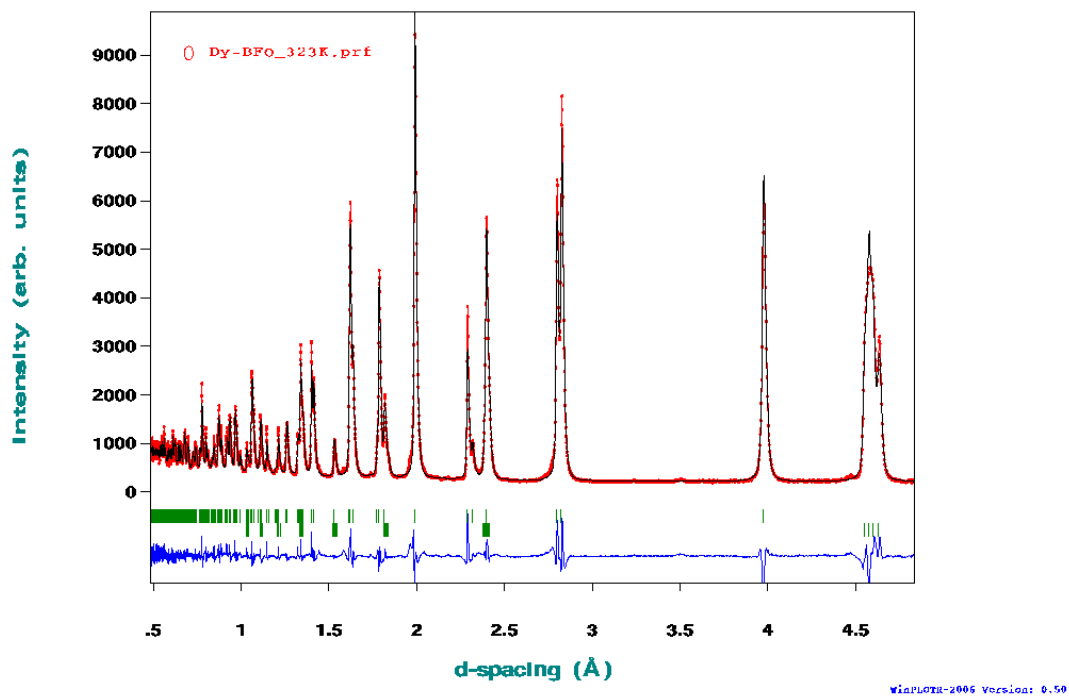
Appendix 3.32 – Rietveld refined WISH diffraction pattern of Dy-BFO at 323 K shown in d-spacing

Dy-BFO 333K
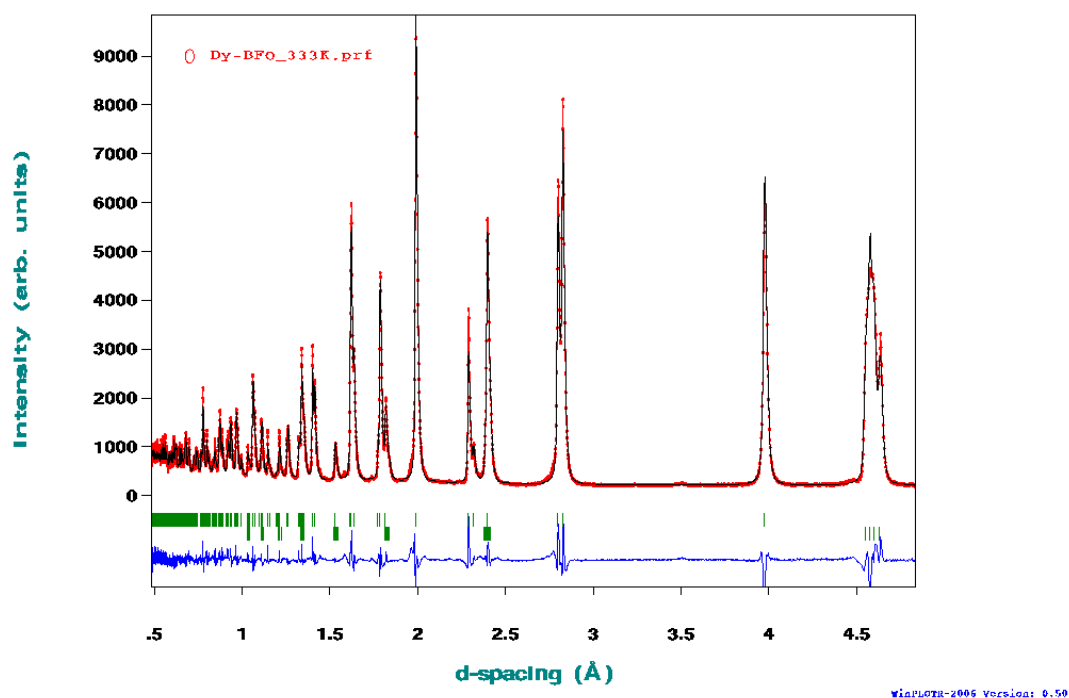
Appendix 3.33 – Rietveld refined WISH diffraction pattern of Dy-BFO at 333 K shown in d-spacing

Dy-BFO 343K
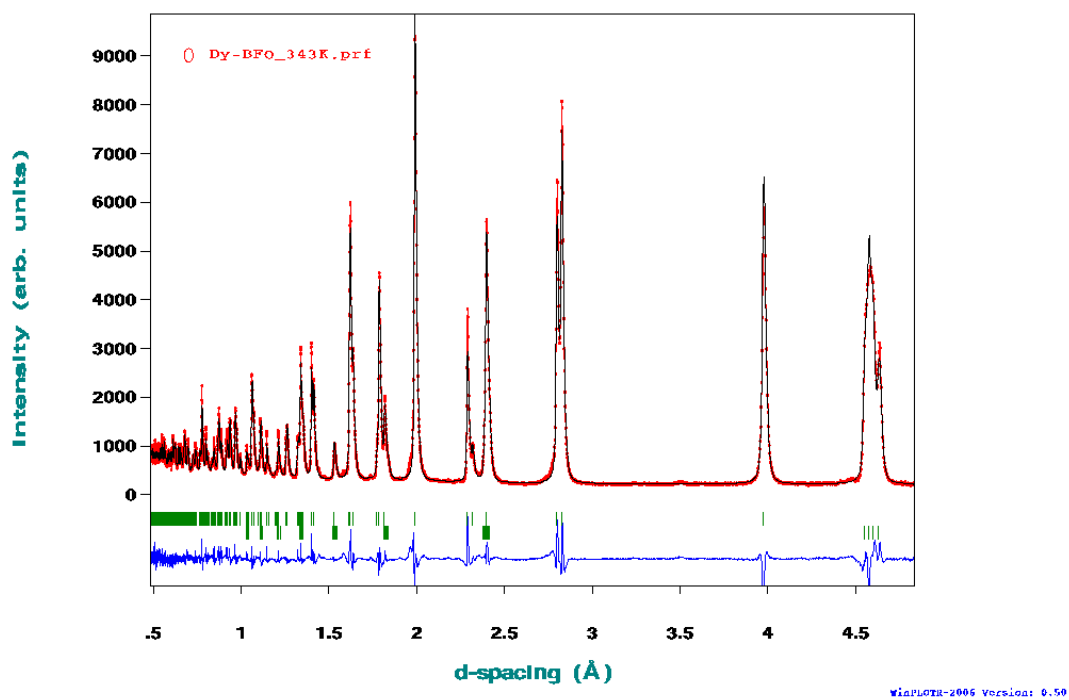
Appendix 3.34 – Rietveld refined WISH diffraction pattern of Dy-BFO at 343 K shown in d-spacing
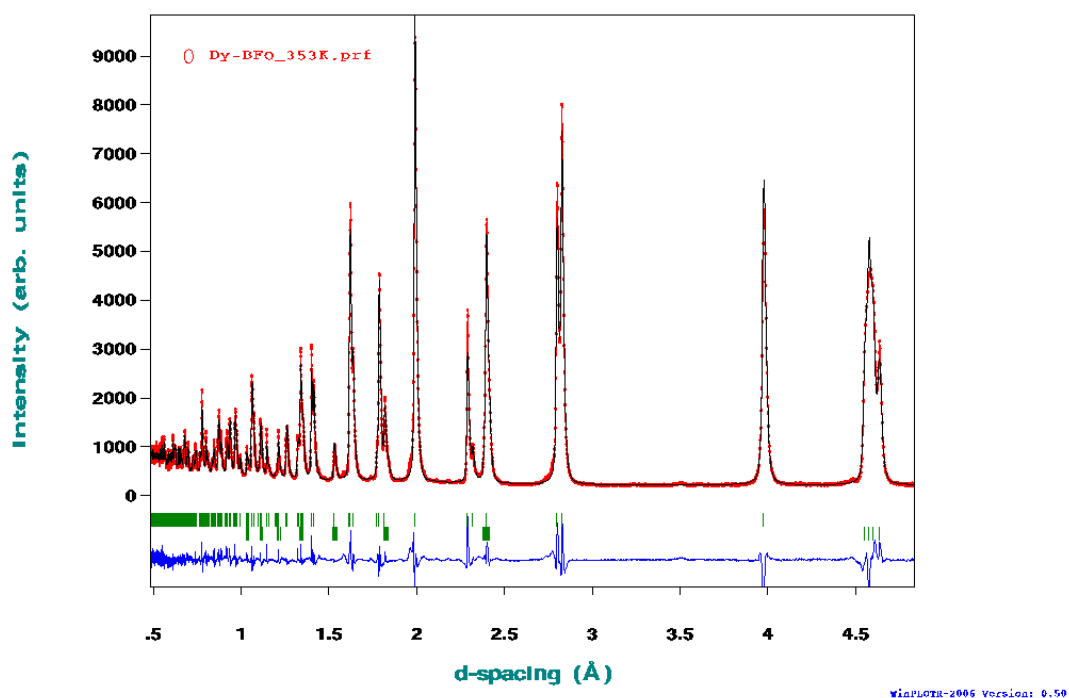
Appendix 3.35 – Rietveld refined WISH diffraction pattern of Dy-BFO at 353 K shown in d-spacing
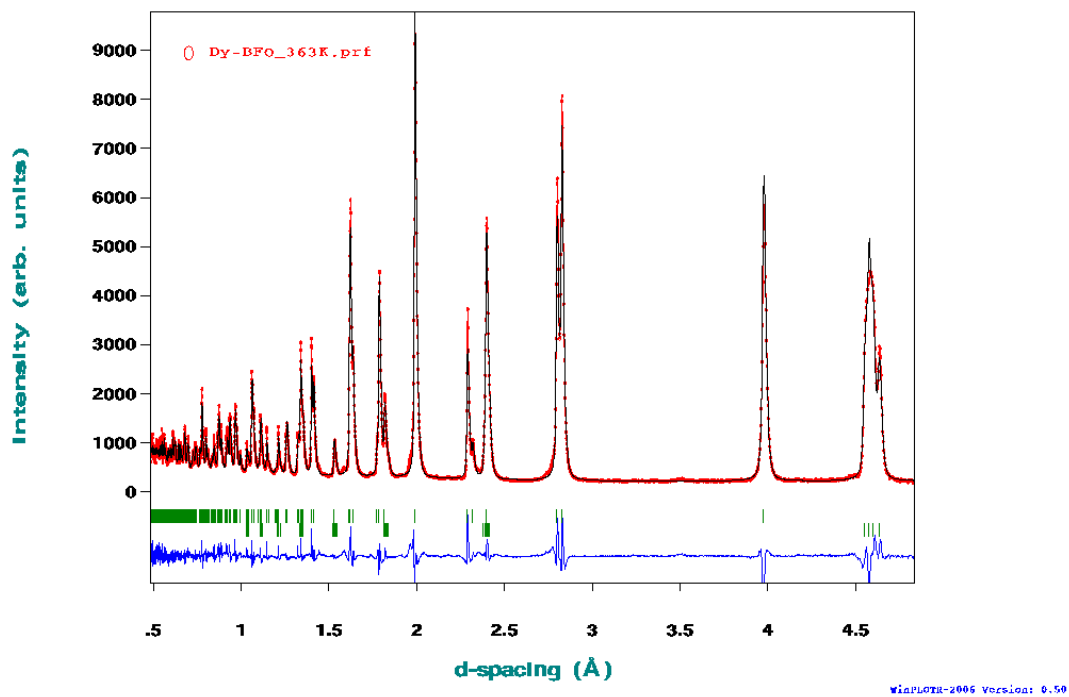
Appendix 3.36 – Rietveld refined WISH diffraction pattern of Dy-BFO at 363 K shown in d-spacing

Dy-BFO 373K
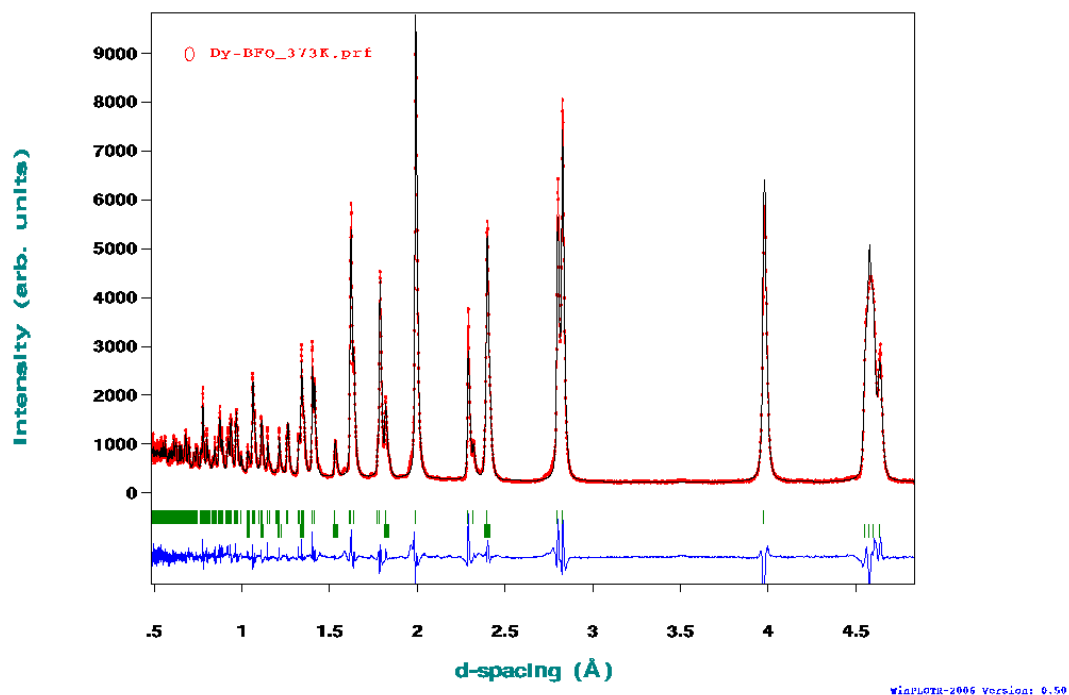
Appendix 3.37 – Rietveld refined WISH diffraction pattern of Dy-BFO at 373 K shown in d-spacing

Dy-BFO 383K
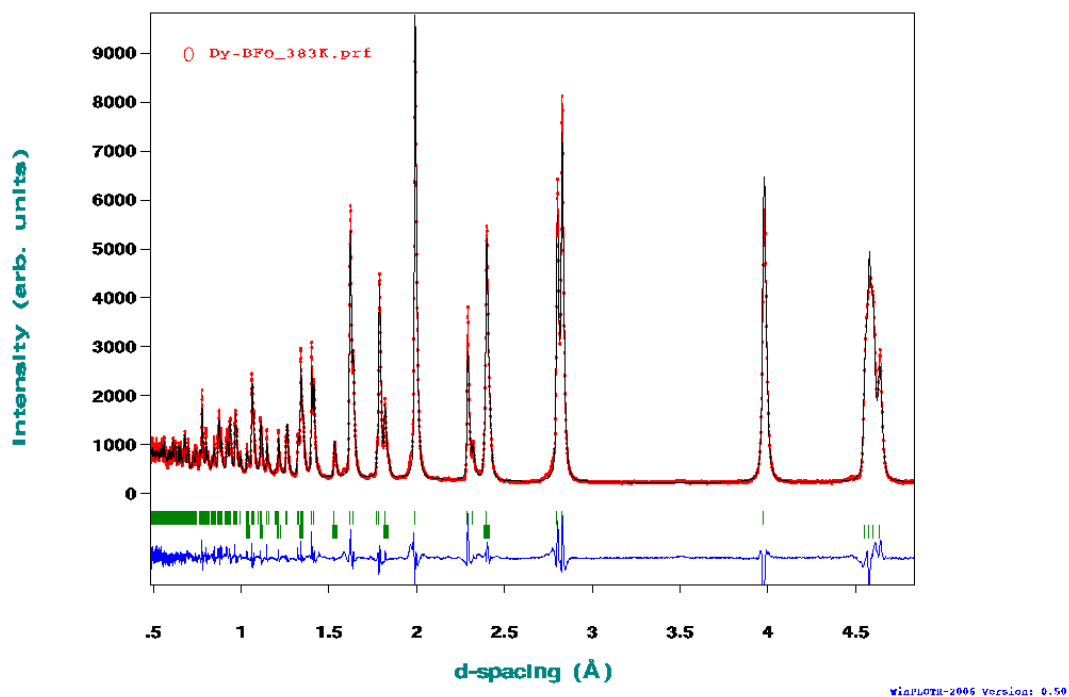
Appendix 3.38 – Rietveld refined WISH diffraction pattern of Dy-BFO at 383 K shown in d-spacing
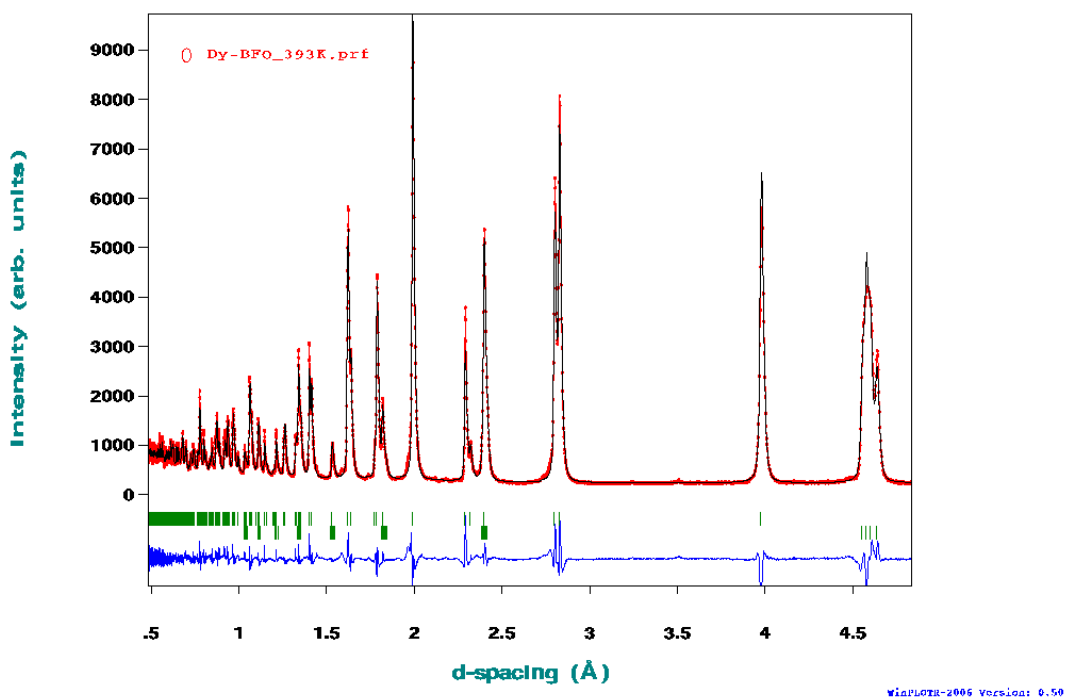
Appendix 3.39 – Rietveld refined WISH diffraction pattern of Dy-BFO at 393 K shown in d-spacing
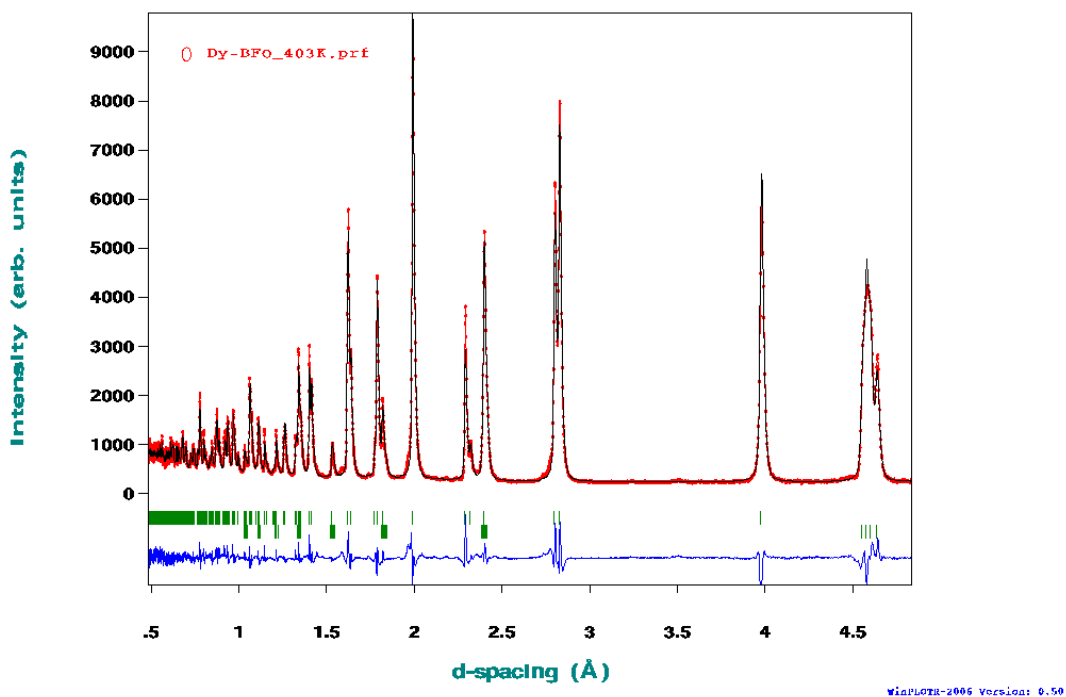
Appendix 3.40 – Rietveld refined WISH diffraction pattern of Dy-BFO at 403 K shown in d-spacing

Dy-BFO 413K
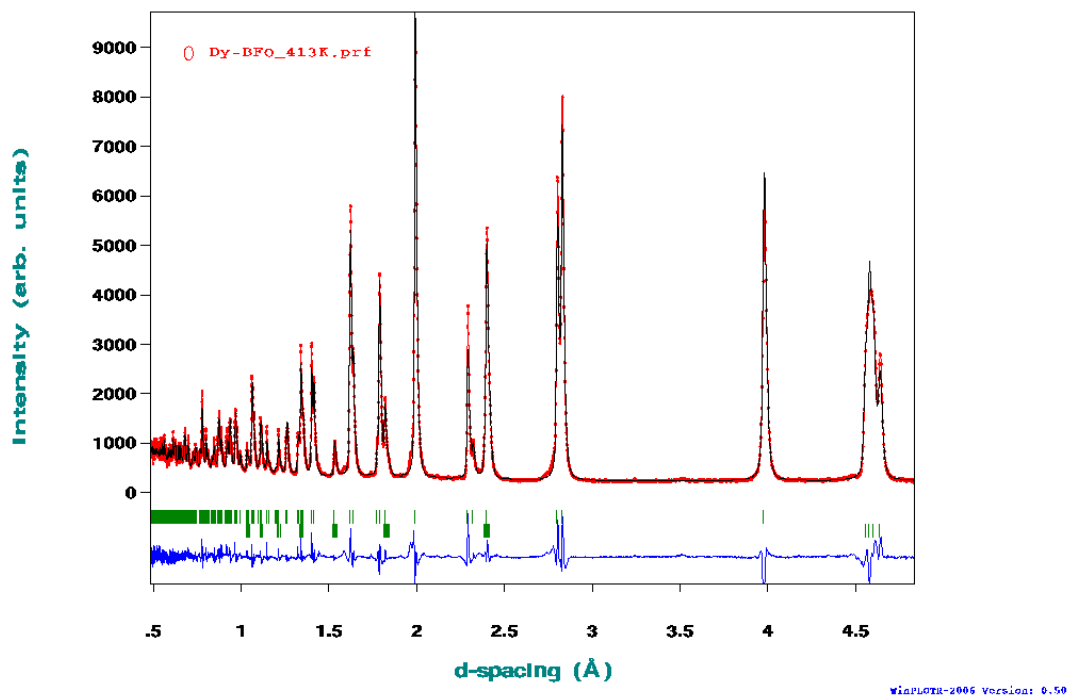
Appendix 3.41 – Rietveld refined WISH diffraction pattern of Dy-BFO at 413 K shown in d-spacing

Dy-BFO 423K
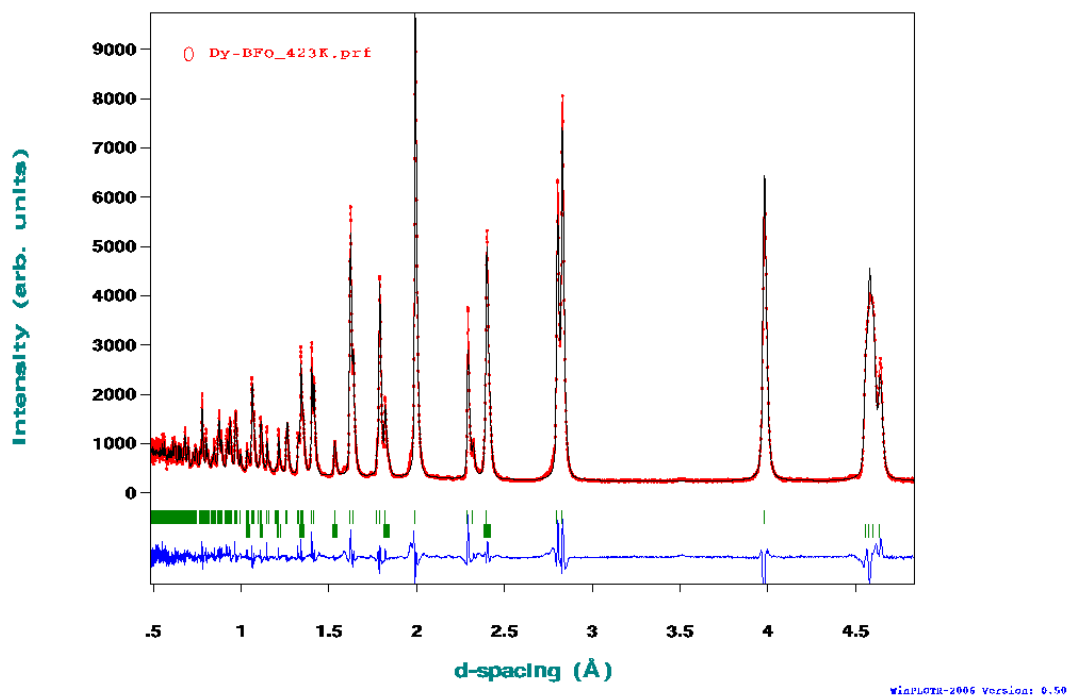
Appendix 3.42 – Rietveld refined WISH diffraction pattern of Dy-BFO at 423 K shown in d-spacing

Dy-BFO 433K
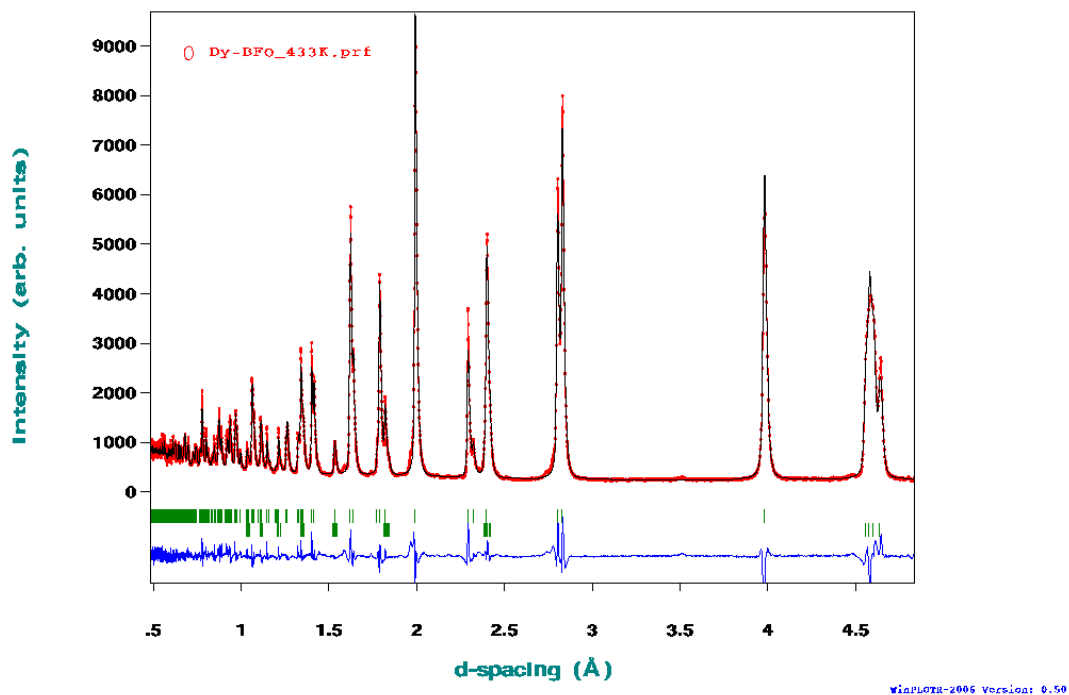
Appendix 3.43 – Rietveld refined WISH diffraction pattern of Dy-BFO at 433 K shown in d-spacing

Dy-BFO 443K
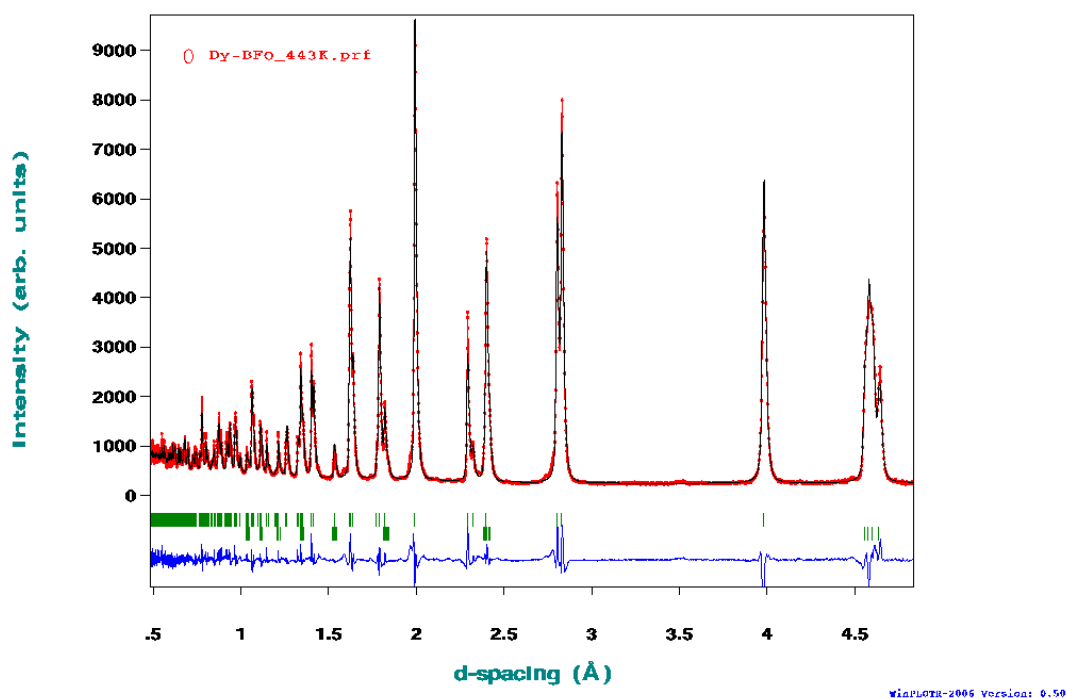
Appendix 3.44 – Rietveld refined WISH diffraction pattern of Dy-BFO at 443 K shown in d-spacing

Dy-BFO 453K
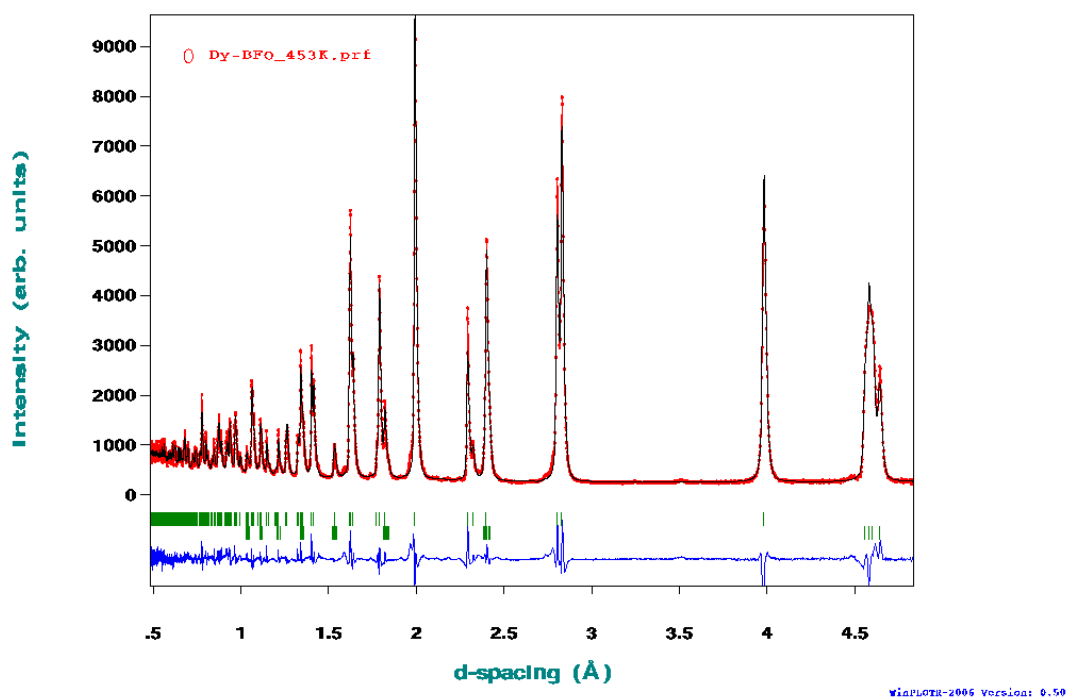
Appendix 3.45 – Rietveld refined WISH diffraction pattern of Dy-BFO at 453 K shown in d-spacing

Dy-BFO 463K
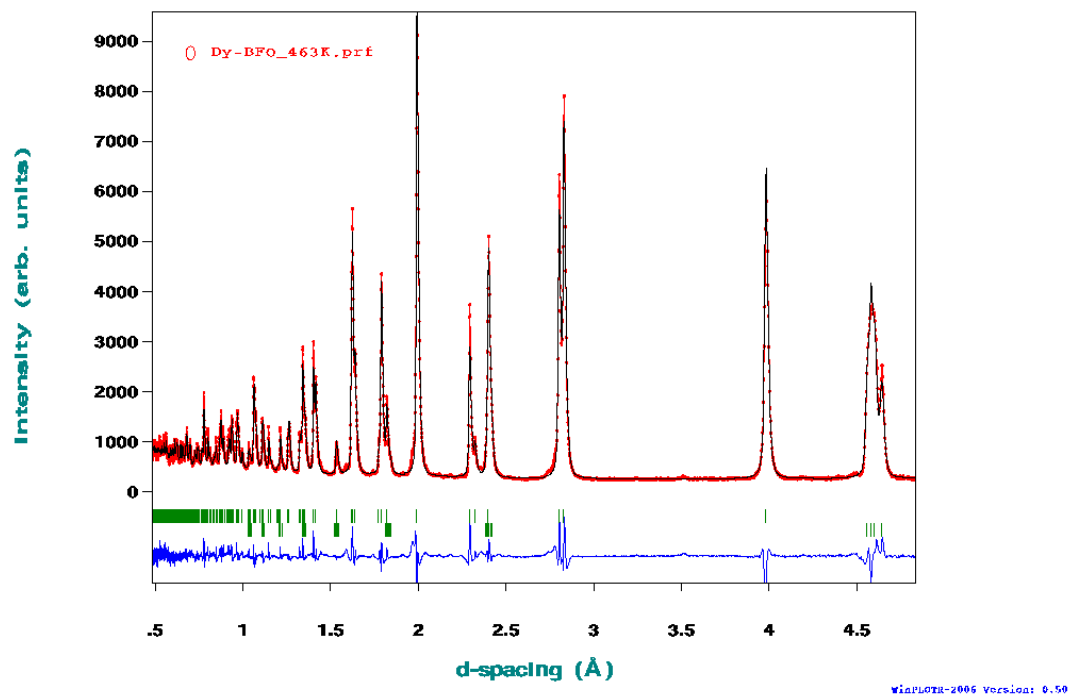
Appendix 3.46 – Rietveld refined WISH diffraction pattern of Dy-BFO at 463 K shown in d-spacing

Dy-BFO 473K
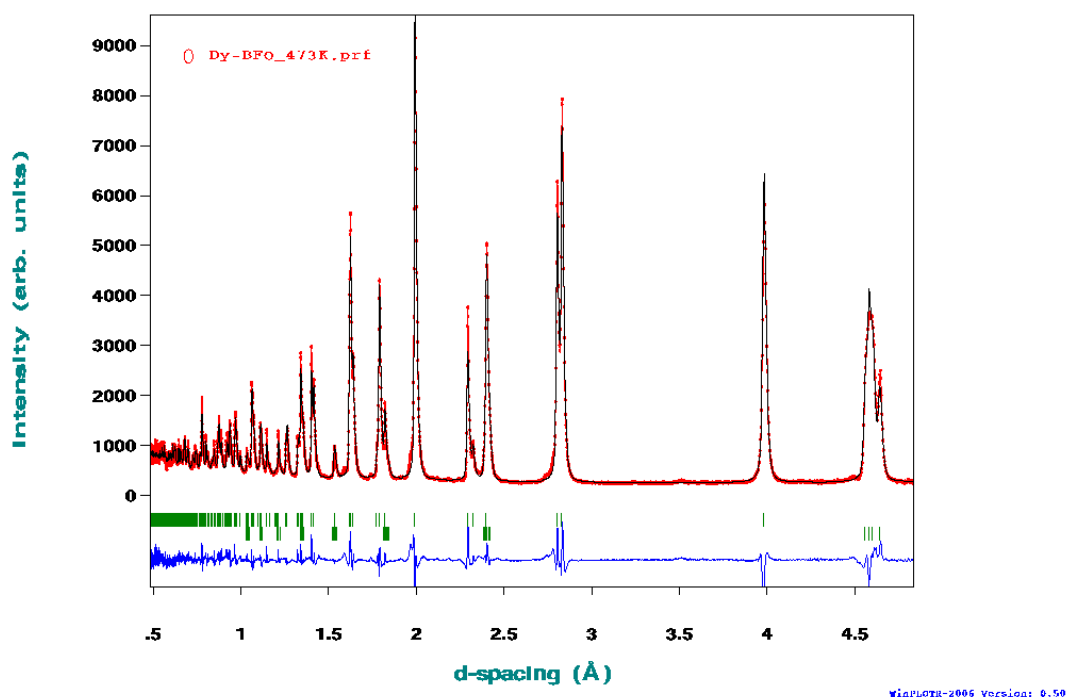
Appendix 3.47 – Rietveld refined WISH diffraction pattern of Dy-BFO at 473 K shown in d-spacing

Dy-BFO 483K
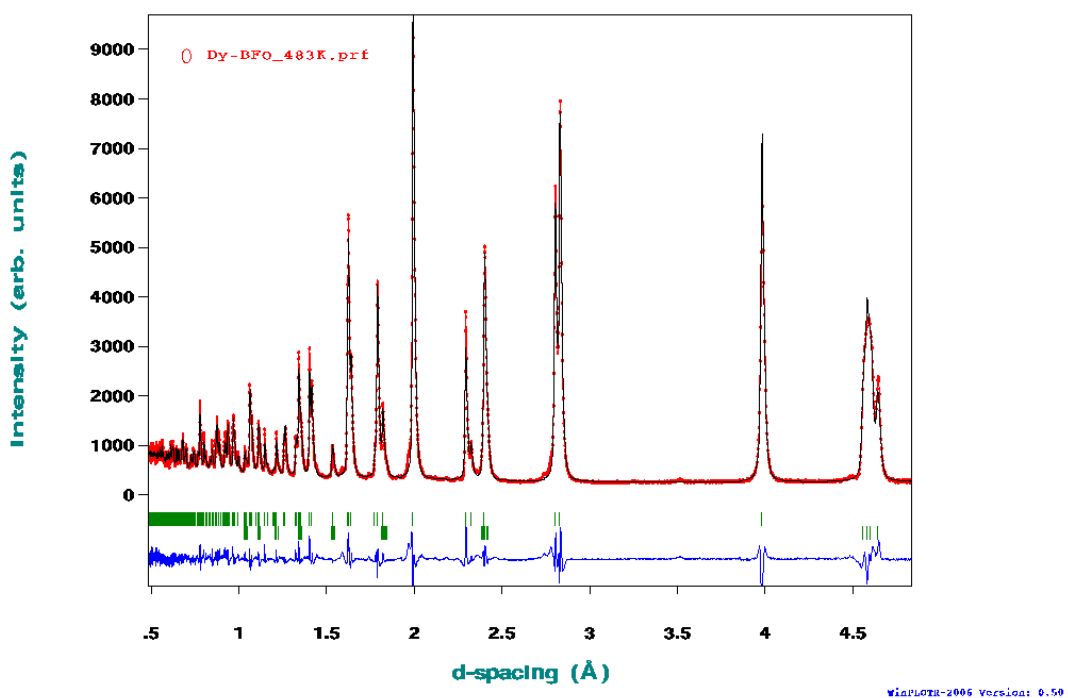
Appendix 3.48 – Rietveld refined WISH diffraction pattern of Dy-BFO at 483 K shown in d-spacing

Dy-BFO 493K
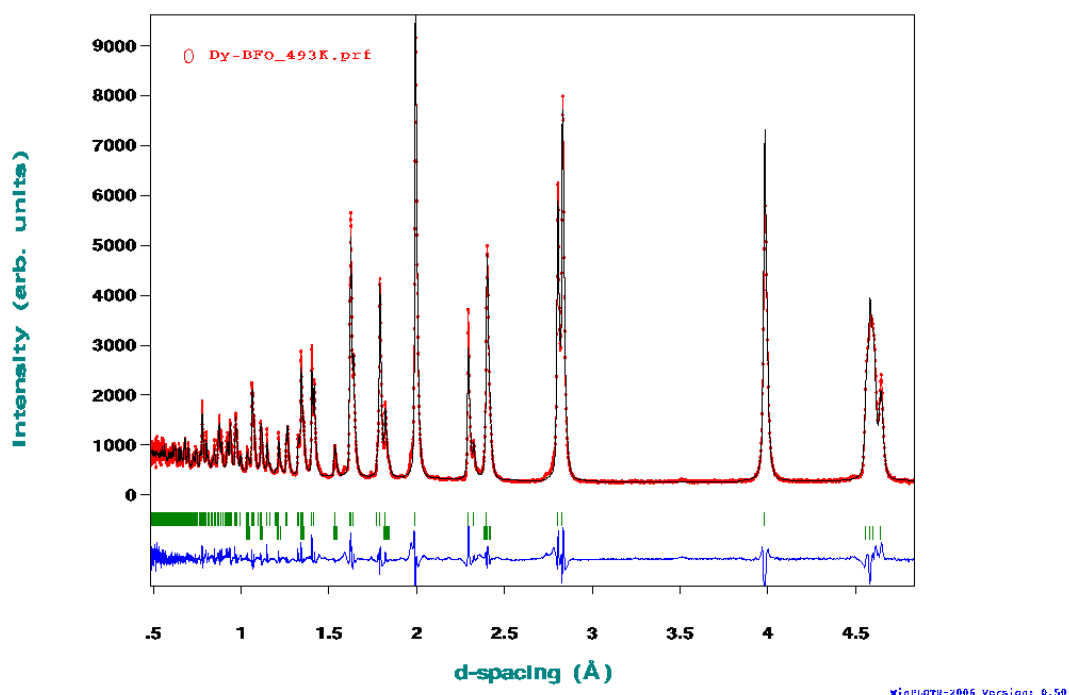
Appendix 3.49 – Rietveld refined WISH diffraction pattern of Dy-BFO at 493 K shown in d-spacing

Dy-BFO 503K
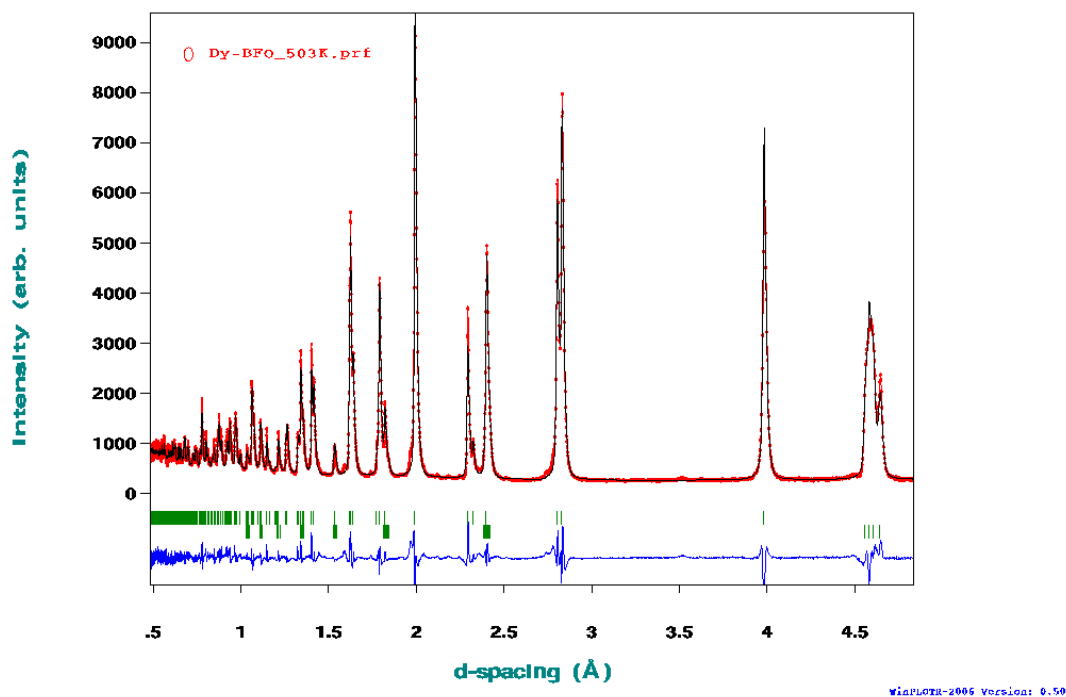
Appendix 3.50 – Rietveld refined WISH diffraction pattern of Dy-BFO at 503 K shown in d-spacing

Dy-BFO 513K
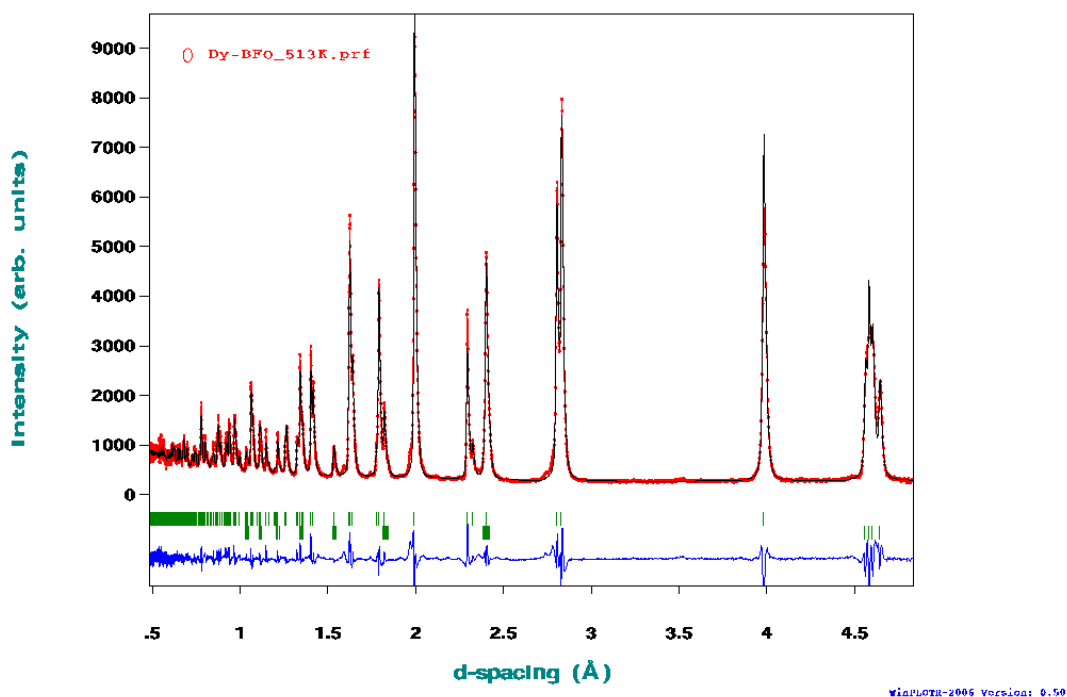
Appendix 3.51 – Rietveld refined WISH diffraction pattern of Dy-BFO at 513 K shown in d-spacing

Dy-BFO 523K
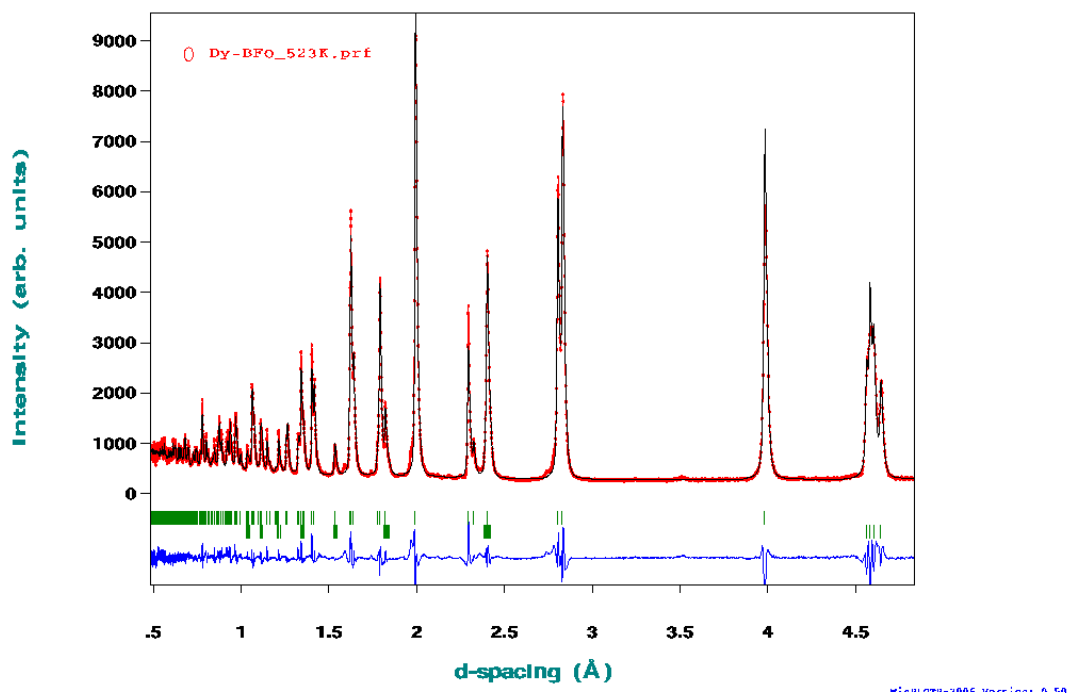
Appendix 3.52 – Rietveld refined WISH diffraction pattern of Dy-BFO at 523 K shown in d-spacing

Dy-BFO 533K
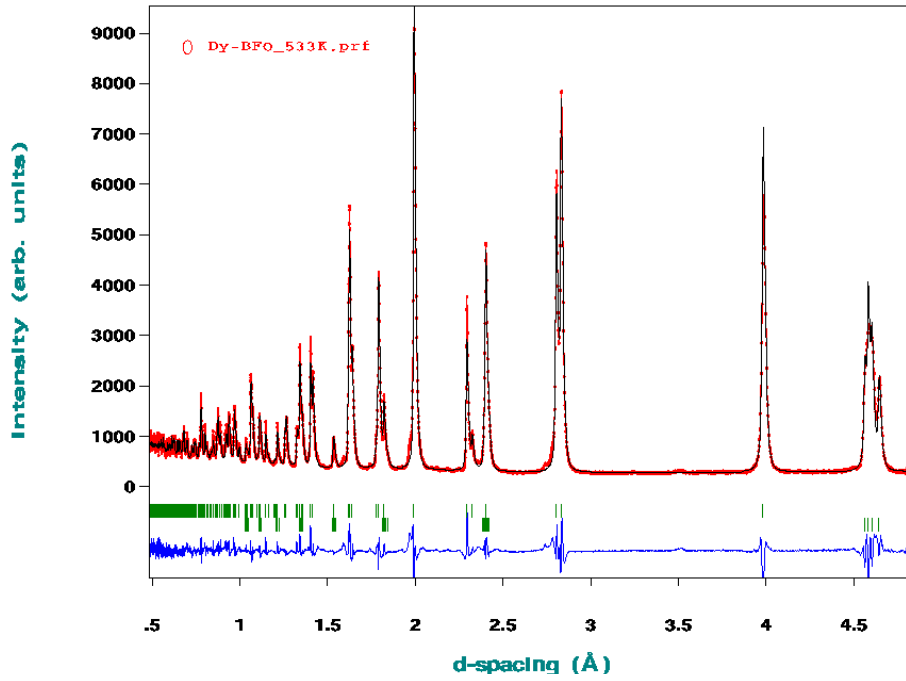
Appendix 3.53 – Rietveld refined WISH diffraction pattern of Dy-BFO at 533 K shown in d-spacing

Dy-BFO 543K
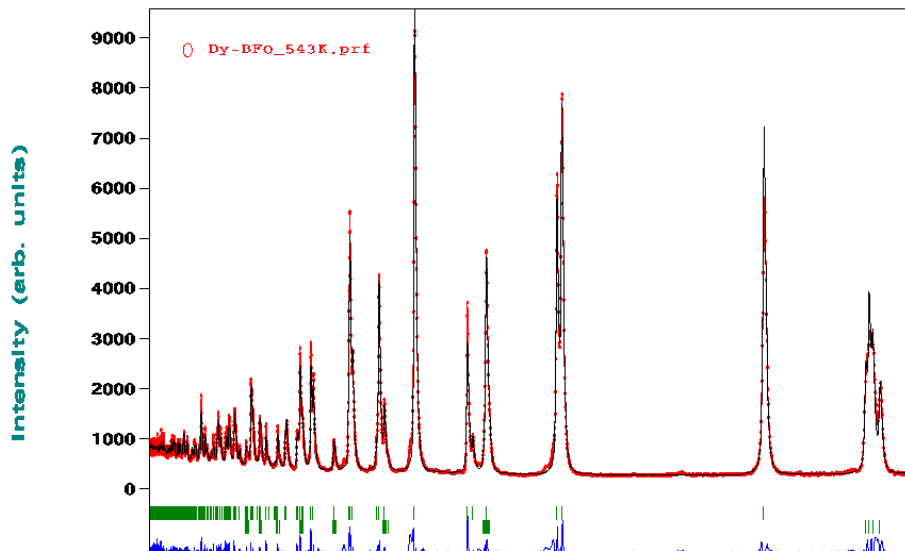
Appendix 3.54 – Rietveld refined WISH diffraction pattern of Dy-BFO at 543 K shown in d-spacing
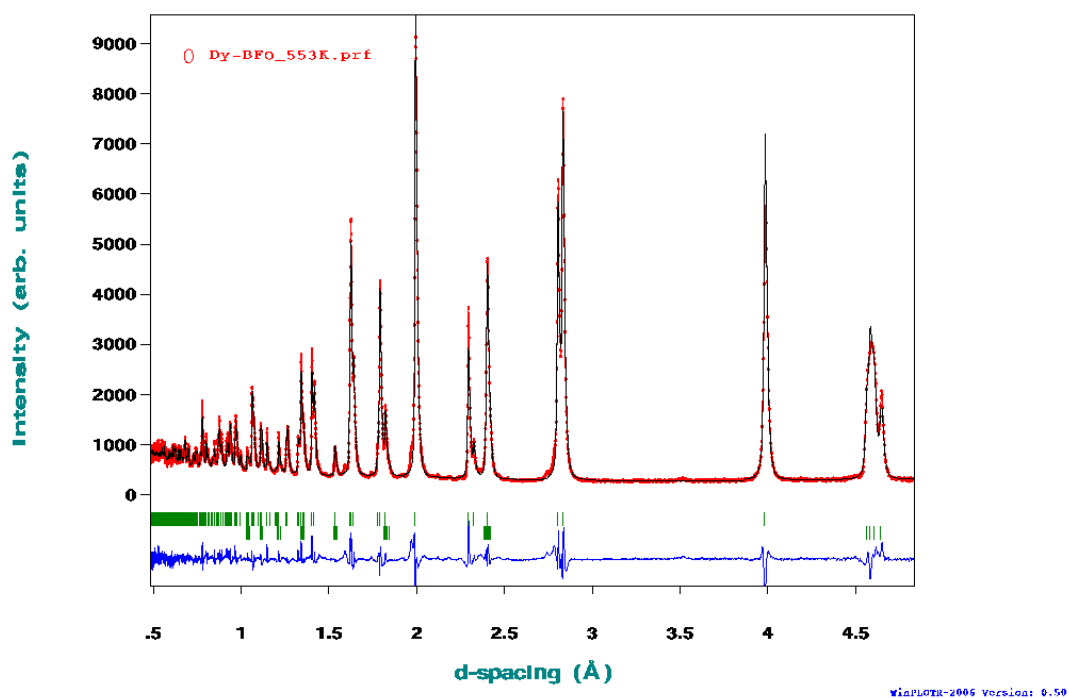
Appendix 3.55 – Rietveld refined WISH diffraction pattern of Dy-BFO at 553 K shown in d-spacing
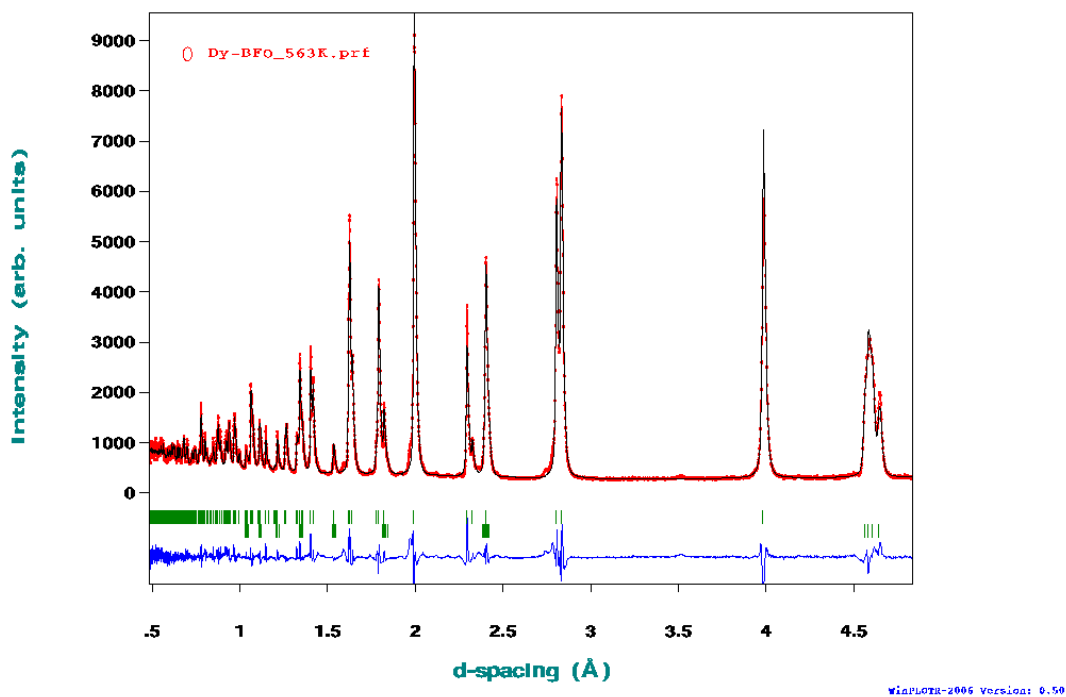
Appendix 3.56 – Rietveld refined WISH diffraction pattern of Dy-BFO at 563 K shown in d-spacing

Dy-BFO 573K
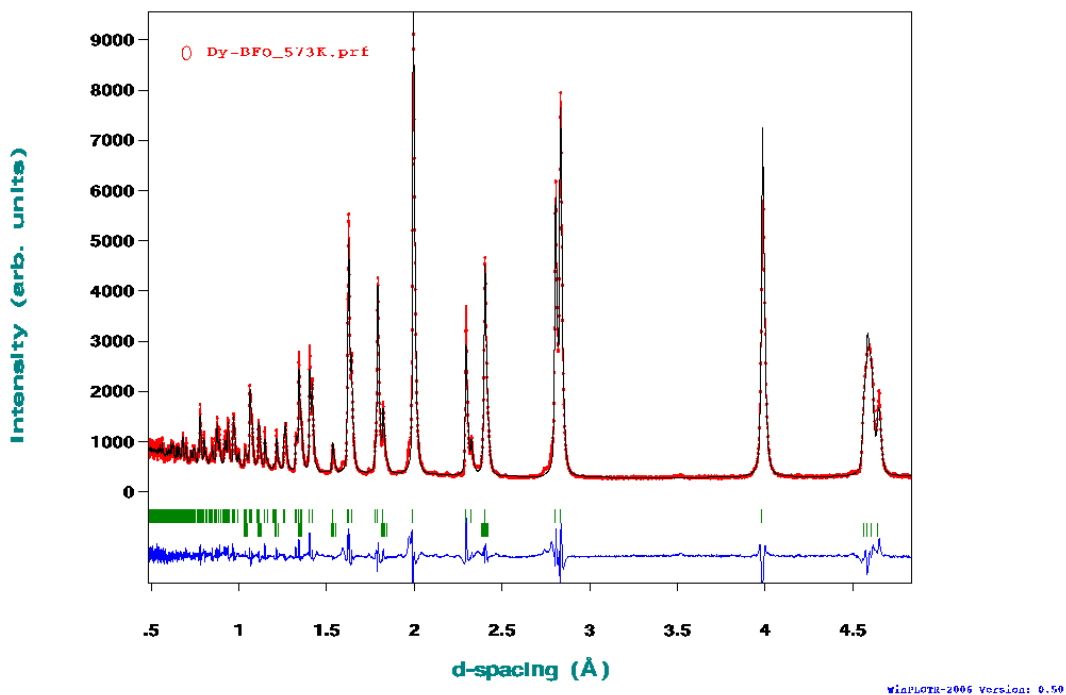
Appendix 3.57 – Rietveld refined WISH diffraction pattern of Dy-BFO at 573 K shown in d-spacing

Dy-BFO 583K
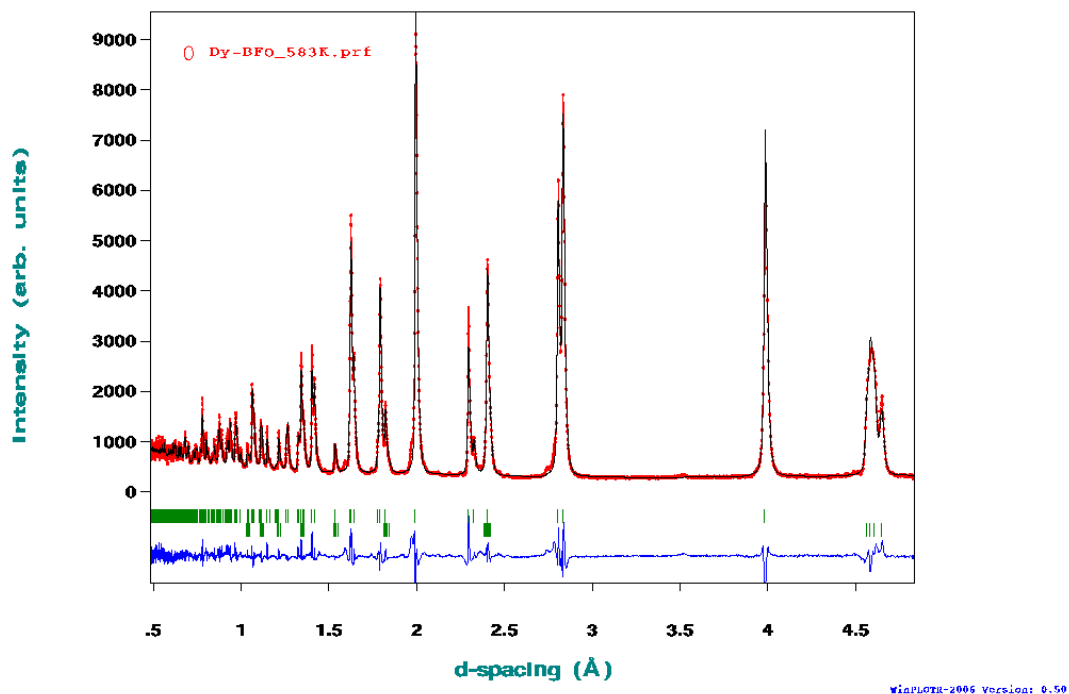
Appendix 3.58 – Rietveld refined WISH diffraction pattern of Dy-BFO at 583 K shown in d-spacing
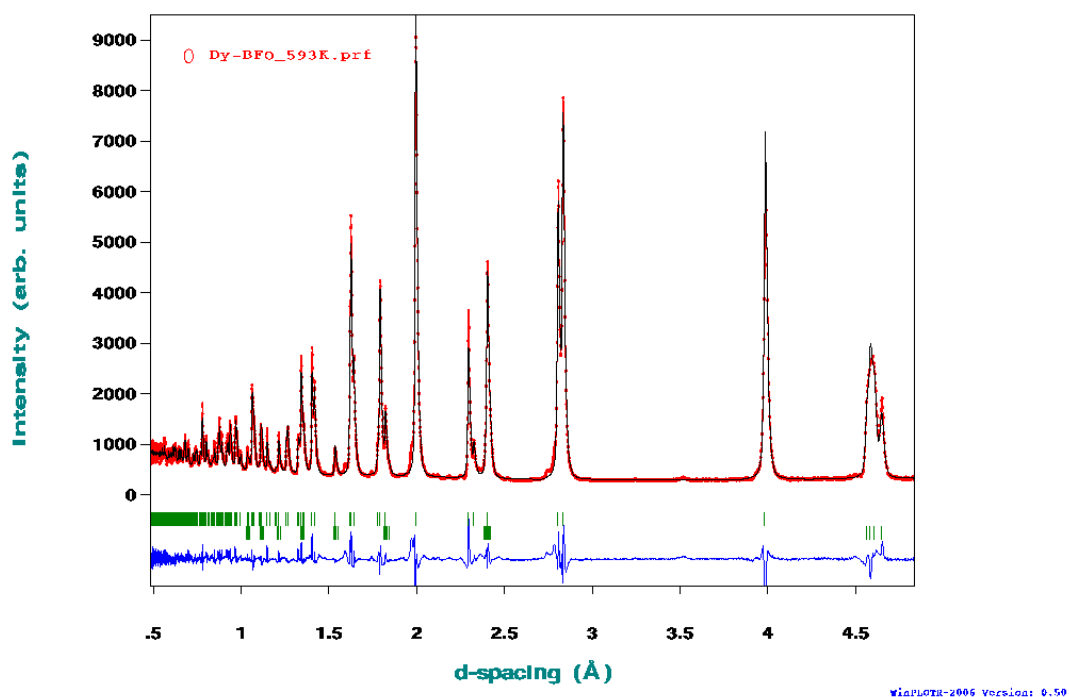
Appendix 3.59 – Rietveld refined WISH diffraction pattern of Dy-BFO at 593 K shown in d-spacing
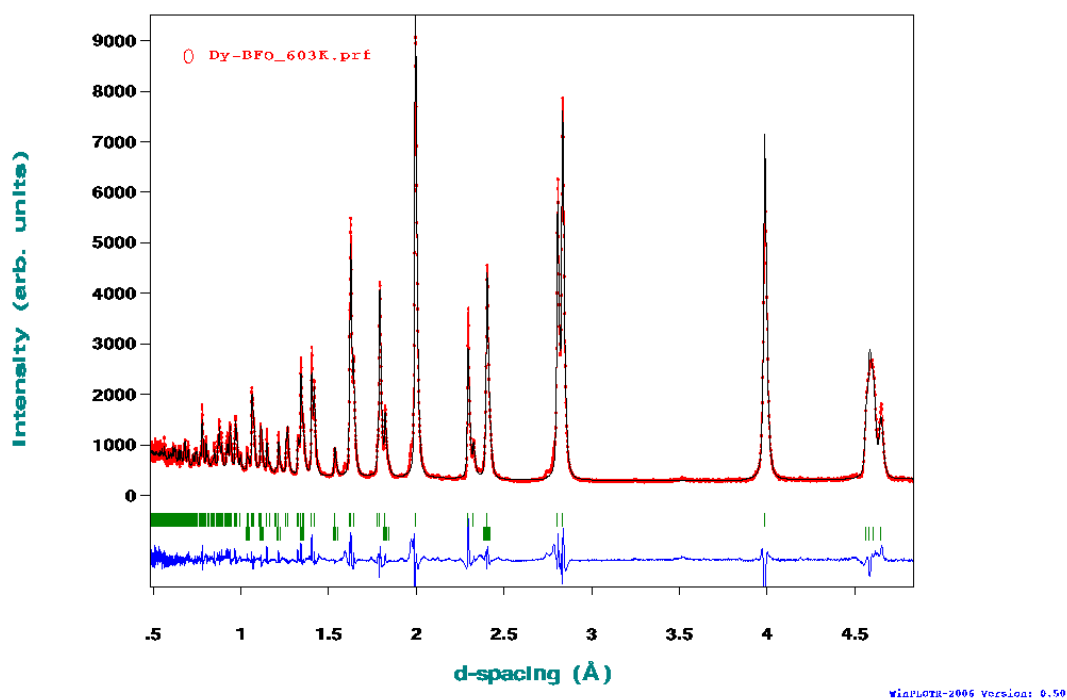
Appendix 3.60 – Rietveld refined WISH diffraction pattern of Dy-BFO at 603 K shown in d-spacing
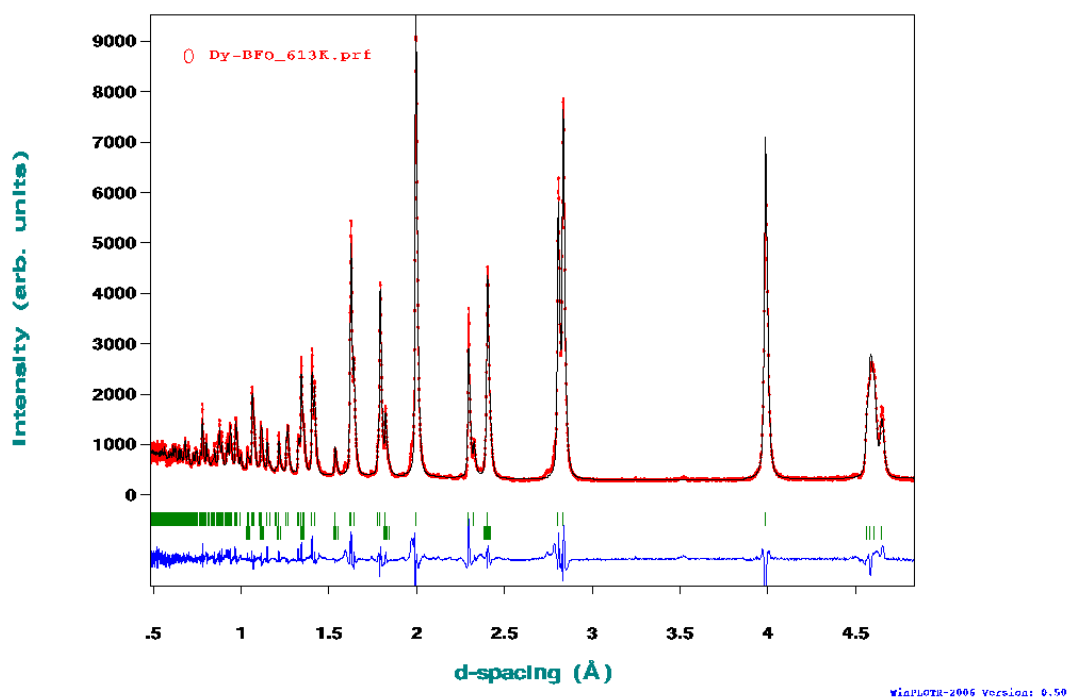
Appendix 3.61 – Rietveld refined WISH diffraction pattern of Dy-BFO at 613 K shown in d-spacing
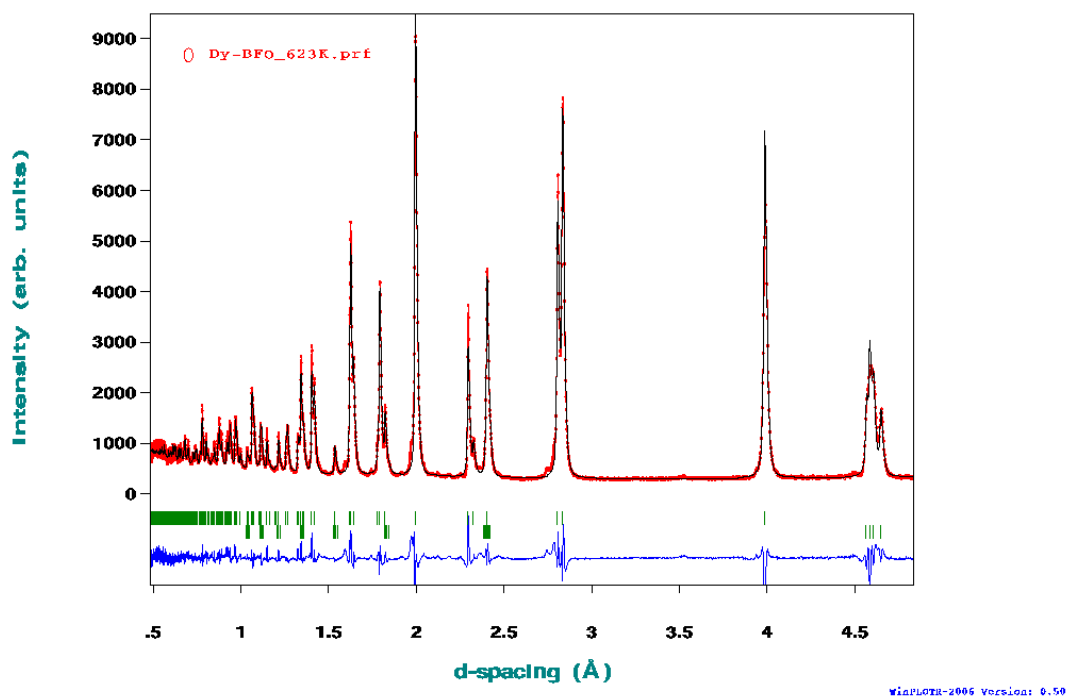
Appendix 3.62 – Rietveld refined WISH diffraction pattern of Dy-BFO at 623 K shown in d-spacing

Dy-BFO 633K
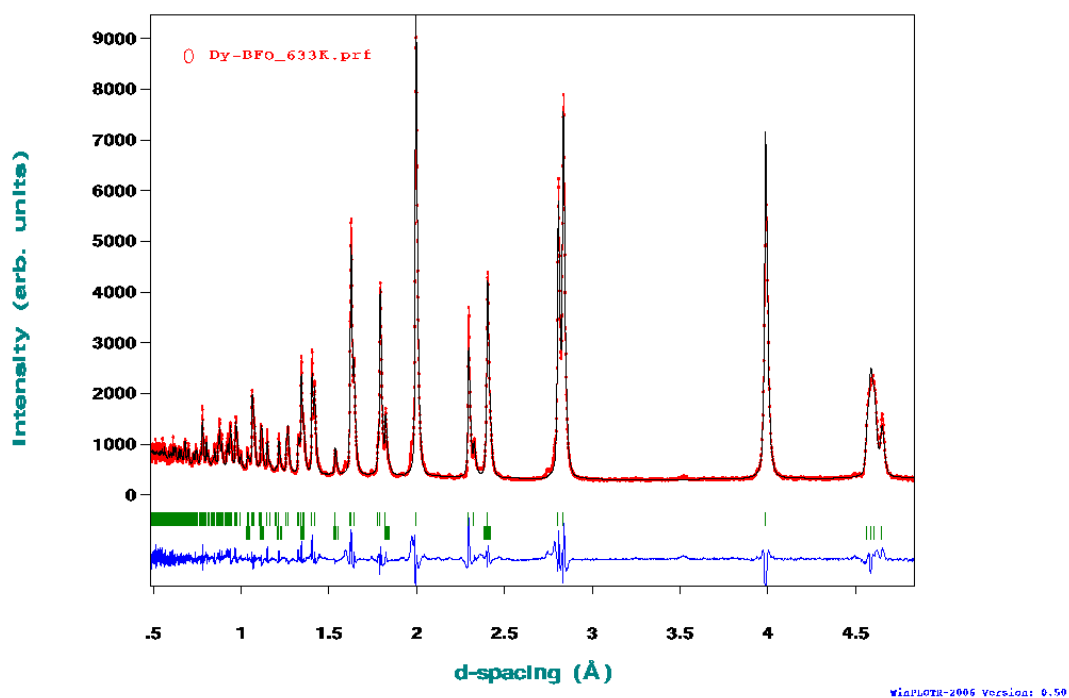
Appendix 3.63 – Rietveld refined WISH diffraction pattern of Dy-BFO at 633 K shown in d-spacing

Dy-BFO 643K
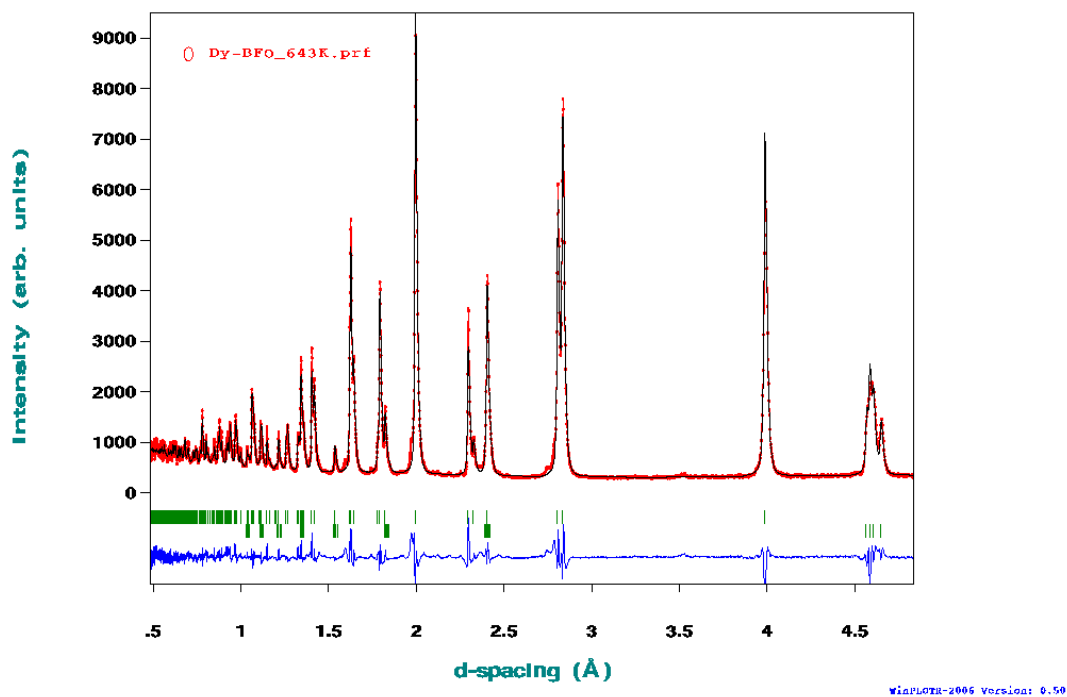
Appendix 3.64 – Rietveld refined WISH diffraction pattern of Dy-BFO at 643 K shown in d-spacing

Dy-BFO 653K
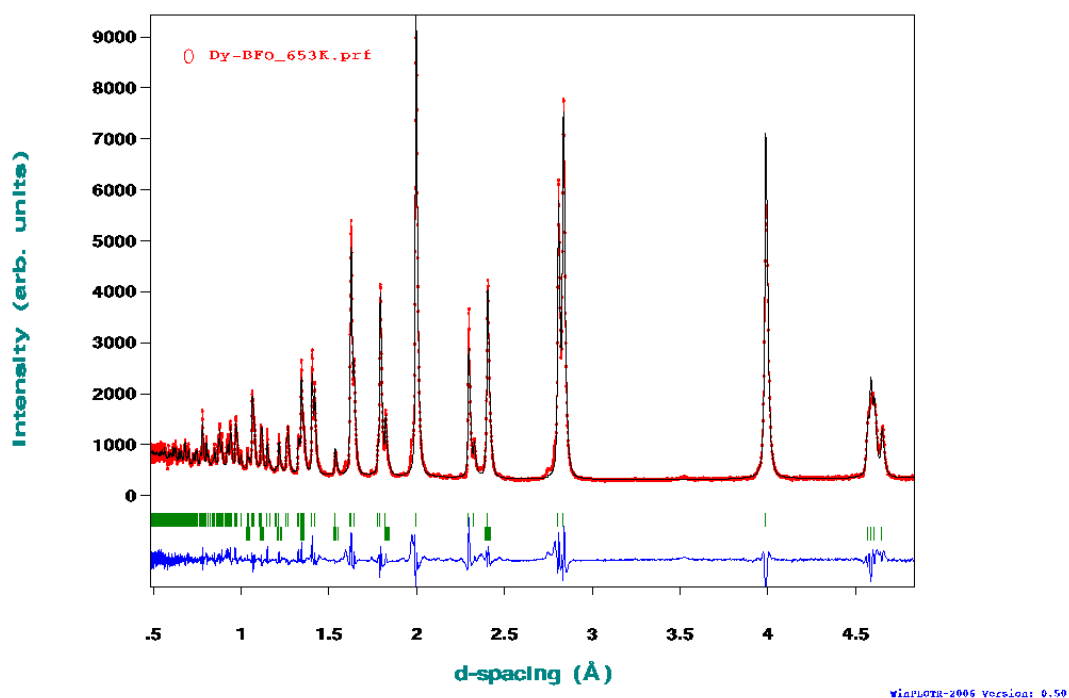
Appendix 3.65 – Rietveld refined WISH diffraction pattern of Dy-BFO at 653 K shown in d-spacing

Dy-BFO 663K
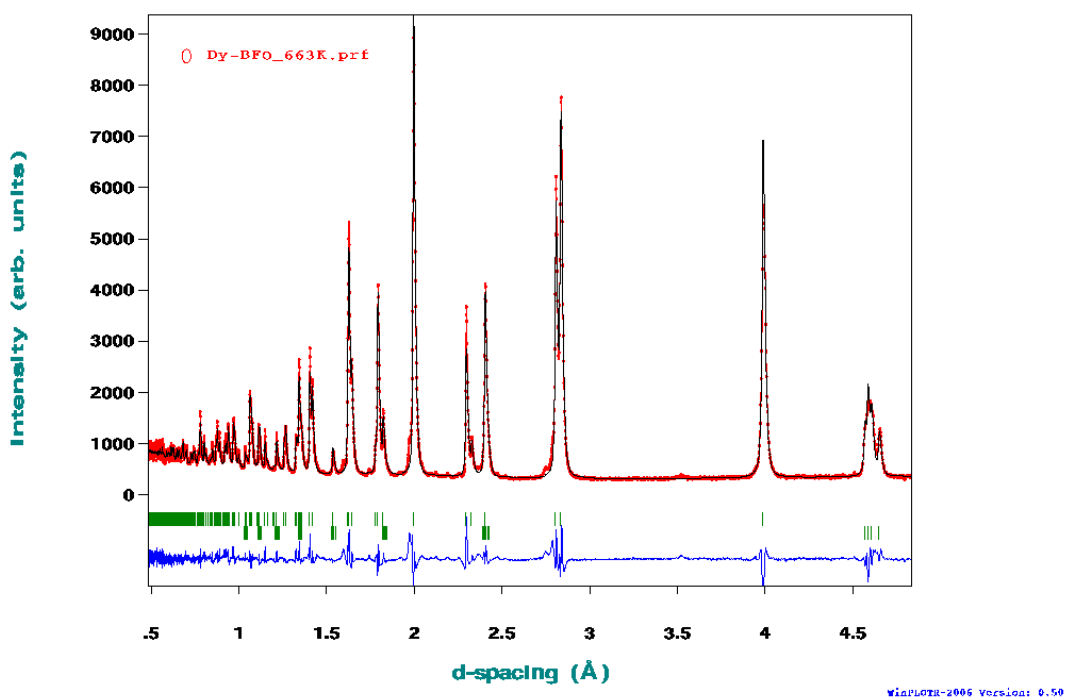
Appendix 3.66 – Rietveld refined WISH diffraction pattern of Dy-BFO at 663 K shown in d-spacing

Dy-BFO 673K
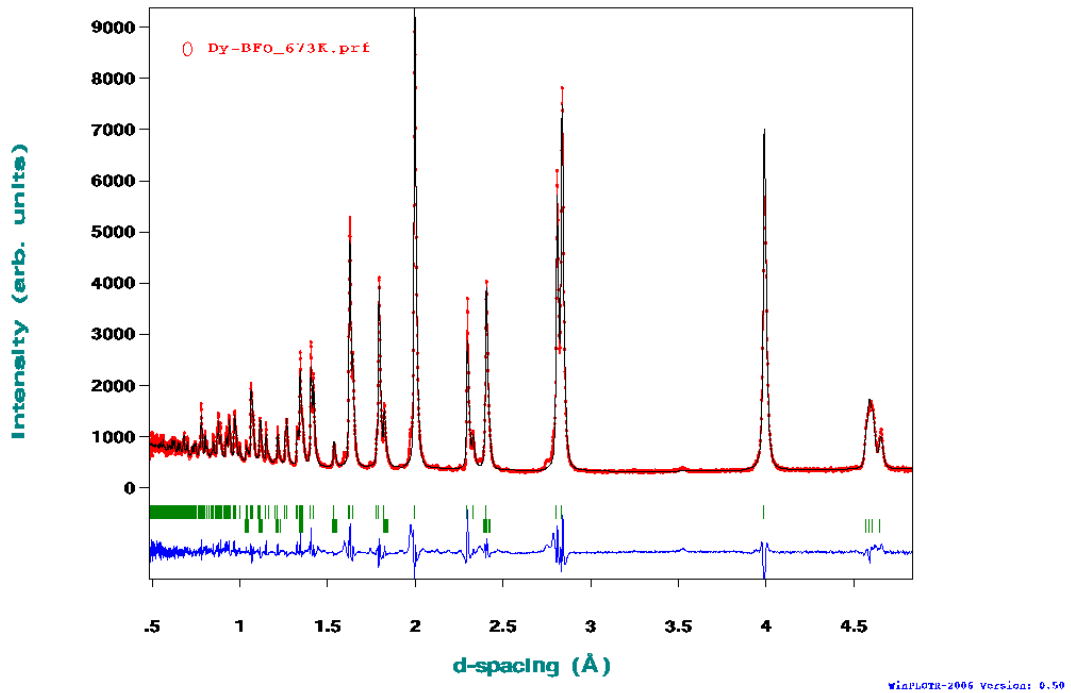
Appendix 3.67 – Rietveld refined WISH diffraction pattern of Dy-BFO at 673 K shown in d-spacing

Appendix 3.68 – Rietveld refined WISH diffraction pattern of Dy-BFO at 683 K shown in d-spacing
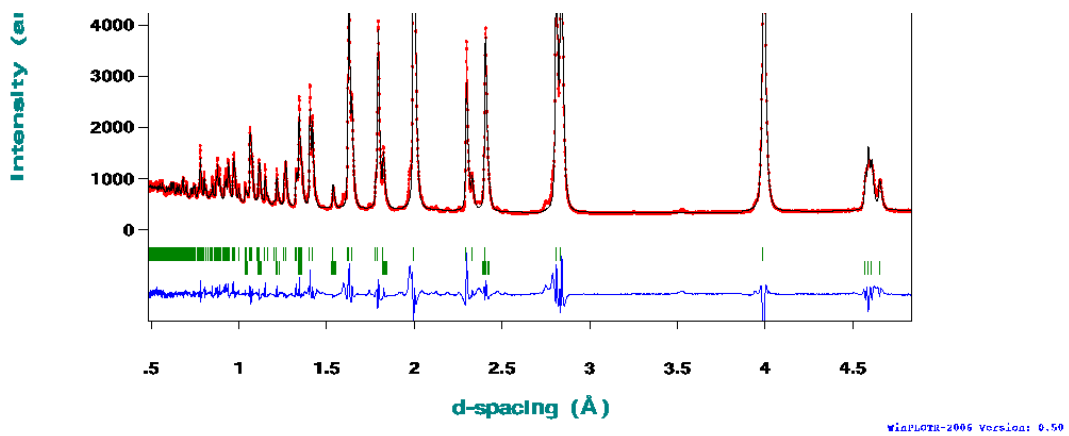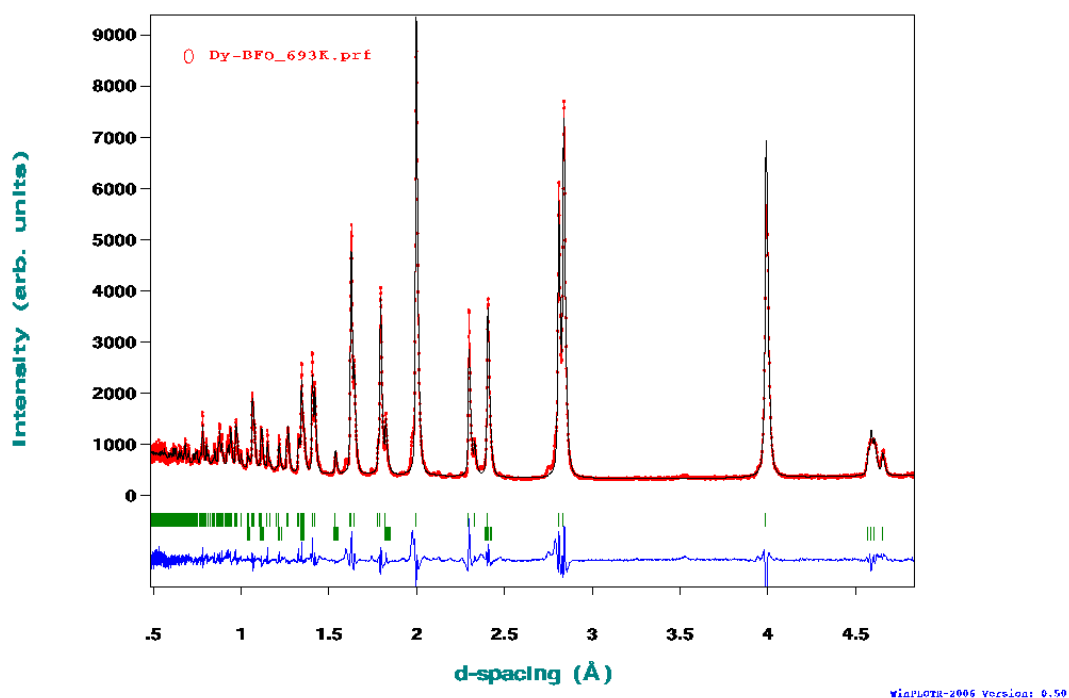
Appendix 3.69– Rietveld refined WISH diffraction pattern of Dy-BFO at 693 K shown in d-spacing
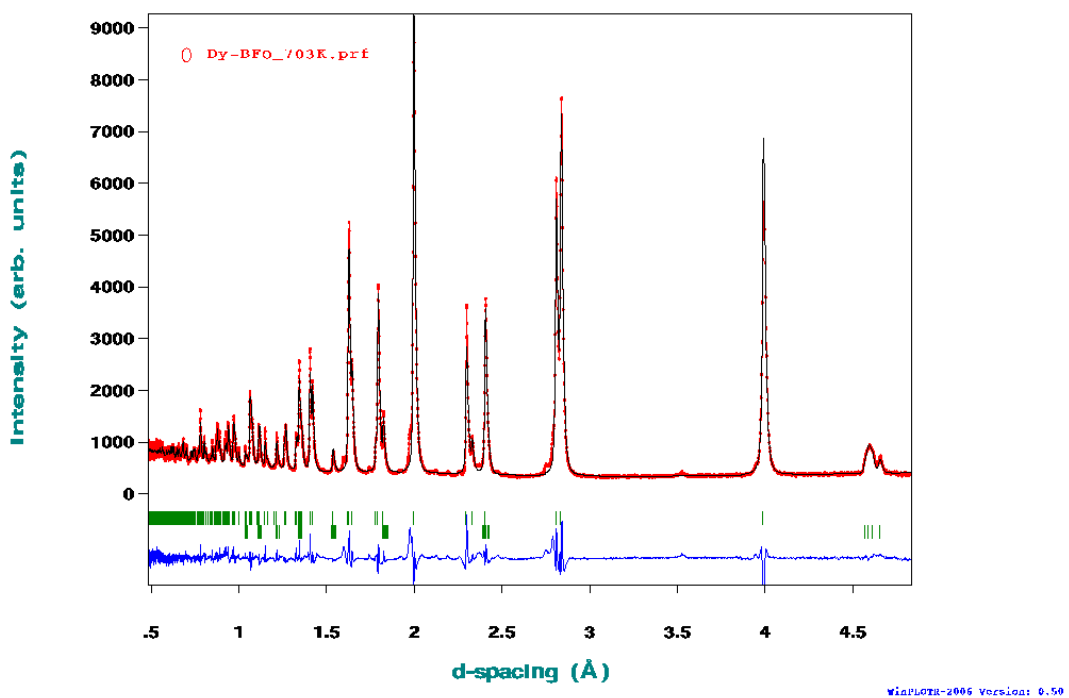
Appendix 3.70 – Rietveld refined WISH diffraction pattern of Dy-BFO at 703 K shown in d-spacing
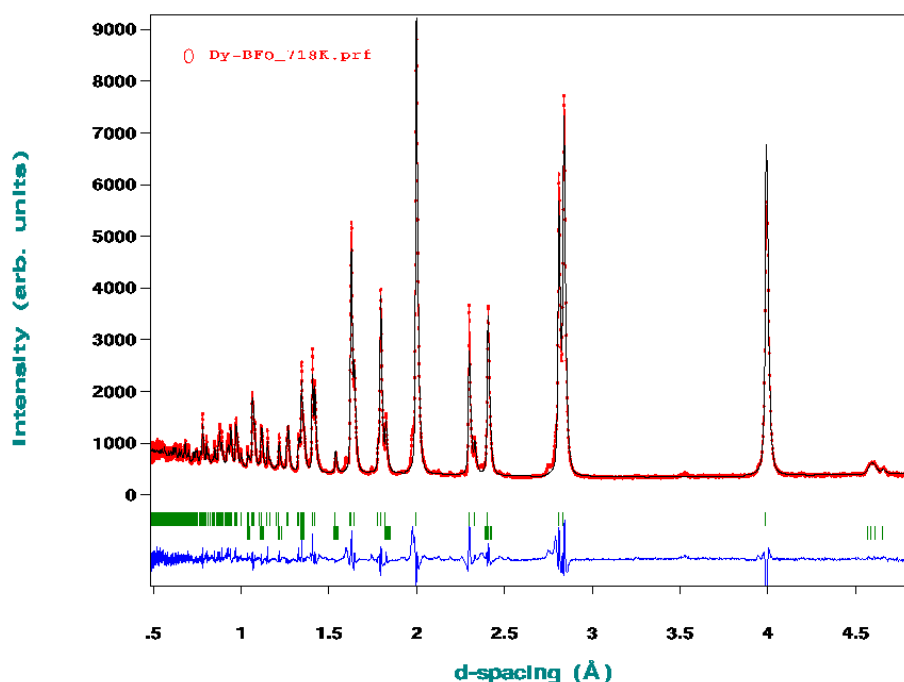
Appendix 3.71 – Rietveld refined WISH diffraction pattern of Dy-BFO at 713 K shown in d-spacing

Appendix 3.72 – bond length/angle data collected from HRPD of *R3c* and *Pbnm* phase

	R3C			Pbnm		
	Bond lengths Å		Bond angle °	Bond lengths Å		Bond angle °
Temp (K)	Fe-O	Fe-O	Fe-O-Fe	Fe-O	Fe-O	Fe-O-Fe
30	2.1042(2)	1.9522(1)	154.100(7)			
50	2.1049(2)	1.9509(1)	154.130(7)			
70	2.1038(2)	1.9521(1)	154.150(7)			
90	2.1041(2)	1.9513(1)	154.250(7)			
110	2.1053(2)	1.9511(1)	154.170(7)			
130	2.1030(2)	1.9528(2)	154.300(7)			
150	2.1035(2)	1.9528(2)	154.290(7)			
170	2.1028(2)	1.9526(2)	154.350(7)			
190	2.1031(2)	1.9539(2)	154.340(7)			
210	2.1028(2)	1.9528(2)	154.480(7)			
230	2.1043(2)	1.9542(2)	154.320(7)			
250	2.1050(2)	1.9533(2)	154.420(8)			
270	2.1053(2)	1.9533(2)	154.460(7)			
373	2.1045(2)	1.9581(2)	154.530(8)			
473	2.1086(2)	1.9572(2)	154.700(9)			
573	2.1101(2)	1.9603(2)	154.76(10)			
673	2.1115(3)	1.9627(3)	154.98(11)			
773	2.1232(2)	1.9514(2)	155.650(9)	2.011(8)	0.71(34)	156.8(22)
778	2.1215(3)	1.9543(3)	155.52(12)	1.995(8)	0.75(5)	161.7(28)
793	2.1224(3)	1.9518(3)	155.81(12)	2.003(7)	0.84(5)	159.2(22)
803	2.1179(3)	1.9564(3)	155.78(12)	2.008(5)	0.71(4)	157.9(16)
813	2.1260(4)	1.9500(4)	155.81(13)	1.991(5)	0.72(25)	164.0(20)
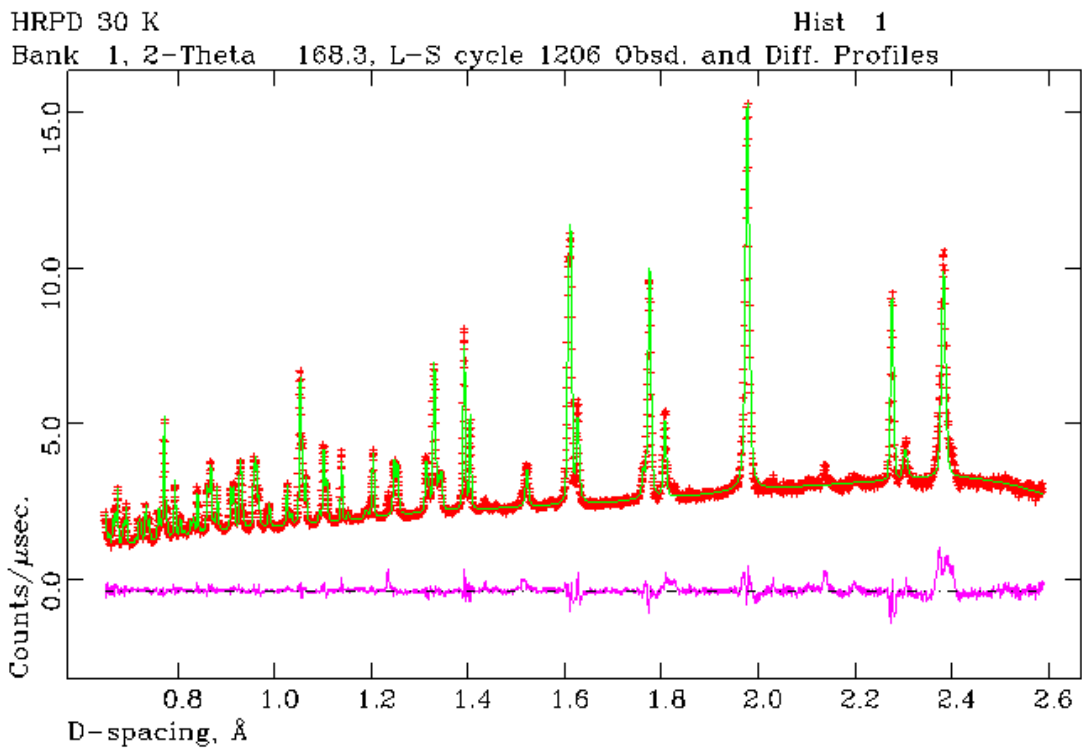
Appendix 3.73 – Rietveld refined HRPD pattern of Dy-BFO at 30 K shown in d-spacing
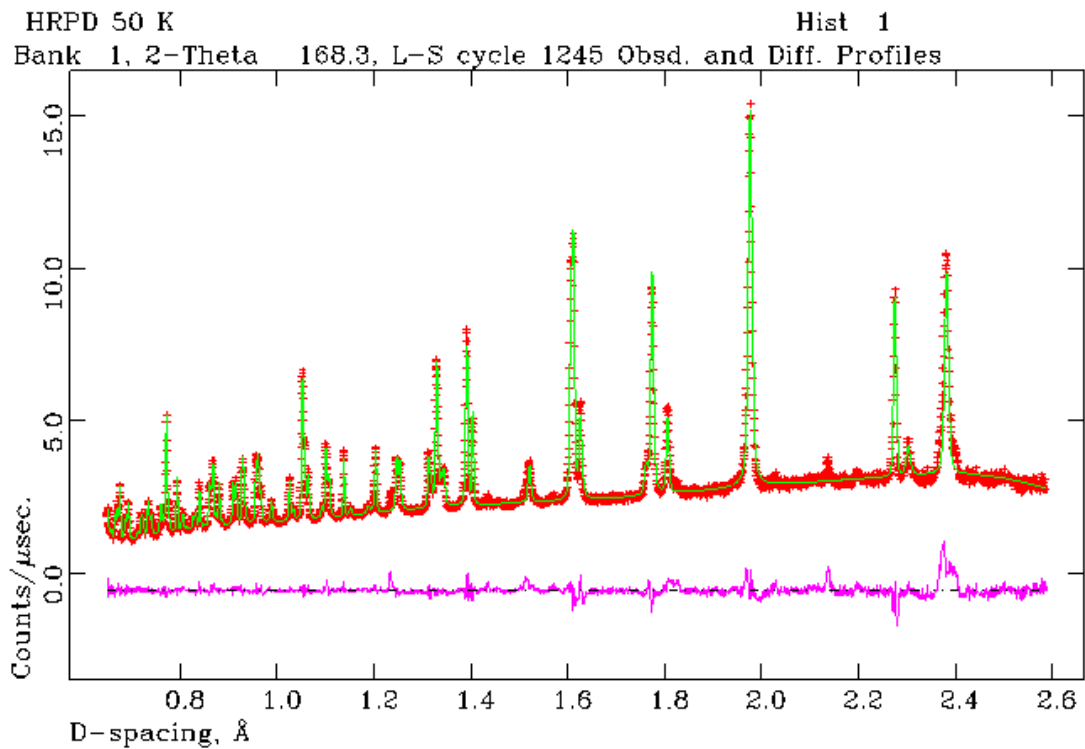
Appendix 3.74 – Rietveld refined HRPD pattern of Dy-BFO at 50 K shown in d-spacing
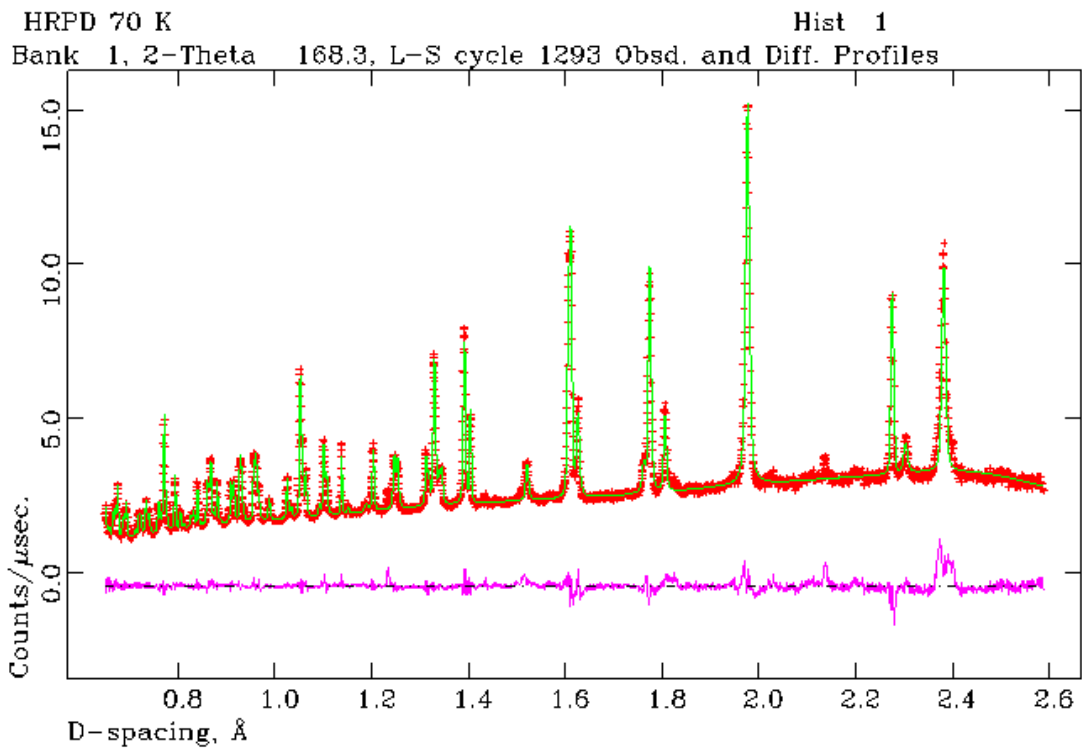
Appendix 3.75 – Rietveld refined HRPD pattern of Dy-BFO at 70 K shown in d-spacing
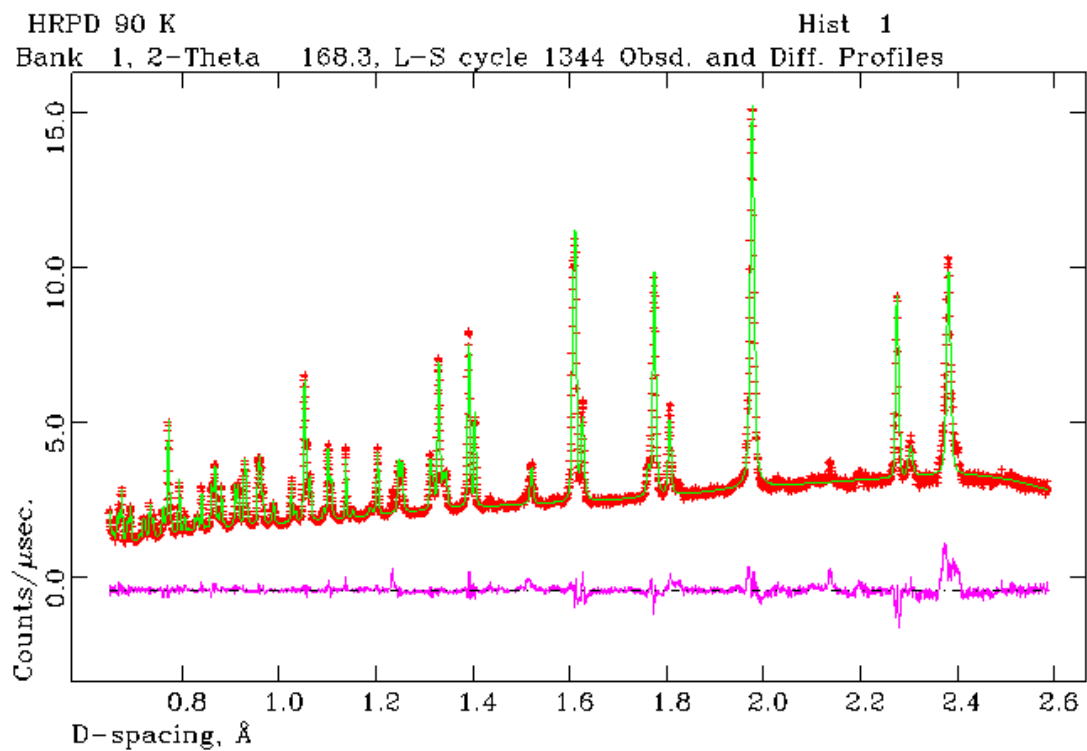
Appendix 3.76 – Rietveld refined HRPD pattern of Dy-BFO at 90 K shown in d-spacing
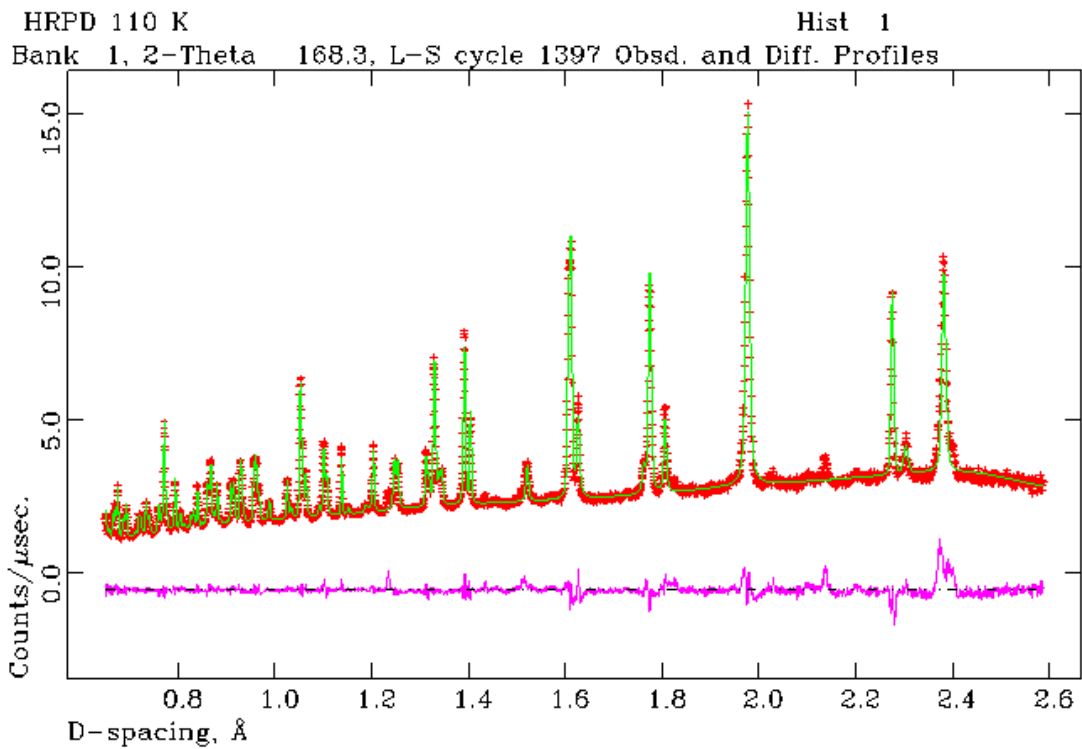
Appendix 3.77 – Rietveld refined HRPD pattern of Dy-BFO at 110 K shown in d-spacing
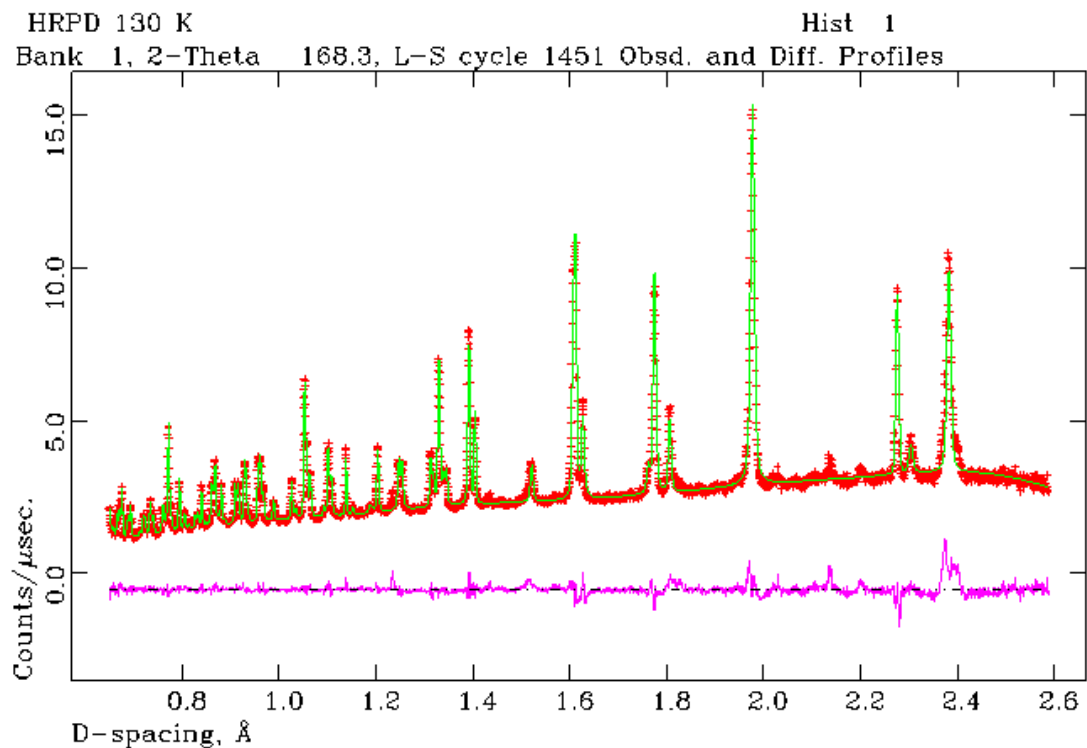
Appendix 3.78 – Rietveld refined HRPD pattern of Dy-BFO at 130 K shown in d-spacing
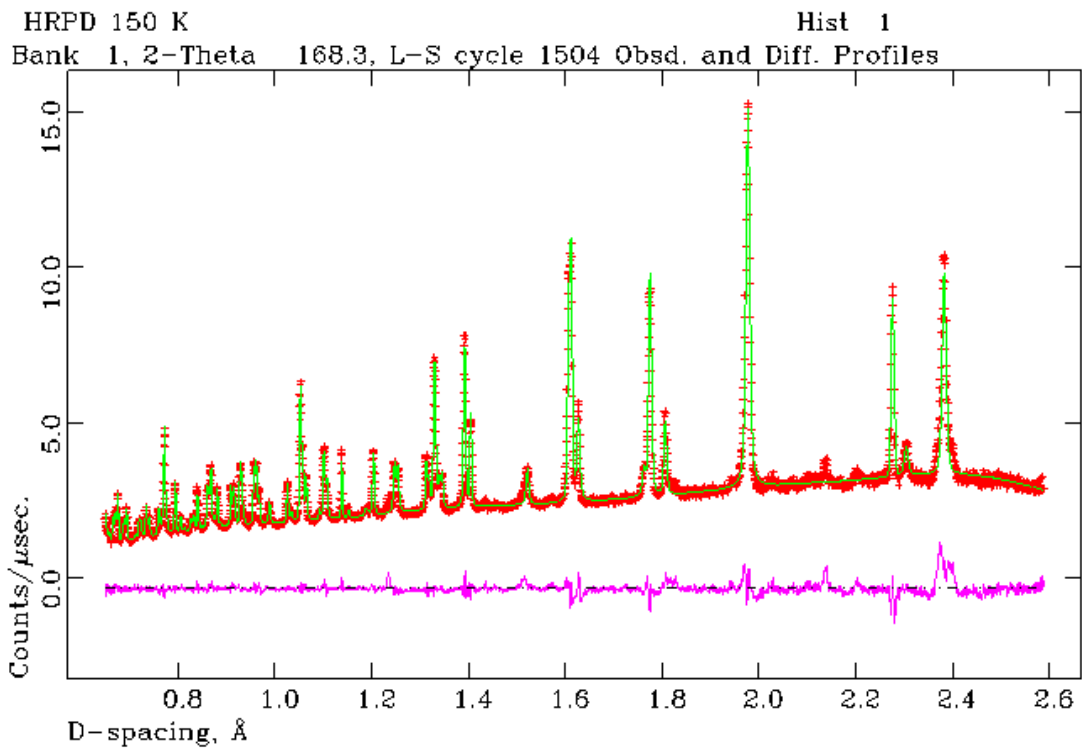
Appendix 3.79 – Rietveld refined HRPD pattern of Dy-BFO at 150 K shown in d-spacing
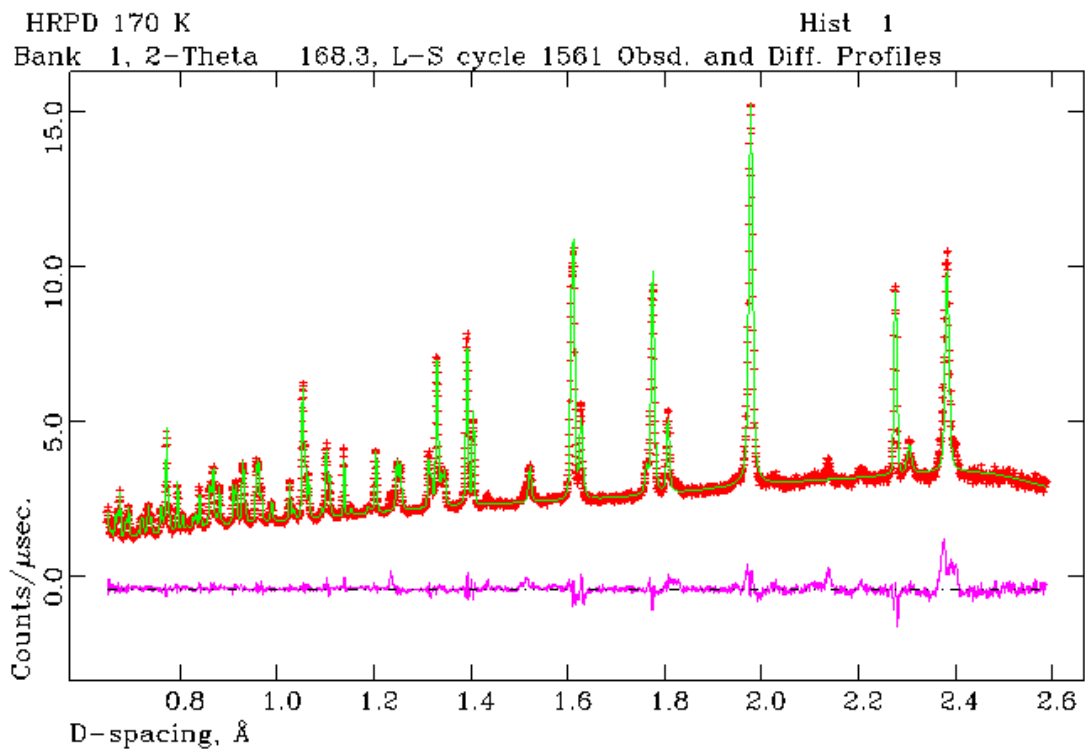
Appendix 3.80 – Rietveld refined HRPD pattern of Dy-BFO at 170 K shown in d-spacing
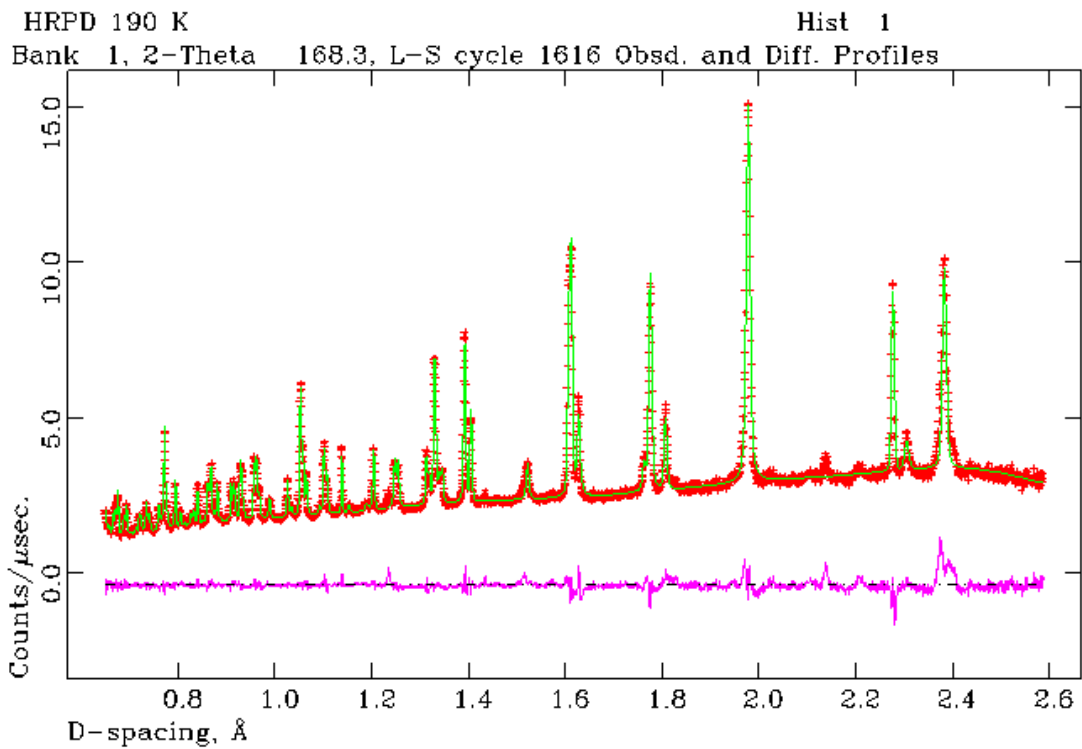
Appendix 3.81 – Rietveld refined HRPD pattern of Dy-BFO at 190 K shown in d-spacing
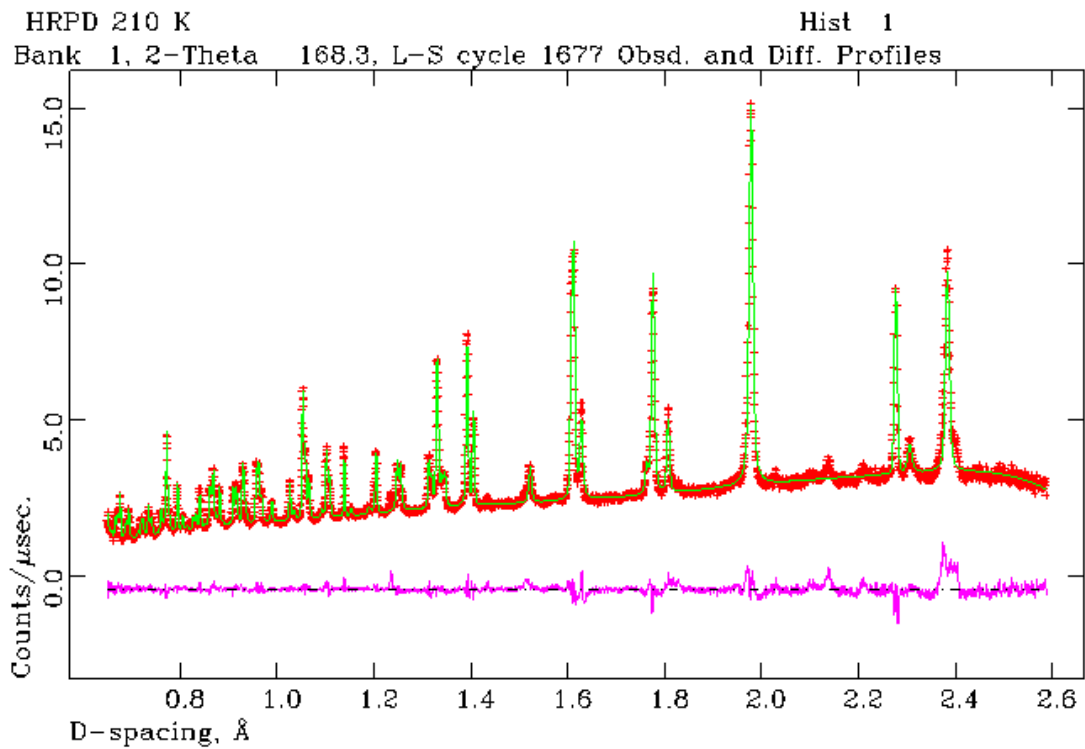
Appendix 3.82 – Rietveld refined HRPD pattern of Dy-BFO at 210 K shown in d-spacing
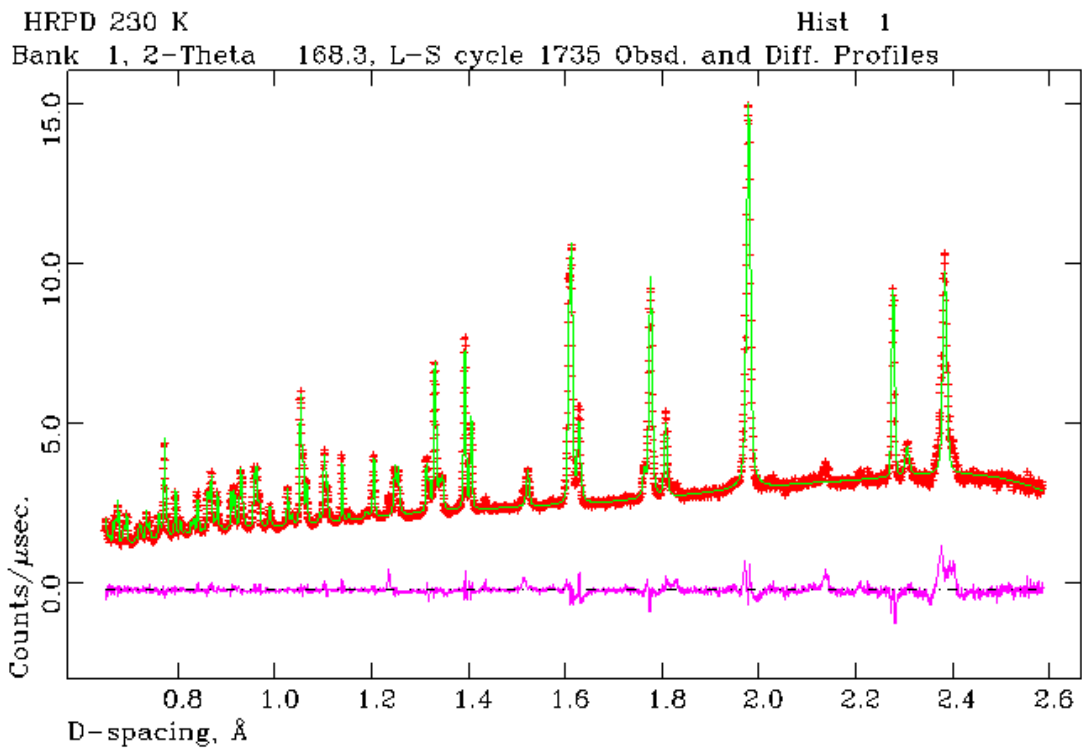
Appendix 3.83 – Rietveld refined HRPD pattern of Dy-BFO at 230 K shown in d-spacing
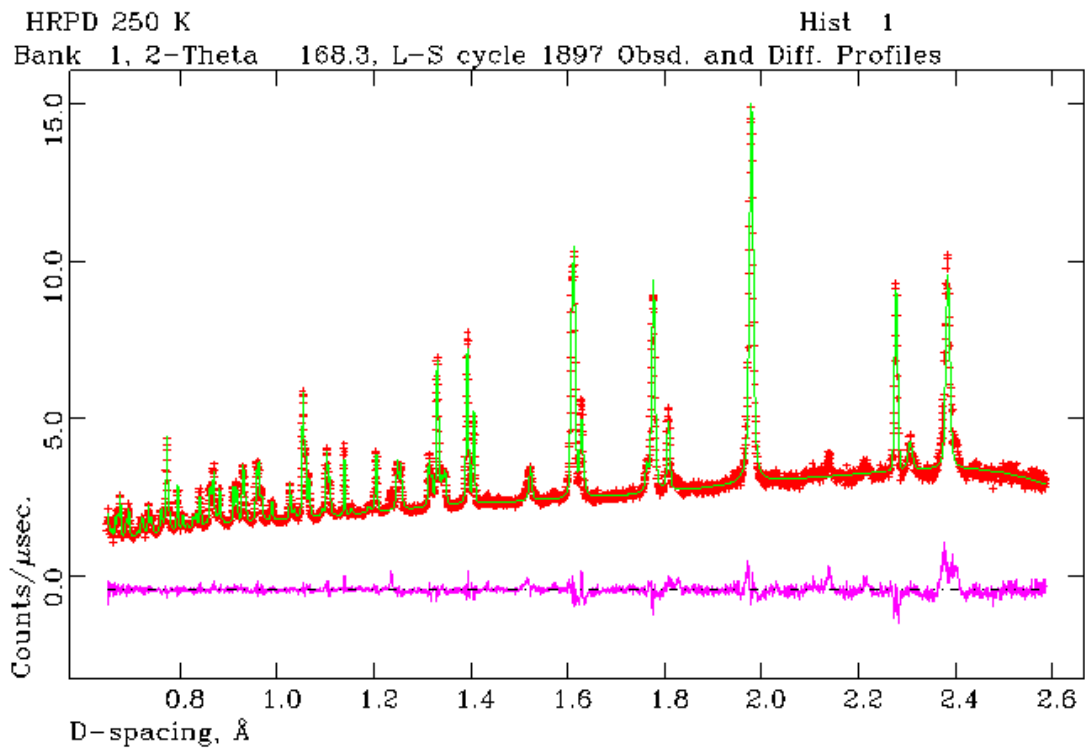
Appendix 3.84 – Rietveld refined HRPD pattern of Dy-BFO at 250 K shown in d-spacing
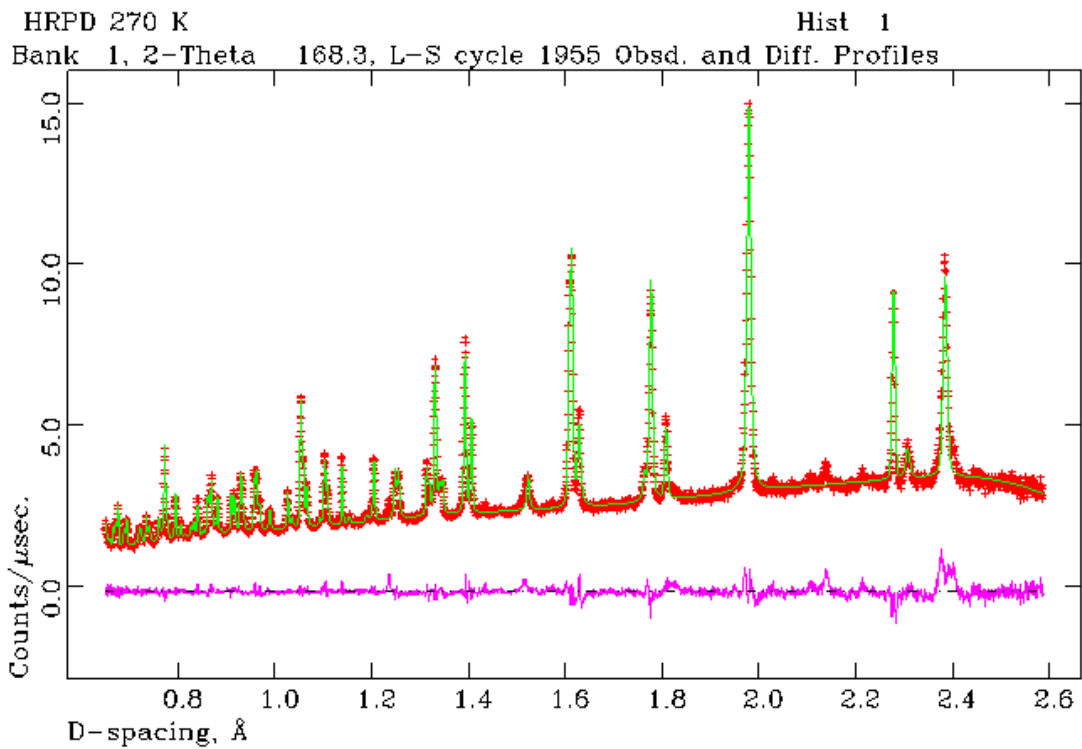
Appendix 3.85 – Rietveld refined HRPD pattern of Dy-BFO at 270 K shown in d-spacing
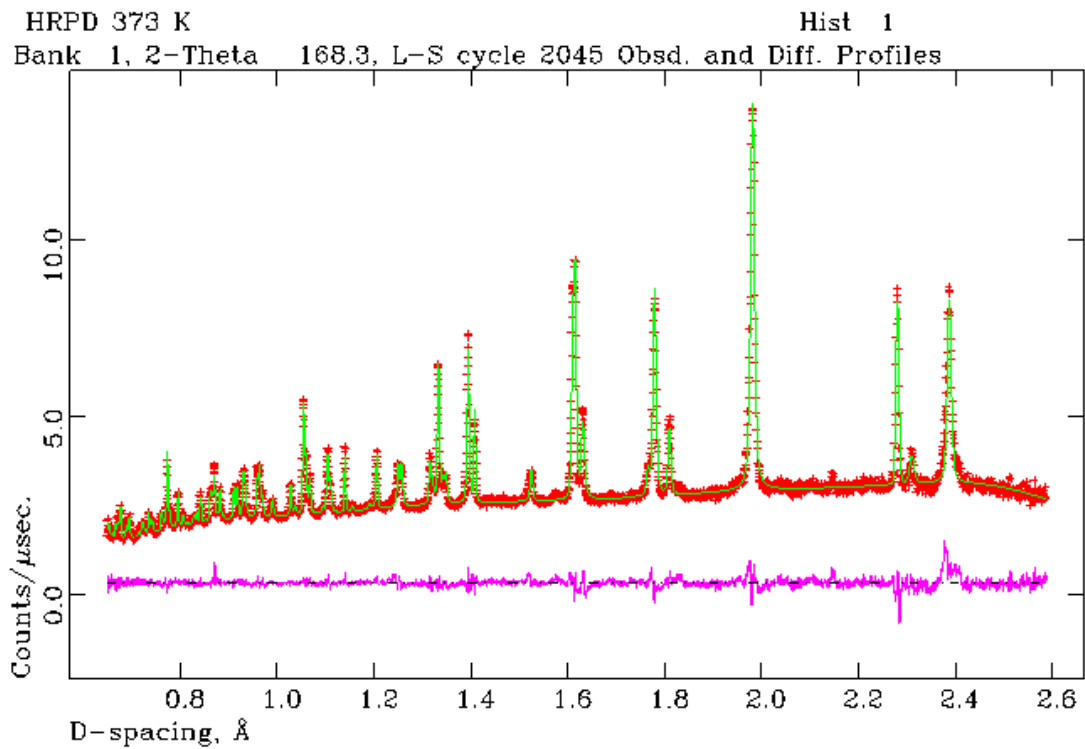
Appendix 3.86 – Rietveld refined HRPD pattern of Dy-BFO at 373 K shown in d-spacing
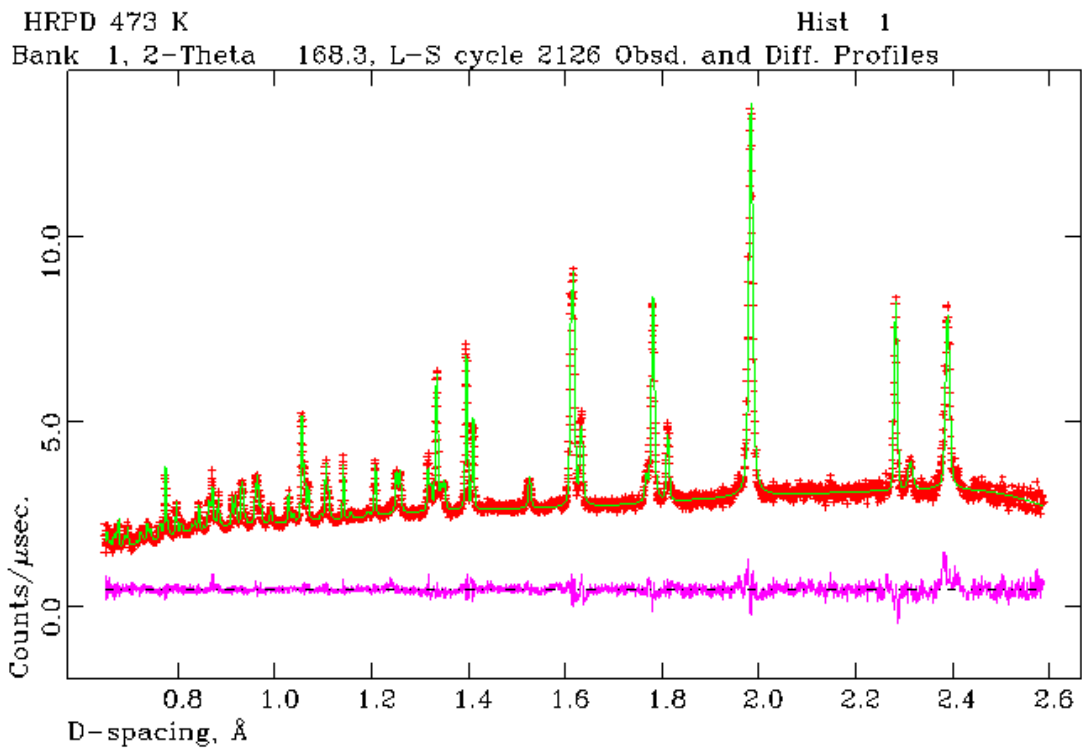
Appendix 3.87 – Rietveld refined HRPD pattern of Dy-BFO at 473 K shown in d-spacing
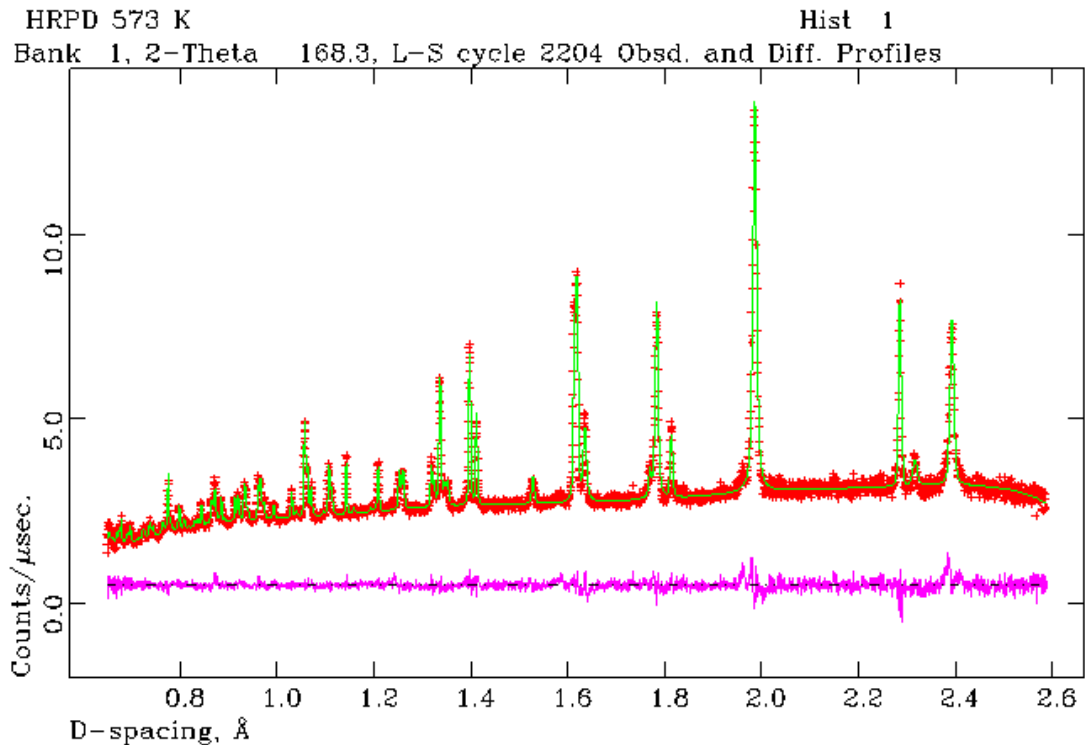
Appendix 3.88 – Rietveld refined HRPD pattern of Dy-BFO at 573 K shown in d-spacing
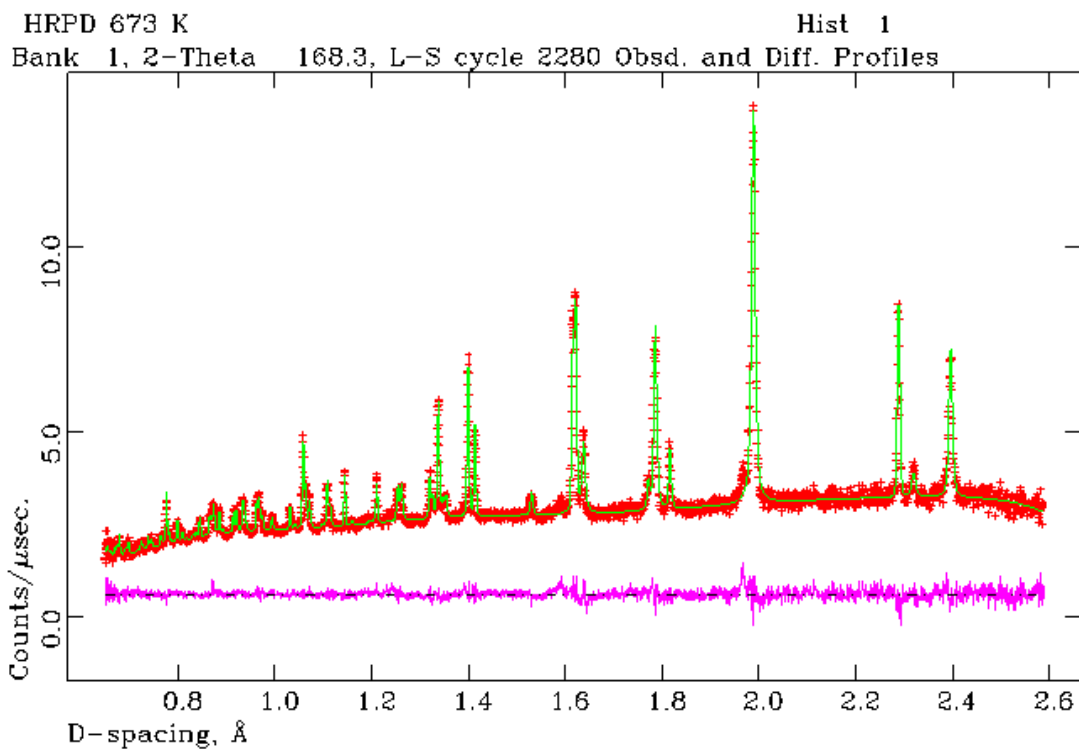
Appendix 3.89 – Rietveld refined HRPD pattern of Dy-BFO at 673 K shown in d-spacing
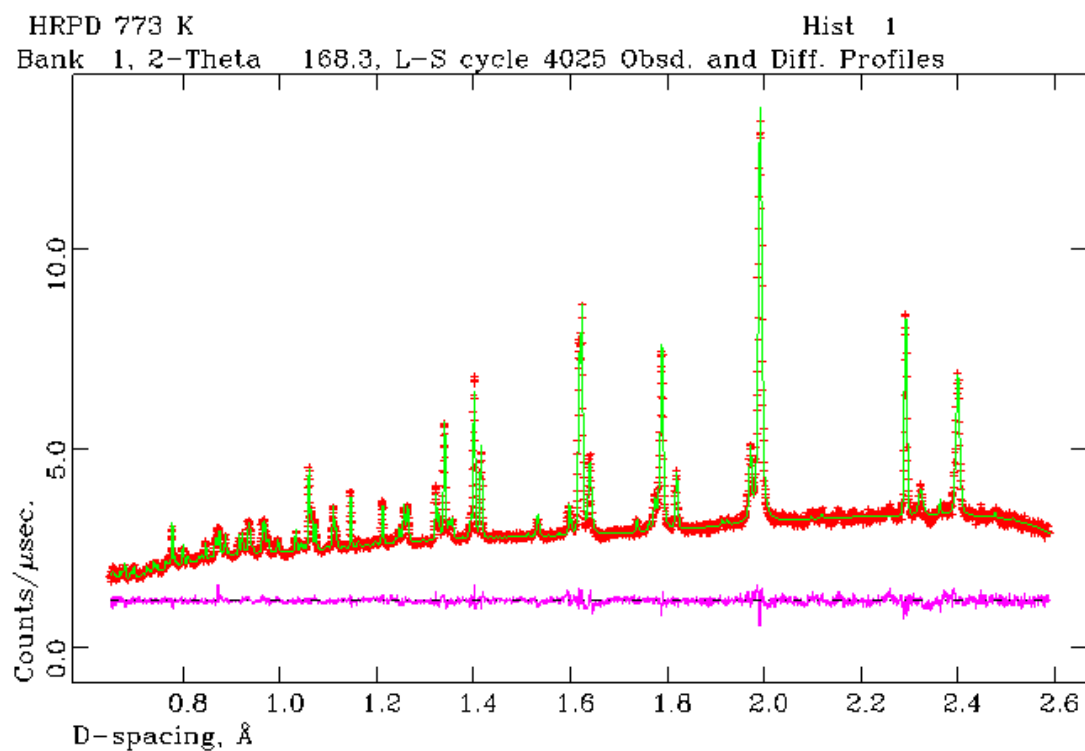
Appendix 3.90 – Rietveld refined HRPD pattern of Dy-BFO at 773 K shown in d-spacing
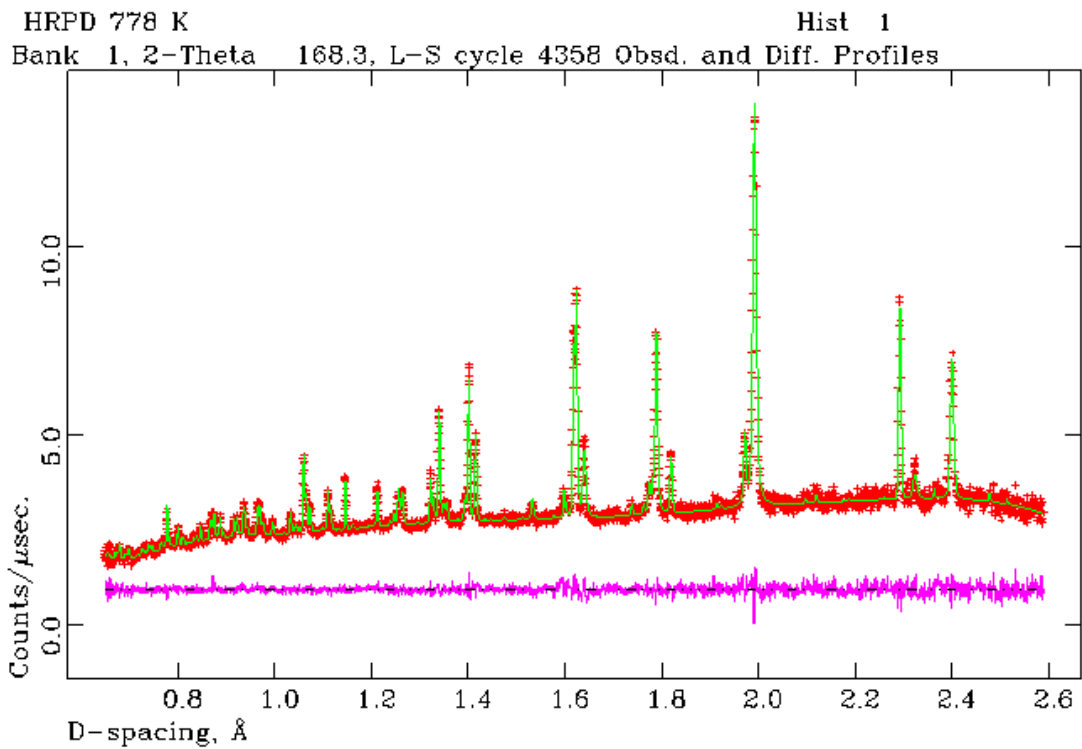
Appendix 3.91 – Rietveld refined HRPD pattern of Dy-BFO at 778 K shown in d-spacing
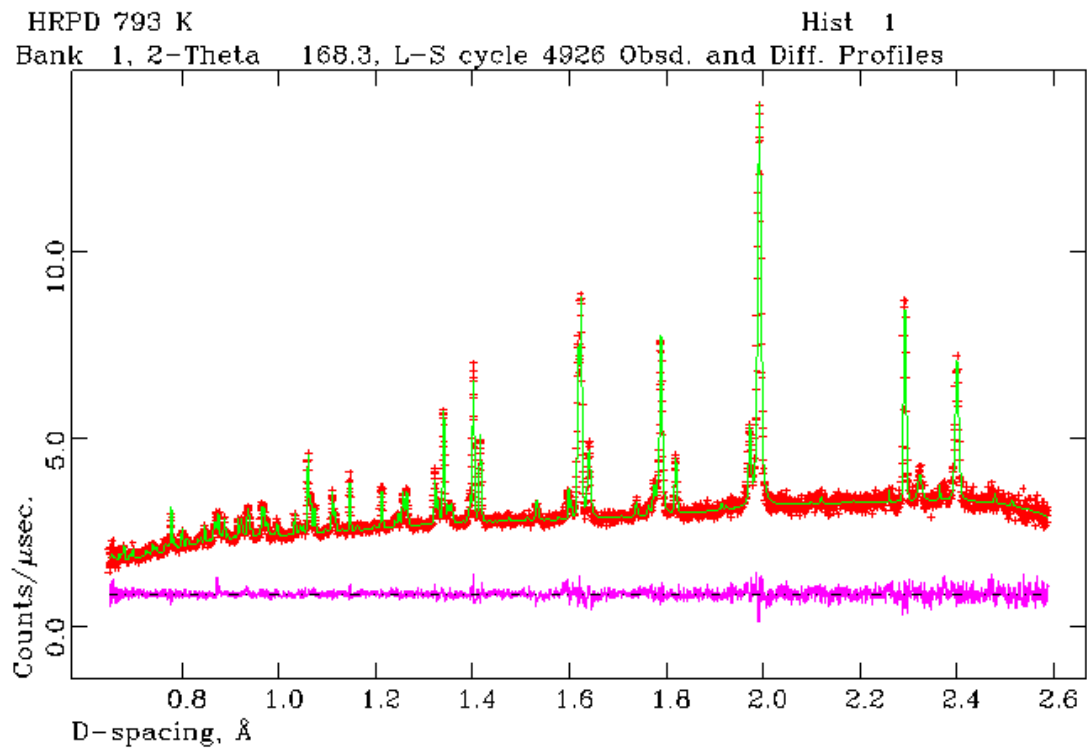
Appendix 3.92 – Rietveld refined HRPD pattern of Dy-BFO at 793 K shown in d-spacing
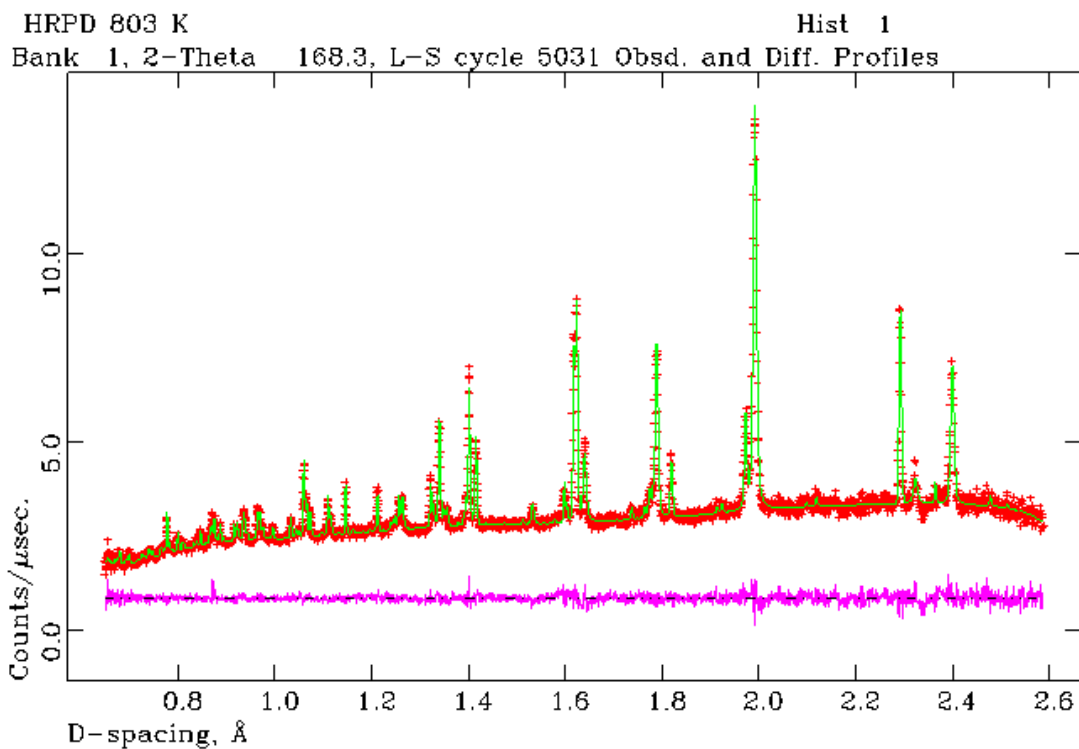
Appendix 3.93 – Rietveld refined HRPD pattern of Dy-BFO at 803 K shown in d-spacing
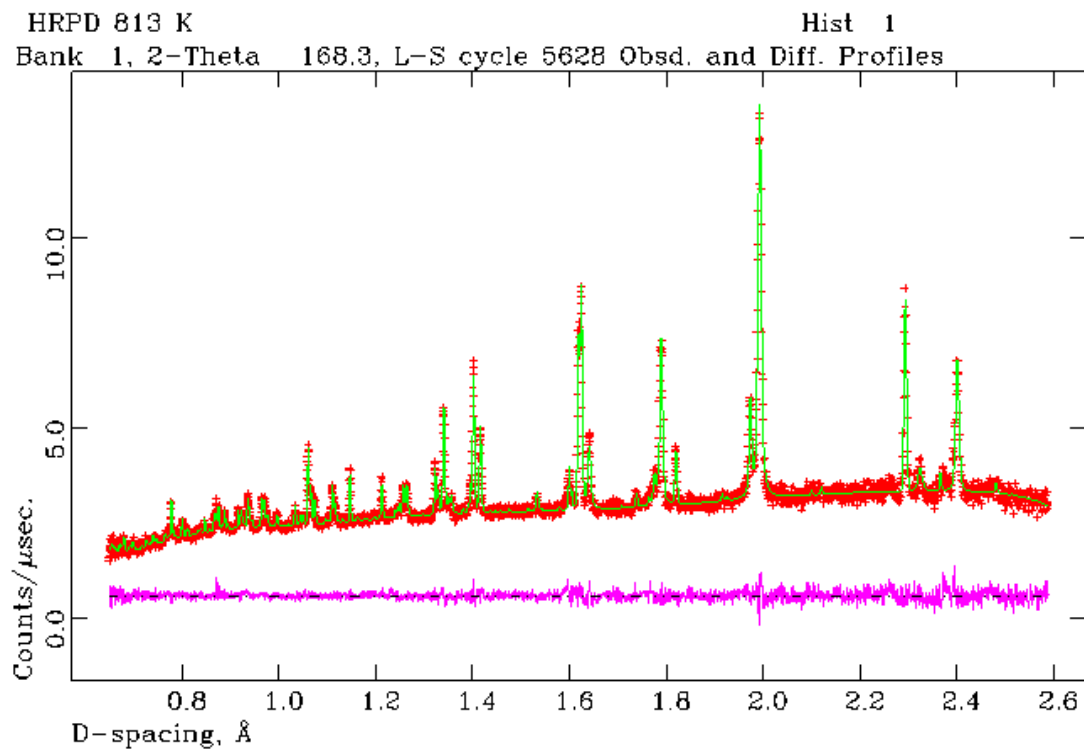
Appendix 3.94 – Rietveld refined HRPD pattern of Dy-BFO at 813 K shown in d-spacing
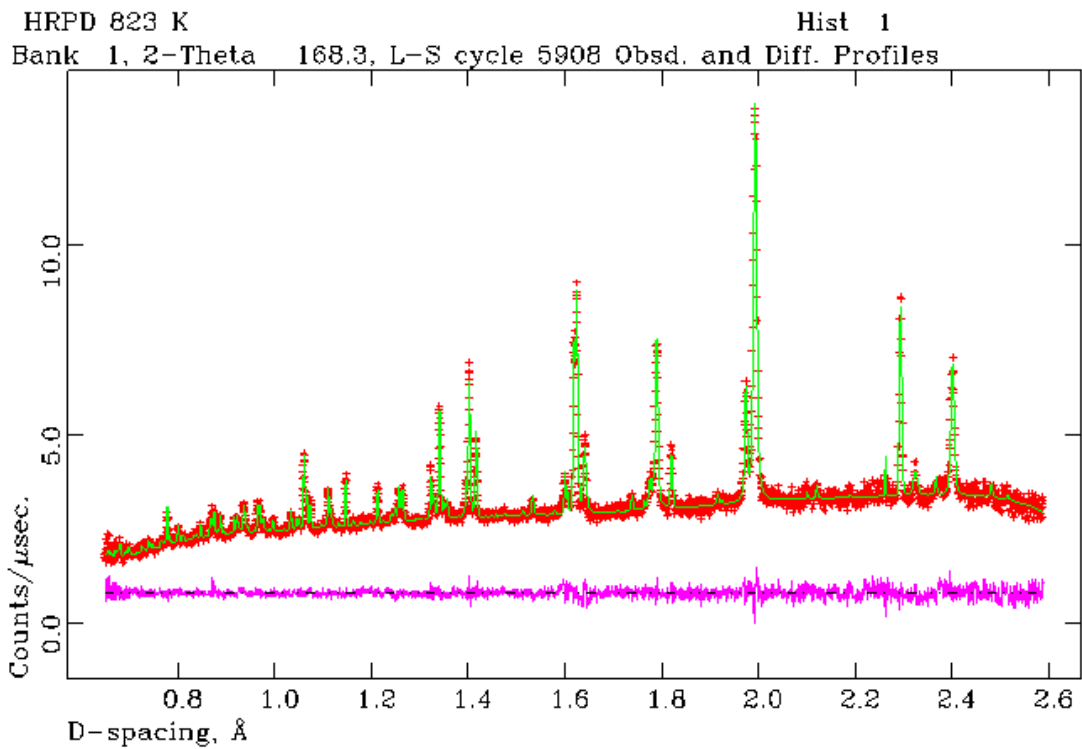
Appendix 3.95 – Rietveld refined HRPD pattern of Dy-BFO at 823 K shown in d-spacing
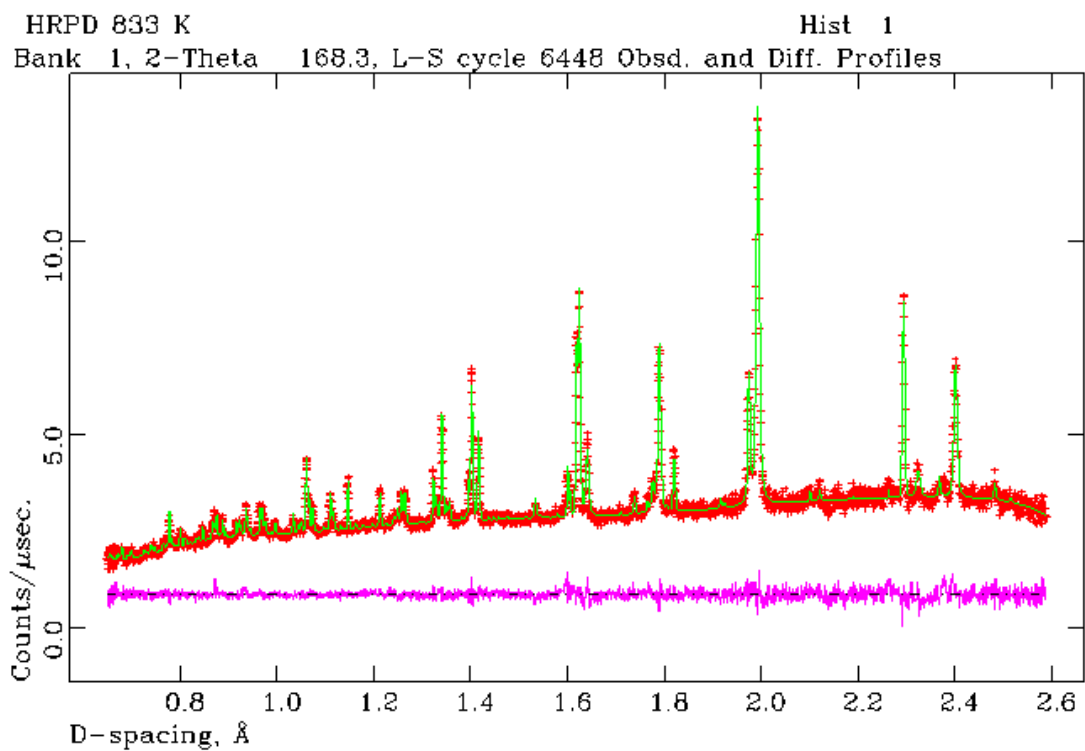
Appendix 3.96 – Rietveld refined HRPD pattern of Dy-BFO at 833 K shown in d-spacing
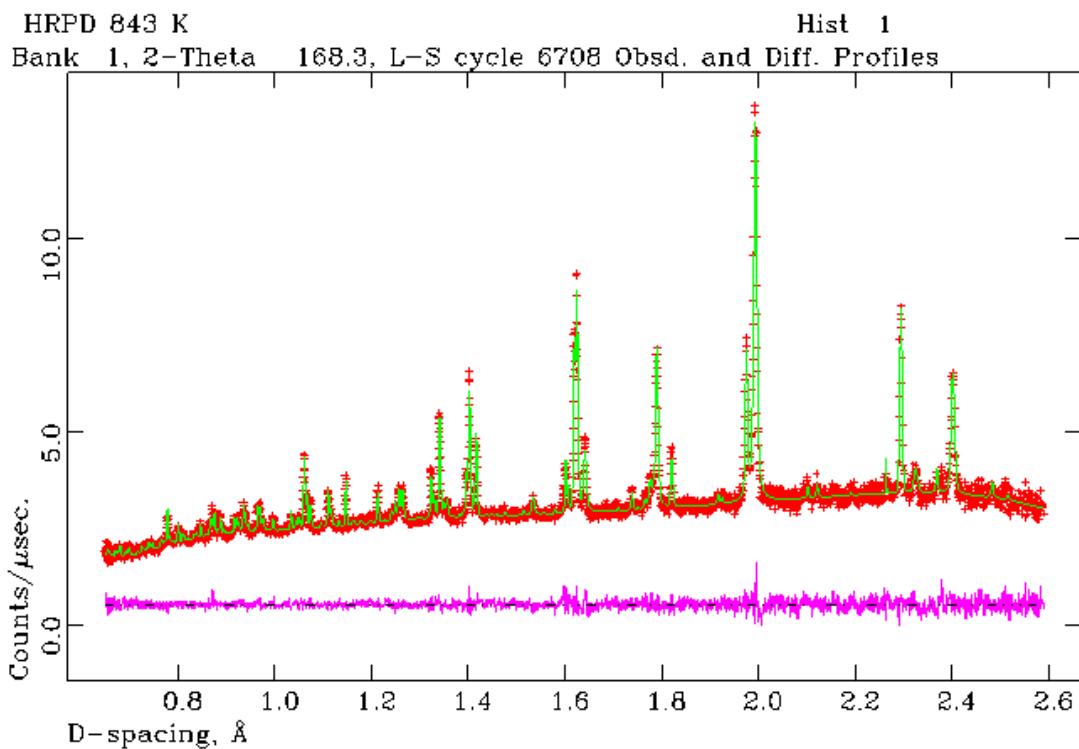
Appendix 3.97 – Rietveld refined HRPD pattern of Dy-BFO at 843 K shown in d-spacing
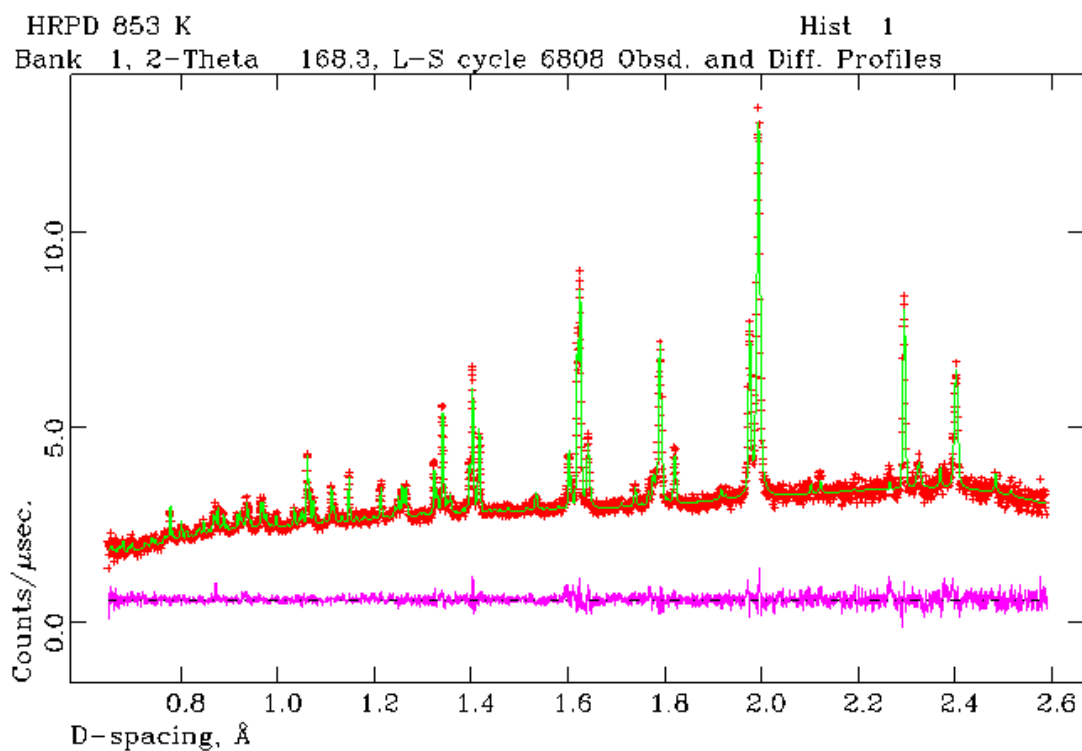
Appendix 3.98 – Rietveld refined HRPD pattern of Dy-BFO at 853 K shown in d-spacing
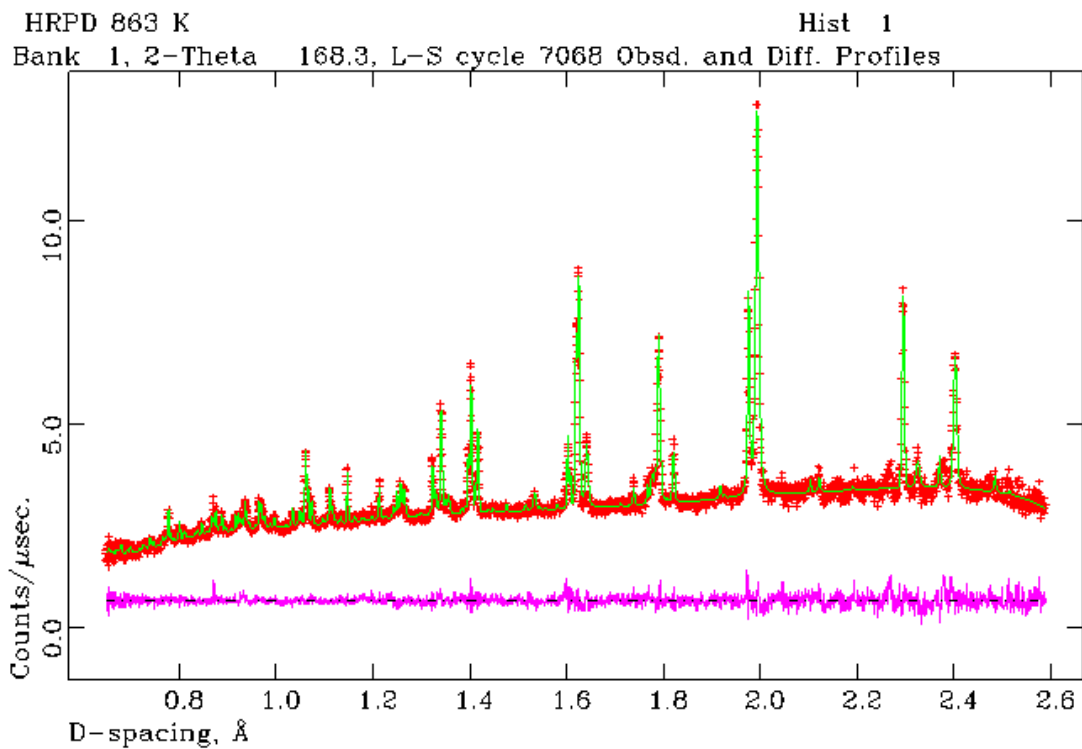
Appendix 3.99 – Rietveld refined HRPD pattern of Dy-BFO at 863 K shown in d-spacing
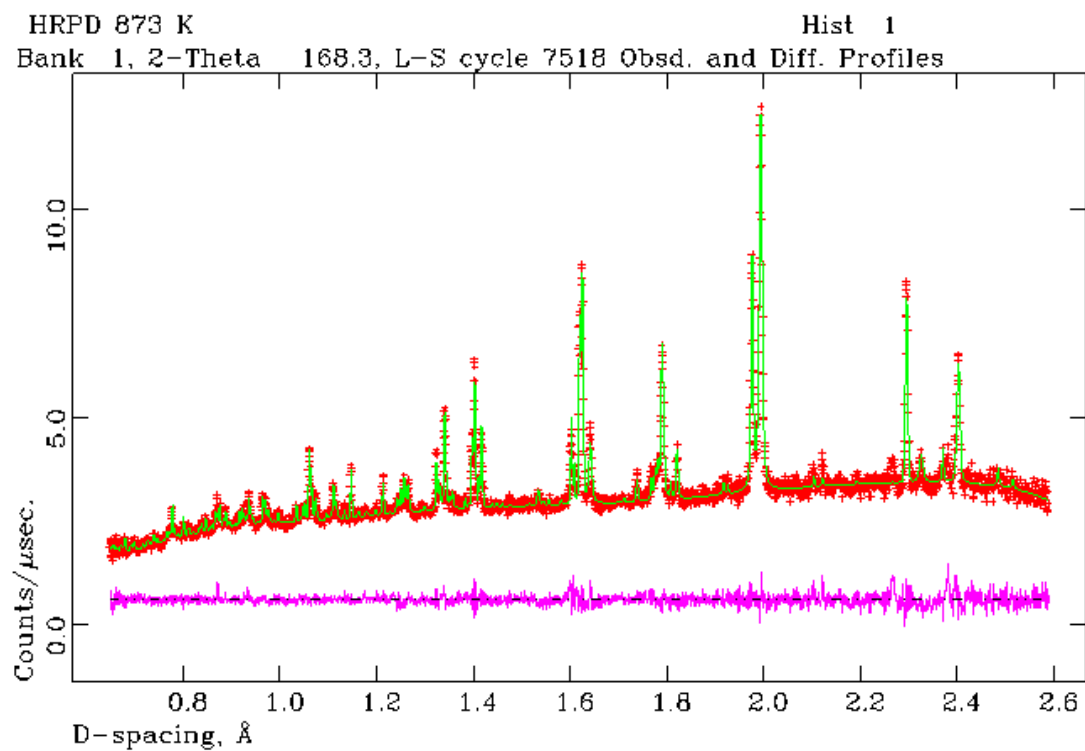
Appendix 3.100 – Rietveld refined HRPD pattern of Dy-BFO at 873 K shown in d-spacing
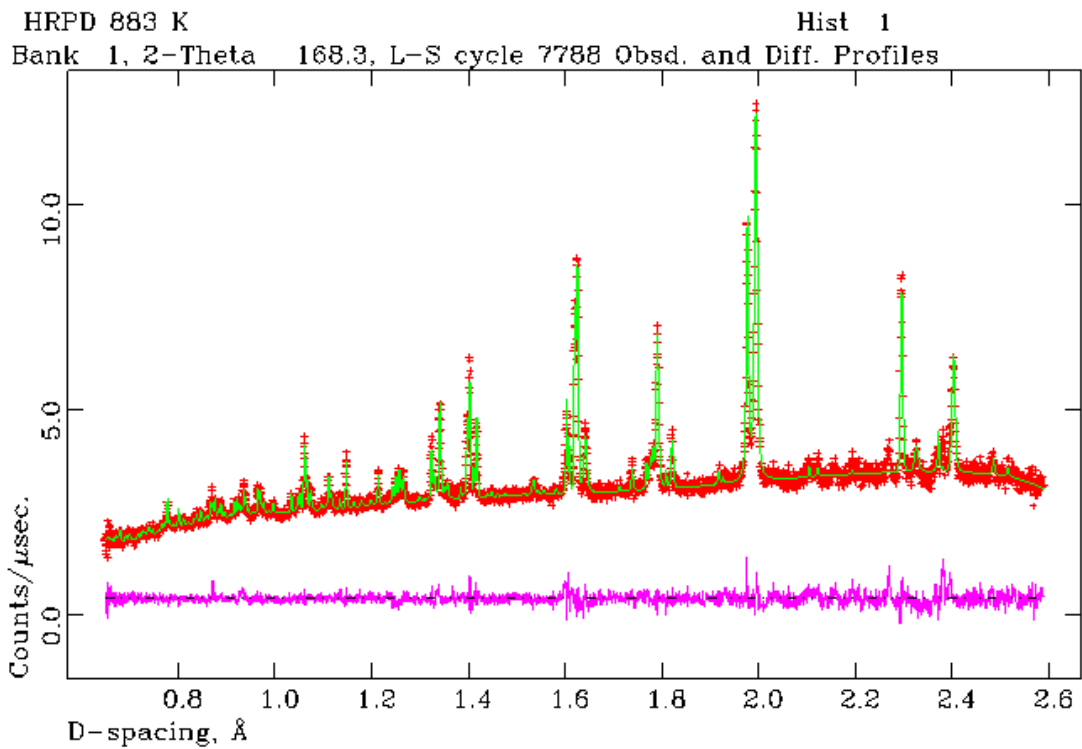
Appendix 3.100 – Rietveld refined HRPD pattern of Dy-BFO at 883 K shown in d-spacing
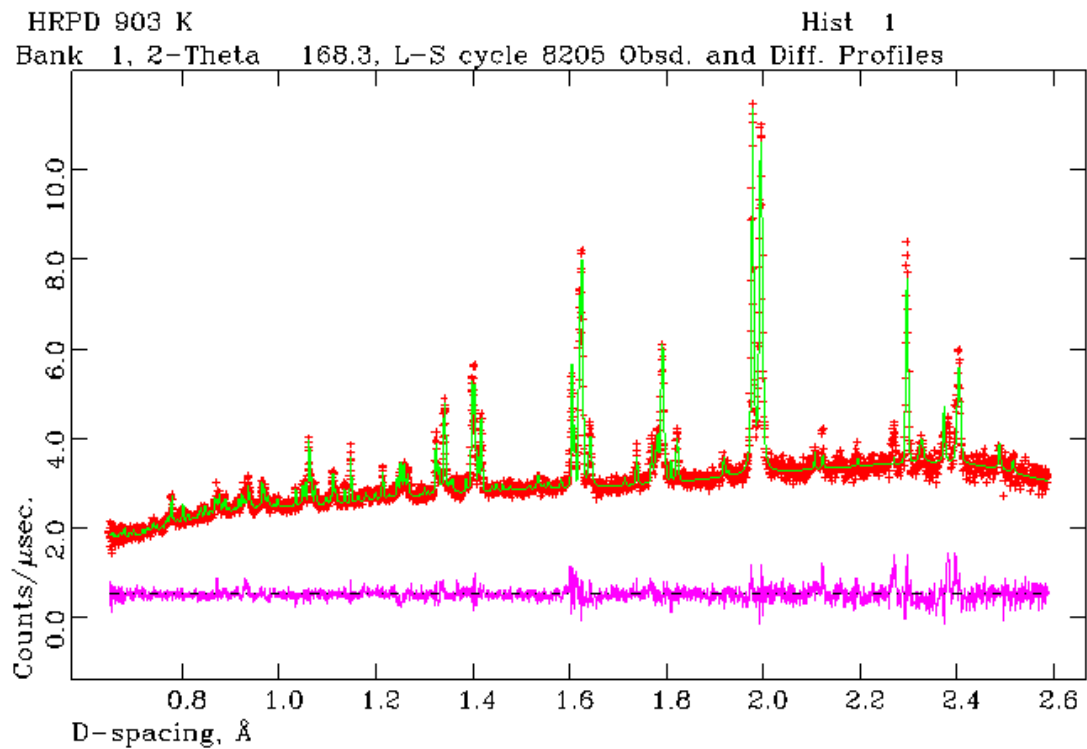
Appendix 3.101 – Rietveld refined HRPD pattern of Dy-BFO at 903 K shown in d-spacing
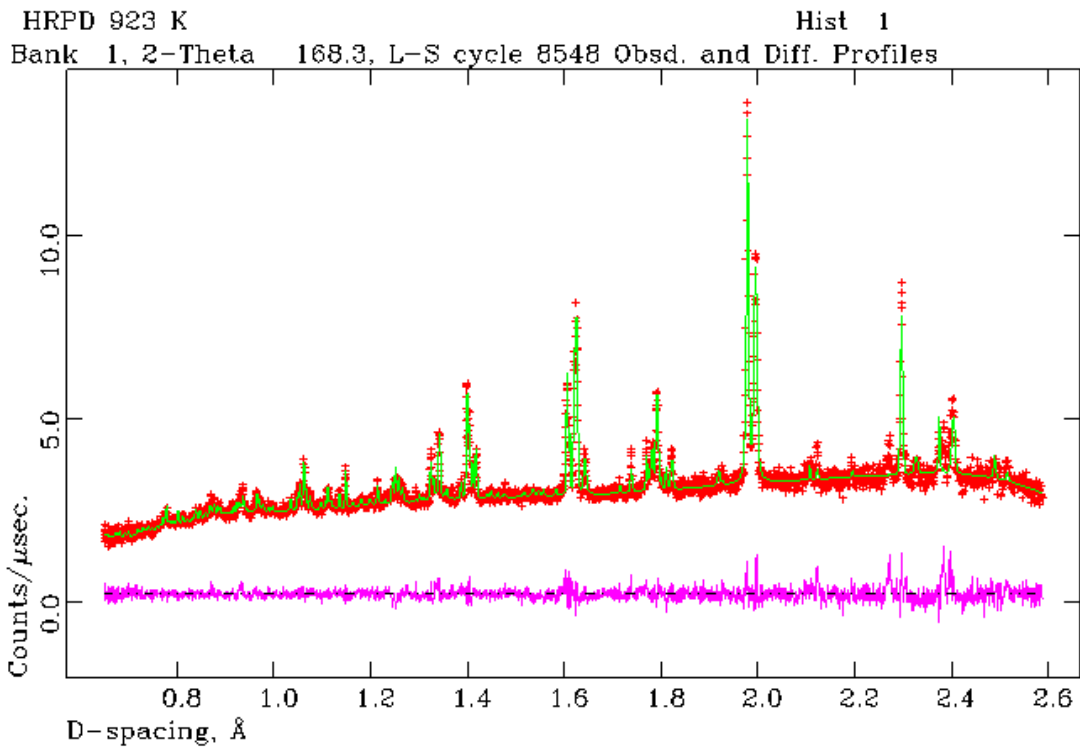
Appendix 3.102 – Rietveld refined HRPD pattern of Dy-BFO at 923 K shown in d-spacing
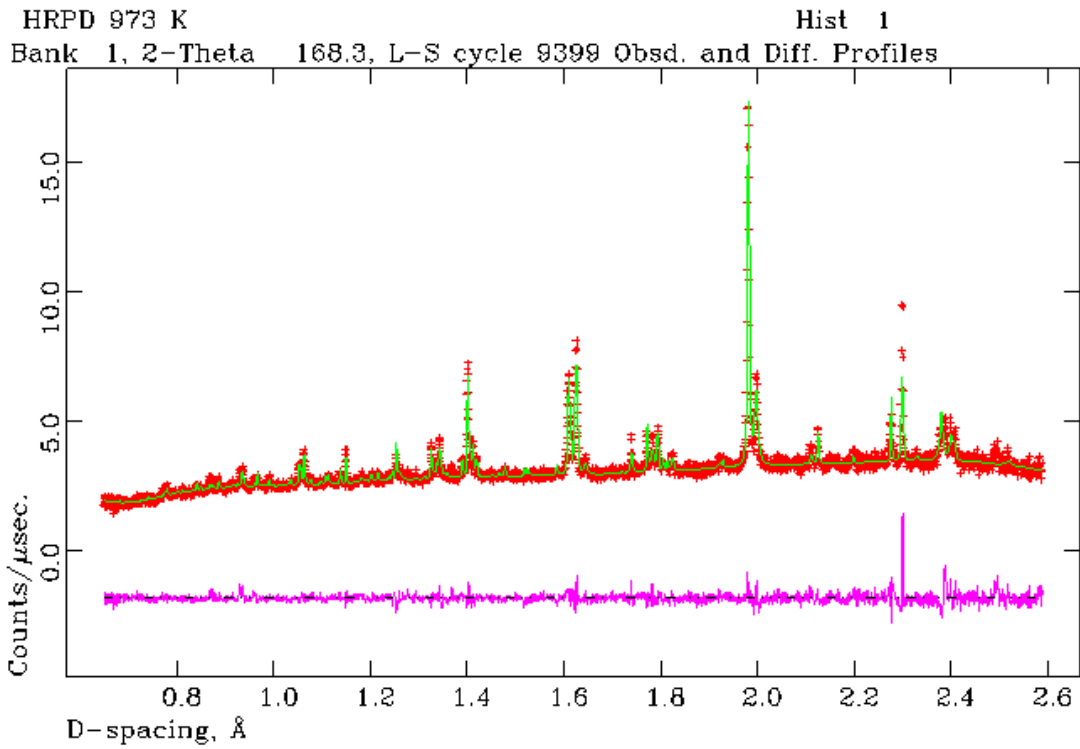
Appendix 3.103 – Rietveld refined HRPD pattern of Dy-BFO at 973 K shown in d-spacing
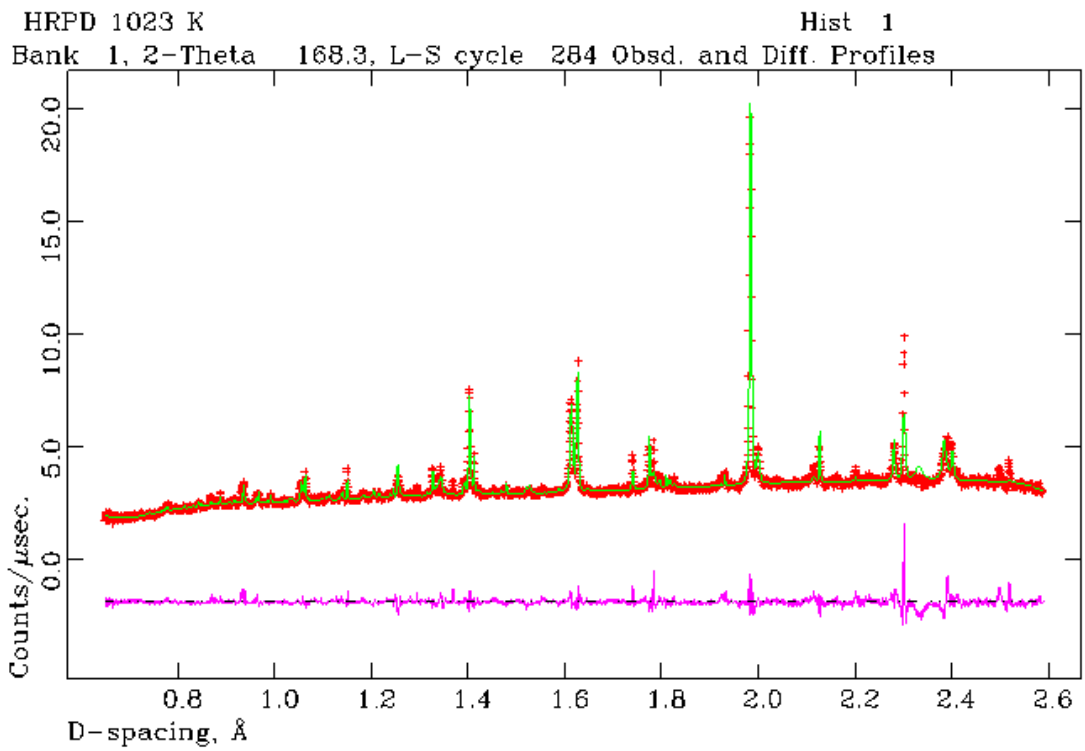
Appendix 3.104 – Rietveld refined HRPD pattern of Dy-BFO at 1023 K shown in d-spacing

Appendix 3.105 – Overlay of Raman spectra over the temperature ranges 77 – 307 K showing the 13 *R*3*c* peaks. Inset of the analysed A₁-1 and A₁-2 peaks.
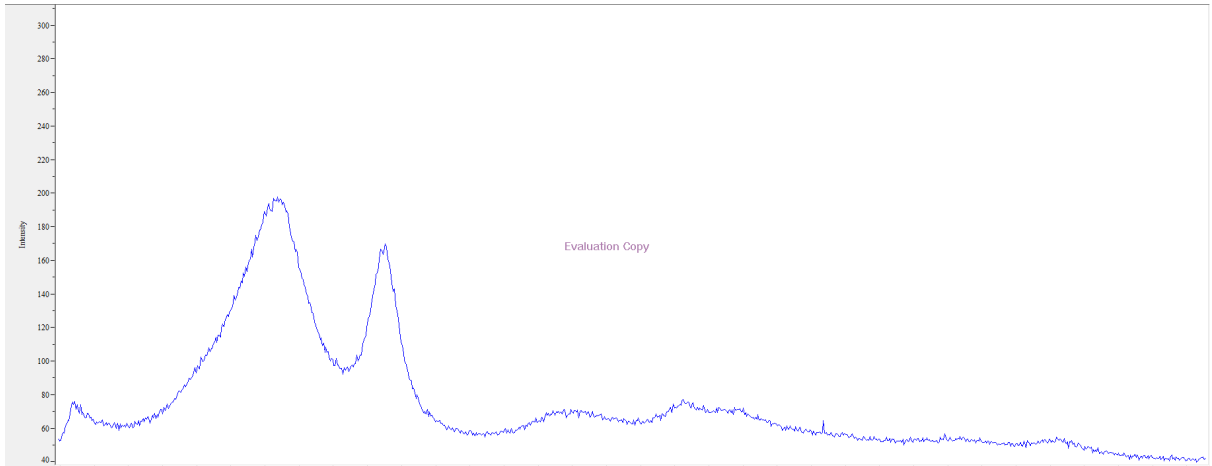
Appendix 3.106 – Raman map spectrum recorded for 5% Dy-BFO between 80-420 cm^{-1}
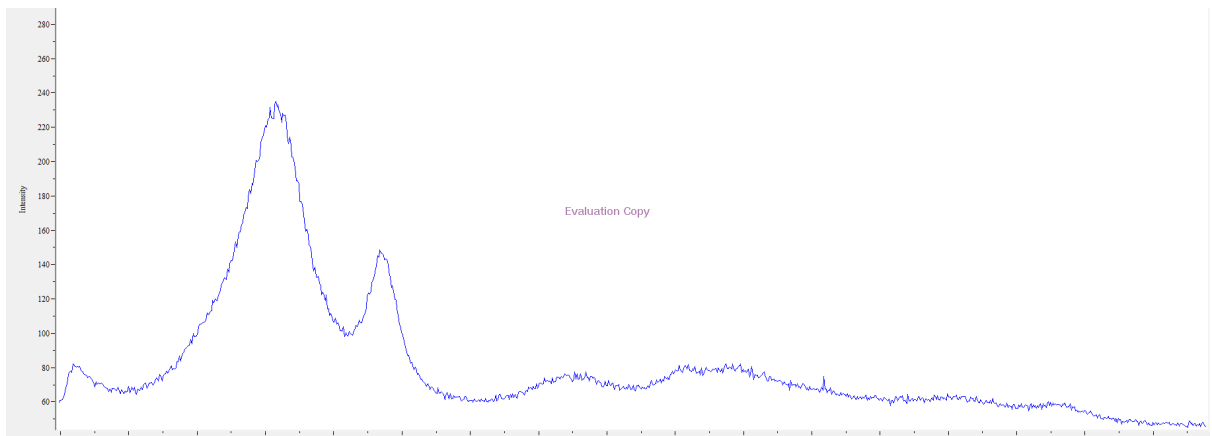
Appendix 3.107 – Raman map spectrum recorded for 5% Dy-BFO between 80-420 cm^{-1}

Appendix 4.1 – refined Bond length/angle data of $DyFeO_3$ and $SmFeO_3$ at 12 K and 298 K

	Fe-O bond	Fe-O bond	Fe-O bond	Fe-O-Fe angle
DyFeO3 12K	1.996(5)	2.023(4)	2.023(4)	145.3(1)
DyFeO3 298 K	1.999(7)	2.011(6)	2.024(6)	145.32(1)
SmFeO3 12K	2.02(22)	2.00(23)	2.014(7)	145.5(14)
SmFeO3 298 K	2.09(22)	1.94(23)	2.004(7)	148.1(13)
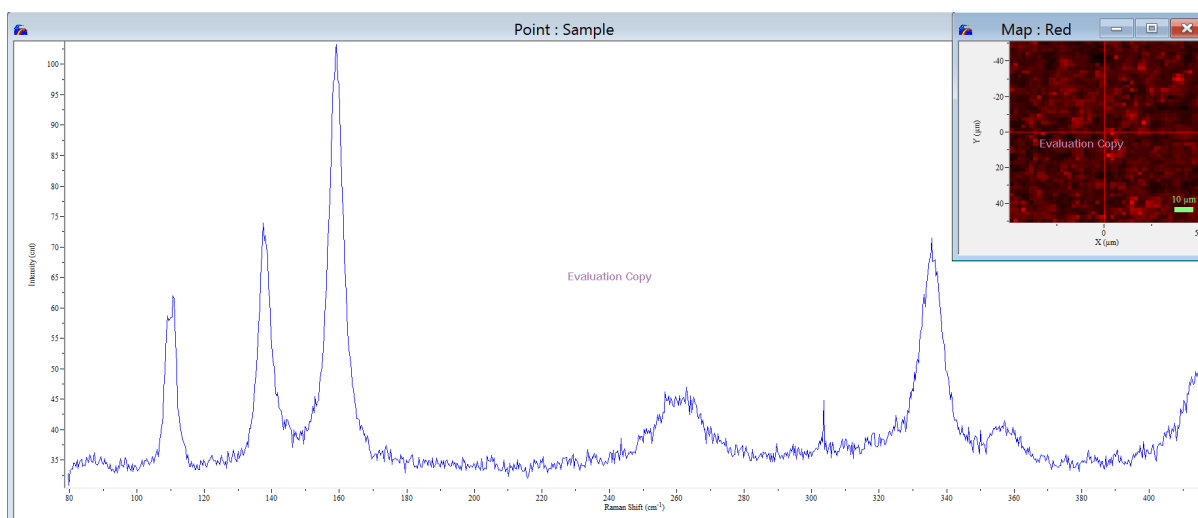
Appendix 4.2 – Raman Map Spectrum of $DyFeO_3$ taken at 0, 0 of the 50 μm^2
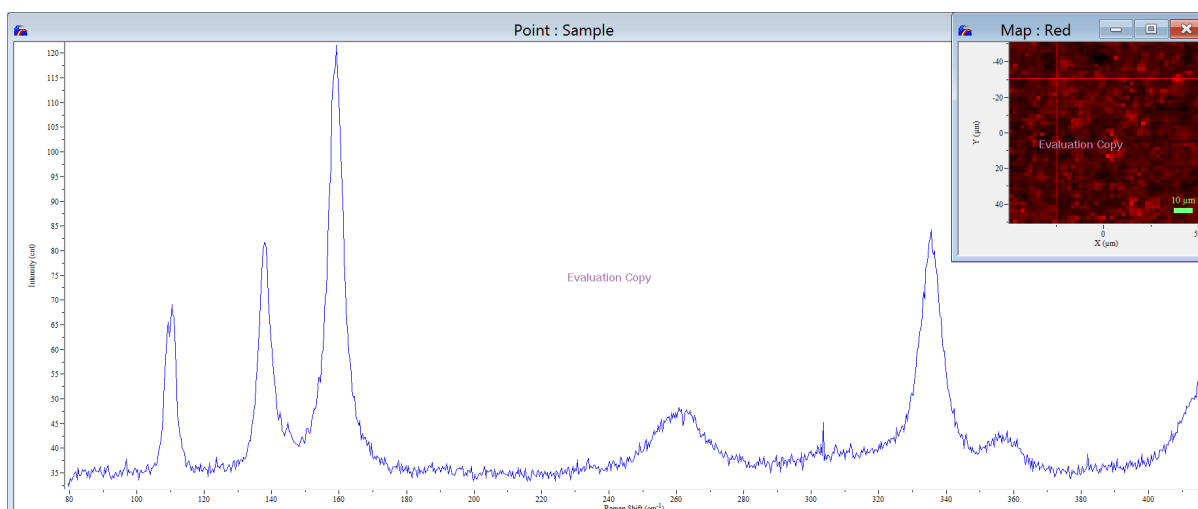
Appendix 4.3 – Raman Map Spectrum of $DyFeO_3$ taken at -25, -30 of the 50 μm^2
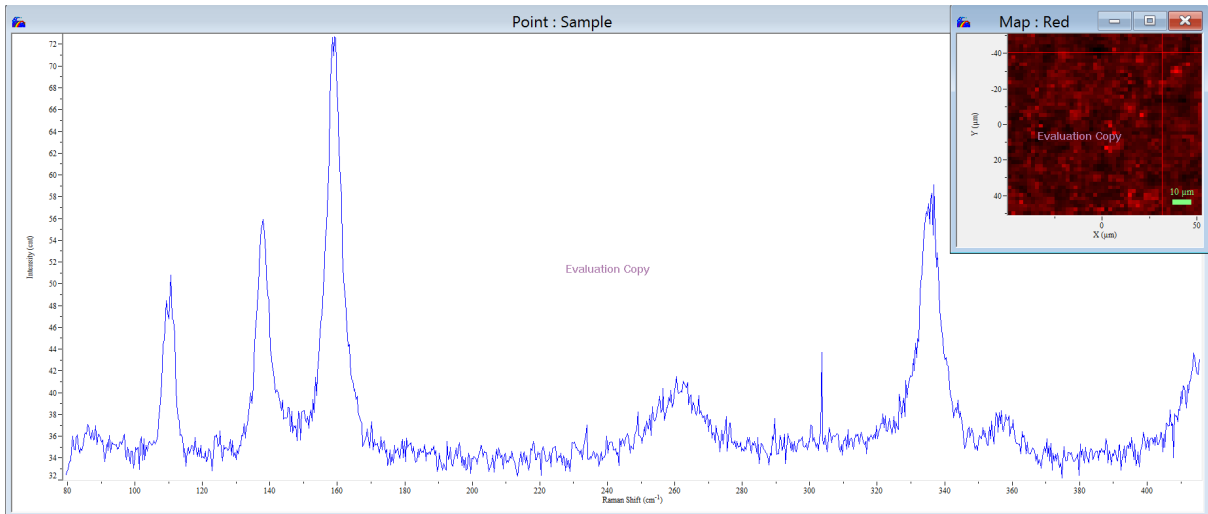
Appendix 4.4 – Raman Map Spectrum of DyFeO$_3$ taken at 30, -40 of the 50 μm^2
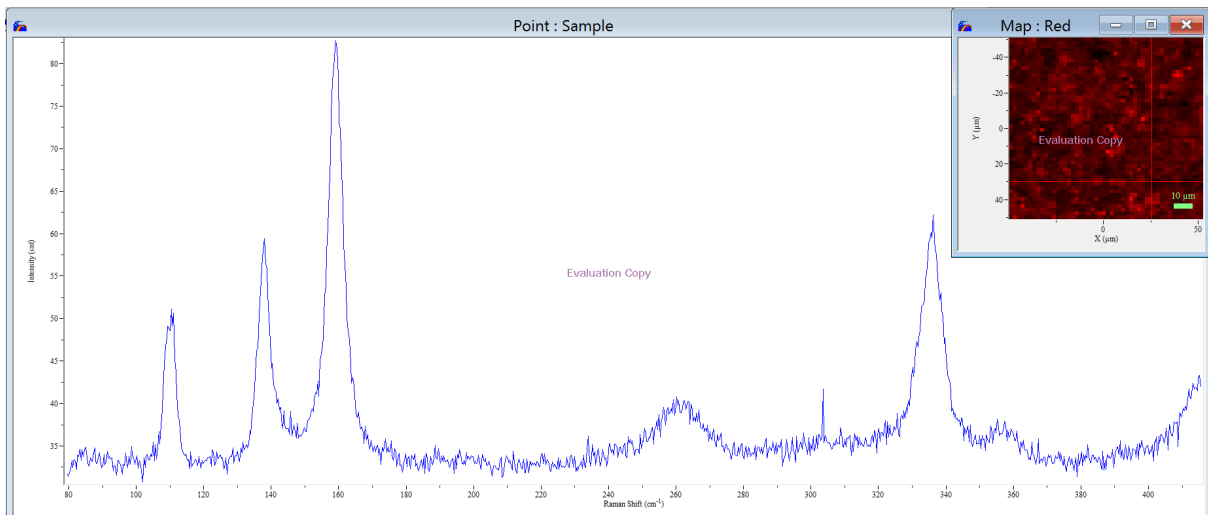
Appendix 4.5 – Raman Map Spectrum of DyFeO$_3$ taken at 25, 30 of the 50 μm^2
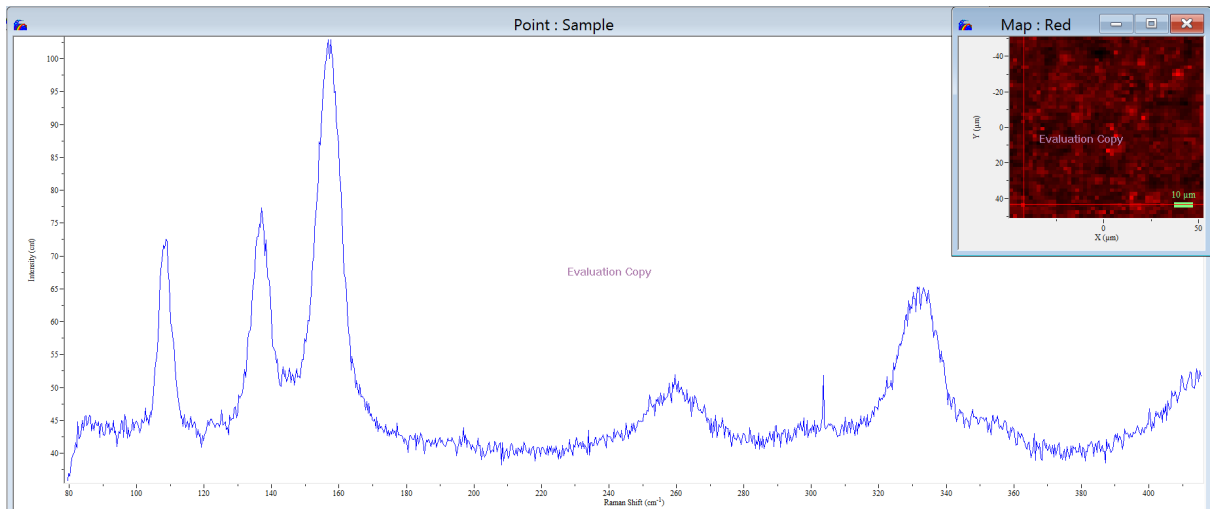
Appendix 4.6 – Raman Map Spectrum of DyFeO$_3$ taken at 45, 42 of the 50 μm^2
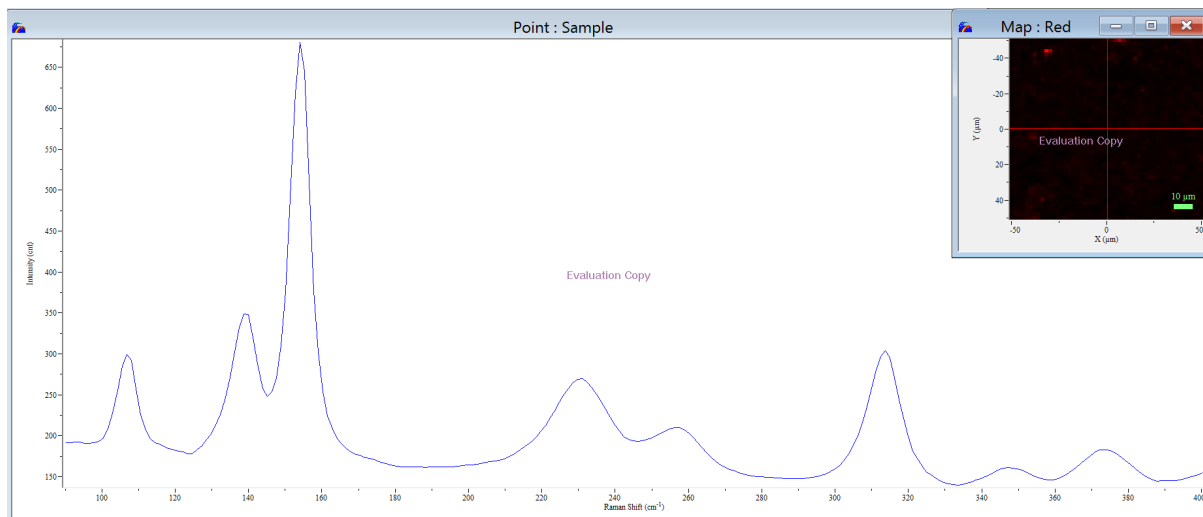
Appendix 4.7 – Raman Map Spectrum of SmFeO$_3$ taken at 0, 0 of the 50 μm^2
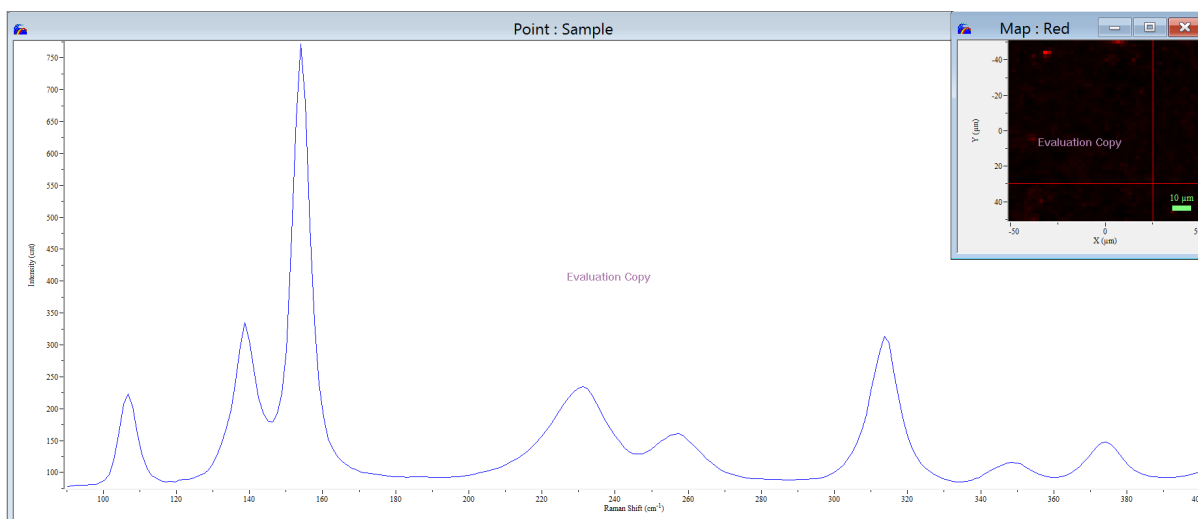
Appendix 4.8 – Raman Map Spectrum of SmFeO$_3$ taken at 25, -30 of the 50 μm^2
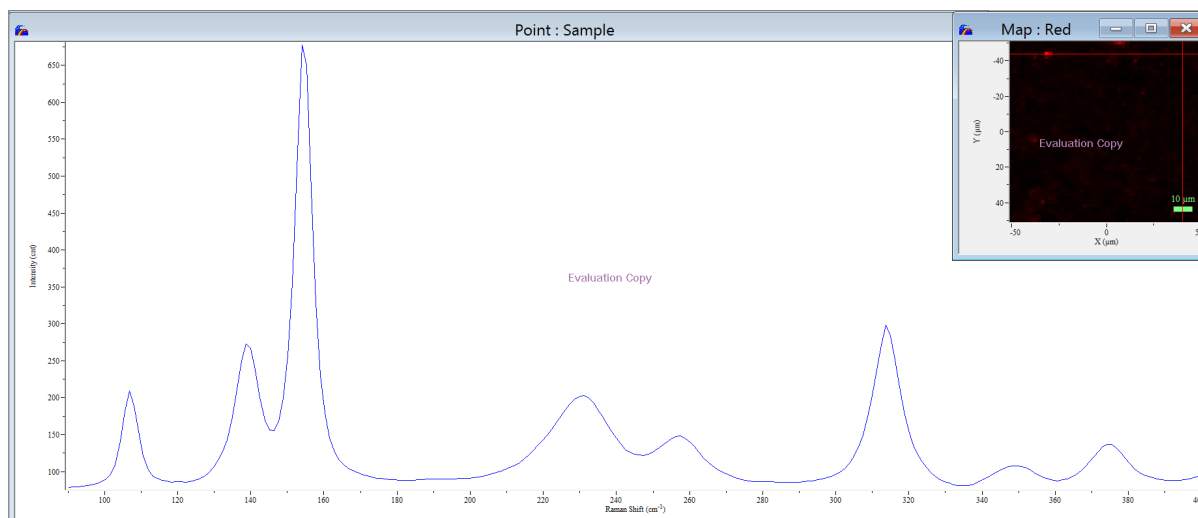
Appendix 4.9 – Raman Map Spectrum of SmFeO$_3$ taken at 45, -42 of the 50 μm^2
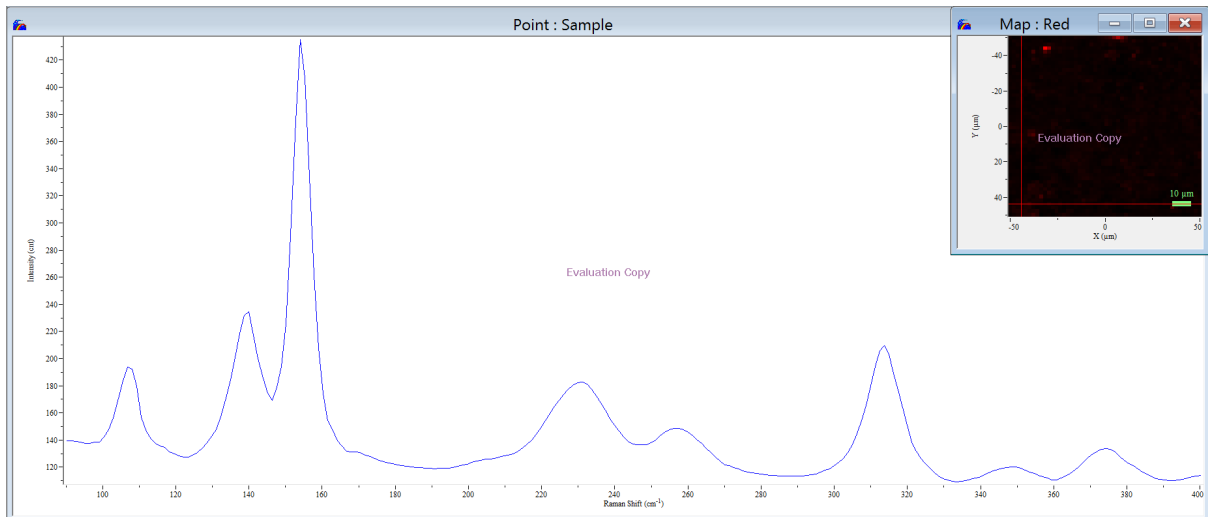
Appendix 4.10 – Raman Map Spectrum of $SmFeO_3$ taken at -45, 42 of the 50 μm^2
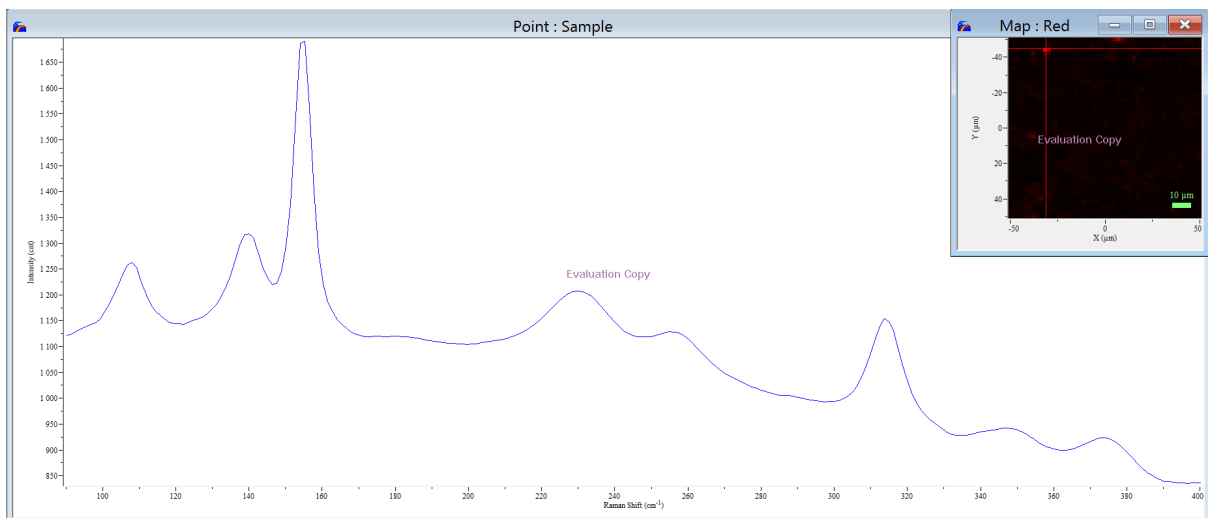
Appendix 4.11 – Raman Map Spectrum of $SmFeO_3$ taken at -25, -42 of the 50 μm^2
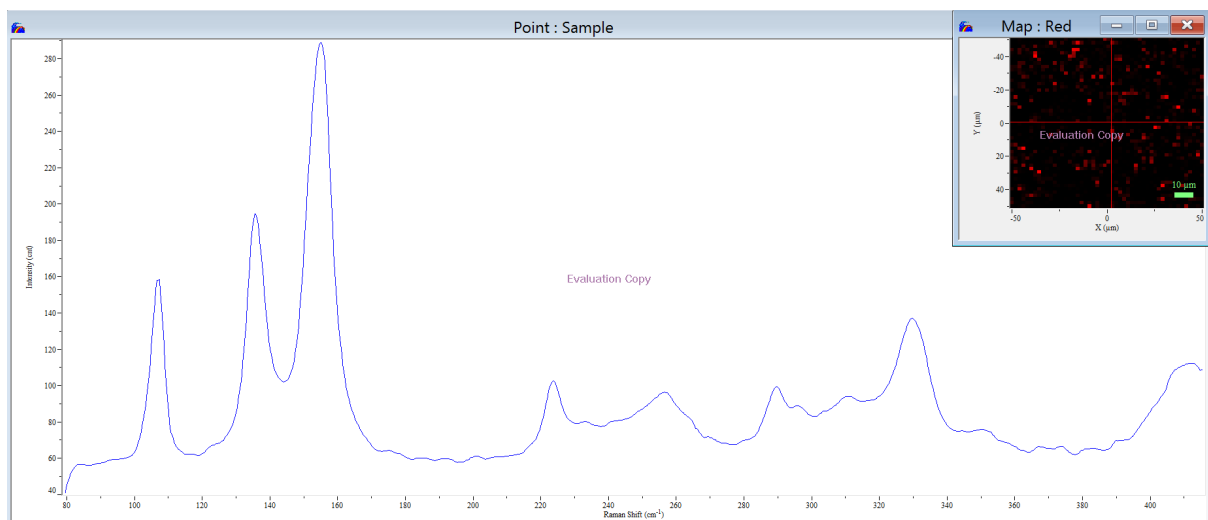
Appendix 4.12 – Raman Map Spectrum of $Dy_{0.75}Sm_{0.25}FeO_3$ taken at 0, 0 of the 50 μm^2
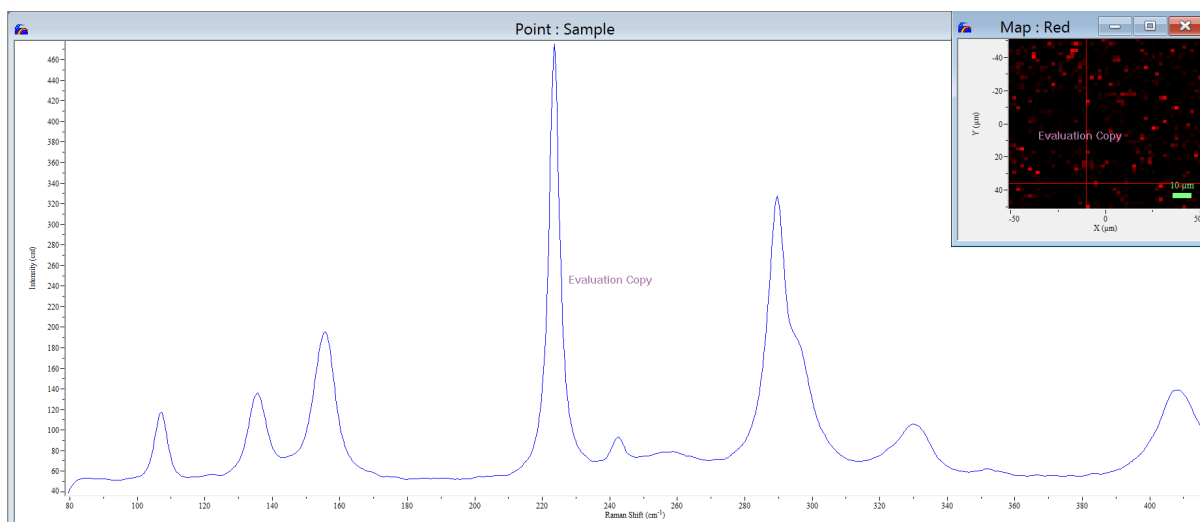
Appendix 4.13 – Raman Map Spectrum of $Dy_{0.75}Sm_{0.25}FeO_3$ taken at -12, 37 of the 50 μm^2
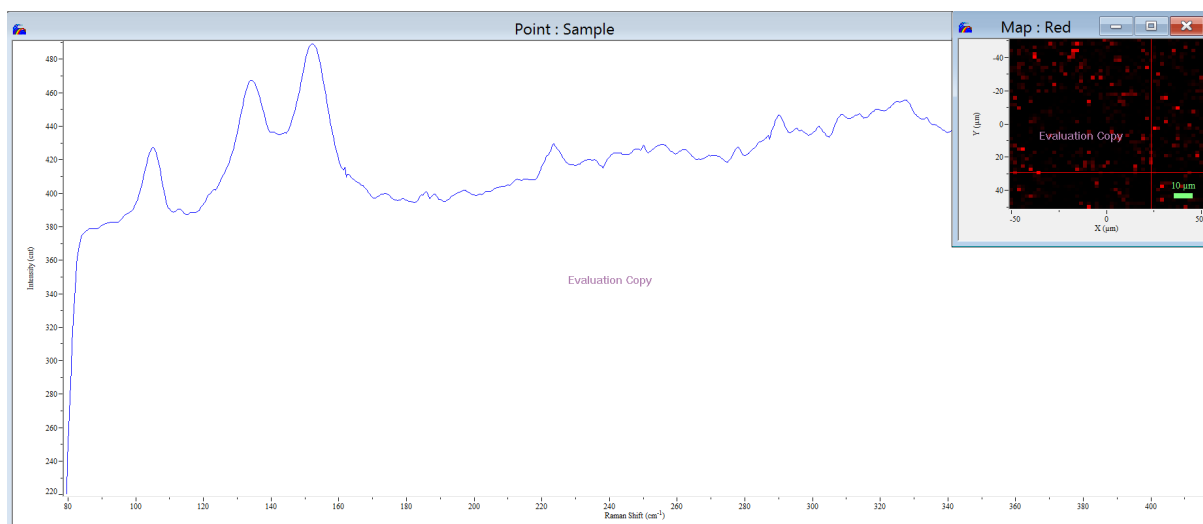
Appendix 4.14 – Raman Map Spectrum of $Dy_{0.75}Sm_{0.25}FeO_3$ taken at 24, 30 of the 50 μm^2
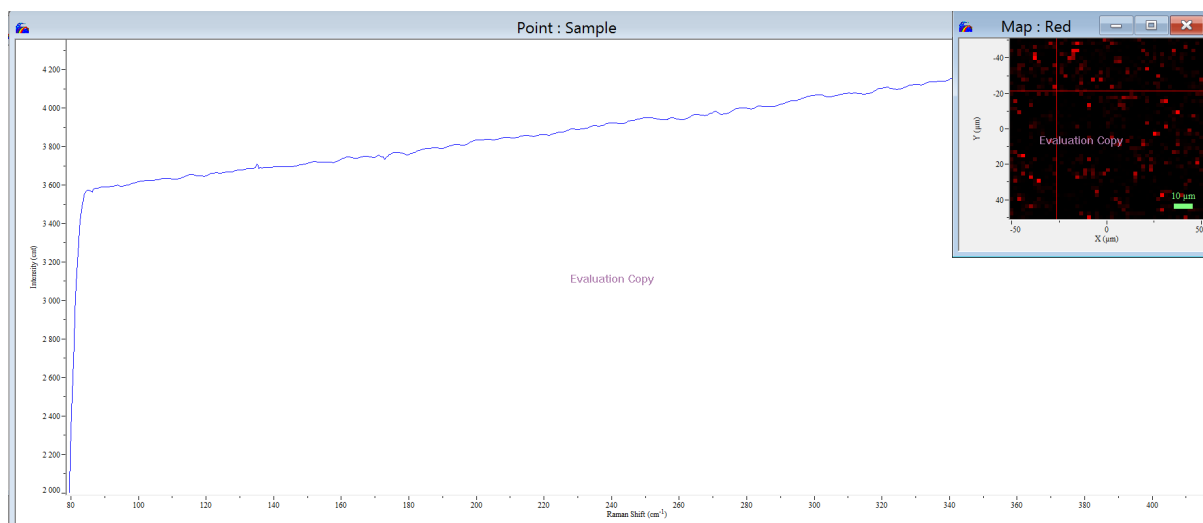
Appendix 4.15 – Raman Map Spectrum of $Dy_{0.75}Sm_{0.25}FeO_3$ taken at -25, -20 of the 50 μm^2
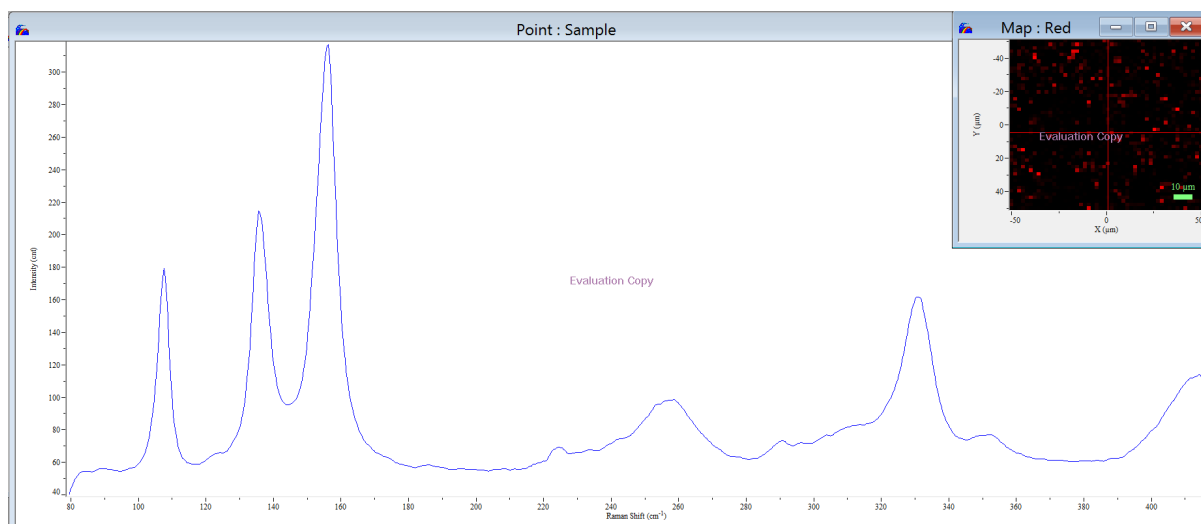
Appendix 4.16 – Raman Map Spectrum of $Dy_{0.75}Sm_{0.25}FeO_3$ taken at 0, 5 of the 50 μm^2
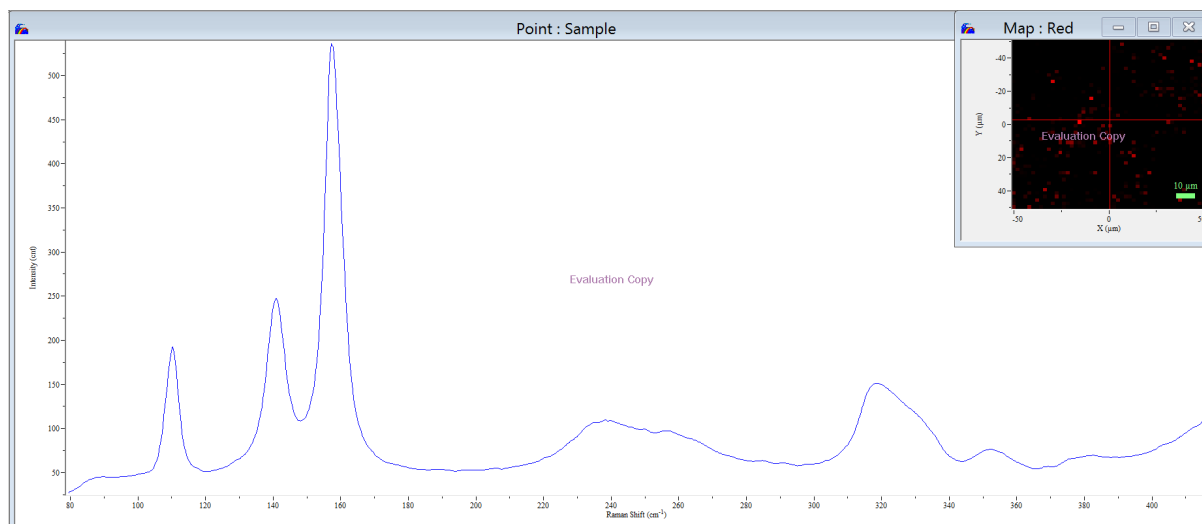
Appendix 4.17 – Raman Map Spectrum of $Dy_{0.5}Sm_{0.5}FeO_3$ taken at 0, 0 of the 50 μm^2
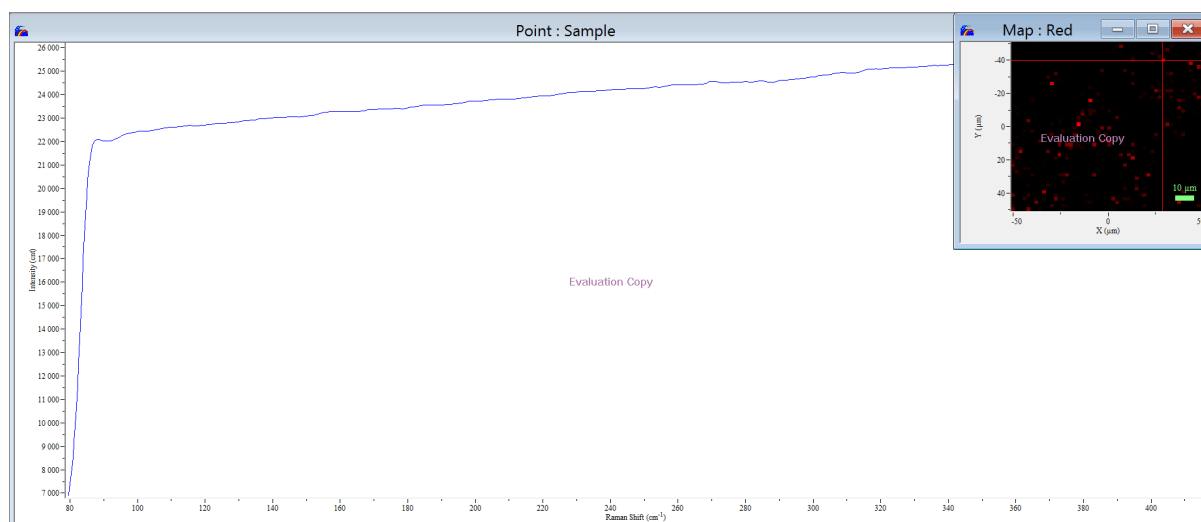
Appendix 4.18 – Raman Map Spectrum of $Dy_{0.5}Sm_{0.5}FeO_3$ taken at 26, -40 of the 50 μm^2
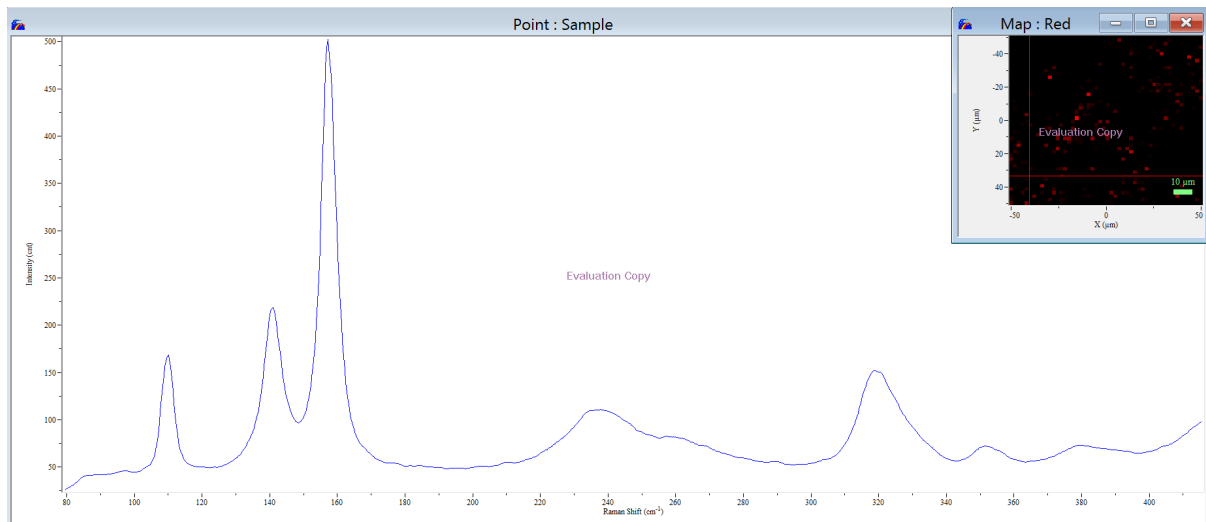
Appendix 4.19 – Raman Map Spectrum of $Dy_{0.5}Sm_{0.5}FeO_3$ taken at -40, 35 of the 50 μm^2
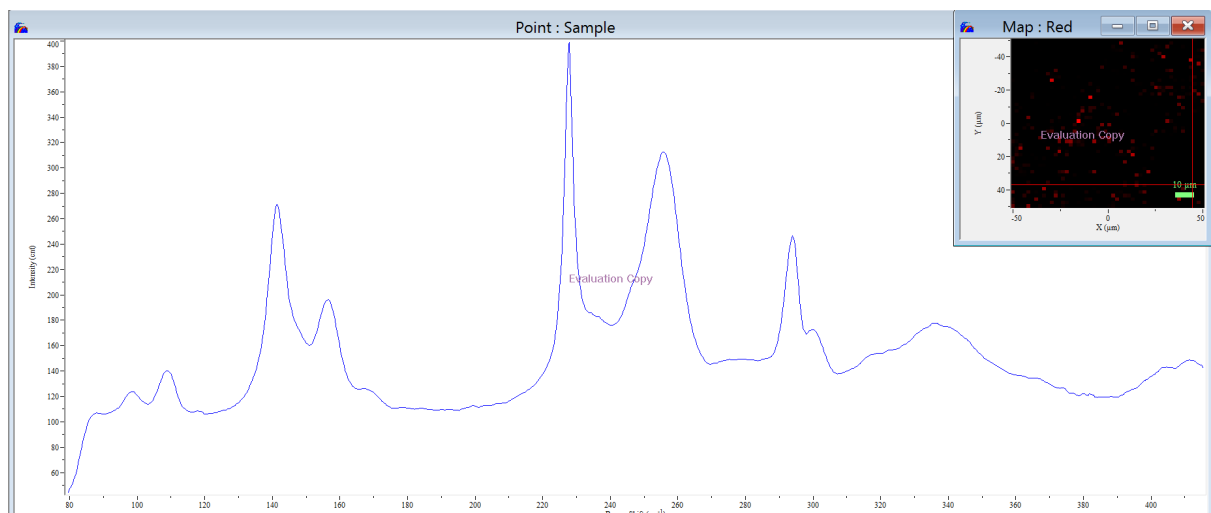
Appendix 4.20 – Raman Map Spectrum of $Dy_{0.5}Sm_{0.5}FeO_3$ taken at 45, 38 of the 50 μm^2
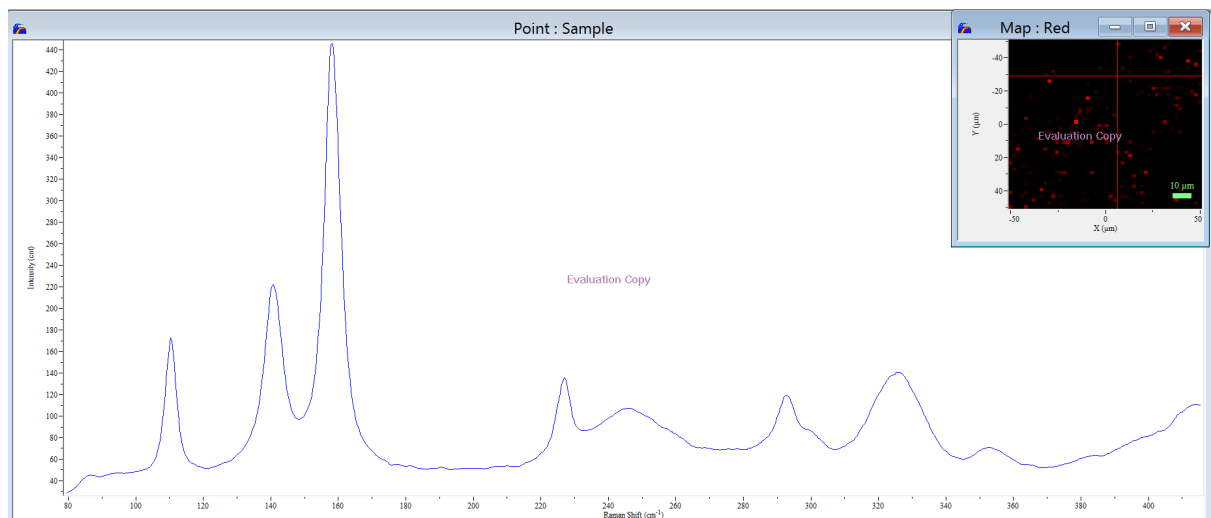
Appendix 4.21 – Raman Map Spectrum of $Dy_{0.5}Sm_{0.5}FeO_3$ taken at 5, -30 of the 50 μm^2
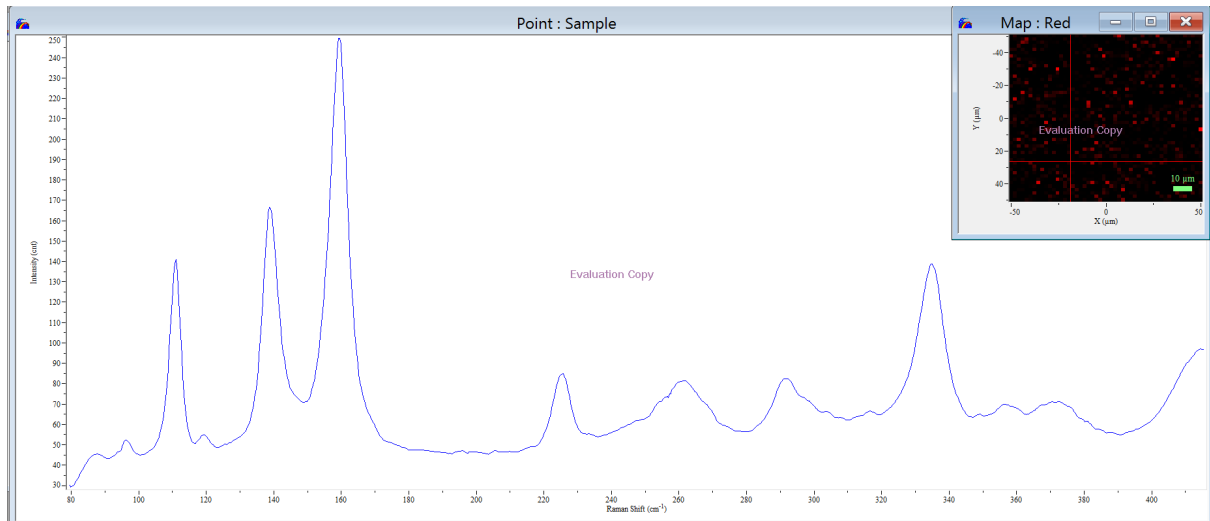
Appendix 4.22 – Raman Map Spectrum of $Dy_{0.25}Sm_{0.75}FeO_3$ taken at -20, 27 of the 50 μm^2
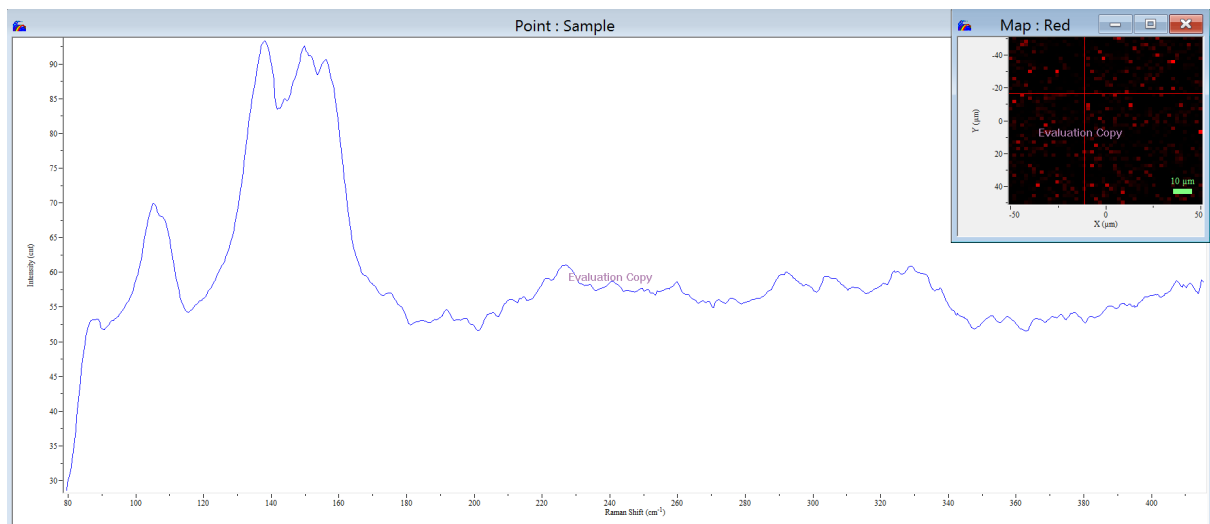
Appendix 4.23 – Raman Map Spectrum of $Dy_{0.25}Sm_{0.75}FeO_3$ taken at -15, -18 of the 50 μm^2
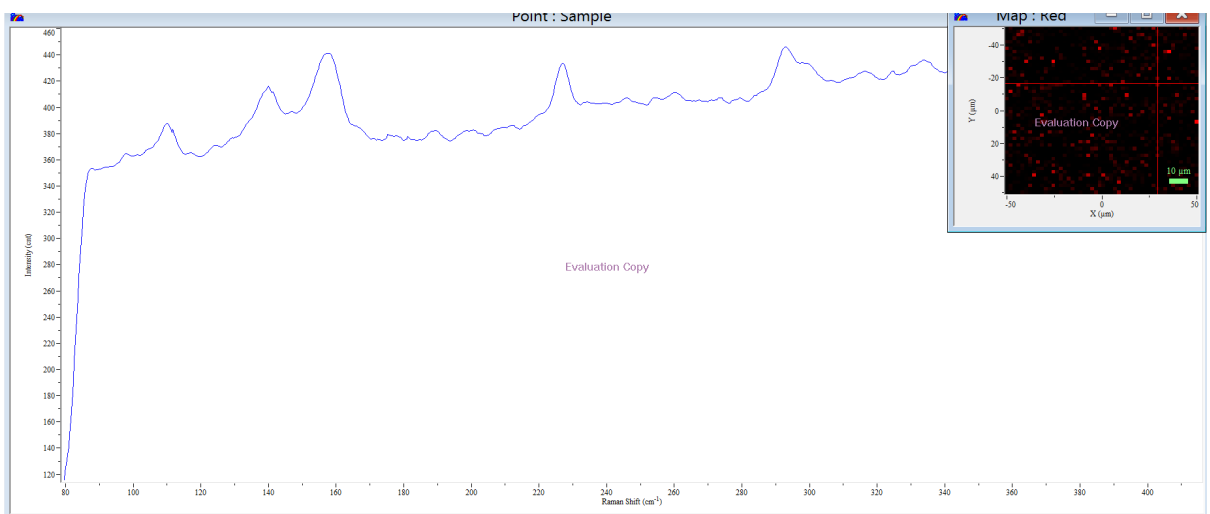
Appendix 4.24 – Raman Map Spectrum of $Dy_{0.25}Sm_{0.75}FeO_3$ taken at 27, -20 of the 50 μm^2
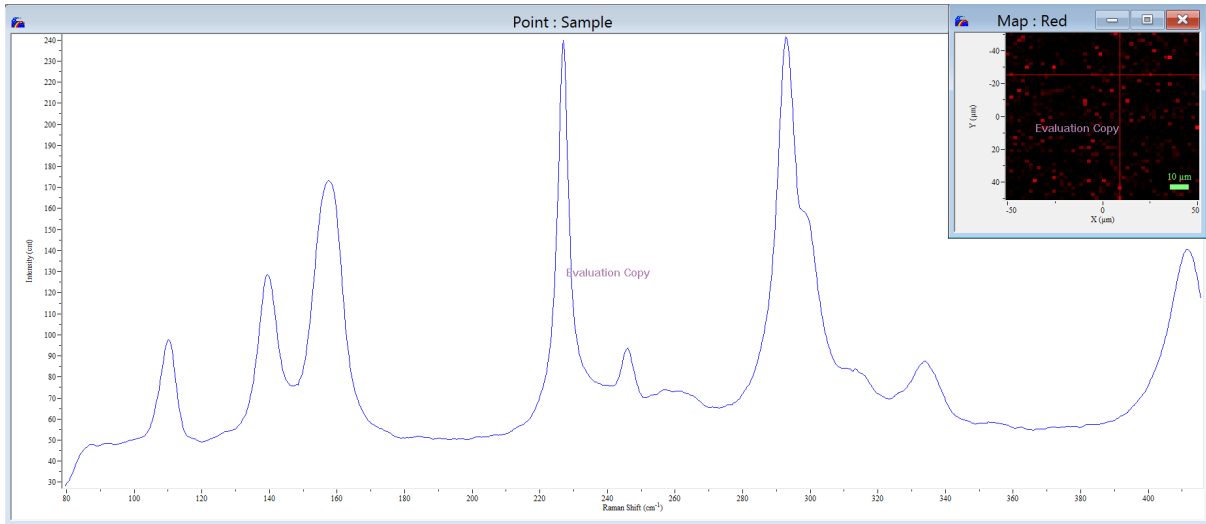
Appendix 4.25 – Raman Map Spectrum of $Dy_{0.25}Sm_{0.75}FeO_3$ taken at 5, -23 of the 50 μm^2
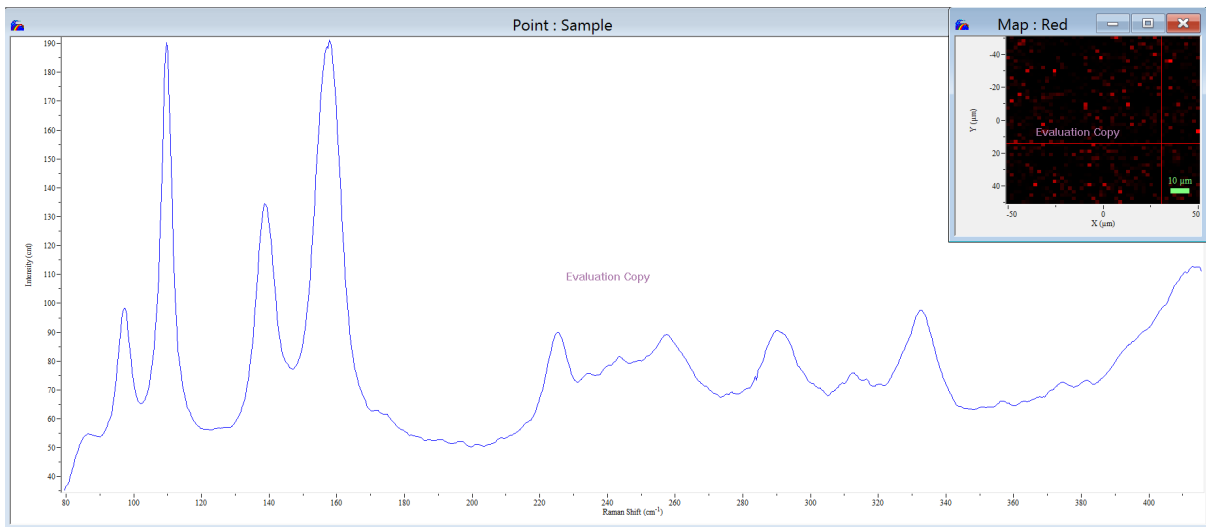
Appendix 4.26 – Raman Map Spectrum of $Dy_{0.25}Sm_{0.75}FeO_3$ taken at 27, 17 of the 50 μm^2
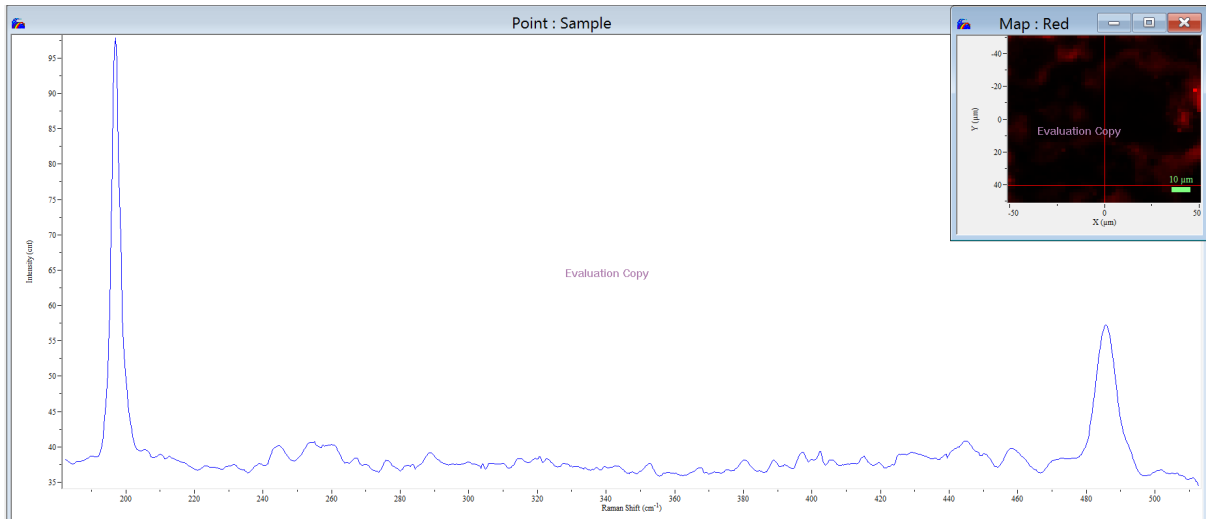
Appendix 5.1 – Raman Map Spectrum of $LiCoPO_4$ taken at 0, 40 of the 50 μm^2
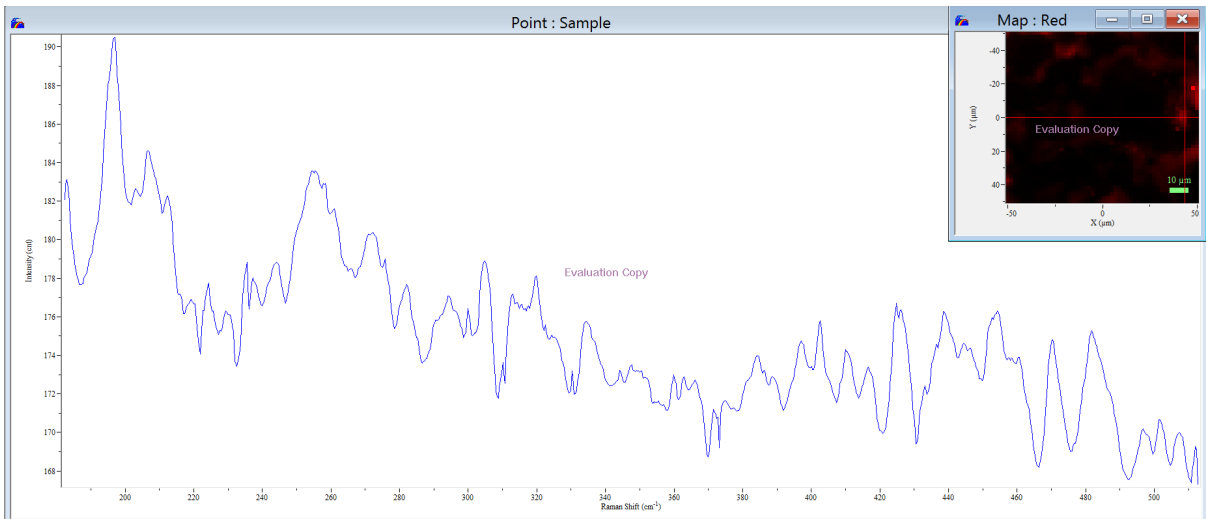
Appendix 5.2 – Raman Map Spectrum of $LiCoPO_4$ taken at 45, 0 of the 50 μm^2
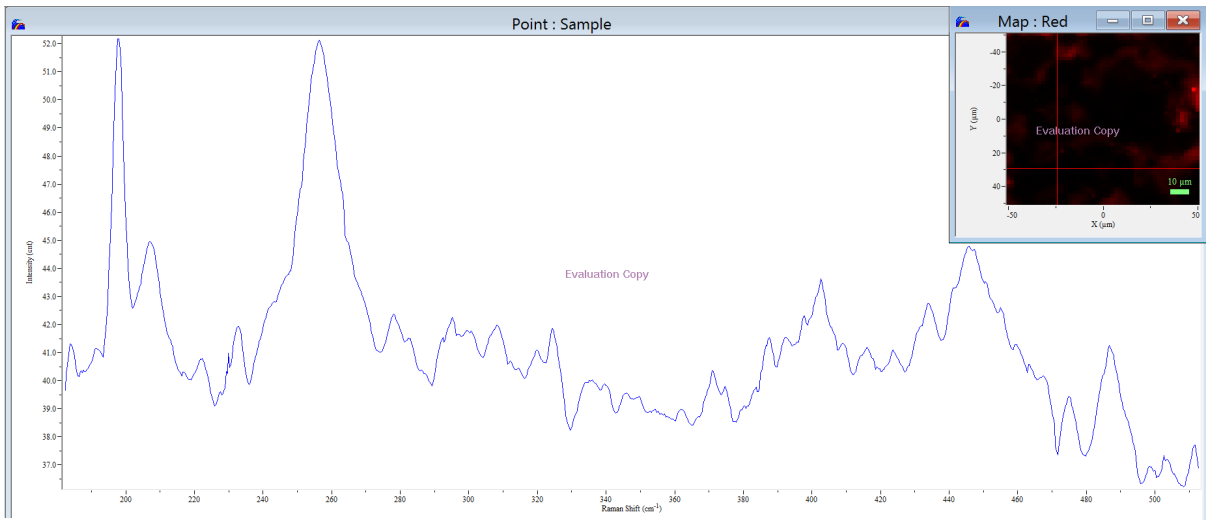
Appendix 5.3 – Raman Map Spectrum of $LiCoPO_4$ taken at -25, 30 of the 50 μm^2
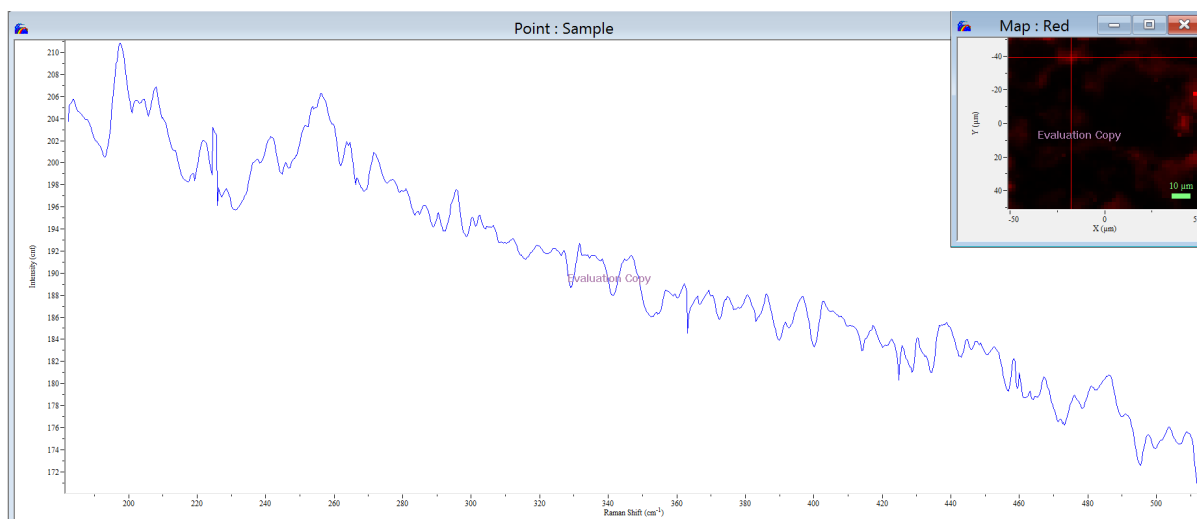
Appendix 5.4 – Raman Map Spectrum of $LiCoPO_4$ taken at -20, -40 of the 50 μm^2
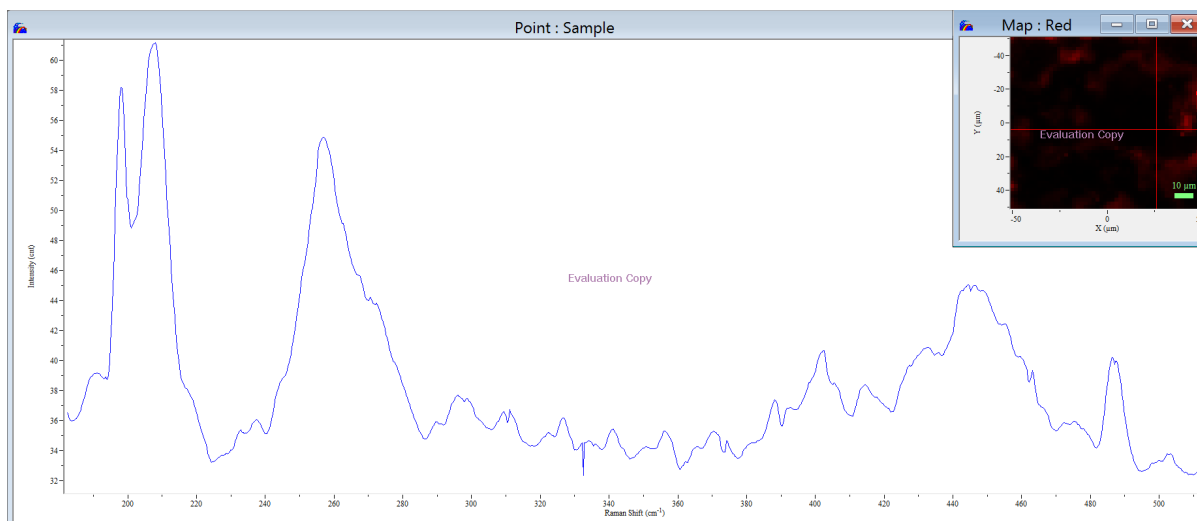
Appendix 5.5 – Raman Map Spectrum of $LiCoPO_4$ taken at 25, 5 of the 50 μm^2
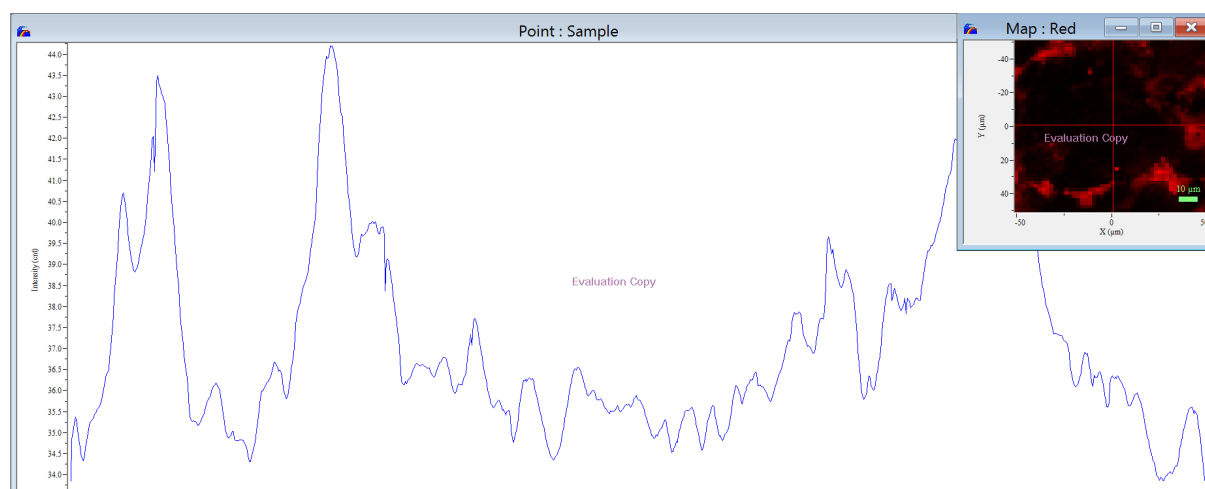
Appendix 5.6 – Raman Map Spectrum of $Li_{0.9}Na_{0.1}CoPO_4$ taken at 0, 0 of the 50 μm^2
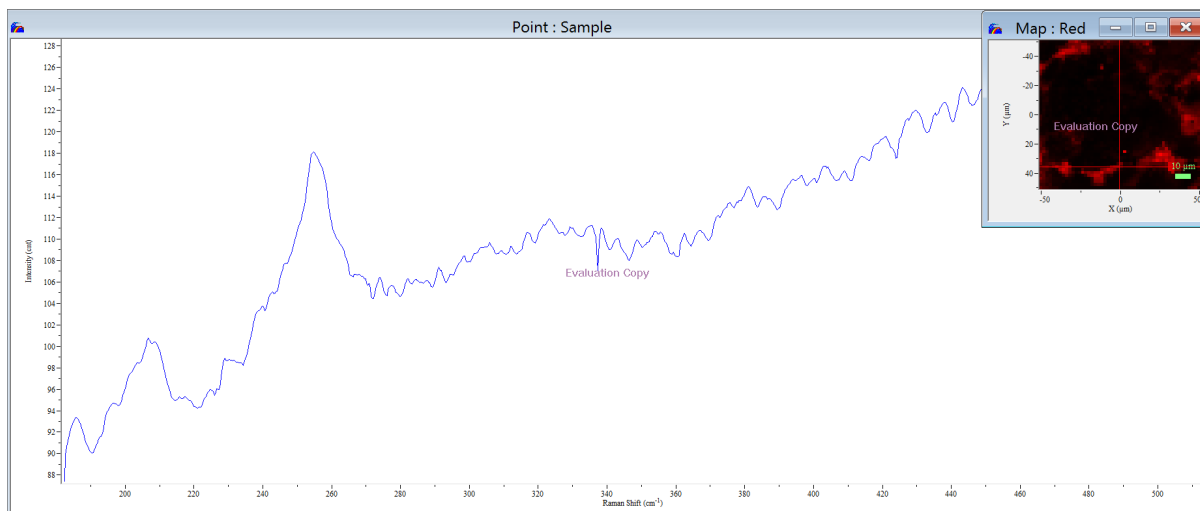
Appendix 5.7 – Raman Map Spectrum of $Li_{0.9}Na_{0.1}CoPO_4$ taken at 0, 37 of the 50 μm^2
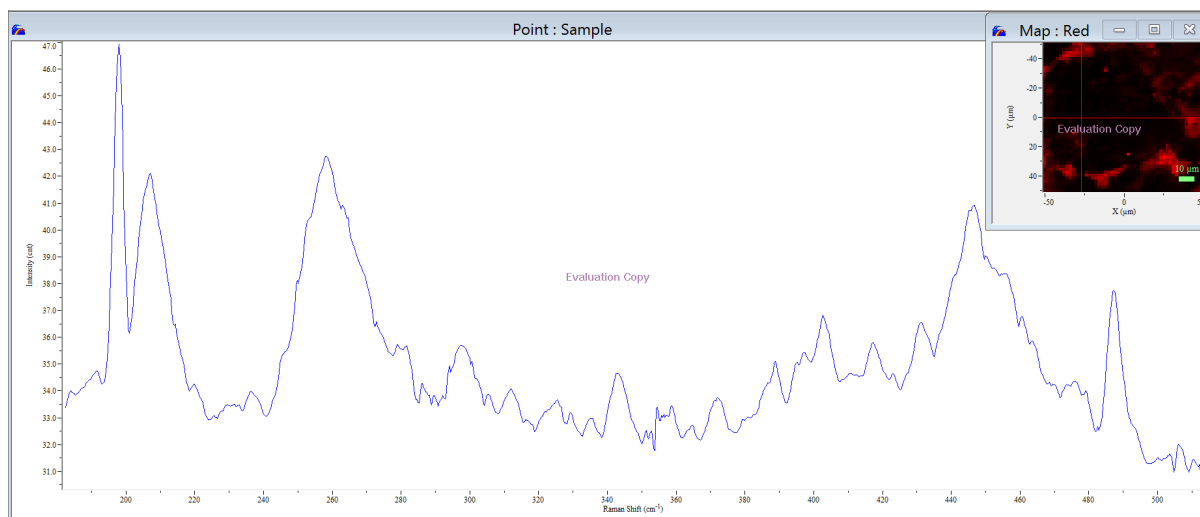
Appendix 5.8 – Raman Map Spectrum of $Li_{0.9}Na_{0.1}CoPO_4$ taken at -26, 0 of the 50 μm^2
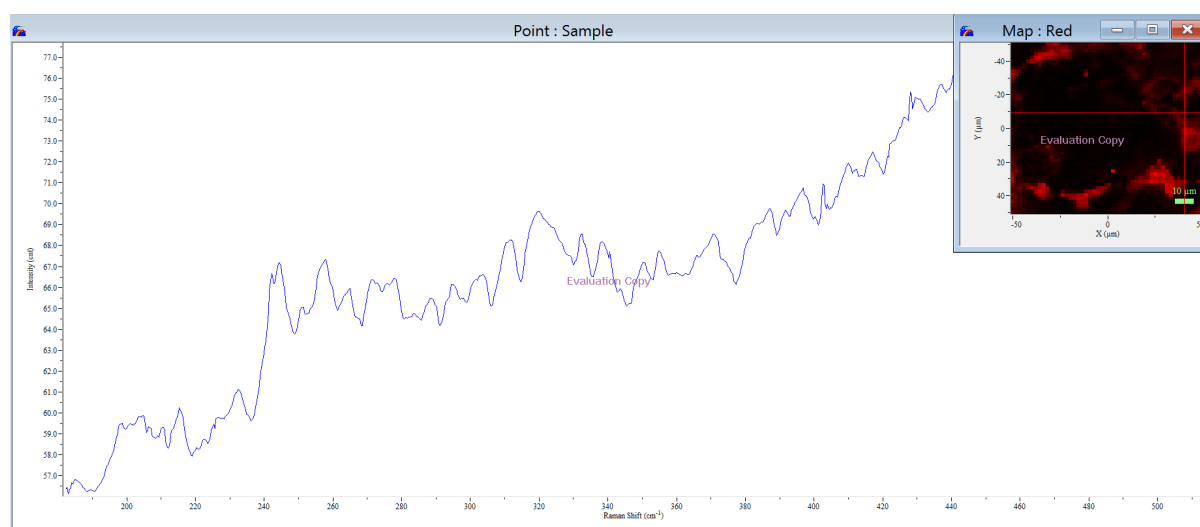
Appendix 5.9 – Raman Map Spectrum of $Li_{0.9}Na_{0.1}CoPO_4$ taken at 40, -10 of the 50 μm^2
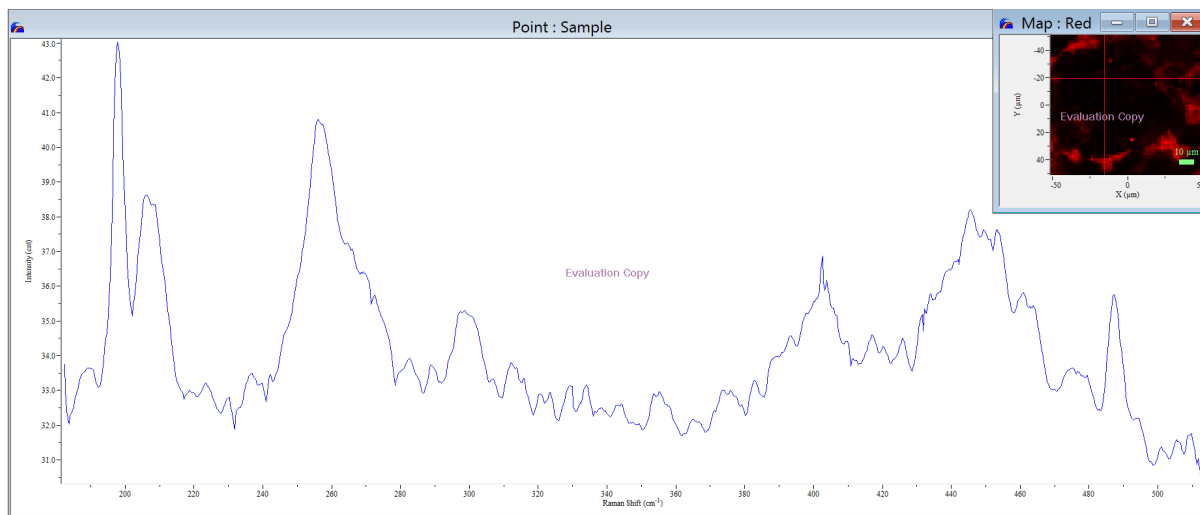
Appendix 5.10 – Raman Map Spectrum of $Li_{0.9}Na_{0.1}CoPO_4$ taken at -20, -20 of the 50 μm^2
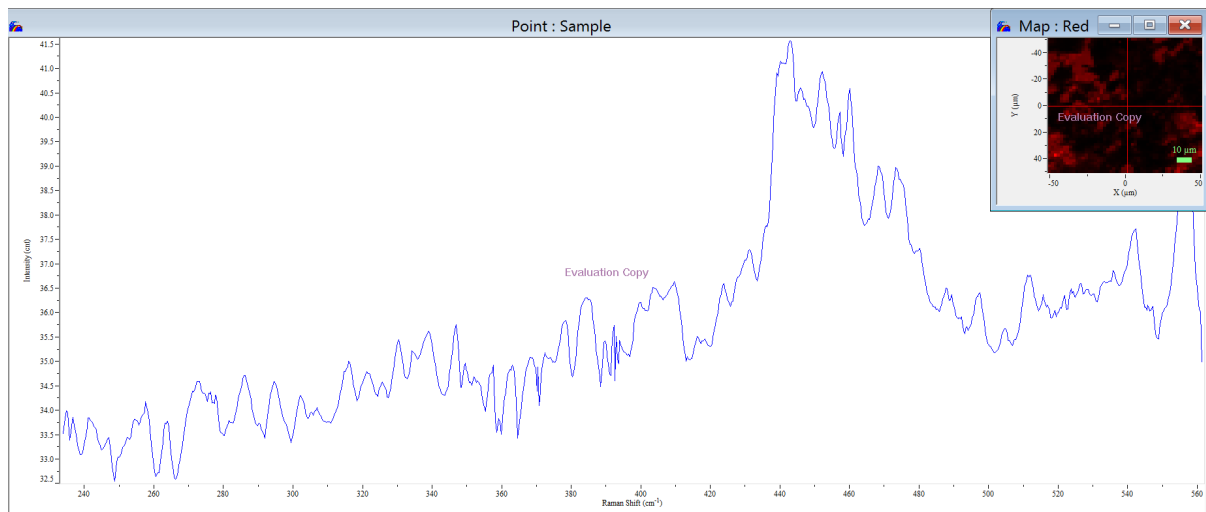
Appendix 5.11 – Raman Map Spectrum of $Li_{0.8}Na_{0.2}CoPO_4$ taken at 0, 0 of the 50 μm^2
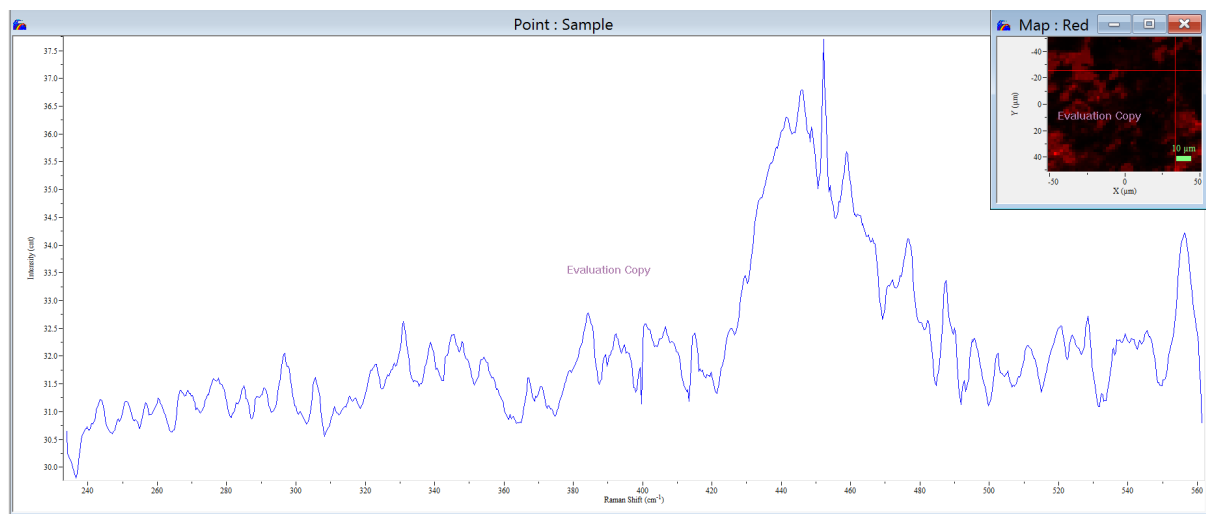
Appendix 5.12 – Raman Map Spectrum of $Li_{0.8}Na_{0.2}CoPO_4$ taken at 30, -25 of the 50 μm^2
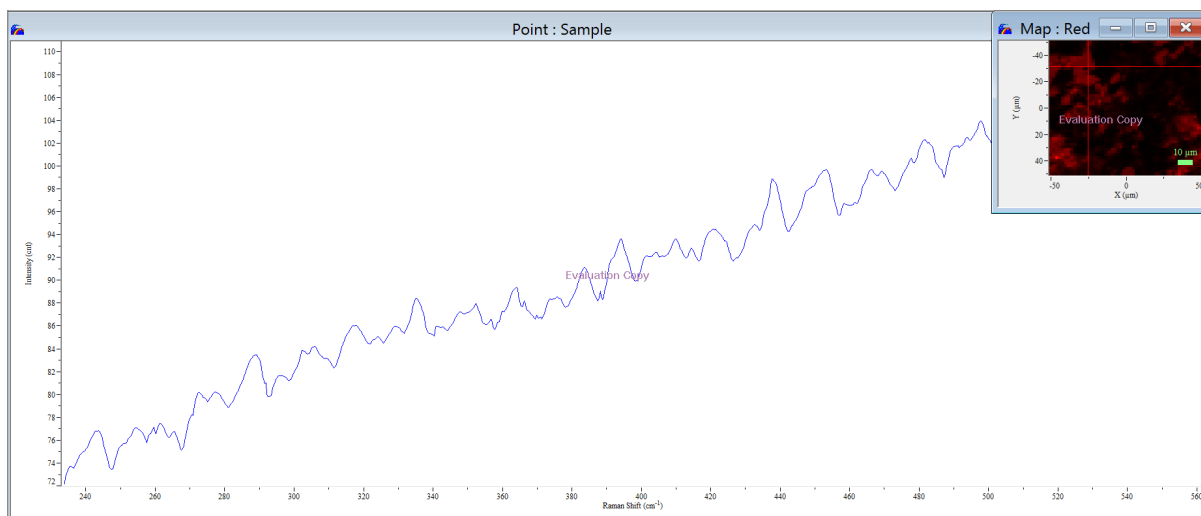
Appendix 5.13 – Raman Map Spectrum of $Li_{0.8}Na_{0.2}CoPO_4$ taken at -25, -30 of the 50 μm^2
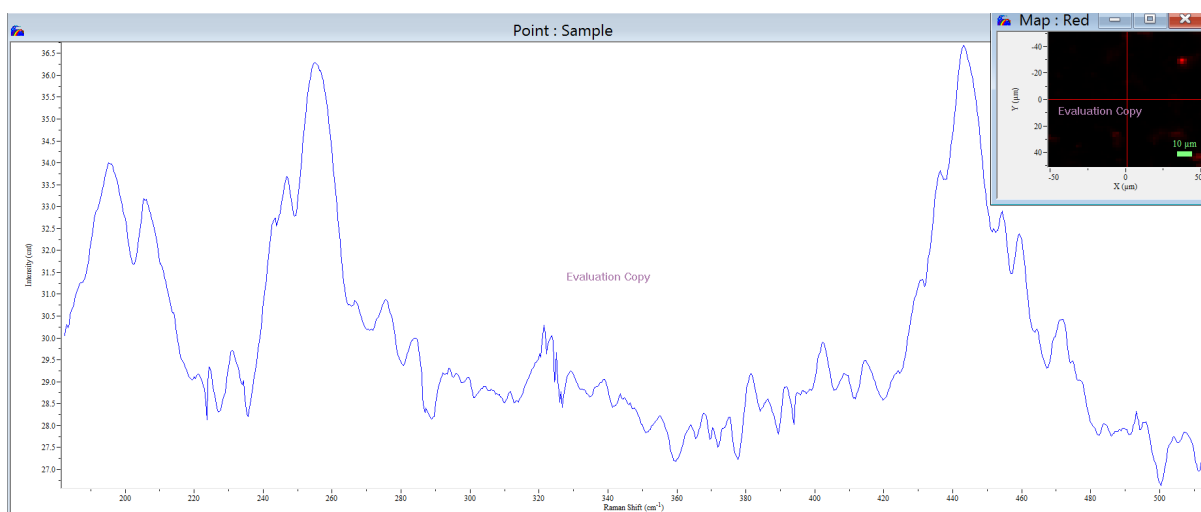
Appendix 5.14 – Raman Map Spectrum of $Li_{0.7}Na_{0.3}CoPO_4$ taken at 0, 0 of the 50 μm^2
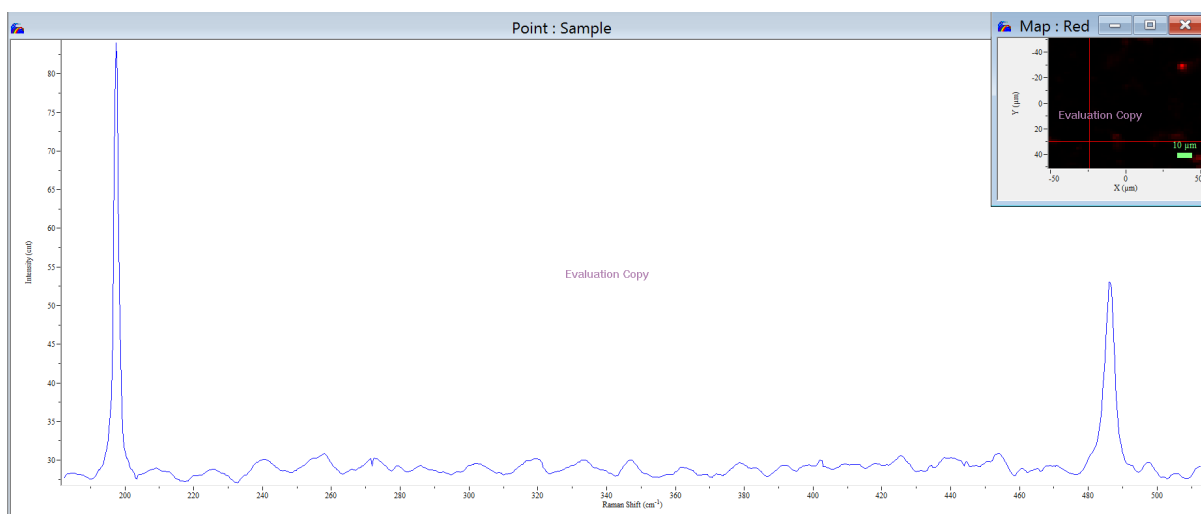
Appendix 5.15 – Raman Map Spectrum of $Li_{0.7}Na_{0.3}CoPO_4$ taken at -25, 30 of the 50 μm^2
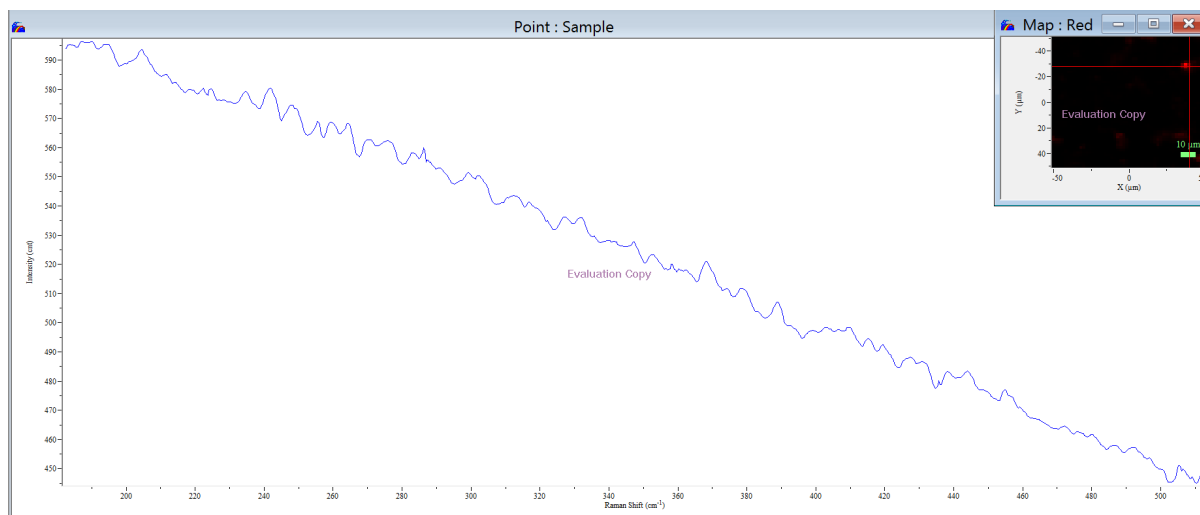
Appendix 5.16 – Raman Map Spectrum of $Li_{0.7}Na_{0.3}CoPO_4$ taken at 40, -30 of the 50 μm^2
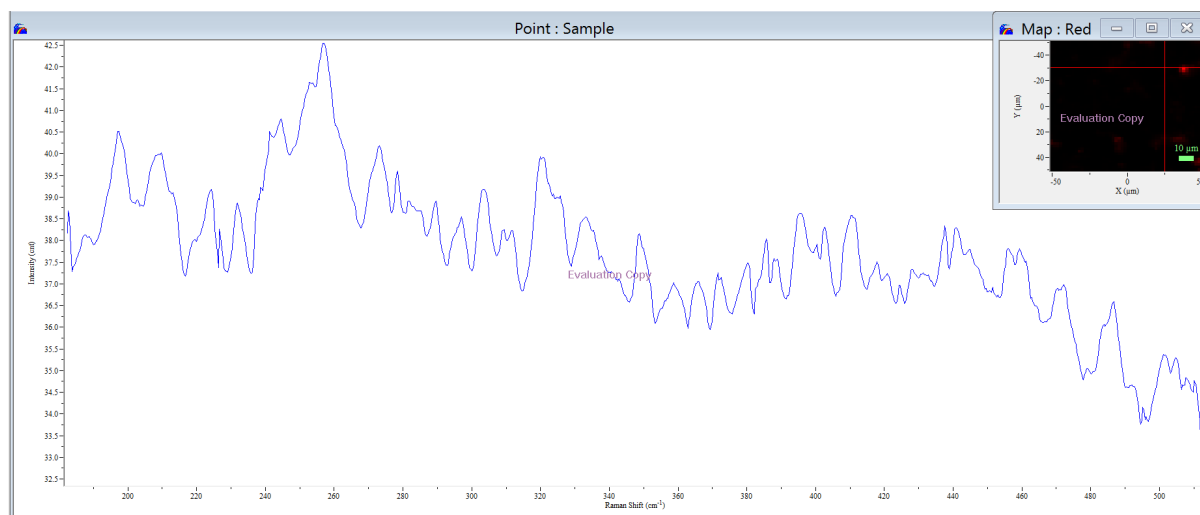
Appendix 5.17 – Raman Map Spectrum of $Li_{0.7}Na_{0.3}CoPO_4$ taken at 25, -30 of the 50 μm^2
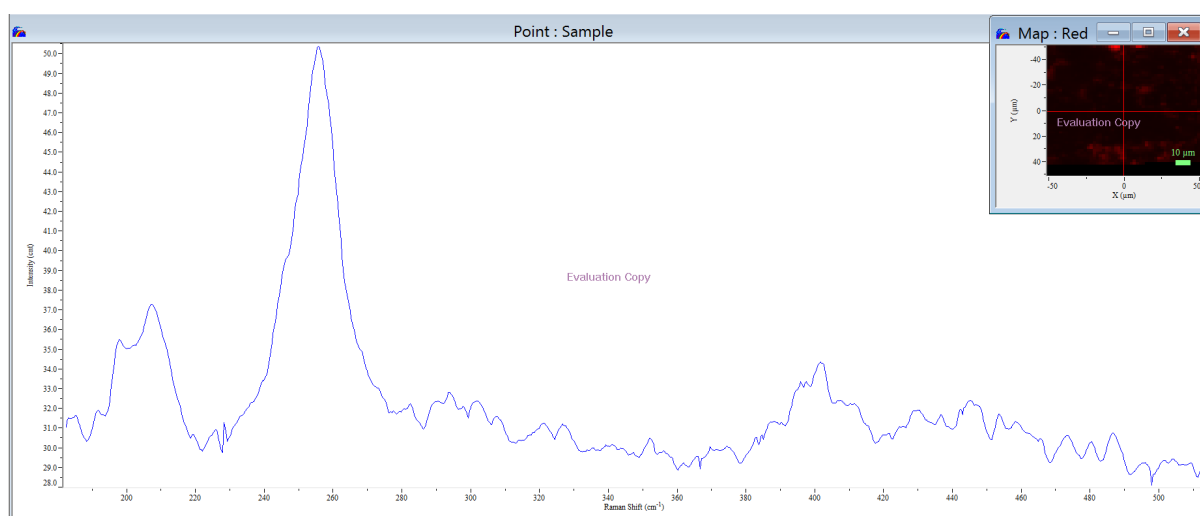
Appendix 5.18 – Raman Map Spectrum of $Li_{0.6}Na_{0.4}CoPO_4$ taken at 0, 0 of the 50 μm^2
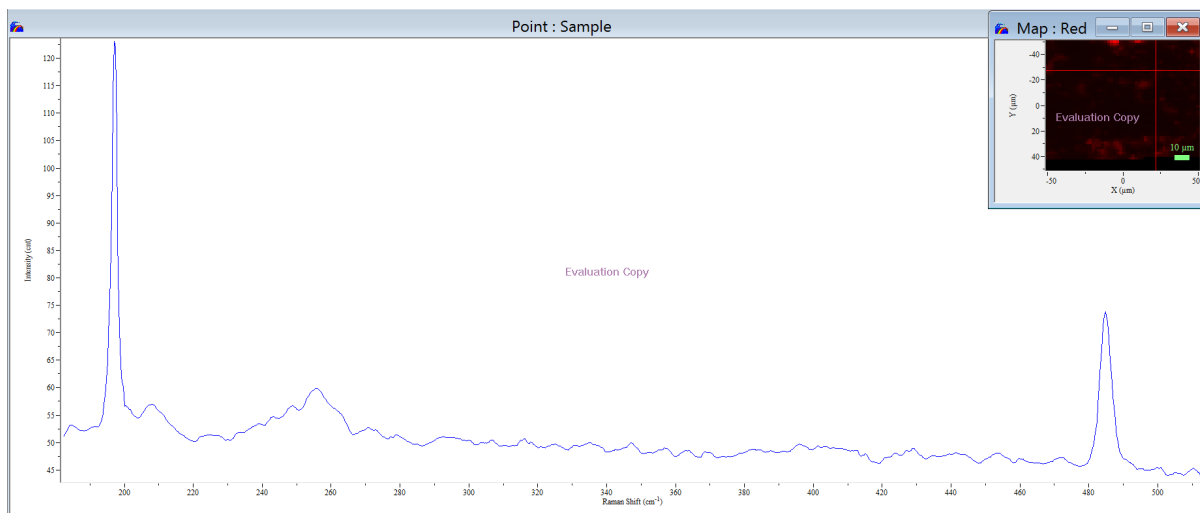
Appendix 5.19 – Raman Map Spectrum of $Li_{0.6}Na_{0.4}CoPO_4$ taken at 24, -28 of the 50 μm^2
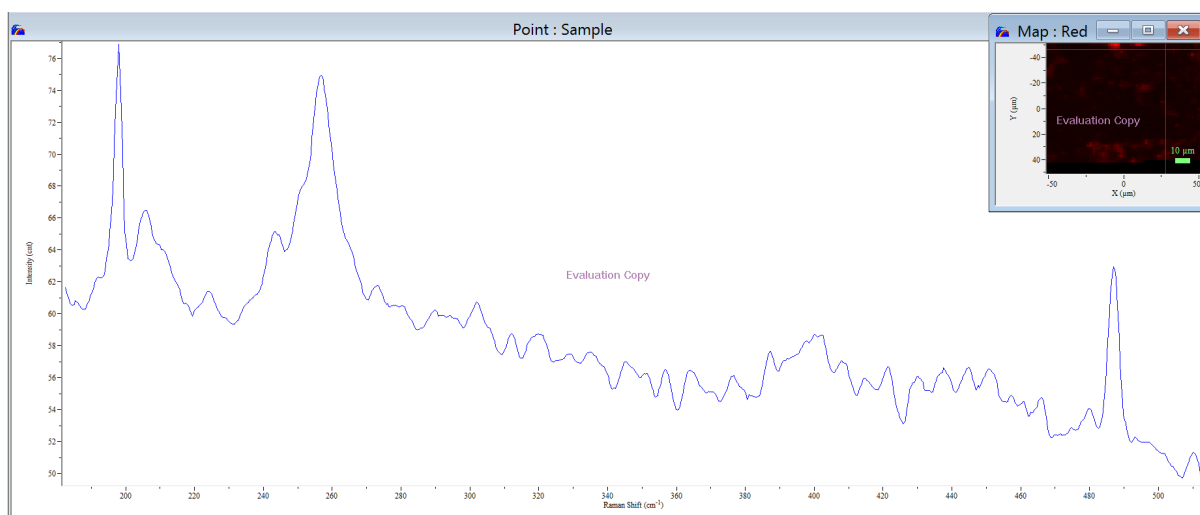
Appendix 5.20 – Raman Map Spectrum of $Li_{0.6}Na_{0.4}CoPO_4$ taken at 25, -45 of the 50 μm^2
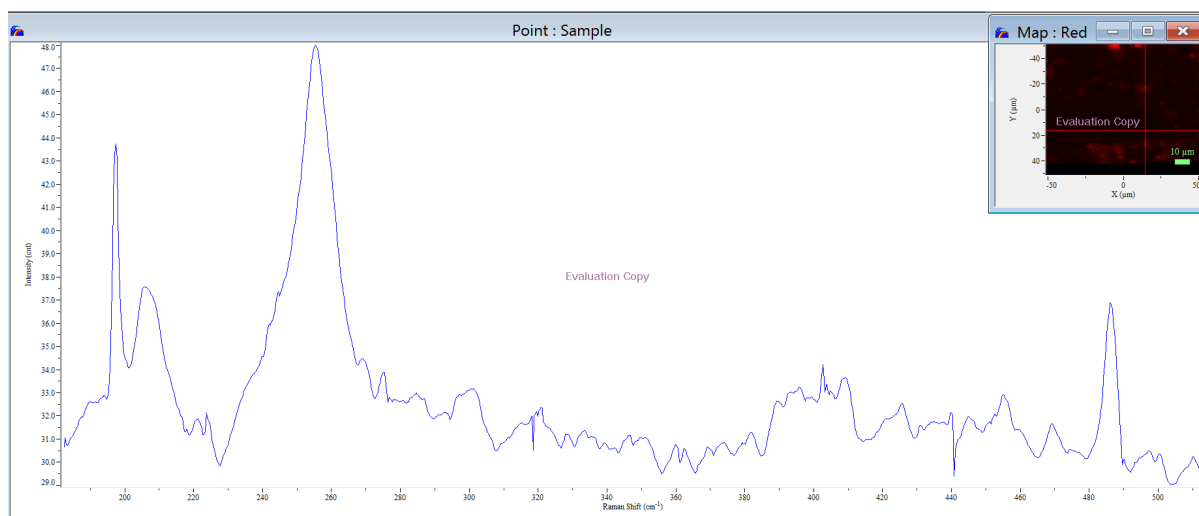
Appendix 5.21 – Raman Map Spectrum of $Li_{0.6}Na_{0.4}CoPO_4$ taken at 15, 15 of the 50 μm^2